Fall 1996

Analysis and design of AC induction motors with squirrel cage rotors

Shine Ho
University of New Hampshire, Durham

INFORMATION TO USERS

This manuscript has been reproduced from the microfilm master. UMI films the text directly from the original or copy submitted. Thus, some thesis and dissertation copies are in typewriter face, while others may be from any type of computer printer.

The quality of this reproduction is dependent upon the quality of the copy submitted. Broken or indistinct print, colored or poor quality illustrations and photographs, print bleedthrough, substandard margins, and improper alignment can adversely affect reproduction.

In the unlikely event that the author did not send UMI a complete manuscript and there are missing pages, these will be noted. Also, if unauthorized copyright material had to be removed, a note will indicate the deletion.

Oversize materials (e.g., maps, drawings, charts) are reproduced by sectioning the original, beginning at the upper left-hand corner and continuing from left to right in equal sections with small overlaps. Each original is also photographed in one exposure and is included in reduced form at the back of the book.

Photographs included in the original manuscript have been reproduced xerographically in this copy. Higher quality 6" x 9" black and white photographic prints are available for any photographs or illustrations appearing in this copy for an additional charge. Contact UMI directly to order.

UMI

ANALYSIS AND DESIGN OF AC INDUCTION MOTORS WITH SQUIRREL CAGE ROTORS

BY

SHINE HO

B.S., University of New Hampshire, 1988
M.S., University of New Hampshire, 1990

DISSERTATION

Submitted to the University of New Hampshire
in Partial Fulfillment of
the Requirements for the Degree of

Doctor of Philosophy

in

Engineering

September, 1996
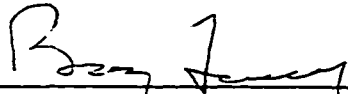
UMI Number: 9703356

UMI
300 North Zeeb Road
Ann Arbor, MI 48103
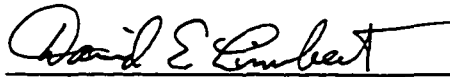
This dissertation has been examined and approved.
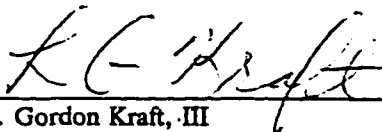
Dissertation Director, Barry K. Fussell
Associate Professor of Mechanical Engineering

Steven R. Prina
Parker Hannifin Corporation

David E. Limbert
Professor of Mechanical Engineering

L. Gordon Kraft, ·III
Professor of Electrical and Computer Engineering

Loren D. Meeker
Professor of Mathematics

1 August 1996
Date

DEDICATION

I dedicate this dissertation with love to my parents for giving me all the support and encouragement. I am eternally indebted to you, dearest mom and dad.

ACKNOWLEDGEMENTS

Without the support of numerous people the successful completion of this dissertation would not have materialized. I am especially grateful for the supervision of my dissertation director, Dr. Barry Fussell, with his tremendous depth in technical expertise. Thank you for granting me this marvelous learning experience. The devotion of Dr. Steven Prina's valuable assistance has been essential. Thank you for taking me under your wings. I express gratitude toward Dr. David Limbert, Dr. Gordon Kraft, and Dr. D. Meeker for donating their time and specialization in becoming an active part of my dissertation committee.

I am indebted to Parker Hannifin Motor Design Center for the financial support and the provision of necessary resources and equipment. Dr. Steven Huard and Dr. Timothy Harned, all of your contributions and crea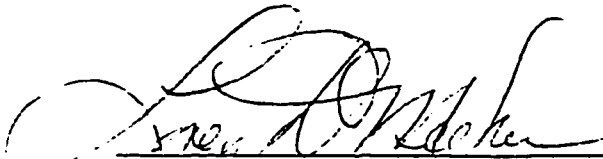tive ideas have been invaluable. Harold Buzzell, with his spirited disposition, has been generous in lending me years of practical experience in getting my hands dirty.

I thank Tim Burke for sharing his expertise. To Dr. Charles Taft, thank you for your wealth of wisdom and for directing me on this journey.

And to my special friend, Michelle, all your help coupled with being patient and understanding has been greatly appreciated. I also extend appreciation to all my family members and friends for their concern and help.

iv

TABLE OF CONTENTS

vii

LIST OF TABLES

viii

LIST OF FIGURES

Page

x

LIST OF SYMBOLS

a^k ≡ cross-sectional area in k^{th} element

a_{rb} ≡ rotor bar cross-sectional area

A^k ≡ magnetic vector potential in k^{th} element

A_h ≡ motor housing surface area

B ≡ magnetic flux density

B^{max} ≡ lamination steel maximum flux density

B_g^{max} ≡ maximum air gap flux density per pole

B_{rib}^{max} ≡ maximum rotor back iron flux density per pole

B_{rst}^{max} ≡ maximum rotor steel tooth flux density per pole

B_{sib}^{max} ≡ maximum stator back iron flux density per pole

B_{sst}^{max} ≡ maximum stator steel tooth flux density per pole

c_{ph} ≡ motor housing specific heat

c_{pr} ≡ rotor squirrel cage specific heat

c_{prs} ≡ rotor lamination steel specific heat

c_{ps} ≡ stator winding specific heat

c_{pss} ≡ stator lamination steel specific heat

C_h ≡ motor housing thermal capacitance

C_r ≡ rotor squirrel cage thermal capacitance

C_{rs} ≡ rotor stack thermal capacitance

C_s ≡ stator winding thermal capacitance

C_{ss} ≡ stator stack thermal capacitance

d_r ≡ rotor squirrel cage skin effects depth

D_{ri} ≡ rotor lamination inner diameter

D_{ro} ≡ rotor lamination outer diameter

D_{si} ≡ stator lamination inner diameter

D_{so} ≡ stator lamination outer diameter

f ≡ lamination steel eddy current frequency

$\mathscr{F}_r^k$ ≡ rotor MMF source in k^{th} rotor tooth from all rotor bar currents

$\mathscr{F}_{rle}$ ≡ rotor end ring MMF source from all rotor bar currents

$\mathscr{F}_{rtz}$ ≡ rotor zig-zag MMF source from all rotor bar currents

$\mathscr{F}_s^k$ ≡ stator MMF source in k^{th} stator tooth from all stator winding currents

$\mathscr{F}_{sle}$ ≡ stator end turn MMF source from all stator winding currents

$\mathscr{F}_{slot}$ ≡ stator or rotor slot MMF source from all stator winding or rotor bar currents

$\mathscr{F}_{stz}$ ≡ stator zig-zag MMF source from all stator winding currents

h_h ≡ housing to ambient convection heat transfer coefficient

H ≡ magnetic field intensity

i_2^k ≡ referred rotor bar current in k^{th} rotor phase to k^{th} stator phase

i_r^l ≡ rotor bar current in l^{th} rotor phase

i_{r2D}^l ≡ rotor bar current in l^{th} rotor phase in the two-dimensional FEA

i_{r3D}^l ≡ rotor bar current in l^{th} rotor phase from rotor three-dimensional leakage flux linkage

i_{re}^k ≡ rotor end ring segment current between k^{th} and $(k+1)^{th}$ or first rotor phases

i_s^k ≡ stator winding current in k^{th} stator phase

I_r ≡ rotor bar current amplitude

I_{re} ≡ rotor end ring segment current amplitude

I_s ≡ stator winding current amplitude

J_s^l ≡ input stator current density amplitude in l^{th} element

k^l ≡ k^{th} stator phase in l^{th} element

k_{air} ≡ thermal conductivity of air

k_h	$\equiv$ effective thermal conductivity of housing body
k_{sl}	$\equiv$ effective thermal conductivity of slot liner
K_o	$\equiv$ lamination steel loss coefficient
K_1	$\equiv$ lamination steel loss flux density exponential coefficient
K_2	$\equiv$ lamination steel loss frequency exponential coefficient
K_c	$\equiv$ Carter's coefficient
K_d	$\equiv$ winding distribution constant
K_{rb}	$\equiv$ rotor bar skin effects constant
K_{re}	$\equiv$ rotor end ring skin effects constant
K_{rT}	$\equiv$ rotor squirrel cage mean temperature coefficient of resistivity
K_{rv}	$\equiv$ rotor EMF trigonometric identity constant
K_s	$\equiv$ steel reluctance constant
K_{se}	$\equiv$ stator end turn extension axial height constant
K_{sT}	$\equiv$ stator winding wire mean temperature coefficient of resistivity
K_{sv}	$\equiv$ stator EMF trigonometric identity constant
K_w	$\equiv$ skew constant
l_g	$\equiv$ air gap radial length
l_{rt}	$\equiv$ rotor steel tooth radial length
l_{st}	$\equiv$ stator steel tooth radial length
L_{2l}	$\equiv$ referred rotor leakage inductance per rotor phase to per stator phase
L_{3D}	$\equiv$ stator and rotor three-dimensional end and skew leakage inductance per stator phase
L_{r3D}	$\equiv$ rotor three-dimensional end and skew leakage inductance per rotor phase
L_{rg}	$\equiv$ rotor air gap inductance per rotor phase
L_{rl}	$\equiv$ rotor leakage inductance per rotor phase
L_{s3D}	$\equiv$ stator three-dimensional end and skew leakage inductance per stator phase
L_{sg}	$\equiv$ stator air gap inductance per stator phase
L_{sl}	$\equiv$ stator leakage inductance per stator phase
m	$\equiv$ number of stator winding phases
n	$\equiv$ number of magnetic poles
n_s^k	$\equiv$ winding turns per stator phase per pole in k^{th} stator concentric winding tier
N_r	$\equiv$ turns per rotor bar pair
N_s	$\equiv$ winding turns per stator phase per pole
P_h	$\equiv$ hysteresis and eddy current power losses in stator and rotor steel
P_{hs}	$\equiv$ hysteresis and eddy current power losses in stator steel
P_{hr}	$\equiv$ hysteresis and eddy current power losses in rotor steel
q_r	$\equiv$ rotor squirrel cage heat source
q_{rh}	$\equiv$ rotor hysteresis and eddy current heat source
q_s	$\equiv$ stator winding heat source
q_{sh}	$\equiv$ stator hysteresis and eddy current heat source
R_2	$\equiv$ referred rotor squirrel cage resistance per rotor phase to per stator phase
R_g^{cnd}	$\equiv$ air gap conduction thermal resistance
R_h^{cnv}	$\equiv$ housing to ambient convection thermal resistance
R_h^{rad}	$\equiv$ housing to ambient radiation thermal resistance
R_r	$\equiv$ rotor squirrel cage resistance per rotor phase
R_{rb}	$\equiv$ rotor bar resistance
R_{re}	$\equiv$ rotor end ring resistance
R_{rch}^{cnd}	$\equiv$ rotor end rings to housing conduction thermal resistance
R_s	$\equiv$ stator winding resistance per stator phase
R_{sch}^{cnd}	$\equiv$ stator end turns to housing conduction thermal resistance
R_{sh}^{cnd}	$\equiv$ stator stack to housing conduction thermal resistance
R_{ss}^{cnd}	$\equiv$ stator windings to stator stack conduction thermal resistance
R_{wire}	$\equiv$ stator winding wire resistance per length at reference temperature
$\mathfrak{R}_g$	$\equiv$ air gap reluctance per pole
$\mathfrak{R}_{sb}$	$\equiv$ stator or rotor slot body leakage reluctance

$\mathfrak{R}_{lsm}$	$=$	stator or rotor slot mouth leakage reluctance
$\mathfrak{R}_{lz}$	$=$	average zig-zag leakage reluctance per slot
$\mathfrak{R}_{rl}$	$=$	rotor leakage reluctance per pole
$\mathfrak{R}_{rlb}$	$=$	rotor belt leakage reluctance per pole
$\mathfrak{R}_{rle}$	$=$	rotor end leakage reluctance per pole
$\mathfrak{R}_{rls}$	$=$	rotor slot leakage reluctance per pole
$\mathfrak{R}_{rlsb}$	$=$	adjusted rotor slot main body leakage reluctance
$\mathfrak{R}_{rlso}$	$=$	adjusted rotor slot mouth opening leakage reluctance
$\mathfrak{R}_{rlw}$	$=$	rotor skew leakage reluctance per pole
$\mathfrak{R}_{rlz}$	$=$	rotor zig-zag leakage reluctance per pole
$\mathfrak{R}_{rnb}$	$=$	rotor back iron reluctance per pole
$\mathfrak{R}_{rnt}$	$=$	rotor steel tooth reluctance per pole
$\mathfrak{R}_{sl}$	$=$	stator leakage reluctance per pole
$\mathfrak{R}_{slb}$	$=$	stator belt leakage reluctance per pole
$\mathfrak{R}_{sle}$	$=$	stator end leakage reluctance per pole
$\mathfrak{R}_{sle1}$	$=$	parallel stator end leakage reluctance per pole
$\mathfrak{R}_{sle2}$	$=$	parallel stator end leakage reluctance per pole
$\mathfrak{R}_{sls}$	$=$	stator slot leakage reluctance per pole
$\mathfrak{R}_{slsb}$	$=$	adjusted stator slot main body leakage reluctance
$\mathfrak{R}_{slso}$	$=$	stator slot mouth opening leakage reluctance
$\mathfrak{R}_{slw}$	$=$	stator skew leakage reluctance per pole
$\mathfrak{R}_{slz}$	$=$	stator zig-zag leakage reluctance per pole
$\mathfrak{R}_{ssb}$	$=$	stator back iron reluctance per pole
$\mathfrak{R}_{sst}$	$=$	stator steel tooth reluctance per pole
s	$=$	slip
S_r	$=$	number of rotor steel teeth or rotor squirrel cage bars
S_s	$=$	number of stator steel teeth or stator slots
t	$=$	time
t_{coil}	$=$	stator coil average tooth span
t_{coil}^k	$=$	stator coil tooth span in k^{th} concentric winding tier
t_h	$=$	motor housing radial thickness
t_{sl}	$=$	slot liner thickness
T	$=$	steady state output torque
T_h	$=$	motor housing steady state temperature at operating speed
T_r	$=$	rotor squirrel cage steady state temperature at operating speed
T_{rr}	$=$	rotor squirrel cage reference temperature
T_s	$=$	stator winding wire steady state temperature at operating speed
T_{sr}	$=$	stator winding wire reference temperature
T_{ss}	$=$	stator stack steady state temperature at operating speed
T_∞	$=$	ambient temperature
v	$=$	lamination steel volume
v_h	$=$	motor housing volume
v_{in}^k	$=$	input stator winding voltage in k^{th} stator phase
v_r	$=$	rotor squirrel cage volume
v_f^k	$=$	sum of EMF voltages in k^{th} rotor phase
v_{rg}^l	$=$	EMF in l^{th} rotor phase from rotor air gap flux linkage
v_{rl}^l	$=$	EMF in l^{th} rotor phase from rotor leakage flux linkage
v_{rs}	$=$	rotor stack volume
v_{rs}^l	$=$	EMF in l^{th} rotor phase from stator air gap flux linkage
v_s	$=$	stator winding volume
v_{sg}^k	$=$	EMF in k^{th} stator phase from stator air gap flux linkage
v_{sl}^k	$=$	EMF in k^{th} stator phase from stator leakage flux linkage
v_{sr}^k	$=$	EMF in k^{th} stator phase from rotor air gap flux linkage
v_{ss}	$=$	stator stack volume

V_{in}	$\equiv$	input stator winding voltage amplitude
V_r	$\equiv$	amplitude of sum of EMF voltages in rotor phase
w_{rso}	$\equiv$	rotor slot mouth opening width
w_{rib}	$\equiv$	rotor back iron radial width
w_{rst}	$\equiv$	rotor steel tooth average tangential width
w_{sso}	$\equiv$	stator slot mouth opening width
w_{ssb}	$\equiv$	stator back iron radial width
w_{sst}	$\equiv$	stator steel tooth average tangential width
W_c	$\equiv$	coenergy
W_s	$\equiv$	magnetic stored energy
X	$\equiv$	independent relationship
z	$\equiv$	stator and rotor stack average axial heights
z_{reh}	$\equiv$	end ring to end cap axial height
z_{seh}	$\equiv$	end turns to end cap axial height
Z_{2D}	$\equiv$	input impedance per stator phase in the two-dimensional FEA
Z_{3D}	$\equiv$	stator and rotor three-dimensional end and skew leakage impedance per stator phase
Z_{in}	$\equiv$	input impedance per stator phase
α	$\equiv$	phase angle lag from input stator winding voltage to stator winding current
γ	$\equiv$	phase angle lag from rotor bar current to rotor end ring segment current
ϵ	$\equiv$	emissivity of nonblackbody material surface
θ	$\equiv$	spatial phase angle
θ_r	$\equiv$	rotor squirrel cage spatial phase angle
$\dot{\theta}_r$	$\equiv$	rotor squirrel cage mechanical rotational frequency
θ_{rtw}	$\equiv$	rotor skew tangential arc angle
λ_{s2D}^k	$\equiv$	stator winding flux linkage in k^{th} stator phase in the two-dimensional FEA
μ^k	$\equiv$	material permeability in k^{th} element
μ_0	$\equiv$	permeability of air
μ_r	$\equiv$	rotor squirrel cage permeability
μ_{rib}	$\equiv$	permeability of steel in rotor back iron
μ_{rst}	$\equiv$	permeability of steel in rotor teeth
μ_{ssb}	$\equiv$	permeability of steel in stator back iron
μ_{sst}	$\equiv$	permeability of steel in stator teeth
ρ	$\equiv$	lamination steel density
ρ_{hd}	$\equiv$	motor housing density
ρ_r	$\equiv$	rotor squirrel cage resistivity at reference temperature
ρ_{r2D}	$\equiv$	rotor bar resistivity in the two-dimensional FEA
ρ_{rd}	$\equiv$	rotor squirrel cage density
ρ_{rsd}	$\equiv$	rotor lamination steel density
ρ_{sd}	$\equiv$	stator winding density
ρ_{ssd}	$\equiv$	stator lamination steel density
σ	$\equiv$	Stefan-Boltzmann radiation heat transfer proportionality constant
ϕ^{ave}	$\equiv$	average air gap flux per pole
ϕ^{max}	$\equiv$	maximum air gap flux per pole
ϕ_{rg}^l	$\equiv$	rotor air gap flux per pole from rotor bar current in l^{th} rotor phase
ϕ_{rl}^l	$\equiv$	rotor leakage flux per pole from rotor bar current in l^{th} rotor phase
ϕ_{sg}^k	$\equiv$	stator air gap flux per pole from stator winding current in k^{th} stator phase
ϕ_{sl}^k	$\equiv$	stator leakage flux per pole from stator winding current in k^{th} stator phase
ψ	$\equiv$	phase angle lag from stator winding current to rotor bar current
ω_e	$\equiv$	stator winding excitation frequency
ω_s	$\equiv$	rotor bar slip frequency
?	$\equiv$	relationship is highly sensitive to rated speed
↑	$\equiv$	increasing relationship
↓	$\equiv$	decreasing relationship

xiv

ABSTRACT

ANALYSIS AND DESIGN OF AC INDUCTION MOTORS WITH SQUIRREL CAGE ROTORS

by

Shine Ho
University of New Hampshire, September, 1996

The traditional approach to modelling the AC induction motor revolves around the well-known equivalent "T" circuit model. In this approach, the direct connection from geometry to performance is suppressed. For better understanding of magnetic, electrical, and thermal behaviors, three lumped models based on the actual geometry are developed in this dissertation. Based on these lumped models, an iterative design model is also developed.

In order to analyze and design induction motors, the relationships of basic motor variables to motor performance must be known. For determining the relationships, three new mathematical lumped models are developed. The magnetic model describes flux behavior. The electrical model, which is similar to the equivalent circuit model, is used to derive simple closed-form expressions of performance. The thermal model describes the effect of heat generation on temperature.

The traditional approach of modelling the induction motor using the finite element analysis (FEA) is through the equivalent circuit model. Three new FEA methods are developed in this dissertation to calculate motor performance directly from the finite element field solution. The equivalent circuit model is no longer needed.

The developed lumped models and FEA methods are applied to two commercial induction motors. Calculated performance is shown to closely match experimental results. The developed iterative design model is then utilized to design an induction motor for desired requirements. The motor is fabricated and calculated performance is also shown to closely match the experimental results.

CHAPTER I

INTRODUCTION

Having been in existence for over a hundred years, the induction motor is often labelled the grandfather of all motors. Many books and technical papers have been published on the design process for achieving specific performances. The traditional approach to modelling the induction motor revolves around the well-known equivalent "T" circuit model. Originating from a transformer model, the equivalent circuit model is presently the most common method of induction motor analysis and design. The traditional approach of modelling the induction motor using the finite element analysis (FEA) is through the equivalent circuit model. The traditional design approach relies on empirical data from existing motors and the equivalent circuit model. Cyril Veinott outlined a design strategy using the model. Accepting much of this approach requires faith in the collected empirical data and his experience.

Although the model may sometimes yield good results, the magnetic basis is not clear. The direct connection from geometry to performance parameters is suppressed. The model by itself serves more as an analysis tool than a design tool.

For better understanding of magnetic, electrical, and thermal behaviors, three new lumped models based on actual motor geometry are developed in this dissertation. The magnetic model describes flux behavior. The electrical model, which is similar to the equivalent circuit model, is used to derive simple closed-form expressions of performance. The thermal model describes the effect of heat generation on temperature. Based on these lumped models, an iterative design model is also developed. In addition, three new FEA methods are developed to calculate motor performance directly from the finite element field solution rather than through the equivalent circuit model. Although the emphasis in this work has been placed on the three-phase induction motor with a squirrel cage rotor, the same modelling approaches hold for the induction motor of any number of phases and any rotor type.

The developed lumped models and FEA methods are applied to two commercial induction motors. Calculated performance is shown to closely match experimental results. The developed iterative design

-1-

model is then utilized to design an induction motor for desired requirements. The motor is fabricated and calculated performance is also shown to closely match the experimental results.

I.A. Background

Induction motors are mechanically simple devices that operate reliably with little or no maintenance. Their inherent robustness allows them to withstand harsh surroundings, even to the point of explosive conditions. Furthermore, they have a good capacity to handle infrequent overloading on a short duration basis. Material costs are low, availability is wide, and installation is simple.

The origin of the induction motor is in the late nineteenth century. Nikola Tesla (1856-1943) invented the polyphase AC induction motor not as a result of intense research, but surprisingly, while on vacation. Educated in Hungary, he immigrated to the United States in 1884. On one vacation at the seashore he sketched the stator, excitation configuration, rotor, and other drawings in the sand. He proved that the rotating field produces torque. In 1888, he was granted a patent, the rights to which were later sold to George Westinghouse.

Over a span of fifteen years in the forties and fifties, materials and design techniques advanced very quickly. Output power ratings doubled and even tripled for any given motor frame size of integral horsepower polyphase induction motors with squirrel cage rotors.[1] Beyond the fifteen-year interval, progress further accelerated. Around 1950, about fifteen million single-phase induction motors were produced annually. In that period, some estimates surpassed thirty million polyphase induction motors producing approximately one hundred million horsepower. This corresponds to an annual increase of about one percent in all American industry.[2] In the late sixties, more than ninety percent of industrial application motors were polyphase induction motors.[3] The value of induction motors applied to laundry

---

[1]Cyril G. Veinott, *Theory and Design of Small Induction Motors*, New York: McGraw-Hill Book Company, Inc., 1959, p. xv.

[2]Philip L. Alger, *The Nature of Polyphase Induction Machines*, New York: John Wiley & Sons, Inc., 1951, p. 95.

[3]Tom C. Lloyd, *Electric Motors and Their Applications*, New York: John Wiley & Sons, Inc., 1969, p. 108.

equipment alone surpassed an annual amount of fifty million dollars in the United States during that period.[4] It is easy to see how any slight improvement in manufacturing cost or efficiency would have had, and will continue to have, a dramatic effect.

I.B. Description of the Induction Motor

An AC induction motor primarily consists of a stationary member, called the stator, and a rotating member, called the rotor. The stator stack resembles a thick donut made of steel with slots cut out along the inner perimeter to carry coil windings. Coils of insulated copper wire filling the stator slots are wound around the stator teeth, the steel regions between adjacent slots. The rotor fits snugly into the stator forming a concentric structure with a small radial air gap between them.

The rotor stack also resembles a thick doughnut made of steel, but with slots cut out along the outer perimeter. Rotor slots are filled with conductors composed of coils of copper wire or bars of copper or aluminum. When bars are used, they are all short circuited at the axial ends by end rings usually constructed of the same material. End rings form closed loops for the bars so currents can have return paths. A rotor that contains the conducting bars short circuited by end rings is classified as a squirrel cage rotor because of the structural resemblance. The cutaway view of a squirrel cage induction motor is shown in Figure 1.1, taken directly from the footnoted reference[5]. Fans protrude from the end rings to help ventilate the motor.

A protective housing frame with end caps encloses the stator but can allow for adequate ventilation. A shaft attached to the rotor runs axially through its center for transferring the produced torque to the application. Bearings attached to the shaft support the rotor within the stator. The most distinct difference between the induction motor and other electric motors lies in the rotor. The induction motor rotor can have windings of copper wire or a squirrel cage construction. The former is especially common in large horsepower applications due to the wire cost advantage. Unlike most other types of motors, no

---

[4]Tom C. Lloyd, *Electric Motors and Their Applications*, New York: John Wiley & Sons, Inc., 1969, p. 135.

[5]A. E. Fitzgerald, Charles Jr. Kingsley, and Stephen D. Umans, *Electric Machinery*, Fifth Edition, New York: McGraw-Hill, Inc., 1990, p. 158.

-3-
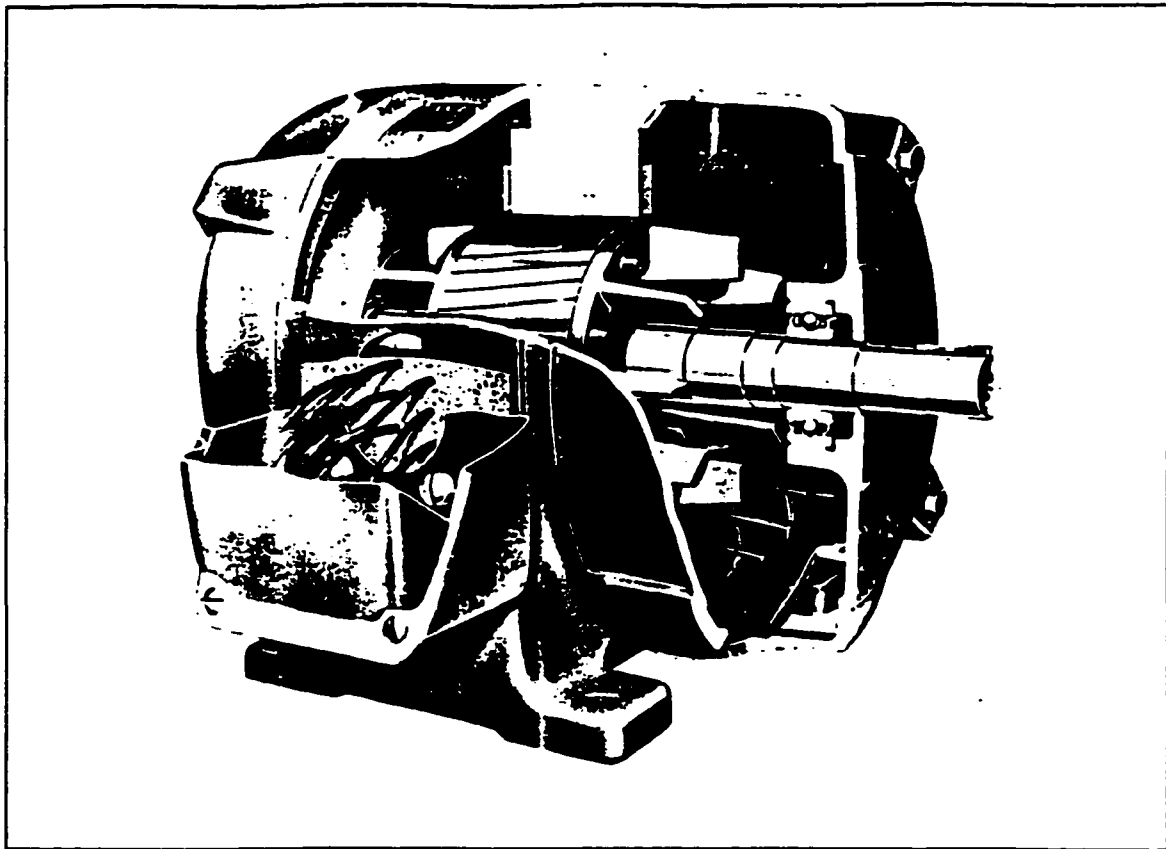
Figure 1.1 Cutaway view of an AC induction motor with squirrel cage rotor.

permanent magnet exists in the rotor. As a result, material costs are low.

I.C. Energizing the Induction Motor

Single-phase excitation is common for most fractional horsepower induction motor applications, and three-phase excitation is common for most integral horsepower applications. Polyphase excitation customarily refers to three-phase AC excitation despite the literal definition of the prefix, poly-, intended for any number more than one. Single-phase AC excitation requires additional starting mechanisms because no inherent starting torque is produced. Induction motors with polyphase excitation, which eliminates the necessity of a mechanism for starting, operate more efficiently, but also cost more in general than single-phase induction motors. Regardless, three-phase power may not always be readily available except in major commercial and industrial establishments.

The stator is usually wound with a balanced winding scheme and energized with a sinusoidal balanced polyphase excitation that forces currents in the stator windings. A balanced winding scheme has

-4-

windings that are spatially distributed evenly around the stator. Since spatial phase angles are invariably expressed by electrical phase angles which are defined later, this trend is applied herein unless otherwise specified. A balanced polyphase excitation has three phases of voltage or current with equal amplitude that are evenly phase shifted in time relative to each other.

AC power is used to energize the stator windings. The typical low cost voltage drive feeds a sinusoidal excitation at constant voltage amplitude and frequency. The voltage driven motor normally runs at relatively low efficiency and generates low levels of heat at rated speed. However, no drive electronics are required as long as three-phase power is available for polyphase motors. Until the early seventies, the majority of induction motors produced were voltage driven.

The most popular method of controlling variable speed induction motors is called scalar control. Both amplitude and frequency of the input sinusoidal voltages or currents are regulated. Steady state, but not transient, performance characteristics are tuned effectively. With scalar control, the induction motor presently rivals permanent magnet motors in many industrial applications such as pumps, compressors, and conveyor belts. Since neither instantaneous speed nor instantaneous torque is precisely monitored, accurate position control is difficult. In today's competitive motion control market more demanding specifications require better designs. In response, vector control, briefly described in Appendix B, has been recently developed to provide the induction motor with the ability to produce higher torque at variable speeds and to attain higher running efficiency.

The Field Orientation Principle, which is the theory behind vector control, was first developed in 1968 by Hasse[6] and then in 1970 by Blaschke[7]. Due to a deficiency in technology for implementation, the idea did not thrive until the eighties. Motors are designed to always operate at optimal torque production by monitoring steady state as well as transient performance characteristics. To achieve this, both the amplitude and phase angle of the currents from the current supply can be adjusted. With vector

---

[6]K. Hasse, "About the Dynamics of Adjustable-Speed Drives with Converter-Fed Squirrel-Cage Induction Motors" (in German), Dissertation, *Darmstadt Technische Hochschule*, 1969.

[7]F. Blaschke, "The Principle of Field-Orientation as Applied to the New 'Transvektor' Closed-Loop Control System for Rotating-Field Machines," *Siemens Review*, Vol. 34, No. 5, 1972, pp. 217-220.

control, the induction motor can provide accurate position control. Vector control ensures optimal output even under changing load conditions. Overloading occurs only when the maximum supply current is exceeded. Vector control can even provide better dynamic performance than DC drives due to faster allowable speeds and shorter motor time constants.

I.D. Magnetic Fields in the Induction Motor

When electric current flows in a conductor, it produces magnetic flux. The strength and direction of the flux describe a magnetic field map. The stator in a motor consists of many conductors in slots, most of which may accommodate conductors excited by more than one phase. The vector sum of all the individual magnetic fields from the current in individual conductors results in a net magnetic field produced by all the stator currents.

In an AC motor, the currents vary sinusoidally with time causing the magnetic field to also vary sinusoidally with time. The field of a balanced winding scheme with sinusoidal balanced polyphase excitation, in effect, rotates with virtually constant amplitude about the shaft. For single-phase excitation, on the other hand, the field grows and decays in strength, but does not rotate. Maintaining a smooth field rotation is advantageous because it minimizes torque ripple. It is usually desirable for output torque to remain constant over time when operating at constant speed.

When magnetic flux flows through a coil of wire, it "links" that conductor. Faraday's law of induction states that a changing magnetic field linking a conductor induces in the conductor a voltage proportional to the rate of change of the flux linkage. Therefore, as long as the conductors on the rotor experience the time varying magnetic field established by the stator currents, voltages are induced across the conductors. Thus, the origin of the induction motor name can be readily appreciated. The induced voltages force currents to flow in the rotor conductors setting up another magnetic field that also rotates about the shaft like the field from stator currents of polyphase excitation. Furthermore, when the conductors on the stator experience the time varying magnetic field established by the rotor currents, voltages are also induced across the stator windings opposing the input stator excitation.

The stator magnetic field originates from the stator currents, while the rotor magnetic field originates from the induced rotor currents. The actual field existing in the motor is the combination of the

-6-

two fields. The strengths of the two magnetic fields in the air gap can be described using two magnetic flux vectors. Stator and rotor air gap flux vectors point radially outward from the shaft in the direction of highest instantaneous flux levels in the air gap due to respective stator and rotor currents. The interaction of the stator and rotor flux vectors produces torque on the shaft.

Single-phase excitation produces stationary air gap flux vectors that pulsate, thus requiring an external starting mechanism. Multiple-phase excitation, mostly for high performance applications, produces rotating air gap flux vectors. The flux vectors rotate virtually smoothly with constant amplitudes when the multiple-phase sinusoidal excitation is balanced in time and space. When relative motion exists between the stator flux vector and the conductors on the rotor, voltages are induced across the conductors. Furthermore, the relative motion between the rotor flux vector and the conductors on the stator also causes voltages to be induced across the stator windings opposing the input stator excitation.

The complexities of modelling the induction motor concern its rotor flux vector. The flux vector is purely the result of the induction process, which depends on the difference between the stator excitation frequency and the rotor mechanical speed. This causes the strength and direction of the rotor flux vector to vary with rotor speed. The rotor flux vector of permanent magnet motors, on the other hand, is attached to the rotor. Neither the strength nor direction is a function of rotor speed.

A variable called slip defines the difference between synchronous speed and actual rotor speed. Slip is more commonly expressed as a percentage of synchronous speed. Slip frequency specifies the frequency at the slip speed. When the rotor is stalled at starting, slip is one hundred percent and slip frequency equals the excitation frequency. When the rotor rotates at synchronous speed, slip and slip frequency are both zero.

The motor synchronous speed is dictated by the stator winding excitation frequency and the number of magnetic poles for which the motor is wound. A pair of poles, which rotate with flux vectors, exists where flux flowing in opposite directions merge and emerge[8] in the stator back iron, the steel region radially away from the stator slots. Without friction, the synchronous speed is the fastest rotor mechanical

---

[8]David Halliday and Robert Resnick, *Fundamentals of Physics*, Second Edition, Extended Version, New York: John Wiley & Sons, Inc., 1970, p. 608.

-7-

rotational speed occurring under no load. At this speed, no rotor currents are induced since rotor conductors rotate in phase with the stator magnetic field. Therefore, freely operating at the synchronous speed is not possible because no torque is produced to sustain rotor rotation.

The induced voltages in the rotor operate at the slip frequency due to the relative motion between the stator magnetic field and the rotor conductors. Rotor currents resulting from the induced voltages also operate at the slip frequency. A rotor flux vector is produced that rotates at the slip frequency relative to the rotor. Unless otherwise specified, the rotational velocity of flux vectors is measured in electrical phase angles per unit of time. The flux vectors spatially rotate through one pole pair over a temporal cycle. Therefore, the electrical phase angle equals the product of the spatial phase angle and the number of pole pairs.

The interaction between the stator magnetic field and the rotor currents that the field induced causes a rotor rotation in the direction of the stator flux vector. The two flux vectors and the rotor itself all rotate in the same direction. When the rotation of the rotor flux vector is superimposed onto the mechanical rotation of the rotor, the vector rotates at the excitation frequency relative to the stator. Since the flux vectors rotate at the same frequency when in the same reference frame, a steady torque is generated sustaining a constant rotor rotation.

I.E. Leakage Flux in the Induction Motor

If all the flux flows across the air gap to link conductors on the other side, then modelling the induction motor would be much simpler. However, leakage flux exists across slots, at the axial ends, and in other regions. Only air gap flux produces torque, while leakage flux decreases torque production. Therefore, it is desirable to minimize leakage flux for maximum torque. In permanent magnet motors, leakage flux is not as critical because it is usually small relative to air gap flux and it does not affect rotor flux. In the induction motor, leakage flux not only decreases stator currents that induce rotor flux, but also decreases rotor currents. Relative to the effective air gaps of permanent magnet motors, induction motors therefore have characteristically small air gaps to decrease the effects of leakage flux on torque.

Using steel in the stator and rotor helps to minimize some leakage by directing flux through the back iron and teeth and across the air gap. Back iron is the steel region that is not between adjacent slots.

-8-

In the stator, back iron is the region radially away from the slots, but in the rotor, back iron is the region radially between the shaft and the slots.

A laminated stack construction helps to minimize axial eddy currents that are induced in the steel. Many axially thin lamination slices are coated with insulation and pressed together with nonconductive adhesive to increase the electrical resistance to current flow in the axial direction. Much of the current is confined to conductors running axially in the stack. Some eddy currents may also run in the plane of the steel laminations due to currents in the stator end turns and rotor end rings as well as due to rotor skewing. Rotor skewing is explained later. Eddy current losses in the steel which are dissipated as heat are decreased through a laminated stack, and so efficiency is increased. Also dissipated as heat, hysteresis power losses occur when materials experience magnetic cycling.

One type of leakage flux causes skin effects. Due to leakage flux across slots, conductors connected in parallel at the radial top and bottom of a slot link different amounts of flux. An induced voltage gradient occurs throughout the parallel conductors causing the current distribution in the conductors within the slot to be nonuniform. The gradient grows with increasing current frequency and radial slot length. Circulating currents form pushing the through currents to the peripheral conductors, thereby increasing the effective resistance of the conductors. This phenomenon, called skin effects, occurs primarily in squirrel cage rotors. Radially deep bars and end rings cause increased skin effects that boost torque and heat generated at stall while maintaining relatively high rated torque and speed. Since most motors are serially wound with thin conductors relative to the squirrel cage, skin effects can be neglected in the stator and in the wound rotors.

The discovery of skin effects is credited to the inventor of the polyphase induction motor, Nikola Tesla, through use of the "Tesla coil". Interestingly, the coil, which has seen almost no use in the commercial world, was only utilized in some carnivals where the public could see one million AC volts connected to a little lady. One of her hands touched one terminal of the transformer's secondary coils which delivered the high voltage cycling at five hundred thousand hertz. Sparks stemmed from her other hand to nearby grounded objects. Skin effects acted as a shield to prevent the high frequency current from penetrating deeply enough to make contact with nerve endings. "The little lady felt nothing at all except

-9-

a slight prickling sensation as the spark jumped."[9]

I.F. Harmonics in Flux Density Distributions

In the induction motor, a sinusoidal spatial distribution of stator and rotor fluxes across the air gap is critical. A nonsinusoidal distribution can be represented by a Fourier series. Unfortunately, only the fundamentals of the series produce useful torque. The higher harmonics cause undesirable effects such as vibration, noise, and heat. Therefore, many techniques are used to minimize harmonics in the air gap flux density distributions.

A popular scheme to decrease harmonics is to use concentric stator windings where tiers of coils centering on the same tooth are wound from one wire. The coils of each successive tier span successively less teeth and usually contain less winding turns. Two matching sets of tiers are used to wind a pole pair with all tiers connected in series for a phase. More tiers lead to a more sinusoidal air gap distribution. On the other hand, many tiers require many slots and cause winding difficulties as well as narrow teeth. Leakage flux is increased in narrow teeth because some of the flux is forced to seek alternate paths other than down the lengths of the teeth. Also, saturation of magnetic flux may result. Saturation is a condition where a material has been magnetized to the highest possible degree so that the material can no longer carry any more flux. Saturation in the teeth causes harmonics by flattening the peak of the virtually sinusoidal air gap flux density distributions.

A solution to the trade-off between the number of winding tiers and the number of stator slots is to allow for more than one bundle of coils from more than one phase in each slot. This multiple-layer technique reduces the necessary number of slots by more evenly allocating the amount of coils. Slot are used more efficiently. Winding for more than two layers is rare because of overcrowding and winding difficulties.

Still another technique that reduces harmonics in the air gap flux density distributions is cutting ears at the radial ends of teeth. Steel ears, which tangentially protrude to both sides at the tooth tips, extend the steel arc area to better distribute the concentrated flux flowing down the length of the teeth

---

[9]Tom C. Lloyd, *Electric Motors and Their Applications*, New York: John Wiley & Sons, Inc., 1969, p. 108.

across the air gap. Longer ears lead to larger arc areas and improved distributions. Unfortunately, overextended ears foster heavy flux leakage across the ear tips as well as structural problems.

Ordinarily, the rotor is skewed to further reduce harmonics in the rotor air gap flux density distribution. Skewing cancels out some harmonic interactions between the stator and rotor air gap flux density distributions despite causing some additional torque disturbance from axial flux. Conceptually, rotor skewing is a circumferential twisting of the squirrel cage from the end rings in opposite directions. Rotor bars no longer stand axially and no longer run parallel to the shaft. Designing for many rotor bars also decreases harmonics in the rotor air gap flux density distribution, but can cause saturation in the rotor teeth and can increase rotor heat generation.

Figure 1.2 illustrates a cross section of the basic components of a simple polyphase AC induction motor wound for two poles. The three stator phases designated by squares, triangles, and circles sit in only twelve stator slots. The windings of each phase consist of one tier per pole with one layer of windings in each slot. The air gap has been exaggerated for clarity. Twelve rotor bars are represented by the semirectangular darkened areas tangent to the rotor outer diameter. Rotor skewing and rotor end rings are not shown. The rotor teeth do not have any ears. The shaft is axially inserted through the rotor inner diameter. Except at the tooth tips, the width of the stator teeth is constant throughout the radial length, while the width of the rotor teeth is tapered.

I.G. Overview of Chapters

This dissertation has been divided into eight chapters along with two appendices. Chapter I introduced the induction motor and its components. A brief history of the invention of the motor was given. A comparison of single-phase excitation versus polyphase excitation was made. Methods of driving and controlling the induction motor were provided. The basic theory behind the production of torque in the induction motor was presented. Since torque is produced from only the fundamental of the air gap flux density distributions, many techniques for decreasing harmonics were explained.

For determining output performance by lumped models, the magnetic, electrical, and thermal behaviors of the induction motor are addressed. Chapter II discusses the lumped magnetic model which determines the flux behavior in critical parts of the motor from motor geometry and material properties.

-11-
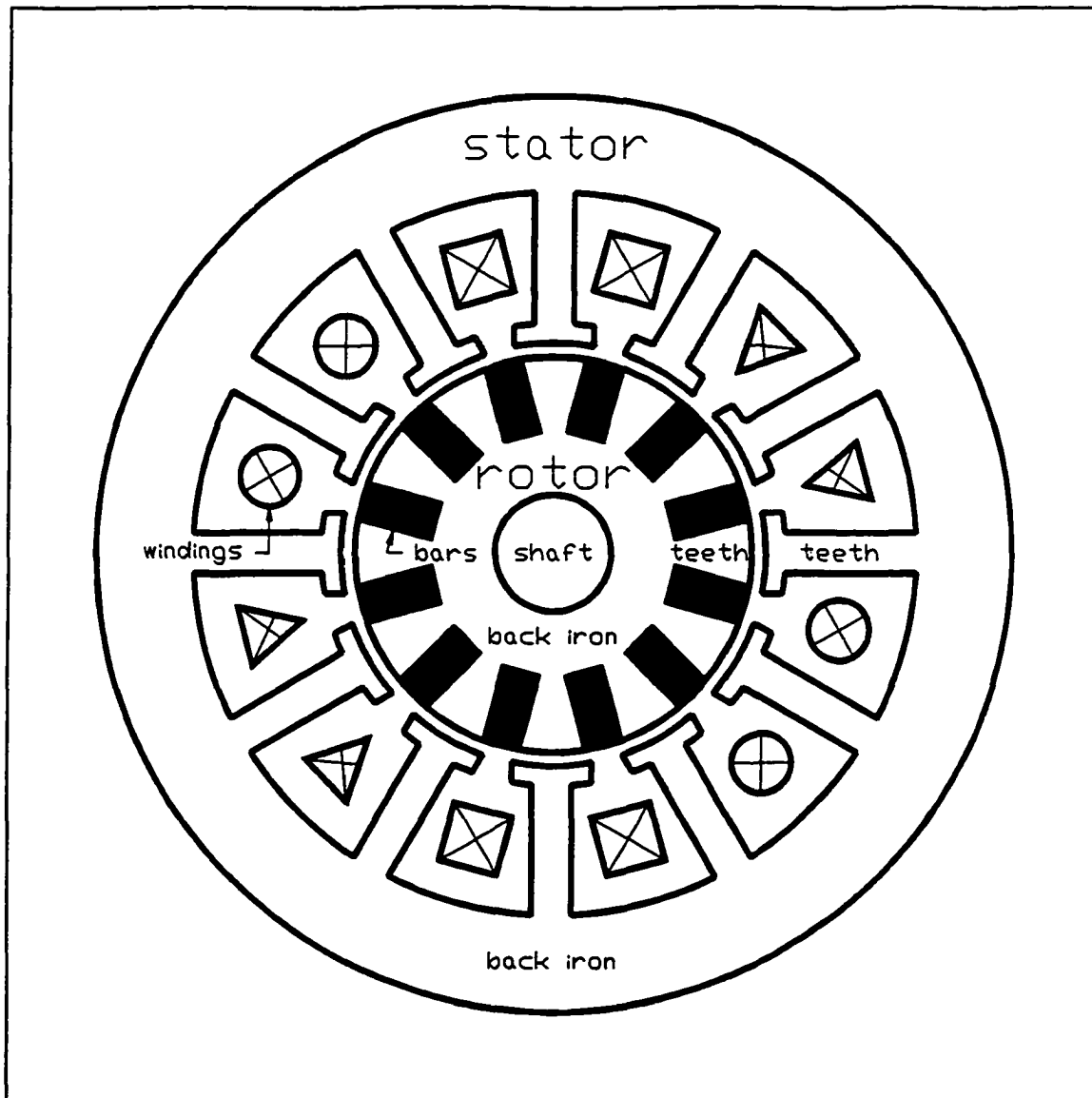
Figure 1.2 Cross section of a simple polyphase AC induction motor wound for two poles.

Stator and rotor air gap fluxes, the interaction of which produces useful torque, are formulated. Magnetomotive force (MMF) drops in the steel are included because they are significant due to the characteristically small induction motor air gap. Stator and rotor leakage fluxes, which decrease useful tangential force and produce harmful radial force, are also formulated. Leakage flux, ordinarily divided into five parts commonly referred to as slot, zig-zag, end, belt, and skew leakage fluxes, is briefly explored.

Chapter III discusses the lumped electrical model consisting of resistances and inductances. Stator winding resistance is formulated. The complete squirrel cage is modelled to include both the bar and end

-12-

ring resistances. The inductances are used to model the electromotive force (EMF) voltages from the time derivative of linkage with stator and rotor air gap and leakage fluxes. Stator and rotor currents are expressed in terms of the resistances and inductances. Voltage equations that describe the lumped electrical model are compared with those that describe the general equivalent "T" circuit model. Simple closed-form expressions of output performance characteristics are derived from input voltages, stator currents, rotor currents, resistances, and inductances.

Chapter IV discusses the lumped thermal model which describes the effect of heat generation on temperature in terms of motor geometry and material properties. The temperature information is used to evaluate resistances. Steady state and transient temperatures are derived from heat sources, thermal capacitances, and thermal resistances. Heat sources arise from power losses in the motor. Thermal capacitances are used to model materials storing thermal energy. Thermal resistances model heat transfer through conduction, convection, and radiation.

Chapter V describes three magnetic FEA methods to determine performance in the induction motor from two-dimensional field solvers. Three-dimensional effects estimated from the lumped models are included. In the first method, torque is calculated through the method of virtual work directly from the steady state and static field solutions. In the second method, torque is derived through the power difference method directly from the steady state field solution. For the current driven motor, torque, horsepower, and power losses are derived in the two methods. For the voltage driven motor, torque, horsepower, power losses, power factor, and efficiency are derived in the two methods. In the third method, performance calculations are made directly from the transient field solution.

Chapter VI presents the experimental results of two commercial induction motors. The experimental configuration is described. The experimental results are compared with current and voltage driven torques determined from the lumped models and FEA methods. Also, transient temperature is calculated at stall from the lumped thermal model and compared to experimental results. Sources of error are explained.

Chapter VII discusses the iterative design model for the voltage driven induction motor. Necessary inputs are explained. The model iterates around main motor dimensions to design for desired flux density

-13-

levels. Performance is determined from the lumped models and compared with desired requirements. The model is verified by using two existing motors. It is then utilized to design an induction motor for desired requirements.

Chapter VIII, contains concluding remarks and strategies for future work. Suggestions are made on improvements and additions to the developed lumped models, design model, and FEA methods.

Appendix A presents the general equivalent "T" circuit model. Output performance expressions derived from the model are discussed. The traditional strategy of FEA modelling the induction motor through the equivalent circuit model is briefly described. The traditional design approach which uses the equivalent circuit model is introduced.

Lastly, Appendix B briefly describes the classical approach to vector control of the induction motor through the rotor flux vector. The flux vector can be detected using direct or indirect rotor flux oriented scheme.

CHAPTER II

LUMPED MAGNETIC MODEL

II.A. Introduction

In order to analyze and design induction motors, the relationships of basic motor variables to motor performance must be known. A set of mathematical equations, derived from the magnetic, electrical, and thermal models, are developed in the next chapter to determine the relationships. This chapter derives the magnetic model, which uses electromagnetic theory to describe flux behavior from motor geometry and material properties.

Developing an accurate magnetic model for the induction motor is much more difficult than for permanent magnet motors. In the latter motors, MMF drops in the steel and leakage flux can be neglected. However, due to the characteristically small air gap in the induction motor, the MMF drops must be considered here because they significantly influence performance. Furthermore, permanent magnet motors are often represented by very simple magnetic models that contain only air gap flux. In the induction motor, leakage flux must be included as well because it also significantly influences performance.

To obtain the flux behavior in the induction motor, a lumped magnetic model that includes MMF drops in the steel and leakage flux is developed. The MMF drops and leakage flux along with MMF sources and air gap reluctance in the model are formulated. Flux in critical regions of the motor is then derived.

II.B. Development of the Lumped Magnetic Model

In developing flux behavior in the induction motor, a simple lumped magnetic model that contains only flux crossing the air gap is first introduced to initially simplify the analysis. MMF drops in the steel and leakage flux are neglected for now. Also, the number of stator and rotor teeth is constrained to be equivalent. Later, a general lumped magnetic model that includes the MMF drops and leakage flux is derived for any combination of stator and rotor tooth counts.

-15-

In a lumped magnetic model approach, the flux density distribution is assumed to be uniform throughout a material body that is placed inside a coil of current carrying wire. In theory, however, the assumption is not exactly valid. Figure 2.1 shows the cross section of the flux density distribution in a block of unsaturated steel. The steel is wrapped around by a wire carrying static current. Flux flows inside the coil through the highly permeable steel and around the coil through air. The coil is assumed to be axially deep enough so that flux produced by current in the end turns is neglected.
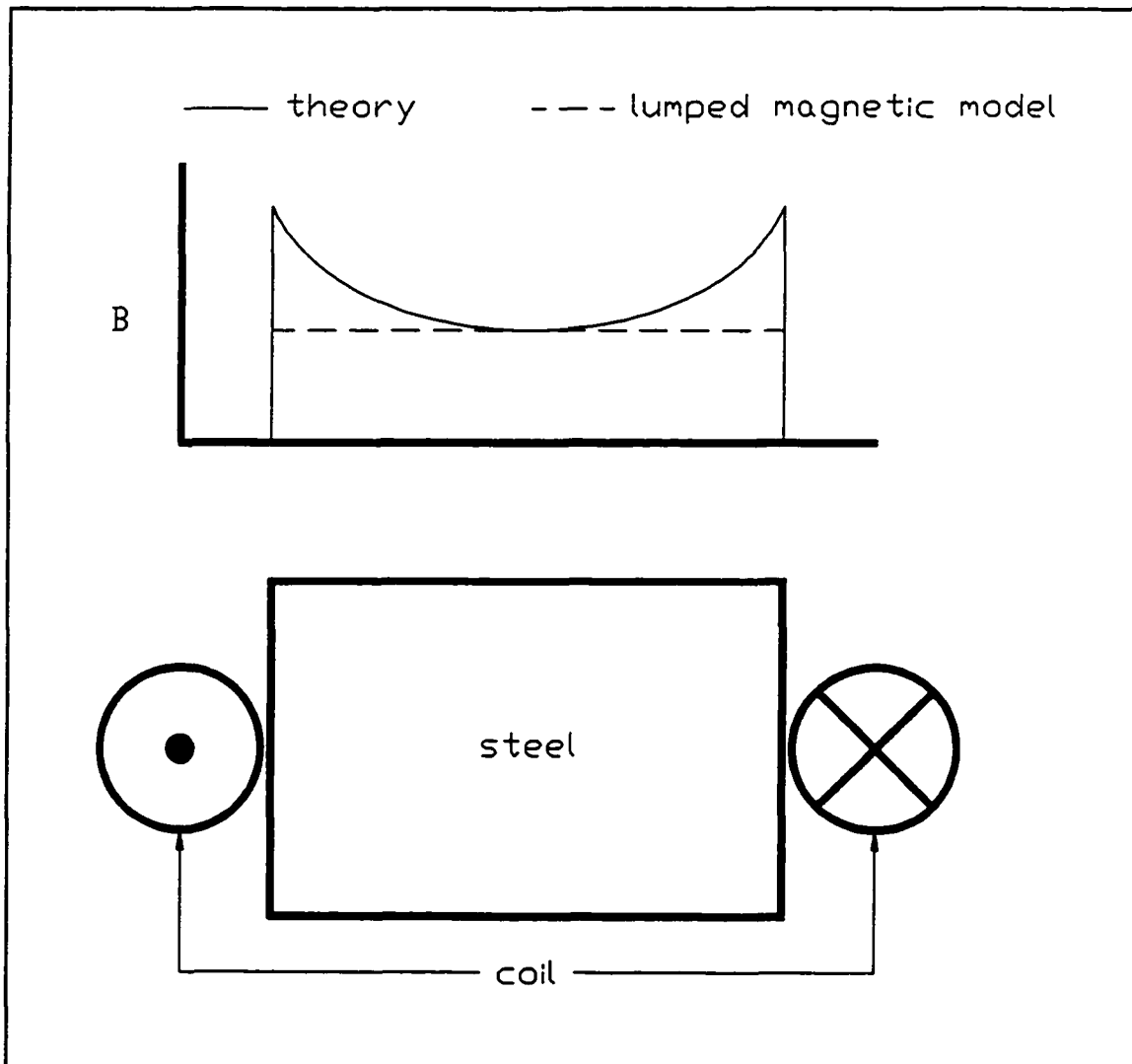
Figure 2.1 Flux density distribution in steel cross section.

The theoretical flux density distribution has a smooth valley in between two sharp peaks. The lumped approach uses the magnitude at the valley as the amplitude of the uniform flux density distribution. Ignoring the peaks causes an error in the lumped magnetic model. The peaks, however, can be

-16-

dramatically reduced by completely wrapping the steel around the wire with a small air gap. In this case, the air gap is of constant length and spreads the whole width inside the coil. The induction motor therefore has a small air gap between the stator and rotor and has windings placed in slots surrounded almost completely by steel. But, if more accuracy is still necessary in taking the lumped approach, then material bodies can be modelled as parallel sections in the direction of flux flow. A uniform flux density distribution would be assumed in each section.

Under the assumption of uniform distribution, magnetic behavior is directly analogous to electrical behavior. Thus, well-known electrical circuit theory is used to develop the lumped magnetic circuit model. A voltage across an electrically conductive material produces a current flowing through the material resistance. Similarly, a current called a magnetomotive force, MMF, induces magnetic flux flowing through a magnetically conductive material. The voltage is analogous to the MMF, the current is analogous to the flux, and the material electrical resistance is analogous to material magnetic reluctance. The reluctance resists flux flow just as the resistance resists current flow. Both are material properties. Flux flowing through a material is derived from the MMF drop across the reluctance of the material just as current flowing through a material is derived from the voltage drop across the resistance of the material.

II.B.1. The Air Gap Lumped Magnetic Model

The lumped magnetic model considers only motor sections that contain significant flux levels. Since only flux that crosses the air gap produces torque, a simple magnetic model that contains only air gap flux is presented here. Although leakage flux exists along with the air gap flux, it is neglected for now. In addition, MMF drops in the steel are also neglected for now.

The simple magnetic model is derived by first drawing the air gap flux path. Figure 2.2 shows a cross section of the instantaneous stator air gap flux for a very simple polyphase induction motor wound for two poles. The three stator phases designated by squares, triangles, and circles are spatially balanced. The air gap has been exaggerated for clarity. Leakage flux and rotor end rings are not shown. A differential time slice is taken of the flux path across the air gap through the six stator and six rotor teeth. The flux travels tangentially in the back iron and radially in the teeth. The nonpermeable motor shaft at the center of the rotor forces flux to flow around it. For a magnetically permeable shaft, the flux would

-17-

flow straight through.
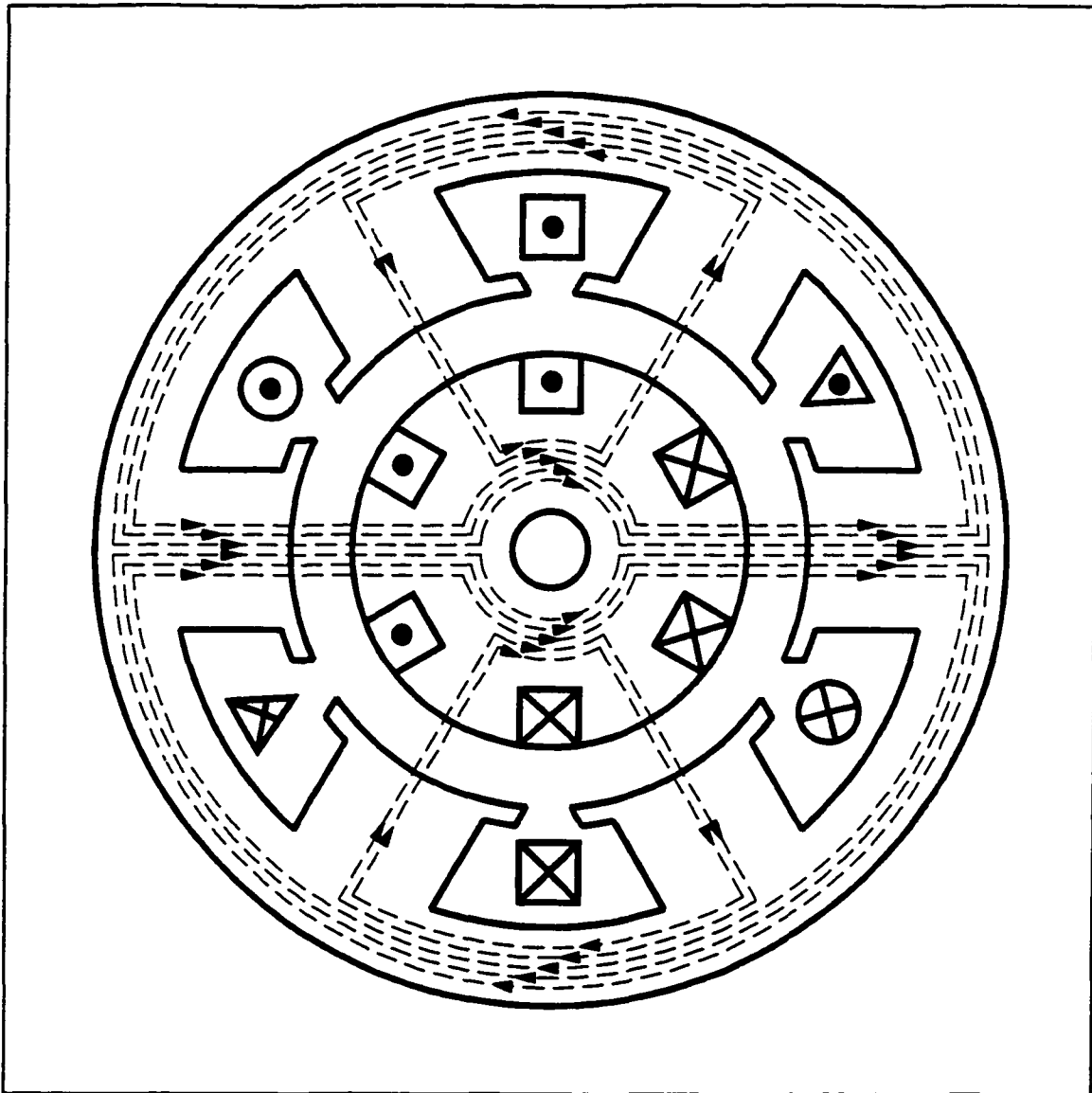
Figure 2.2 Cross section of stator air gap flux for a simple two-pole polyphase motor.

The flux that is drawn arises from the stator currents. The time varying flux links the rotor and induces voltages across the six bars. This forces current to flow in the bars establishing rotor flux that also crosses the air gap. The interaction of stator and rotor air gap fluxes produces a torque on the rotor.

Since most of the flux is guided radially across the air gap by steel teeth, the tangential and axial components of the air gap flux have been neglected. Air gap flux in those directions contributes no useful torque anyway. The steel teeth reduce the tangential flux and a laminated stack construction reduces the axial flux.

-18-

The spatial distribution of the radial air gap flux can be represented by a Fourier series. The interaction from only the fundamentals of stator and rotor air gap fluxes produces useful torque. Higher harmonics are undesirable because they cause heating, vibration and noise problems. Therefore, many techniques are used to minimize the harmonics. As a result, they can be neglected from the derivation so that stator and rotor air gap flux density distributions are modelled only by their fundamentals.

Harmonics in the stator air gap flux density distribution are decreased by concentric windings that are spatially balanced and energized by sinusoidal voltages or currents that are temporally balanced. Concentric windings consist of many tiers of wire bundles wound in series. The tiers span various tooth counts but all center on the same tooth. Under the lumped magnetic model approach, current in each tier produces a uniform air gap flux density distribution. Superposition is applied to sum the distributions over respective tooth spans. The set of all tiers produces a staircase distribution that resembles a sinusoidal function.

The flux density distribution of concentric windings in a rolled-out portion of the stator cross section is shown in Figure 2.3. The cross section, which contains rectangular slots, corresponds to a pole. Each of the three tiers represented by various shapes can contain a different number of coils. When the number of tiers is increased and the coil count is chosen appropriately, the resultant distribution becomes more sinusoidal. Concentric windings utilize many tiers to transform the uniform distribution of each tier into more of a sinusoidal distribution.

Current in each phase can now be assumed to produce an air gap flux density distribution that is sinusoidal. When the sinusoidal balanced excitation is polyphase, a stator air gap flux density distribution results that is still sinusoidal but boosted in amplitude. Slotting effects disturb the smooth distribution since much more flux flows in the highly permeable steel teeth rather than in the slots. Ears cut at the tooth tips dampen the slotting effects by redistributing the flux more evenly across the air gap. Fringing occurs at the tooth tips where flux fans out across the air gap.

Some harmonic interactions between the stator and rotor air gap flux density distributions are canceled by skewing the rotor. Harmonics in the rotor air gap flux density distribution are further decreased by an increase in the number of rotor bars. The transition in current from one bar to the next

-19-
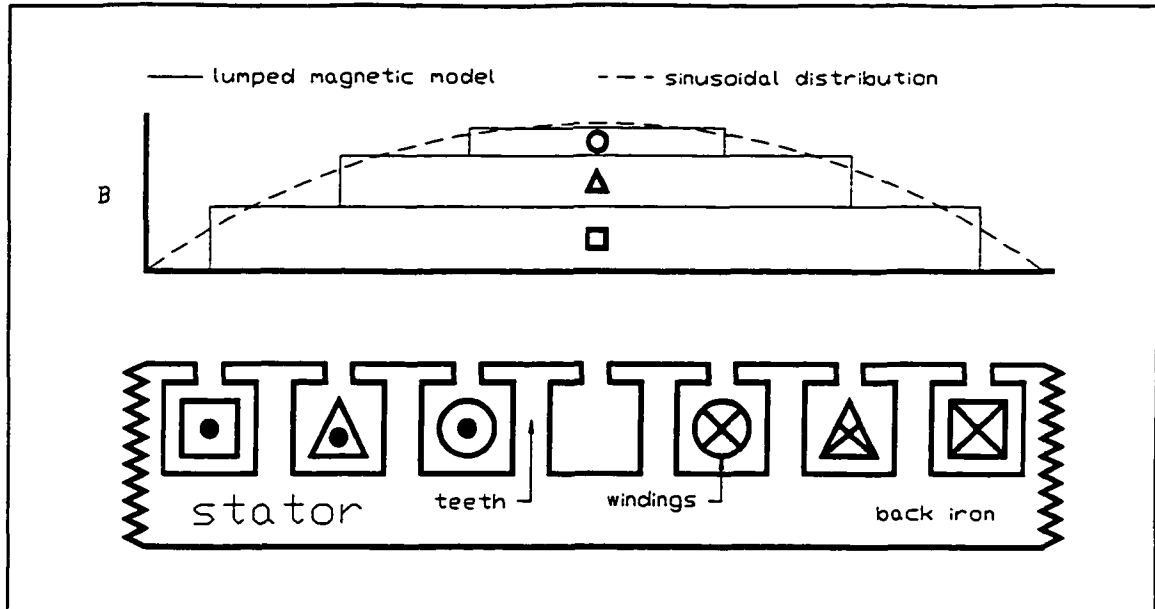
Figure 2.3 Flux density distribution of concentric windings in a rolled-out portion of stator cross section.

becomes more sinusoidal resulting in a more sinusoidal rotor flux density distribution. In addition, rotor slotting effects become less dramatic with an increase in rotor bar count.

When the sinusoidal distribution of flux is applied, the primitive magnetic model of Figure 2.4 is used to formulate the flux in the simple two-pole polyphase motor of Figure 2.2 where:

$\mathscr{F}_s^k$ = stator MMF source in k^{th} stator tooth from all stator winding currents
$\mathscr{F}_r^k$ = rotor MMF source in k^{th} rotor tooth from all rotor bar currents
$\mathfrak{R}_g$ = air gap reluctance per pole

Air gap flux travels from the stator back iron down the stator teeth across the air gap down the rotor teeth to the rotor back iron. The return path is the same from the rotor back iron to the stator back iron.

All stator MMF sources have the same amplitude but are evenly phase shifted in time and space relative to each other. Each source is in temporal phase with current in the windings that are ninety degrees away spatially. Similarly, all rotor MMF sources have the same amplitude but are evenly phase shifted in time and space relative to each other. Each source is also in temporal phase with current in the bar that is ninety degrees away spatially. The temporal phase of the rotor MMF sources relative to the stator MMF sources, however, depends on the rotor currents. The currents, which depend on rotor speed, will be derived after formation of the lumped magnetic, electrical, and thermal models.

Superposition can be applied to formulate flux through the branches due to all the stator and rotor

-20-
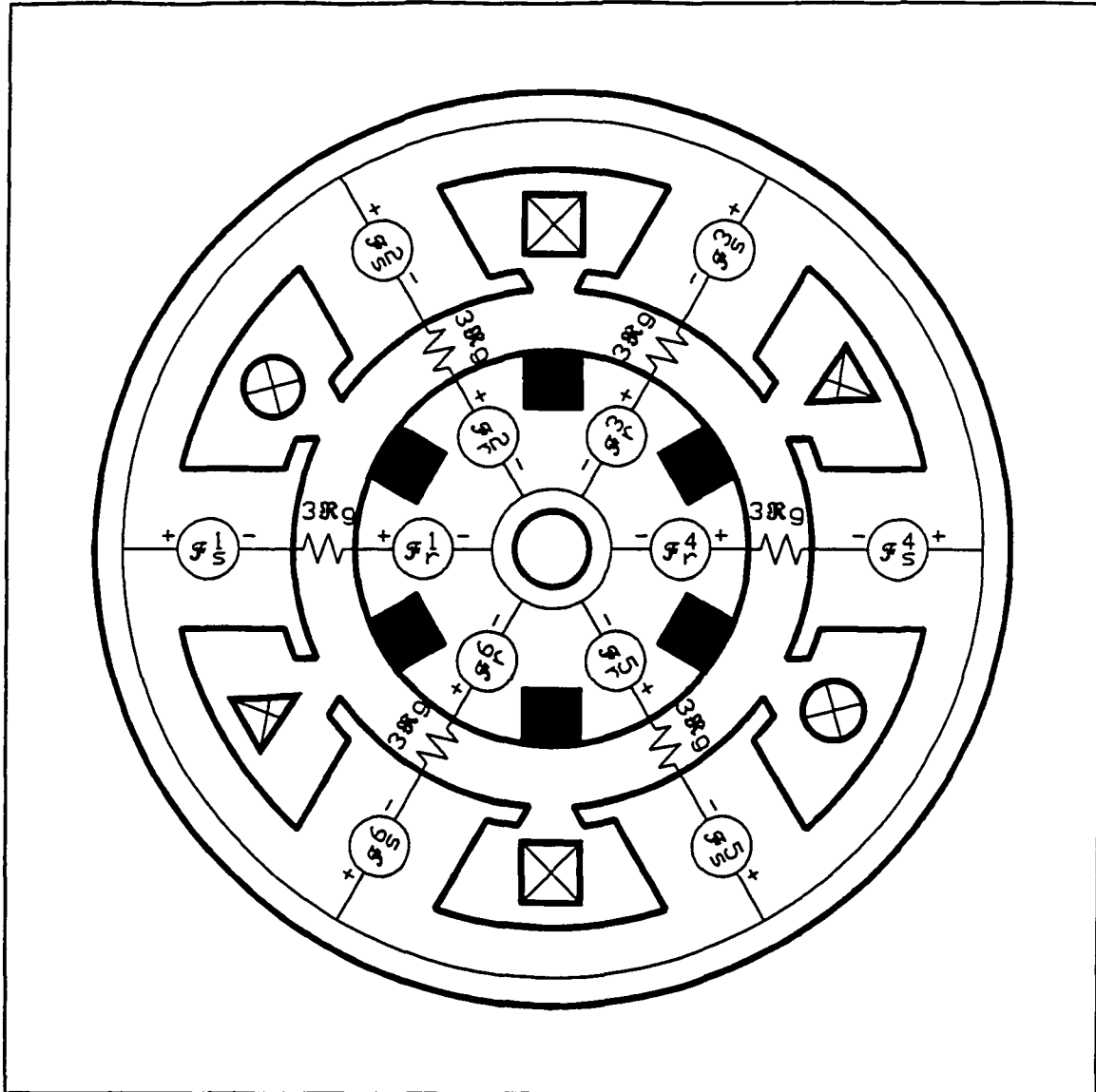
Figure 2.4 Air gap flux model for a simple two-pole polyphase motor.

MMF sources. However, due to symmetry, flux through each of the six air gap branches is equal to the sum of the two MMF sources in the branch divided by the reluctance of the branch. Also as a result of the symmetry in the stator and rotor MMF sources, the air gap flux density distribution is almost sinusoidal except for slotting effects since the air gap reluctance per tooth is constant.

In the lumped magnetic model approach, the reluctance of a material is formulated as the average length of flux path through the material divided by the product of its incremental permeability and its average cross-sectional area. The permeability is evaluated at the average flux density level. The cross-sectional area is evaluated perpendicular to the flux path.

-21-

The air gap reluctance is constant regardless of the time varying air gap flux density because the permeability of air is constant. Air gap flux enters the air gap through one pole and exits through its counterpart, an adjacent pole. The air gap reluctance over a pole becomes:

$$\mathfrak{R}_g = \frac{l_g}{\mu_0 \frac{\pi}{n} \left(\frac{D_{si} + D_{ro}}{2} \right) z}$$

II-1

where:

l_g	$\equiv$ air gap radial length
μ_0	$\equiv$ permeability of air
n	$\equiv$ number of magnetic poles
D_{si}	$\equiv$ stator lamination inner diameter
D_{ro}	$\equiv$ rotor lamination outer diameter
z	$\equiv$ stator and rotor stack average axial heights

A uniform air gap has been assumed, thereby neglecting slotting effects. Later, the Carter's coefficient is used to account for slotting effects. Stator and rotor stack axial heights are usually almost identical so that they can be assumed equivalent. $\mathfrak{R}_g$, which is on a per-pole basis, is multiplied by three in Figure 2.4 because there are three stator and three rotor teeth per pole.

To be more accurate in modelling the air gap flux, MMF drops in the steel can be included since the flux also passes through steel in the back iron and teeth. The MMF drops can be incorporated by adding steel reluctances in series with the air gap reluctance. The steel reluctances can account for magnetic saturation effects since their permeability is dependent on the flux density level in the steel. Saturation limits the amount of flux a material can carry. Saturation in the teeth results in an air gap flux density distribution that is flattened and near sinusoidal instead of the assumed purely sinusoidal. As a result, the fundamental of the distribution is decreased. The steel reluctances model that decrease.

For motors with large effective air gaps, the reluctance of air is more significant than of steel because steel is usually at least two thousand times more permeable than air. These motors can be modelled without considering steel reluctances if saturation is not serious. Since induction motors have characteristically small air gaps, steel reluctances are significant. Although they are neglected in the simple model here, they are included in the model of the next section.

-22-

II.B.2. The General Lumped Magnetic Model

The simple magnetic model of Figure 2.4 contains only flux crossing the air gap. MMF drops in the steel and leakage flux were neglected. However, they must be included because they significantly influence induction motor performance. Also, the number of stator and rotor teeth was constrained to be equivalent. A general lumped magnetic model that includes the MMF drops and leakage flux is developed for any combination of stator and rotor tooth counts. The MMF drops are incorporated by considering flux from all MMF sources. Because superposition applies, the stator and rotor magnetic circuits are separated to individually examine their contribution.

The magnetic model is developed to describe stator and rotor air gap and leakage fluxes resulting from the MMF sources and reluctances. Reluctances, which depend on material properties and geometry, remain virtually constant if saturation is not serious. MMF sources depend on stator and rotor currents. The amplitude of the rotor currents is unknown without also developing the thermal and electrical models. Stator current amplitude is unknown only in the voltage driven motor. For now, the currents are assumed known. They will be derived from input voltages after the development of the other two models.

The complete magnetic model would consist of many stator and rotor magnetic circuits in parallel. The number of stator circuits would equal the number of pole pairs multiplied by the number of stator phases. All stator circuits would be identical except for the temporal phase shifts in the MMF sources. The number of rotor circuits would equal the number of rotor bars pairs. All rotor circuits would also be identical except for the temporal phase shifts in the MMF sources. Fortunately, the complete magnetic model is unnecessary if symmetry exists.

For excitation that is balanced in time and space, symmetry exists if the rotor bars are evenly spaced. Additionally, the rotor bar count must divide evenly into the number of poles. For convenience, the number of rotor bars per pole is labelled the number of rotor phases. Each pole then contains current from all the stator and rotor phases. Furthermore, each pole pair contains identical flux strength and pattern with contribution from current in each of the stator and rotor phases. Due to the symmetry, it is only necessary to analyze the magnetic circuits for one set of the stator and rotor phases within a pole pair. In effect, the rotor circuit is analyzed on a per-bar-pair basis.

-23-

The rotor magnetic circuit assumes an integral number of rotor phases. When that happens, matching bar pairs exist, each containing currents separated in time and space by 180 degrees. When the number of rotor phases is not an integer, however, the rotor magnetic circuit is no longer exact but an approximation. The approximation becomes better with an increasing number of bars because the transition in current from one bar to the next becomes smoother and more sinusoidal. The rotor usually contains a large odd number of bars in order to reduce harmonics in the rotor air gap flux density distribution. As with skewing the rotor, matching an odd rotor bar count with an even stator slot count cancels some harmonic interactions between the stator and rotor air gap flux density distributions.

Figure 2.5 shows the lumped magnetic model for one phase within a pole pair where:

K_d ≡ winding distribution constant
N_s ≡ winding turns per stator phase per pole
i_s^k ≡ stator winding current in k^{th} stator phase
$\mathfrak{R}_{sl}$ ≡ stator leakage reluctance per pole
K_c ≡ Carter's coefficient
K_s ≡ steel reluctance constant
K_w ≡ skew constant
ϕ_{sl}^k ≡ stator leakage flux per pole from stator winding current in k^{th} stator phase
ϕ_{sg}^k ≡ stator air gap flux per pole from stator winding current in k^{th} stator phase
N_r ≡ turns per rotor bar pair
i_r^l ≡ rotor bar current in l^{th} rotor phase
$\mathfrak{R}_{rl}$ ≡ rotor leakage reluctance per pole
ϕ_{rl}^l ≡ rotor leakage flux per pole from rotor bar current in l^{th} rotor phase
ϕ_{rg}^l ≡ rotor air gap flux per pole from rotor bar current in l^{th} rotor phase

The stator MMF sources are no longer in series with the rotor MMF sources as in Figure 2.4 because the number of stator and rotor teeth is no longer constrained to be equivalent. The contribution from each of the stator and rotor phases is separated and leakage flux paths are included. Furthermore, the air gap reluctance per pole instead of per tooth is used because the magnetic circuits represent one phase within one pole pair.

The stator MMF sources arise from current in the concentric windings. Two stator MMF sources are used for the matching sets of tiered wire bundles for each pole pair. N_s represents the total number of coils in all the tiers of one phase within one pole. For multiple-tiered windings, a steel tooth often separates the matching sets of tiered wire bundles between poles. This allows for better utilization of slots through more even distribution of coils per slot.

For consistency, two rotor MMF sources are used for a bar pair. Since N_r equals one for the

-24-

$$\frac{4}{\pi} K_d N_s i_s^k \quad + \quad \Re_{sl} \qquad \Re_{sl} \qquad - \quad \frac{4}{\pi} K_d N_s i_s^k$$

leakage   leakage

stator

$$\frac{\pi}{2} K_c K_s K_w \Re_g \qquad \phi_{sl}^k \qquad \phi_{sg}^k \qquad \phi_{sl}^k \qquad \frac{\pi}{2} K_c K_s K_w \Re_g$$

air gap

$$\frac{\pi}{2} K_c K_s K_w \Re_g \qquad \phi_{rl}^l \qquad \phi_{rg}^l \qquad \phi_{rl}^l \qquad \frac{\pi}{2} K_c K_s K_w \Re_g$$

rotor

leakage   leakage

$$\frac{4}{\pi} \frac{N_r}{2} i_r^l \quad + \quad \Re_{rl} \qquad \Re_{rl} \quad - \quad \frac{4}{\pi} \frac{N_r}{2} i_r^l$$
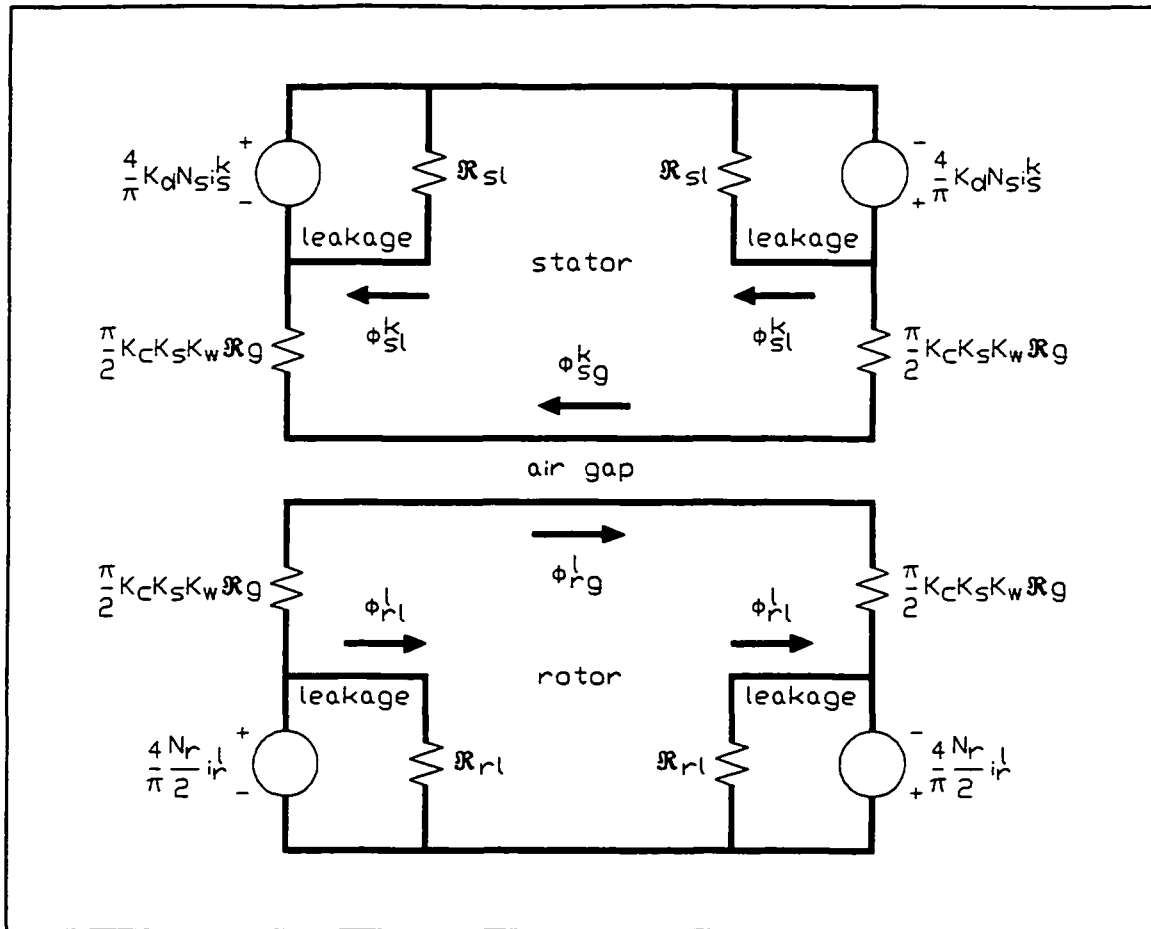
Figure 2.5 Lumped magnetic circuit model per phase per pole pair.

squirrel cage rotor, each source can represent current in half of a bar. The squirrel cage rotor can be conceptualized as being concentrically wound with one tier per phase per pole. Each rotor slot would hold two layers of current from the same phase.

Figure 2.6 shows rotor current in the half-bars for the two-pole motor of Figure 2.2 and Figure 2.4. Rotor end rings are excluded from the figure. The dashed lines denote the currents of one phase. The current in an entire bar is equivalent to the sum of the current in the adjoining half-bars. The half-bar current travels up the axial bar length and across a segment of the end ring corresponding to one pole. The current then continues down the axial bar length at the other end of the end ring pole segment and back across the pole segment of the second end ring. Two half-bar currents that share a bar travel in opposite direction in the end rings. The two currents follow two electrically parallel paths, each of which passes serially through half the poles on one side of the rotor. Like stator currents, rotor currents of each

-25-

phase are modelled to flow serially from one pole to the next.
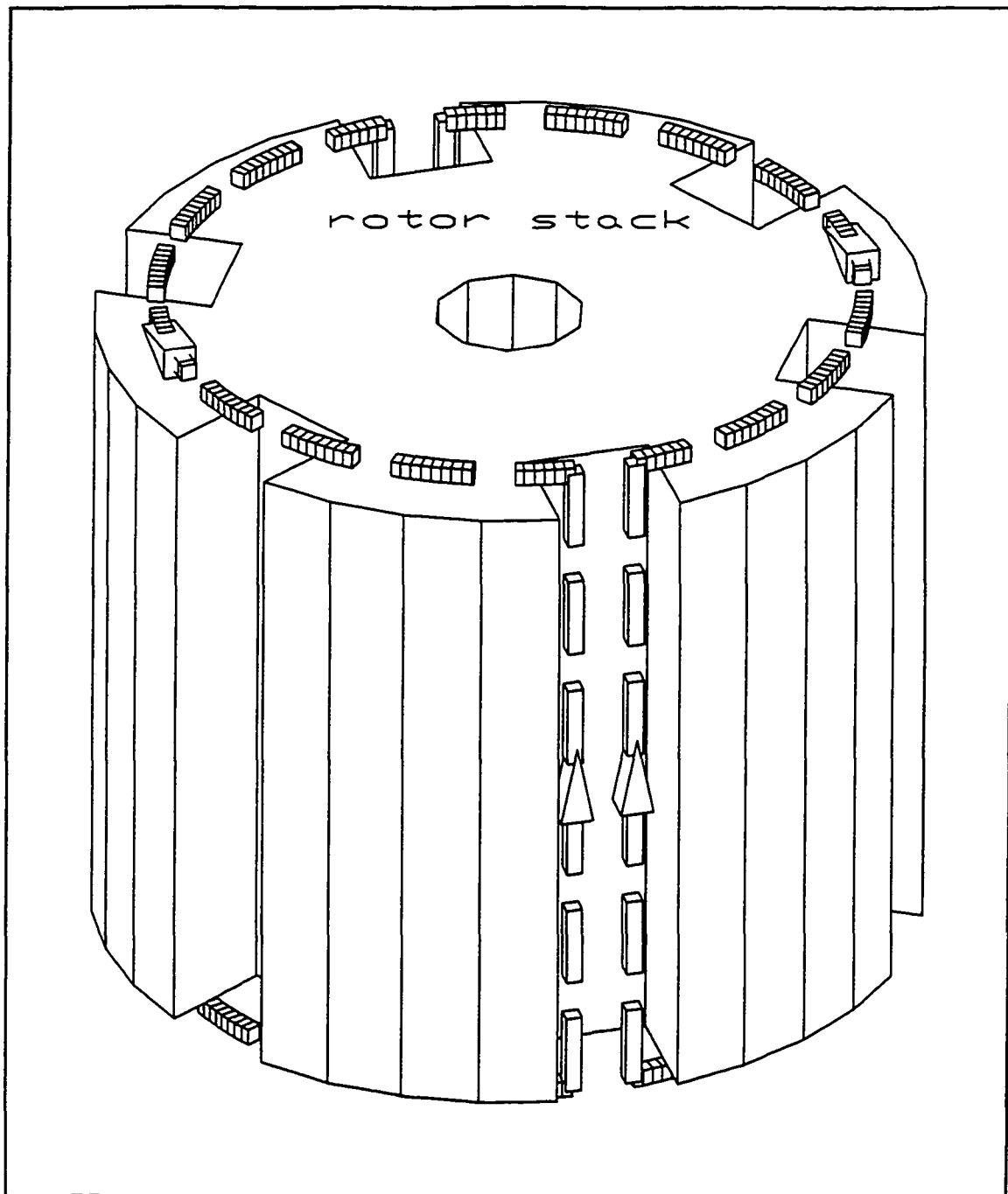
Figure 2.6 Rotor current in half-bars of a two-pole motor.

In modelling stator and rotor air gap flux density distributions by their fundamentals, only the fundamentals of the MMF sources are necessary. Therefore, the stator and rotor MMF sources are scaled for the amplitude of their fundamentals. Scaling the rotor MMF sources is easy because the squirrel cage is conceptualized as being concentrically wound with only one tier that spans all the teeth in a pole. For

-26-

the stator sources, on the other hand, the different tooth spans of the tiers cause the MMF source associated
with each tier to span a different tooth count. Consequently, the amplitudes of the fundamental associated
with the tiers can not be simply summed. The winding distribution constant is used to account for the
different tooth spans:[10]

$$K_d = \sum_{k=1}^{\text{concentric winding tiers}} \frac{n_s^k}{N_s} \sin\left(\frac{n\pi}{2S_s} t_{coil}^k\right) \qquad \text{II-2}$$

where:

n_s^k	= winding turns per stator phase per pole in k^{th} stator concentric winding tier
S_s	= number of stator steel teeth or stator slots
t_{coil}^k	= stator coil tooth span in k^{th} concentric winding tier

The winding distribution constant is unnecessary for the rotor because it equals one.

In deriving air gap flux under the lumped magnetic model approach, the series MMF sources are
simply divided by the series air gap reluctances. But, that yields the flux for a uniform air gap flux density
distribution. On the contrary, the air gap flux density distribution is assumed to be sinusoidal. Therefore,
the air gap reluctance is scaled by a constant fraction in order to take the lumped approach for a sinusoidal
flux density distribution. The fraction arises from the difference in area under the curve of a uniform
distribution and a sinusoidal distribution with the same amplitude. Over a pole, a sinusoidal flux density
distribution integrates to a constant fraction, $2/\pi$, of the flux to which a uniform distribution integrates.

The air gap reluctance is also multiplied by three more constants to improve the accuracy of the
air gap flux. Carter's coefficient is included to elongate the effective air gap length due to fringing at tooth
tips from slotting effects:[11]

$$K_c = \frac{1}{\left[1 - \dfrac{S_s}{\pi D_{st}} \dfrac{w_{stso}^2}{(5l_g + w_{stso})}\right]\left[1 - \dfrac{S_r}{\pi D_{ro}} \dfrac{w_{rtso}^2}{(5l_g + w_{rtso})}\right]} \qquad \text{II-3}$$

[10]Cyril G. Veinott, *Theory and Design of Small Induction Motors*, New York: McGraw-Hill Book
Company, Inc., 1959, pp. 267-270.

[11]Cyril G. Veinott, *Theory and Design of Small Induction Motors*, New York: McGraw-Hill Book
Company, Inc., 1959, p. 304.

-27-

where:

w_{slso} = stator slot mouth opening width
S_r = number of rotor steel teeth or rotor squirrel cage bars
w_{rlso} = rotor slot mouth opening width

The coefficient is based on a theoretical derivation as well as experimental data, but it may not work well when operating outside the scope of the data. The steel reluctance constant, explained in the next section, accounts for MMF drops in the steel along the air gap flux path. The skew constant increases the air gap reluctance to account for effects of skewing the rotor. All other variables are determined for an unskewed rotor, then the skew constant is inserted to compensate for the skewing. Further explanation on rotor skewing is presented in section II.D.5.

Stator currents establish stator air gap flux and stator leakage flux. Similarly, rotor currents establish rotor air gap flux and rotor leakage flux. While the leakage flux only links conductors on the same side, the air gap flux crosses the air gap to also link conductors on the other side. Each of the flux per pole is a function of the MMF source and reluctance:

$$\phi_{sg}^k = \frac{4}{\pi}\frac{2}{\pi}\frac{K_d N j_s^k}{K_c K_s K_w \mathfrak{R}_g}$$

$$\phi_{sl}^k = \frac{4}{\pi}\frac{K_d N j_s^k}{\mathfrak{R}_{sl}}$$

$$\phi_{rg}^l = \frac{4}{\pi}\frac{2}{\pi}\frac{N j_r^l}{2 K_c K_s K_w \mathfrak{R}_g}$$

$$\phi_{rl}^l = \frac{4}{\pi}\frac{N j_r^l}{2 \mathfrak{R}_{rl}}$$

II-4

The leakage flux will be explained and the leakage reluctances will be formulated in section II.D. With the flux functions known from the lumped magnetic model, the lumped electrical model can be developed in the next chapter to determine motor performance using induced voltages due to time derivative of the flux linkages.

II.C. The Steel Reluctance Constant

The inclusion of the steel reluctance constant increases the air gap reluctance to account for the

-28-

steel in the back iron and teeth along the air gap flux path. The constant becomes especially important in low pole count, large diameter motors with tiny air gaps, narrow back irons, and long, narrow teeth. The constant also incorporates saturation in the steel.

To account for MMF drops in the steel, reluctances can be added in the teeth of Figure 2.4 in series with the air gap reluctance and in the back iron regions between the radial air gap flux paths. In the lumped magnetic model of Figure 2.5, however, the flux that is within a pole pair instead of within a tooth is determined. Therefore, the back iron reluctances over a pole can be placed in that model in series with the air gap reluctance and tooth reluctances over a pole. But, because the air gap flux not the steel reluctances is of interest, the air gap reluctance used in formulating the flux can be scaled by a steel reluctance constant to incorporate the series steel reluctances. However, the steel reluctances are needed in calculating the steel reluctance constant.

In formulating the steel reluctances for the steel reluctance constant, the permeability of steel, which depends on the instantaneous flux density levels, is needed. The flux densities are functions of currents evaluated through the lumped electrical model. But, the model requires flux information formulated from the steel reluctances. Thus, some interdependence exists between the reluctances and the currents so that an iterative process is employed at each rotor speed to determine these quantities.

In the iterative process, the steel reluctance constant is initially determined through a conservative approximation of maximum steel reluctances. The steel permeability is thereby evaluated at the maximum flux density levels determined from the maximum air gap flux. This maximum flux is used only in evaluating the initial steel reluctance constant and not used to directly determine motor performance. Initial stator and rotor currents are then calculated through the lumped models. After that, the steel reluctance constant is iteratively corrected through the calculated currents using an average air gap flux.

The steel reluctance constant is formulated as the ratio of the sum of the air gap reluctance and series steel reluctances to the air gap reluctance:[12]

---

[12]Cyril G. Veinott, *Theory and Design of Small Induction Motors*, New York: McGraw-Hill Book Company, Inc., 1959, p. 306.

$$K_s = \frac{\Re_{ssb} + \frac{\pi}{2}\Re_{sst} + \frac{\pi}{2}K_c K_w \Re_g + \Re_{rsb} + \frac{\pi}{2}\Re_{rst}}{\frac{\pi}{2}K_c K_w \Re_g}$$

<div align="right">II-5</div>

where:

$\Re_{ssb}$ = stator back iron reluctance per pole
$\Re_{sst}$ = stator steel tooth reluctance per pole
$\Re_{rsb}$ = rotor back iron reluctance per pole
$\Re_{rst}$ = rotor steel tooth reluctance per pole

The constant $\pi/2$ was also applied in Figure 2.5. It scaled the air gap reluctance in order to take the lumped magnetic model approach of a uniform flux density distribution for a sinusoidal flux density distribution. Here, the constant applies to the air gap reluctance as well as the tooth reluctances because the flux density distribution in the teeth is assumed sinusoidal. The distribution in the teeth, like in the air gap, is also tangentially almost sinusoidal disturbed mainly by slotting effects.

The reluctance in the steel regions is derived from the permeability of steel, length of flux path, and cross-sectional area of flux path in the regions:

$$\Re_{ssb} = \frac{\frac{\pi}{2n}(D_{so} - w_{ssb})}{2\mu_{ssb}w_{ssb}Z}$$

$$\Re_{sst} = \frac{l_{sst}}{\dfrac{\mu_{sst}S_s w_{sst}Z}{n}}$$

<div align="right">II-6</div>

$$\Re_{rsb} = \frac{\frac{\pi}{2n}(D_{rt} + w_{rsb})}{2\mu_{rsb}w_{rsb}Z}$$

$$\Re_{rst} = \frac{l_{rst}}{\dfrac{\mu_{rst}S_r w_{rst}Z}{n}}$$

where:

D_{so} = stator lamination outer diameter
w_{ssb} = stator back iron radial width
μ_{ssb} = permeability of steel in stator back iron
l_{sst} = stator steel tooth radial length
μ_{sst} = permeability of steel in stator teeth
w_{sst} = stator steel tooth average tangential width

-30-

$$\begin{array}{ll} D_{ri} & \equiv \text{rotor lamination inner diameter} \\ w_{rib} & \equiv \text{rotor back iron radial width} \\ \mu_{rib} & \equiv \text{permeability of steel in rotor back iron} \\ l_{rst} & \equiv \text{rotor steel tooth radial length} \\ \mu_{rst} & \equiv \text{permeability of steel in rotor teeth} \\ w_{rst} & \equiv \text{rotor steel tooth average tangential width} \end{array}$$

The length and cross-sectional area are measured over a pole. The radial distance between outer and inner diameters for the stator and rotor comprises the back iron width and tooth length:

$$\frac{D_{so} - D_{si}}{2} = w_{ssb} + l_{sst}$$

$$\frac{D_{ro} - D_{ri}}{2} = w_{rsb} + l_{rst}$$

II-7

The basic lamination dimensions for the simple motor of Figure 2.2 and Figure 2.4 have been labelled in Figure 2.7.

To initially solve for the steel reluctances, maximum air gap flux used to evaluate the maximum steel reluctances is derived. For most practical current and voltage driven motors, this maximum flux occurs at synchronous speed. At that speed, no rotor currents are induced so that no rotor air gap flux exists to counter the stator air gap flux. As rotor speed decreases, rotor currents increase faster than stator currents, but in the negative direction. This causes increased rotor air gap flux in countering the stator air gap flux and results in reduced overall air gap flux.

For the current driven motor, the maximum air gap flux per pole equals the amplitude of the sum of air gap flux per pole from only the stator currents:

$$\phi^{max} = \left| \sum_{k=1}^{n} \frac{4}{\pi} \frac{2}{\pi} \frac{K_d N j_s^k}{K_c \mathfrak{R}_g} \cos\left(\frac{2\pi k}{m}\right) \right|$$

II-8

where:

$$\begin{array}{ll} \phi^{max} & \equiv \text{maximum air gap flux per pole} \\ m & \equiv \text{number of stator winding phases} \end{array}$$

This represents the maximum flux over a temporal cycle. The spatial phase of the individual flux per phase from relative positions of the windings is accounted for. The flux does not include either the steel reluctance constant or the skew constant because they are unknown for now. The skew constant is derived

-31-
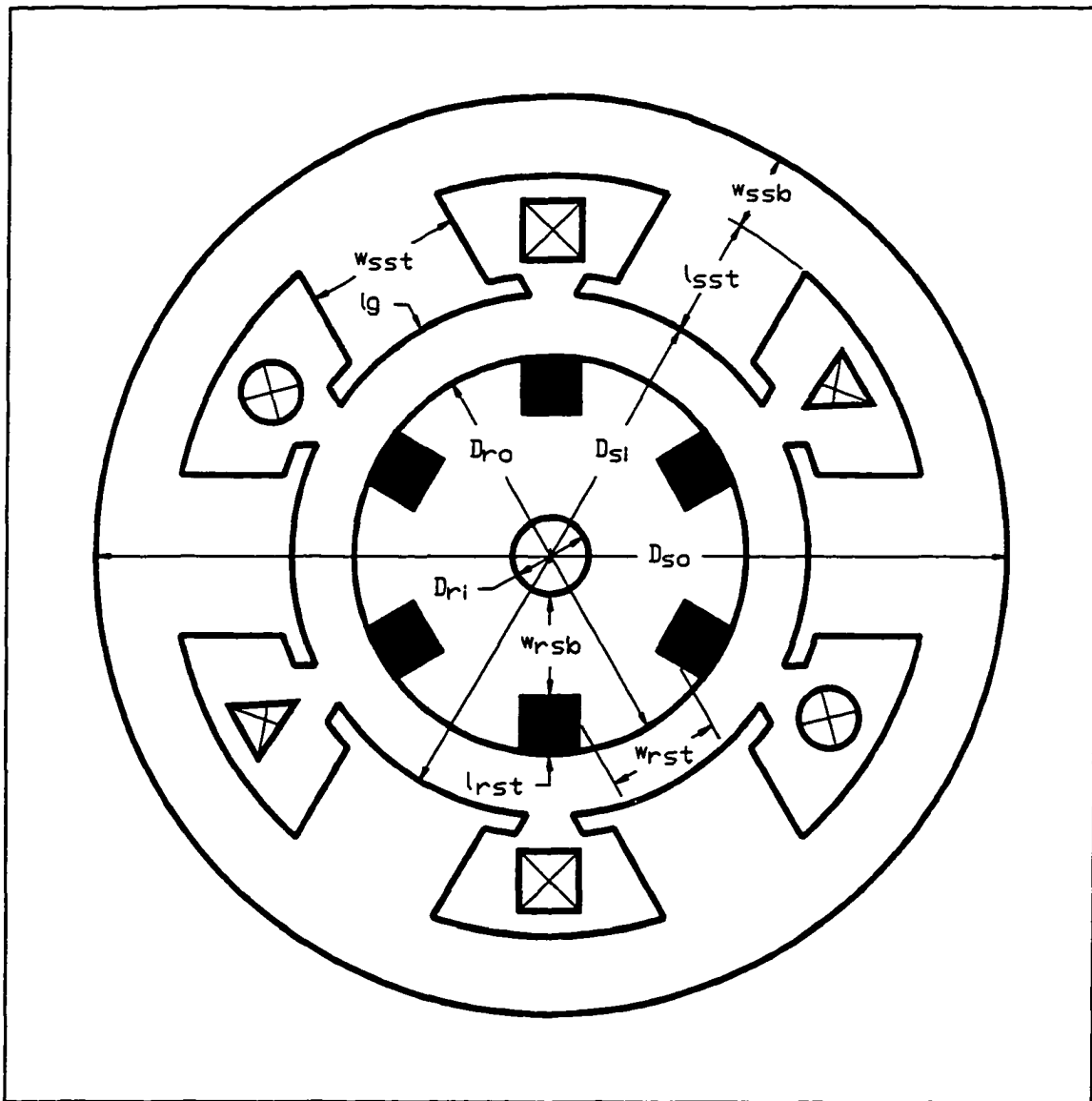
Figure 2.7 Basic lamination dimensions for a simple two-pole polyphase motor.

later as a function of the steel reluctance constant.

Formulating the maximum air gap flux for the voltage driven motor is more complicated. The maximum flux is derived from the input voltages instead of stator currents. The input voltages are assumed to be completely applied to producing flux because voltage drops in the stator windings are normally relatively small. Hysteresis and eddy current losses in the steel as well as leakage flux are also neglected here. Leakage flux is normally small relative to air gap flux anyway.

The relationship between the input voltage amplitude and the maximum air gap flux per pole is

-32-

derived from Faraday's law of induction applied to a sinusoidal excitation:[13]

$$V_{in} = nK_d N_s \omega_e \phi^{max}$$ II-9

where:

V_{in} ≈ input stator winding voltage amplitude

ω_e ■ stator winding excitation frequency

The input voltage equals the sum of all voltages induced in the windings from flux linkage in every pole. The winding distribution constant, K_d, is used because each tier of the concentric windings spans a different tooth count. This prevents the flux from completely linking coils of every tier in inducing voltage.

Now that the maximum air gap flux has been derived for the current and voltage driven motors, maximum flux density in the steel regions can be determined. The steel permeability evaluated at those flux density levels is used in formulating the steel reluctances. The maximum air gap flux flows serially through the four steel regions consisting of stator and rotor back irons and teeth. Therefore, the maximum flux density in the regions can be derived from the maximum flux and the steel cross-sectional area.

The flux density distribution in the back iron is radially virtually uniform between teeth because the flux path length normally varies only by a small amount. Thus, maximum flux density per pole in the back iron is simply ϕ^{max} divided by the back iron cross-sectional area. But, flux in Figure 2.2 travelling across the air gap and through the teeth splits evenly at each pole. Half of the flux flows through the back iron on one side of the pole, and the other half of the flux flows through the opposite side. As a result, each segment of the back iron between the poles carries half the flux per pole:

$$B_{ssb}^{max} = \frac{\phi^{max}}{2w_{ssb}Z}$$

$$B_{rsb}^{max} = \frac{\phi^{max}}{2w_{rsb}Z}$$ II-10

where:

B_{ssb}^{max} ■ maximum stator back iron flux density per pole

B_{rsb}^{max} ■ maximum rotor back iron flux density per pole

---

[13]Cyril G. Veinott, *Theory and Design of Small Induction Motors*, New York: McGraw-Hill Book Company, Inc., 1959, p. 306.

-33-

The flux density distribution in the teeth, like in the air gap, has been assumed sinusoidal. Therefore, the constant $\pi/2$ is also utilized here. It scaled the air gap reluctance in Figure 2.5 in order to take the lumped magnetic model approach of a uniform flux density distribution for a sinusoidal flux density distribution. Maximum tooth flux density is formulated by first dividing ϕ^{max} by the steel cross-sectional area over a pole to arrive at the amplitude of the uniform flux density distribution. Then, that amplitude is scaled by $\pi/2$ to arrive at the amplitude of the sinusoidal flux density distribution:

$$B_{st}^{max} = \frac{\pi}{2} \frac{n\phi^{max}}{S_s w_{st} z}$$

$$B_{rt}^{max} = \frac{\pi}{2} \frac{n\phi^{max}}{S_r w_{rt} z}$$

II-11

where:

B_{st}^{max} = maximum stator steel tooth flux density per pole
B_{rt}^{max} = maximum rotor steel tooth flux density per pole

When tooth width is not constant along the radial length, the flux density along the length deviates. This may cause localized saturation and result in some error. However, since stator and rotor teeth commonly have parallel sides, the localized saturation within the teeth are infrequent.

Now that the maximum flux density level in the steel regions is formulated, the steel permeability in the regions can be evaluated to determine the reluctance in the regions. This incremental permeability can be graphically represented by the slope of the material magnetization curve at the flux density. Figure 2.8 shows the typical permeability of steel to be nonlinear where:

B   = magnetic flux density
H   = magnetic field intensity

Although the actual magnetization curve is also multivalued due to hysteresis loops, it is sufficient here to neglect the loops by using the normal magnetization curve. When saturated, steel presents as much resistance to flux flow as air because the permeability of steel approaches that of air at high flux density levels. The absolute, or static, permeability, on the other hand, equals flux density divided by the field intensity needed to achieve that flux density. When saturation is not serious, the reluctance is more accurately determined from the incremental, not absolute, permeability. Therefore, it is the one referred

-34-
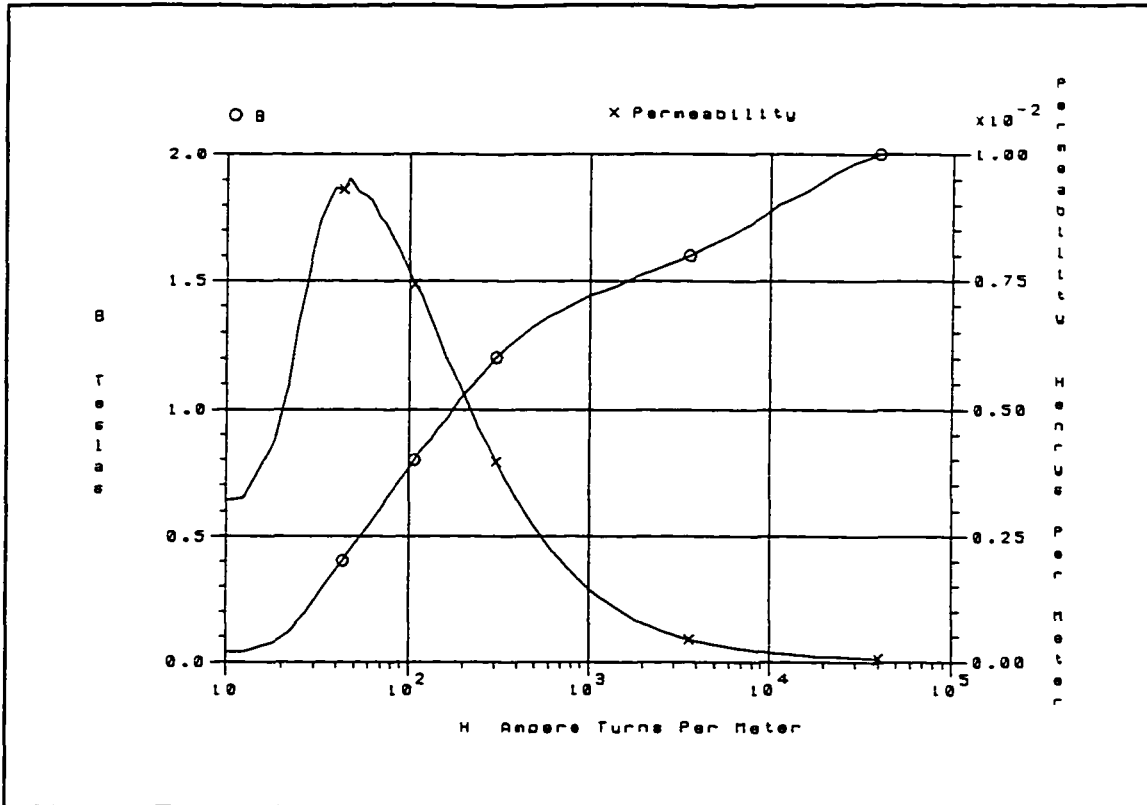
Figure 2.8 Normal magnetization curve and absolute permeability curve of M-19 Fully Processed 26 Gage USS Nonoriented Electrical Steel Sheets.

to herein unless otherwise specified.

With the maximum steel reluctances and the initial steel reluctance constant derived, a more accurate steel reluctance constant is solved iteratively using the average air gap flux. As flux density varies with time, the nonlinear steel permeability causes each steel reluctance to likewise vary. Consequently, the steel reluctance constant also varies, but at a less pronounced rate. It is unnecessary to iterate for the steel reluctance constant at every instant in time. Instead, it is calculated only once at each rotor speed. In doing so, the steel constant is determined through the average air gap flux per pole estimated over a temporal cycle:

-35-

$$\phi^{ave} = \frac{2}{\pi}\left| \sum_{k=1}^{n} \phi_{sg}^{k} \cos\left(\frac{2\pi k}{m}\right) + \sum_{k=1}^{\frac{S_r}{n}} \phi_{rg}^{k} \cos\left(\frac{n\pi k}{S_r}\right)\right|$$

$$= \frac{2}{\pi}\left| \sum_{k=1}^{n} \frac{4}{\pi}\frac{2}{\pi}\frac{K_d N_s j_s^{k}}{K_c K_s K_w \mathcal{R}_g}\cos\left(\frac{2\pi k}{m}\right) + \sum_{k=1}^{\frac{S_r}{n}} \frac{4}{\pi}\frac{2}{\pi}\frac{N_r j_r^{k}}{2 K_c K_s K_w \mathcal{R}_g}\cos\left(\frac{n\pi k}{S_r}\right)\right|$$

II-12

where:

ϕ^{ave} = average air gap flux per pole

The spatial phase of the individual flux per phase from relative positions of the stator windings and rotor bars is accounted for. For flux that varies sinusoidally with time, the constant fraction $2/\pi$ serves to obtain the average from the amplitude.

From this average flux, the average flux density at which the permeability is evaluated is determined in the steel regions. The average flux density is solved from the average flux as the maximum flux density is solved from the maximum flux. After evaluating the permeability in the regions, the steel reluctance constant is again calculated. The iterative process continues until the change in the steel constant is within an acceptable margin.

II.D. Leakage Flux

Leakage flux must be included in magnetic modelling of the induction motor because it significantly influences motor performance. The flux reduces rotor currents as well as the stator currents that induce the rotor currents. The interaction of stator air gap flux produced by the stator currents with rotor air gap flux produced by the rotor currents generates torque. Therefore, torque estimation errors from exclusion of leakage flux are compounded. Leakage flux significantly reduces useful tangential force and also produces harmful radial force. Relative to the effective air gaps of permanent magnet motors, induction motors therefore have characteristically small air gaps to reduce this destructive flux. Leakage flux must be small relative to air gap flux to attain high torque and efficiency levels.

Leakage flux exists across slots, at the axial ends, and in other regions. The leakage flux paths offer additional paths for flux to flow besides radially across the air gap. The paths are thus parallel to

-36-

the air gap flux path in the lumped magnetic model. Leakage flux is very difficult to analytically model so that commonly applied approximate or empirical techniques are used. The flux is ordinarily divided into five parts commonly referred to as slot, zig-zag, end, belt, and skew leakage fluxes.[14] Although other leakage paths may exist, these five are usually sufficient for good performance estimations. The individual flux is explained briefly in the following sections. More detail is given in the footnoted reference.

A lumped leakage magnetic model is developed in Figure 2.9 to determine the individual leakage flux:

$\mathfrak{R}_{sls}$ ≡ stator slot leakage reluctance per pole
$\mathfrak{R}_{slz}$ ≡ stator zig-zag leakage reluctance per pole
$\mathfrak{R}_{sle}$ ≡ stator end leakage reluctance per pole
$\mathfrak{R}_{slb}$ ≡ stator belt leakage reluctance per pole
$\mathfrak{R}_{slw}$ ≡ stator skew leakage reluctance per pole
$\mathfrak{R}_{rls}$ ≡ rotor slot leakage reluctance per pole
$\mathfrak{R}_{rlz}$ ≡ rotor zig-zag leakage reluctance per pole
$\mathfrak{R}_{rle}$ ≡ rotor end leakage reluctance per pole
$\mathfrak{R}_{rlb}$ ≡ rotor belt leakage reluctance per pole
$\mathfrak{R}_{rlw}$ ≡ rotor skew leakage reluctance per pole

This model offers more detail to the leakage flux paths that are in Figure 2.5. The stator and rotor leakage fluxes ϕ_{sl}^k and ϕ_{rl}^l in that model comprise the sum of flux in the five respective parallel paths in this model. Similarly, the stator and rotor leakage reluctances $\mathfrak{R}_{sl}$ and $\mathfrak{R}_{rl}$ there comprise the five respective parallel leakage reluctances here:

$$\mathfrak{R}_{sl} = \frac{\dfrac{\pi}{2}}{\dfrac{1}{\mathfrak{R}_{sls}} + \dfrac{1}{\mathfrak{R}_{slz}} + \dfrac{1}{\mathfrak{R}_{sle}} + \dfrac{1}{\mathfrak{R}_{slb}} + \dfrac{1}{\mathfrak{R}_{slw}}}$$

$$\mathfrak{R}_{rl} = \frac{\dfrac{\pi}{2}}{\dfrac{1}{\mathfrak{R}_{rls}} + \dfrac{1}{\mathfrak{R}_{rlz}} + \dfrac{1}{\mathfrak{R}_{rle}} + \dfrac{1}{\mathfrak{R}_{rlb}} + \dfrac{1}{\mathfrak{R}_{rlw}}}$$

II-13

The stator and rotor MMF sources in the two models are identical.

The leakage flux density distribution, like the air gap flux density distribution, is assumed to be

---

[14]Cyril G. Veinott, *Theory and Design of Small Induction Motors*, New York: McGraw-Hill Book Company, Inc., 1959, pp. 313-314.
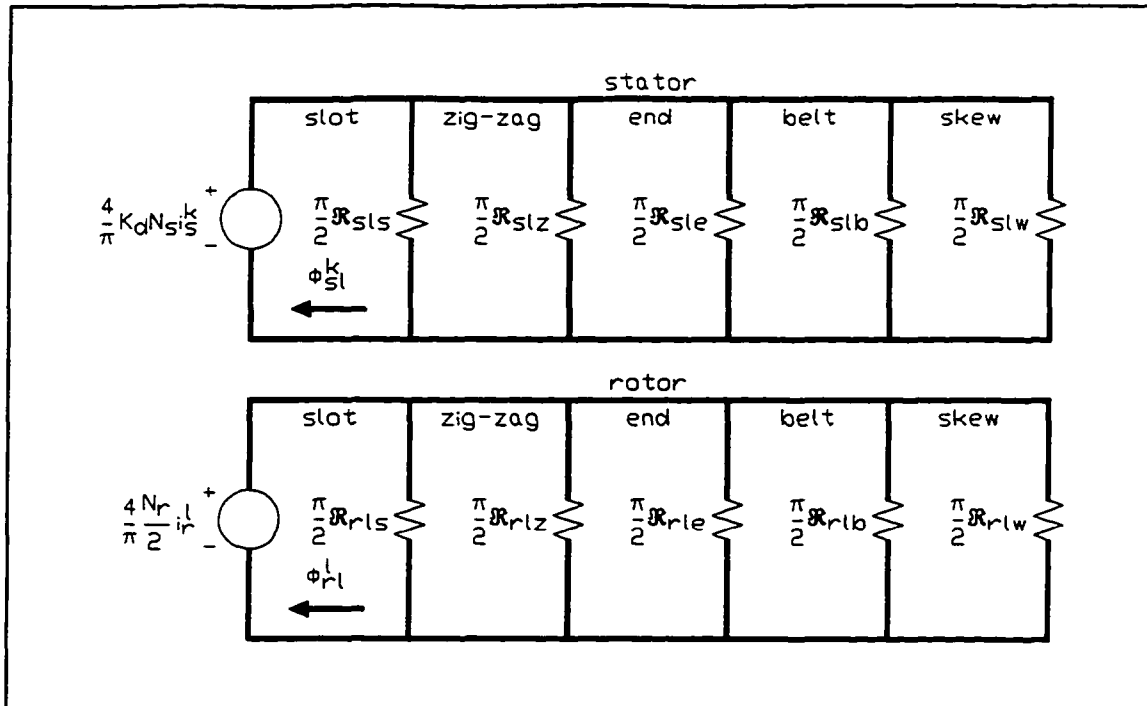
Figure 2.9 Lumped leakage magnetic circuit model per phase per pole.

sinusoidal. But, not all of the individual leakage flux densities form purely sinusoidal distributions. However, leakage flux is usually much smaller than air gap flux so that the assumption does not introduce much error. With the assumption, the constant $\pi/2$ is used to scale the leakage reluctances as it did for the air gap reluctance in Figure 2.5 in taking the lumped magnetic model approach for a sinusoidal flux density distribution. With the sinusoidal assumption, the MMF sources like those in Figure 2.5 are also scaled for the amplitude of their fundamentals.

II.D.1. Slot Leakage Flux

Slot leakage flux tangentially crosses the slot without travelling the entire radial length of the tooth. The flux loops back prematurely without crossing the air gap to link conductors on the other side. Slot leakage flux increases with tooth saturation and decreases with tangentially wide slots. Saturation in the teeth increases the reluctance in the steel and encourages flux to flow across the slots instead of down the tooth lengths. Fatter teeth discourage saturation by carrying more flux down the tooth lengths and across the air gap, but also take up more space that can otherwise be used for windings. More winding space allows for thicker wires that generate less heat. On the other hand, teeth that are too fat necessitate slots

-38-

that are too narrow and result in slot leakage flux that is too high.

To derive the slot leakage reluctance, flux linkage with conductors in a slot is first derived. From the flux linkage per slot and the number of coils in each tier of the concentric windings, flux linkage is derived in a phase. The slot leakage reluctance for a phase is then formulated from that flux linkage per phase given the winding excitation and the winding scheme.

To determine the flux linkage per slot, Figure 2.10 presents the flux paths through the cross section of a rolled-out rectangular slot where:

$\mathscr{F}_{slot}$ = stator or rotor slot MMF source from all stator winding or rotor bar currents
$\mathfrak{R}_{lsb}$ = stator or rotor slot body leakage reluctance
$\mathfrak{R}_{lsm}$ = stator or rotor slot mouth leakage reluctance
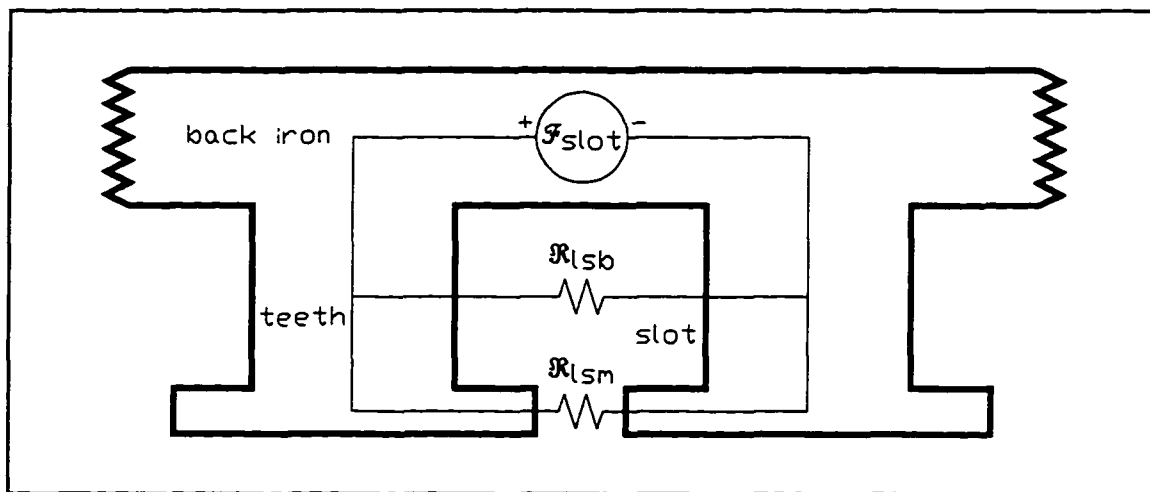
Figure 2.10 Flux paths through cross section of a rolled-out rectangular slot.

For simplicity here, slots are assumed to be rectangular shaped. In reality, slots resemble trapezoids because stator and rotor teeth commonly have constant widths. MMF drops in the steel are neglected because the flux paths through air are much longer than through steel. Two reluctances are used to model the flux crossing the slot through the body and the mouth. Leakage reluctance per slot consists of the two reluctances in parallel. These reluctances in the slot differ from $\mathfrak{R}_{slb}$ and $\mathfrak{R}_{rlb}$ in Figure 2.9 which are reluctances over a pole for a phase.

Almost all of the flux in the lumped magnetic model is assumed to uniformly link conductors in a slot. In other words, all conductors in a slot link the same amount of flux. Stator windings are assumed to uniformly fill only the main body of the slot excluding the mouth, and rotor bars are assumed to

-39-

uniformly fill the entire slot. Therefore, flux linkage across the stator slot mouth is uniform. Flux linkage in the portion of the slot with conductors, however, is considered linearly proportional to radial depth. Each coil in the slot links only the flux that passes through it. Therefore, the deeper a conductor sits in a slot, the more flux it links. A simple method to account for that is to adjust the reluctance so that the flux linkage can be assumed uniform. The sum of flux linkage in the slot mouth and slot body yields the flux linkage in the entire slot.

From the flux linkage per slot and the number of coils in each concentric winding tier, the flux linkage in a phase is calculated. Since the leakage flux in one slot is assumed to link only conductors in that slot, windings of one phase link only the flux in the slots that they sit in. Flux linkage per phase is the sum of the flux linkage in those slots. The linkage in each slot is determined from the number of conductors in the slot. The coils of each tier sit in two slots per pole. Rotor bars can be conceptualized as concentric windings with one tier containing many thin coils per slot. The bars of one phase, however, sit in two half slots per pole.

The calculated stator and rotor flux linkages per phase are used to derive the slot reluctances over a pole for a phase, $\mathfrak{R}_{sl_s}$ and $\mathfrak{R}_{rl_s}$. Slot leakage flux linkages formulated by the lumped electrical model in the next chapter are in terms of these reluctances, the winding excitation, and the winding scheme. To solve for the reluctances, the flux linkages of the lumped electrical model are set equal to the calculated flux linkages. The stator and rotor slot leakage reluctances, explained in detail in the footnoted reference, have been formulated for concentric windings:[15]

---

[15]Cyril G. Veinott, *Theory and Design of Small Induction Motors*, New York: McGraw-Hill Book Company, Inc., 1959, pp. 314-318.

$$\mathfrak{R}_{sls} = \frac{\left[\dfrac{4K_d^2 N_s^2}{\overset{\text{concentric winding tiers}}{\underset{k=1}{\sum}} \pi^2 \left(n_s^k\right)^2}\right]}{\dfrac{1}{\mathfrak{R}_{slsb}} + \dfrac{1}{\mathfrak{R}_{slso}}}$$

$$\mathfrak{R}_{rls} = \frac{\dfrac{8}{\pi^2}}{\dfrac{1}{\mathfrak{R}_{rlsb}} + \dfrac{1}{\mathfrak{R}_{rlso}}}$$

where:

$\mathfrak{R}_{slsb}$ = adjusted stator slot main body leakage reluctance
$\mathfrak{R}_{slso}$ = stator slot mouth opening leakage reluctance
$\mathfrak{R}_{rlsb}$ = adjusted rotor slot main body leakage reluctance
$\mathfrak{R}_{rlso}$ = adjusted rotor slot mouth opening leakage reluctance

The reluctances for other practical slot shapes, such as round bottom slots and closed slots, have been derived in similar manner.[16]

II.D.2. Zig-Zag Leakage Flux

Zig-zag leakage flux crosses the air gap like air gap flux, but reverses direction to travel back across the air gap before linking coils on the other side. After crossing the air gap, the flux travels tangentially across tooth tips instead of radially down tooth lengths. Narrow tooth tips reduce zig-zag leakage flux, but also disrupt a sinusoidal air gap flux density distribution. A large air gap reduces the leakage flux, but also reduces air gap flux that produces torque.

In deriving the zig-zag leakage reluctance, flux linkage in a slot is first determined with the average number of conductors per slot. Average flux linkage in a phase is the product of the average flux linkage per slot and average slot count per phase. The average zig-zag leakage reluctance for a phase is formulated from the flux linkage per phase, the winding excitation, and the winding scheme.

To determine the flux linkage per slot, Figure 2.11 presents the flux paths through the cross section of a rolled-out section of a motor with rectangular slots where:

---

[16]Cyril G. Veinott, *Theory and Design of Small Induction Motors*, New York: McGraw-Hill Book Company, Inc., 1959, pp. 328-330.

-41-

$\mathscr{F}_{slz}$ ≡ stator zig-zag MMF source from all stator winding currents
$\mathfrak{R}_{lz}$ ≡ average zig-zag leakage reluctance per slot
$\mathscr{F}_{rlz}$ ≡ rotor zig-zag MMF source from all rotor bar currents
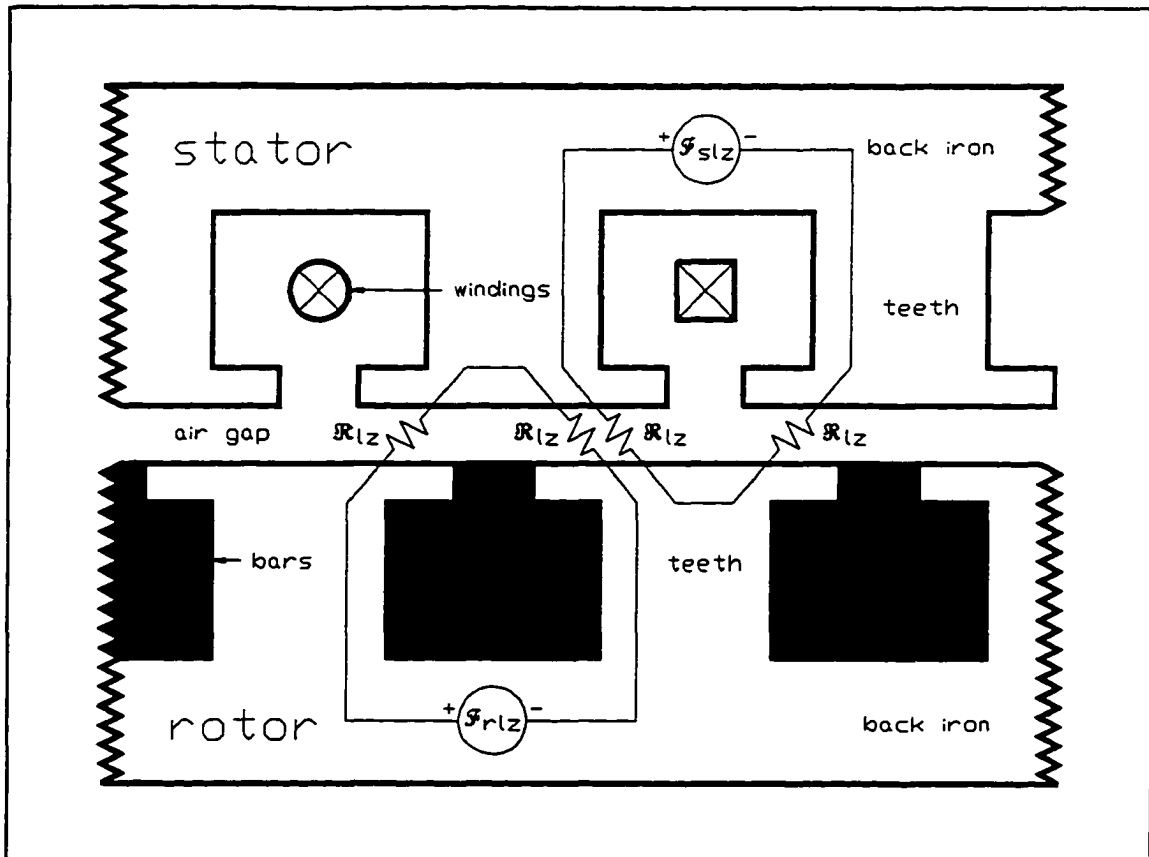
Figure 2.11 Zig-zag flux paths through cross section of a rolled-out portion of motor.

MMF drops in the steel are neglected because the flux paths through air are much longer than through steel. Zig-zag leakage flux can originate in the stator and loop back to the stator, or in the rotor and loop back to the rotor. Stator and rotor zig-zag leakage fluxes around slots facing each other share their paths across the air gap.

Zig-zag leakage reluctance varies depending on the relative stator and rotor tooth pitches as well as the relative positions of stator and rotor tooth faces. To eliminate the dependencies, an average reluctance in a slot, $\mathfrak{R}_{lz}$, is derived over the average of the tooth pitches. $\mathfrak{R}_{lz}$ is on a per-slot basis because two of them are in series per slot and the overlapping tooth faces are shared between the paths around facing slots. Although the stator and rotor tooth pitches are assumed to be equal to the average tooth pitch, assumptions of equal tooth and slot widths are not made.

The average reluctance is explained in detail in the footnoted reference with some approximation

-42-

for fringing of flux at tooth tips due to slotting effects.[17] This approximation for fringing differs from Carter's coefficient which elongates the effective air gap length. Here, the effective overlapping tooth faces are widened to account for extra flux flowing around the tooth sides.

The average reluctance in a slot, $\mathfrak{R}_{tz}$, differs from $\mathfrak{R}_{stz}$ and $\mathfrak{R}_{rtz}$ in Figure 2.9 which are reluctances over a pole for a phase. Though, with $\mathfrak{R}_{tz}$ known, the other reluctances can be derived. The average flux linkage in a slot is calculated from $\mathfrak{R}_{tz}$ and average number of conductors in a slot. Then, the average flux linkage per slot is scaled by the average number of slots in a phase to yield the average flux linkage in a phase. These calculated stator and rotor flux linkages per phase are set equal to zig-zag leakage flux linkages formulated by the lumped electrical model in the next chapter. The zig-zag flux linkages are formulated in terms of $\mathfrak{R}_{stz}$ and $\mathfrak{R}_{rtz}$, the winding excitation, and the winding scheme. The average zig-zag leakage reluctances are then solved:

$$\mathfrak{R}_{stz} = \frac{2S_s \mathfrak{R}_{tz}}{\pi^2 n}$$

$$\mathfrak{R}_{rtz} = \frac{2S_r \mathfrak{R}_{tz}}{\pi^2 n}$$

II-15

II.D.3. End Leakage Flux

End leakage flux arises from current in the stator winding end turns and the rotor squirrel cage end rings. This flux produces a harmful radial force instead of tangential force. As a result, useful torque is reduced and unfavorable torque disturbance is generated.

Figure 2.12 presents the end leakage flux paths around the stator winding end turns and the rotor squirrel cage end rings for a radial cross section of a motor where:

$\mathscr{F}_{sle}$ = stator end turn MMF source from all stator winding currents
$\mathfrak{R}_{sle1}$ = parallel stator end leakage reluctance per pole
$\mathfrak{R}_{sle2}$ = parallel stator end leakage reluctance per pole
$\mathscr{F}_{rle}$ = rotor end ring MMF source from all rotor bar currents

---

[17]Cyril G. Veinott, *Theory and Design of Small Induction Motors*, New York: McGraw-Hill Book Company, Inc., 1959, pp. 318-321.

-43-
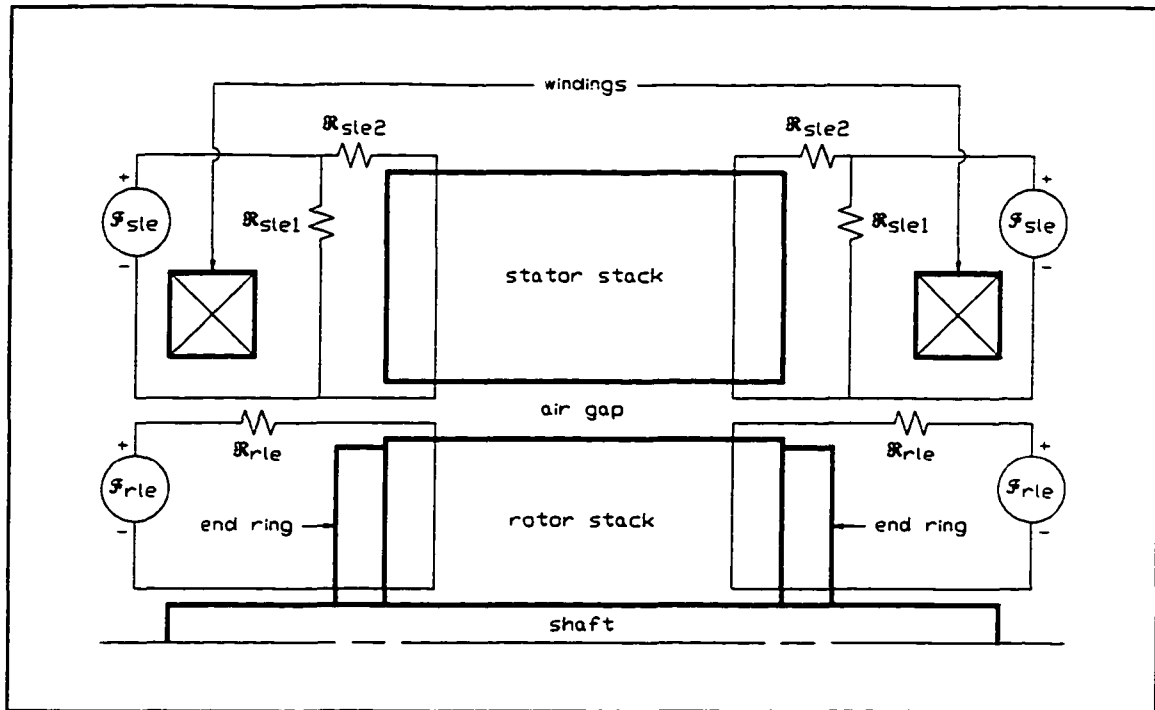
Figure 2.12 Flux paths in stator end turns and rotor end rings of motor radial cross section.

Stator end leakage flux is modelled by two parallel paths. One path flows in air between the winding end turns and the axial edge of the stator stack. The other path flows through the stator stack. Rotor end leakage flux is modelled to flow only through the rotor stack. Although some stator end leakage flux links part of the rotor end rings and some rotor end leakage flux links part of the stator end turns, these flux paths are not shown. MMF drops in the steel are neglected because the flux paths through air are much longer than through steel.

Analytically modelling end leakage flux is very difficult because flux from current of every stator phase and rotor phase all interlink in the end turns and end rings. Therefore, approximate expressions for end leakage reluctances are empirically derived in the footnoted reference:[18]

---

[18]Cyril G. Veinott, *Theory and Design of Small Induction Motors*, New York: McGraw-Hill Book Company, Inc., 1959, pp. 321-322.

-44-

$$\mathcal{R}_{sle} = \frac{4.064}{\pi^2} \frac{S_s}{\mu_0(D_{si}+l_{ssi})t_{coil}}$$

$$\mathcal{R}_{rle} = \frac{4.064}{\pi^2} \frac{n}{\mu_0(D_{ro}-l_{rsi})} \qquad \text{II-16}$$

$$t_{coil} = \sum_{k=1}^{\text{concentric winding tiers}} \frac{n_s^k}{N_s} t_{coil}^k$$

where:

t_{coil} = stator coil average tooth span

The average tooth span is the sum of the tooth span of each concentric winding tier weighted by the fraction of the total number of winding turns in that tier.

II.D.4. Belt Leakage Flux

Belt leakage flux arises from the difference in the air gap flux density distribution generated by the stator and rotor currents. This leakage flux diminishes to zero as the slot counts become equal, as the winding distributions become identical, and as the slots exactly face each other. Belt leakage flux is commonly insignificant in motors with a squirrel cage rotor, but is significant in ones with a wound rotor. Approximate expressions for the belt leakage reluctances are empirically derived in the footnoted reference:[19]

$$\mathcal{R}_{slb} = \mathcal{R}_{rlb} = \frac{\dfrac{2032}{1.18\pi} K_c K_s \mathcal{R}_g}{.739 + \dfrac{7.65}{\dfrac{S_s+S_r}{2n} - 1}} \qquad \text{II-17}$$

When stator and rotor slot counts are low, belt leakage flux is significant and highly sensitive to them.

II.D.5. Skew Leakage Flux

Skew leakage flux arises from rotor skewing. Rotor skewing is a circumferential twisting of the

---

[19]Cyril G. Veinott, *Theory and Design of Small Induction Motors*, New York: McGraw-Hill Book Company, Inc., 1959, pp. 322-323.

-45-

squirrel cage from the end rings in opposite directions. Although skewing can be performed on the stator instead of the rotor, the latter is commonly more convenient to twist. With skewing, rotor bars no longer stand parallel to the shaft and rotor currents no longer flow purely axially.

Despite some slight torque disturbance that is produced, skewing is done to reduce harmonics in the rotor air gap flux density distribution that are detrimental to motor performance. Skewing cancels out some harmonic interactions between the stator and rotor air gap flux density distributions. Undesirable harmonics cause heating, vibration and noise problems.

In deriving the skew leakage reluctance, an average voltage induced in a skewed rotor bar is first determined. Equations describing the voltages experienced by stator windings and rotor bars are then written to include skew. After some equation rearrangements, rotor skewing can be easily incorporated in the lumped magnetic model.

For an unskewed rotor, the amount of air gap flux from one stator phase linking a matching pair of rotor bars is maximum when the bars are directly facing the windings in that phase. Skewing the rotor causes the flux linkage to be less than the maximum and to be a function of the skew. Including skew leakage flux accounts for the reduction in flux linkage.

Conceptually, if the rotor is sectioned into differential slices in the axial direction, then the voltage induced in a bar has the same amplitude in every slice, but is phase shifted in time relative to adjacent slices. The average of the voltage induced in the slices occurs at the axial center. Of course, the average induced voltage in a skewed rotor is less than that of an unskewed rotor.

To account for the reduction in induced voltage, the air gap reluctance is increased by the skew constant. However, only the stator flux linking rotor conductors and the rotor flux linking stator conductors are affected by skewing. Therefore, only the air gap reluctance related to these flux linkages are increased. The air gap reluctance related to the stator flux linking stator conductors and the rotor flux linking rotor conductors is undisturbed.

Equations formulating voltages experienced by stator windings and rotor bars are then written. The skew constant is attached only to the air gap reluctances related to flux linking conductors on the other side of the air gap. The equations can be rearranged so that every air gap reluctance is scaled by the skew

-46-

constant. However, two extra terms appear that are labelled stator and rotor induced voltages due to time derivative of skew leakage flux linkage. To incorporate these terms, skew leakage flux is included in the lumped leakage magnetic model. With the skew constant attached to every air gap reluctance to compensate for skewing, all other variables in the lumped magnetic model can be determined for an unskewed rotor.

To determine the skew leakage reluctances, the calculated stator and rotor skew induced voltages are set equal to the skew induced voltages formulated by the lumped electrical model in the next chapter. The latter induced voltages are formulated in terms of $\mathfrak{R}_{slw}$ and $\mathfrak{R}_{rlw}$, the winding excitation, and the winding scheme. The reluctances are then solved.

The stator and rotor skew leakage reluctances, explained in detail in the footnoted reference, are formulated as a function of the skew constant and the air gap reluctance:[20]

$$\mathfrak{R}_{slw} = \frac{1 + \dfrac{K_c K_s K_w \mathfrak{R}_g}{\dfrac{2}{\pi}\mathfrak{R}_{sl}}}{1 - \dfrac{1}{K_w^2}} - 2K_c K_s \mathfrak{R}_g$$

$$\mathfrak{R}_{rlw} = \frac{1 + \dfrac{K_c K_s K_w \mathfrak{R}_g}{\dfrac{2}{\pi}\mathfrak{R}_{rl}}}{1 - \dfrac{1}{K_w^2}} - 2K_c K_s \mathfrak{R}_g$$

II-18

$$K_w = \frac{\dfrac{\theta_{rlw}}{2}}{\sin\left(\dfrac{\theta_{rlw}}{2}\right)}$$

where:

θ_{rlw} $\quad$ = rotor skew tangential arc angle

The coefficients in the numerator of the first two equations contain $\mathfrak{R}_{sl}$ and $\mathfrak{R}_{rl}$. These reluctances are unknown until the skew leakage reluctances are calculated. However, since the steel reluctance constant

---

[20]Cyril G. Veinott, *Theory and Design of Small Induction Motors*, New York: McGraw-Hill Book Company, Inc., 1959, pp. 323-327.

-47-

which is also in the numerator is solved iteratively, an initial guess can be made. The entire ratio of air gap reluctance to leakage reluctance can usually be approximated initially between two and nine percent.

The skew constant is the ratio of skew arc angle to its chord length. Skew angle is a spatial phase angle measured in radians with respect to the center of the shaft. Increasing the angle decreases skew leakage reluctance and increases skew leakage flux. An ideal skew angle based on stator slot count and pole count has been theorized to dramatically reduce harmonics.[21] Although skewing the rotor also introduces slightly more slot and zig-zag leakage fluxes, the additional refinements are not made.

II.E. Summary

Accurate lumped magnetic modelling of the induction motor is difficult. The characteristically small air gap causes MMF drops in the steel to be significant in formulating the air gap flux which produces useful torque. Leakage flux is also significant in determining motor performance. Since the rotor magnetic field is induced by the stator magnetic field, any errors in modelling the stator compound any errors in modelling the rotor.

A lumped magnetic model that includes the MMF drops and leakage flux has been developed to describe flux behavior in the motor. Parameters of the model are functions of basic motor geometry and material properties. MMF drops in the steel are incorporated through the steel reluctance constant. Due to the interdependence of the steel constant and currents, an iterative process is used to determine these quantities. After the flux behavior in the motor is known, induced voltages from time derivative of the flux linkages can be derived in the lumped electrical model of the next chapter to calculate motor performance.

Permanent magnet motors are often represented by very simple magnetic models in which only the air gap flux producing useful torque is considered. Leakage flux is neglected because it is relatively small. In the induction motor, leakage flux must be included. A lumped leakage magnetic model has been developed to formulate the flux. Due to the difficulties of analytically modelling leakage flux, commonly applied approximate or empirical techniques are used.

---

[21] "The Effect of Harmonics on Induction Motor Performance," Eastern Air Devices, Incorporated, Dover, New Hampshire, Internal Report.

-48-

Leakage flux is ordinarily divided into slot, zig-zag, end, belt, and skew leakage fluxes. Slot leakage reluctances have been derived for concentric windings. Average zig-zag leakage reluctances that do not depend on the rotor position have been derived. Because of the complex interlinking of end leakage flux, end leakage reluctances have been empirically derived. Approximate expressions for belt leakage reluctances have also been empirically derived. The belt leakage flux is commonly insignificant in motors with a squirrel cage rotor, but is significant in ones with a wound rotor. In motors with low stator and rotor slot counts, belt leakage flux is significant and highly sensitive to them. Skew leakage reluctances and the skew constant are formulated to incorporate rotor skewing so that all other lumped magnetic model parameters can be determined for an unskewed rotor.

-49-

CHAPTER III

LUMPED ELECTRICAL MODEL

III.A. Introduction

In the previous chapter, the lumped magnetic model was developed to describe the flux behavior in the motor. An electrical model is developed in this chapter that uses the flux information to derive simple closed-form expressions of performance characteristics. The electrical model also uses temperature information that is formulated from the thermal model in the next chapter. The models give a simplistic yet accurate description of motor performance in terms of motor geometry and material properties.

Developing an accurate electrical model for the induction motor is much more difficult than for permanent magnet motors. In the latter motors, rotor resistance is unimportant, EMF from linkage with leakage flux can be neglected, and rotor flux is always known. Determining rotor resistance in the induction motor, is necessary and complicated by end rings that require the complete squirrel cage to be modelled. Also, permanent magnet motors are often represented by very simple electrical models that contain EMF voltages from linkage with only the air gap flux. In the induction motor, however, EMF voltages from linkage with the leakage flux must be included as well because they significantly influence performance. Furthermore, the rotor flux of permanent magnet rotors is always known given geometry and material composition. EMF from linkage with the flux is induced only in the stator windings and is easily determined. Rotor flux in the induction motor results exclusively from induced rotor currents. EMF from linkage with the flux is induced in the stator windings and rotor bars. The magnitude of the flux is dependent on geometry and material composition as well as the rotor speed.

To determine performance in the induction motor, a lumped electrical model is developed that consists of resistances and EMF voltages from flux linkages. The resistances and voltages are derived then used to relate input voltages to stator and rotor currents. Output performance expressions are formulated in terms of these voltages, currents, resistances, and flux linkages. The developed electrical model is compared to the well-known equivalent "T" circuit model, which has been the traditional approach to

-50-

induction motor analysis.

III.B. Development of the Lumped Electrical Model

The lumped electrical model consists of voltage drops across stator and rotor resistances as well as EMF voltages. The EMF voltages arise due to linkages with stator and rotor air gap and leakage fluxes. Due to symmetry, the model is developed only on a per-phase basis, though linkages with flux from the current in other phases are incorporated.

Just as the lumped magnetic model only considered motor sections carrying significant levels of flux, the lumped electrical model only considers motor sections with significant current flow. Most of the current in the induction motor flows in the highly conductive material of the stator windings and rotor bars. Eddy currents in the steel tend to be relatively small and are commonly neglected from the lumped electrical model. The eddy currents are not, however, neglected in performance calculations.

The lumped electrical model is developed to describe the stator and rotor currents. The currents are induced by input voltages and EMF voltages in the conductors. The EMF voltages arise from the time derivative of flux linkages. A time varying magnetic field induces a voltage called an electromotive force, EMF. The flux linkage occurs when the current in one conductor produces flux that links various conductors. Self coupling is when flux from the current in one phase completely links the conductors of that phase. Mutual coupling is when the flux partially links other conductors that it passes through.

The complete electrical model would consist of many stator and rotor electrical circuits in parallel. The number of stator circuits would equal the number of stator phases. All these circuits would be identical except for the temporal phase shifts in voltages and currents as well as the spatial phase shifts in flux linkages. The spatial phase shifts arise due to the spatial positions of the phases. The number of rotor circuits would equal the number of rotor phases. Likewise, all these circuits would also be identical except for the temporal and spatial phase shifts. Fortunately, the complete electrical model is unnecessary if symmetry exists.

The symmetry is identical to the one that simplified the lumped magnetic model. Excitation is balanced in time and space, rotor bars are evenly spaced, and rotor bar count divides evenly into the pole count. Even when the number of rotor phases is not an integer or the rotor bar count does not divide

-51-

evenly into the pole count, the number of rotor bars is usually large enough so that it does not introduce much error. Also, harmonics from imbalanced excitation and imbalanced windings are neglected. Since the temporal and spatial harmonics degrade motor performance, measures are almost invariably taken to keep them small.

Due to the symmetry, it is only necessary to analyze the electrical circuits for one set of the stator and rotor phases, though linkages with flux from current in other phases must be considered. The lumped electrical model of Figure 3.1 shows the input voltage and the EMF voltages for a set of phases where:[22]

v_{in}^k = input stator winding voltage in k^{th} stator phase
R_s = stator winding resistance per stator phase
v_{sl}^k = EMF in k^{th} stator phase from stator leakage flux linkage
v_{sg}^k = EMF in k^{th} stator phase from stator air gap flux linkage
v_{sr}^k = EMF in k^{th} stator phase from rotor air gap flux linkage
R_r = rotor squirrel cage resistance per rotor phase
v_{rl}^l = EMF in l^{th} rotor phase from rotor leakage flux linkage
v_{rg}^l = EMF in l^{th} rotor phase from rotor air gap flux linkage
v_{rs}^l = EMF in l^{th} rotor phase from stator air gap flux linkage
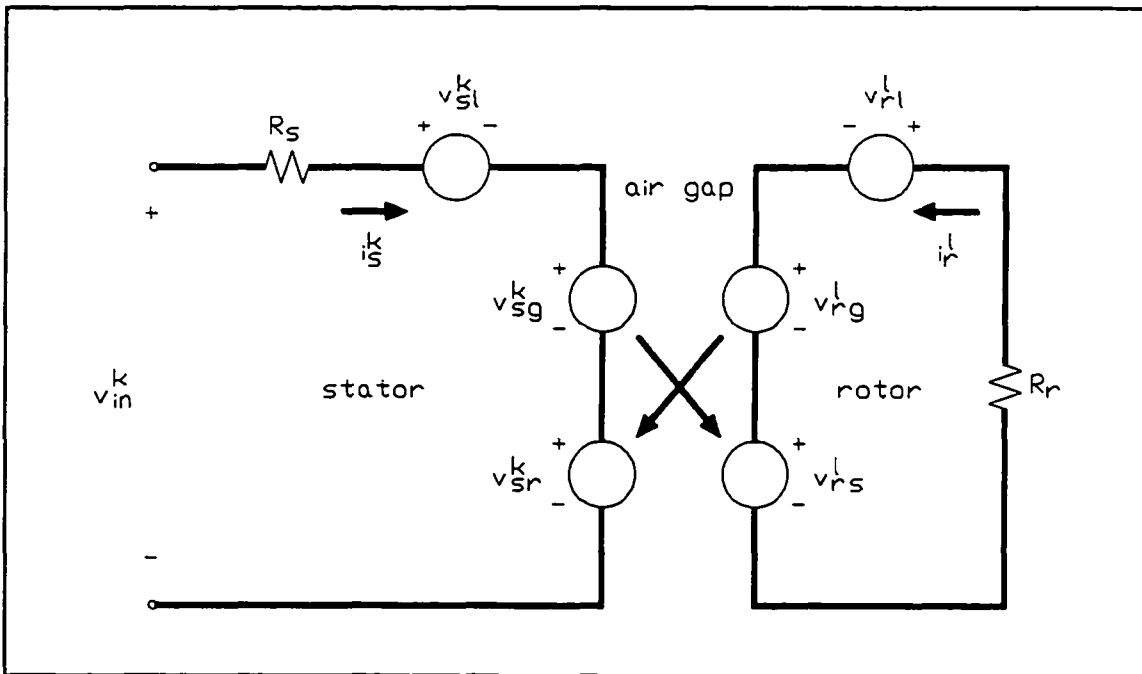
Figure 3.1 Lumped electrical circuit model per phase showing voltage drops.

The crossed arrows represent EMF voltages from flux crossing the air gap to link conductors on the other

---

[22]A. E. Fitzgerald, Charles Jr. Kingsley, and Stephen D. Umans, *Electric Machinery*, Fifth Edition, New York: McGraw-Hill, Inc., 1990, pp. 61-63.

-52-

side. For the circuits of any other set of phases, the voltages and currents are evenly phase shifted in time.

From the stator circuit, stator windings experience the input voltage and the EMF voltages due to linkage with stator air gap flux, stator leakage flux, and rotor air gap flux. The voltages force stator current to flow in the windings. Stator leakage flux links just the stator windings, while stator air gap flux links rotor bars as well by crossing the air gap to travel between the them.

From the rotor circuit, rotor bars experience EMF voltages due to linkage with stator air gap flux, rotor air gap flux, and rotor leakage flux. Similar to the stator flux, rotor leakage flux links just rotor bars, while rotor air gap flux links stator windings as well. The EMF voltages force rotor current to flow in the bars. The current actually flows in the opposite direction as defined in Figure 3.1 according to the polarities that are defined in the EMF voltages. The rotor current is defined in that direction to demonstrate Lenz's law, which states that an induced current opposes the change in flux that produced it.

The stator air gap flux links rotor bars at the slip frequency. This is because the stator magnetic flux vector rotates in the same direction as the rotor, but at the excitation frequency. The slip frequency is the difference between the excitation frequency and the electrical rotational frequency of the rotor. As a result, all rotor voltages and currents oscillate at the slip frequency.

The rotor air gap flux links stator windings at the excitation frequency. The EMF induced by this opposes the input voltage. When the rotation of the rotor flux vector is superimposed onto that of the rotor, the vector rotates at the excitation frequency relative to the stator. All flux oscillates at the slip frequency with respect to the rotating reference frame of the rotor, but at the excitation frequency with respect to the stationary reference frame of the stator. All stator voltages and currents oscillate at the excitation frequency.

Hysteresis and eddy current losses in the steel have been neglected from the lumped electrical model. Interdependence exists between the losses and the stator and rotor currents. The losses affect the currents, which determine the flux density levels in the steel that influence both the hysteresis losses and eddy currents. An iterative process can be used to determine these quantities.

However, an approximate method can be used to incorporate hysteresis and eddy current losses

-53-

in the stator and rotor steel. A resistor can be added in the lumped electrical model parallel to v_{sg}^k and v_{sr}^k.[23] The average power lost across the resistor at no load would approximately simulate the average hysteresis and eddy current losses per phase. No-load current can be measured experimentally in setting the resistance. In any event, the resistor is not included because the losses are commonly neglected. These losses tend to be small relative to the losses in much more conductive materials of the stator windings and rotor bars. Laminations are coated with insulation anyway to decrease axial eddy currents in the steel that oppose useful torque. Though, the hysteresis and eddy current losses can still be relatively significant for high excitation frequency when operating near synchronous speed.

III.C. Resistances

Stator and rotor resistances are formulated in order to derive currents from input voltages using the lumped electrical model. Resistance is a function of temperature, which depends on the heat generated by current. But, the current is dependent on the resistance. Therefore, resistances, currents, and heat generation are all interdependent. To determine these quantities, an iterative process is used where the steady state temperature at each rotor speed is determined from the thermal model in the next chapter.

III.C.1. Stator Winding Resistance

Stator resistance does not influence the torque generated by the current driven motor. In the voltage driven motor, however, an increase in the resistance reduces stator current and torque. Stator winding resistance is a function of motor geometry and material properties. The resistance per phase is calculated by first evaluating the resistance per length at the stator temperature at the operating speed. Then that resistance is multiplied by the length of wire used to wind one phase.

The resistance for an incremental length of wire can be determined from the wire resistivity and cross-sectional area. To evaluate the resistance at the temperature of the operating speed, the mean temperature coefficient is used. The resistance increases linearly with temperature over a wide range of temperatures.

---

[23]Cyril G. Veinott, *Theory and Design of Small Induction Motors*, New York: McGraw-Hill Book Company, Inc., 1959, pp. 169-170.

-54-

Once the resistance per length is known, the length of wire used to wind one phase is derived to determine the stator resistance per phase from the product of the two:

$$R_s = [1 + K_{sT}(T_s - T_{sr})]2nR_{wire}\left[N_s z + \frac{K_{se}\pi(D_{si} + l_{ssh})}{S_s} \sum_{k=1}^{\substack{concentric\ winding\ tiers}} n_s^k t_{coil}^k\right] \qquad \text{III-1}$$

where:

K_{sT} ≡ stator winding wire mean temperature coefficient of resistivity
T_s ≡ stator winding wire steady state temperature at operating speed
T_{sr} ≡ stator winding wire reference temperature
R_{wire} ≡ stator winding wire resistance per length at reference temperature
K_{se} ≡ stator end turn extension axial height constant

The resistance of each phase is identical due to the assumption of balanced windings. Skin effects are neglected since most stators are wound with thin wires.

Figure 3.2 shows the concentric windings in the stator for one phase of the simple two-pole polyphase motor of Figure 2.2 and Figure 2.4. The other phases are identical but spatially phase shifted by 120 degrees. The concentric windings consist of just one tier. Each slot holds two layers of windings of the same phase from matching poles.

The coils of one phase are wound in series over every pole. For a balanced winding scheme, the wire length is identical for every pole, which contains concentric windings of every tier. The concentric windings are separated into an axial section and an end turn section. The axial section is the part that runs axially in the slots. This section equals the product of the number of winding turns per pole in all of the tiers and twice the stator stack height. The doubling arises because coils of each tier sit in two slots.

The end turn section is the part of the windings that extend beyond the end of the stack and runs tangentially in the end turns. The extension arises due to the curvature of the wire bundle. The length of extension depends on many factors such as winding method, length of end turns, wire thickness, wire count in the bundles, and tier count. Instead of accounting for all the factors, a simple multiplier that is dependent on the pole count is used without much error. In the end turns, coils of each tier follow an arc approximately at the radial center of the slots corresponding to the tooth span of that tier. The end turn length of all tiers equals the sum of twice the arc length of each tier scaled by the coil count in that tier. The doubling arises because coils of each tier follow the arc at both ends of the stator stack.

-55-
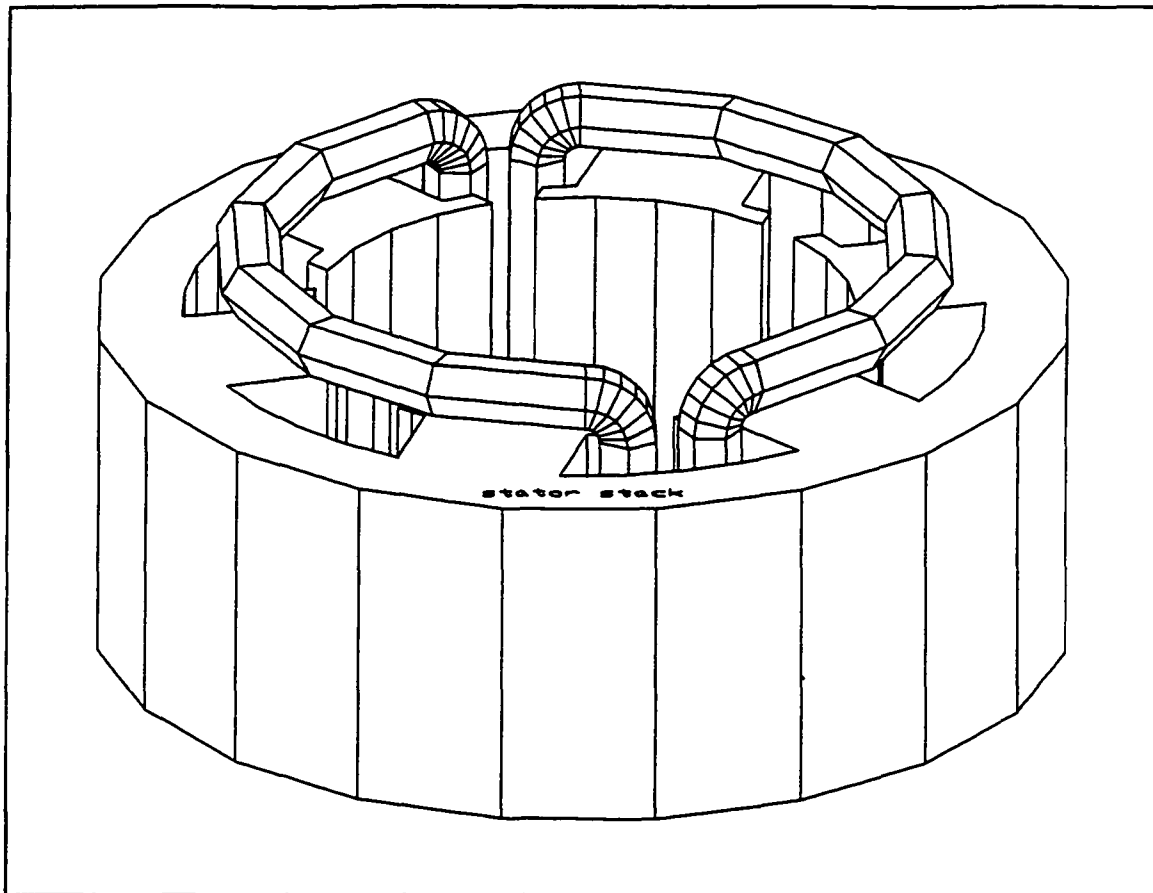
Figure 3.2 One-tier concentric windings of one phase in a two-pole stator with six teeth.

III.C.2. Rotor Squirrel Cage Resistance

Without skin effects as well as hysteresis and eddy current losses in the steel, rotor resistance is independent of the maximum torque in current and voltage driven motors. Figure 3.3 shows that an increase in the resistance effectively linearly stretches the torque-speed curve away from synchronous speed while keeping fixed the torque-speed point at that speed where:[24]

T	≡ steady state output torque
$\dot{\theta}_r$	≡ rotor squirrel cage mechanical rotational frequency

Consequently, torque decreases at low slip frequency and increases at high slip frequency.

Formulating resistance of the wound rotor is very similar to that of the wound stator. Skin effects are also omitted because winding wires are usually thin. Formulating resistance of the squirrel cage rotor,

---

[24]A. E. Fitzgerald, Charles Jr. Kingsley, and Stephen D. Umans, *Electric Machinery*, Fifth Edition, New York: McGraw-Hill, Inc., 1990, p. 341.

-56-
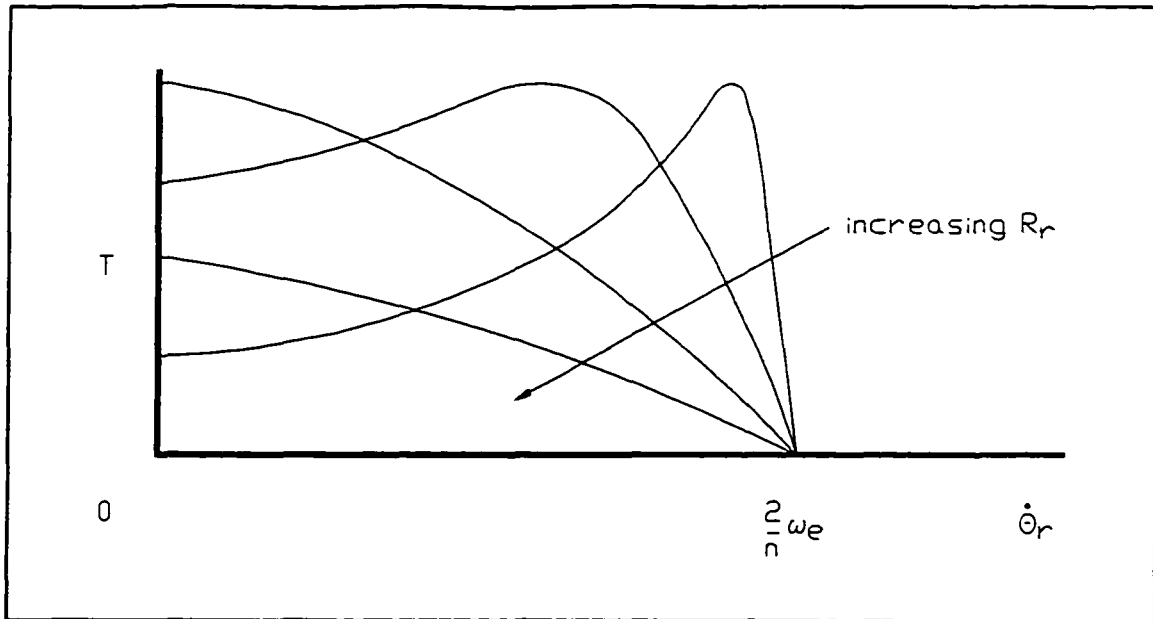
Figure 3.3 Effect of increasing rotor resistance on the torque-speed curve.

on the other hand, is more difficult because skin effects and end rings must be included. The resistance is a function of both the bar and end ring resistances. Determining the resistance per phase in the bar is simple because each bar contains current from only one phase. Determining the resistance associated with a phase in the end ring is complex because segments of the end rings between bars are shared by current from all phases flowing in various directions. As a result, the complete squirrel cage is modelled.

To derive the rotor resistance, a squirrel cage model is developed that contains EMF voltages, bar resistances, and end ring resistances. Kirchhoff's current law is used in the model to determine the current in the end rings as a function of current in the bars. Temperature effects and skin effects are excluded until after formulating the rotor resistance. Kirchhoff's voltage law is then used to sum the voltages around a loop in the squirrel cage model. The rotor resistance per phase is determined by expressing the voltage per phase in terms of the current per phase. Due to the assumption of evenly spaced rotor bars, the resistance of each phase is identical.

Figure 3.4 shows a planar squirrel cage resistance model for the six-bar rotor of the simple

-57-

two-pole motor of Figure 2.2 and Figure 2.4 where:[25]

v_r^k ≡ sum of EMF voltages in k^{th} rotor phase

i_{re}^k ≡ rotor end ring segment current between k^{th} and $(k+1)^{th}$ or first rotor phases

R_{rb} ≡ rotor bar resistance

R_{re} ≡ rotor end ring resistance
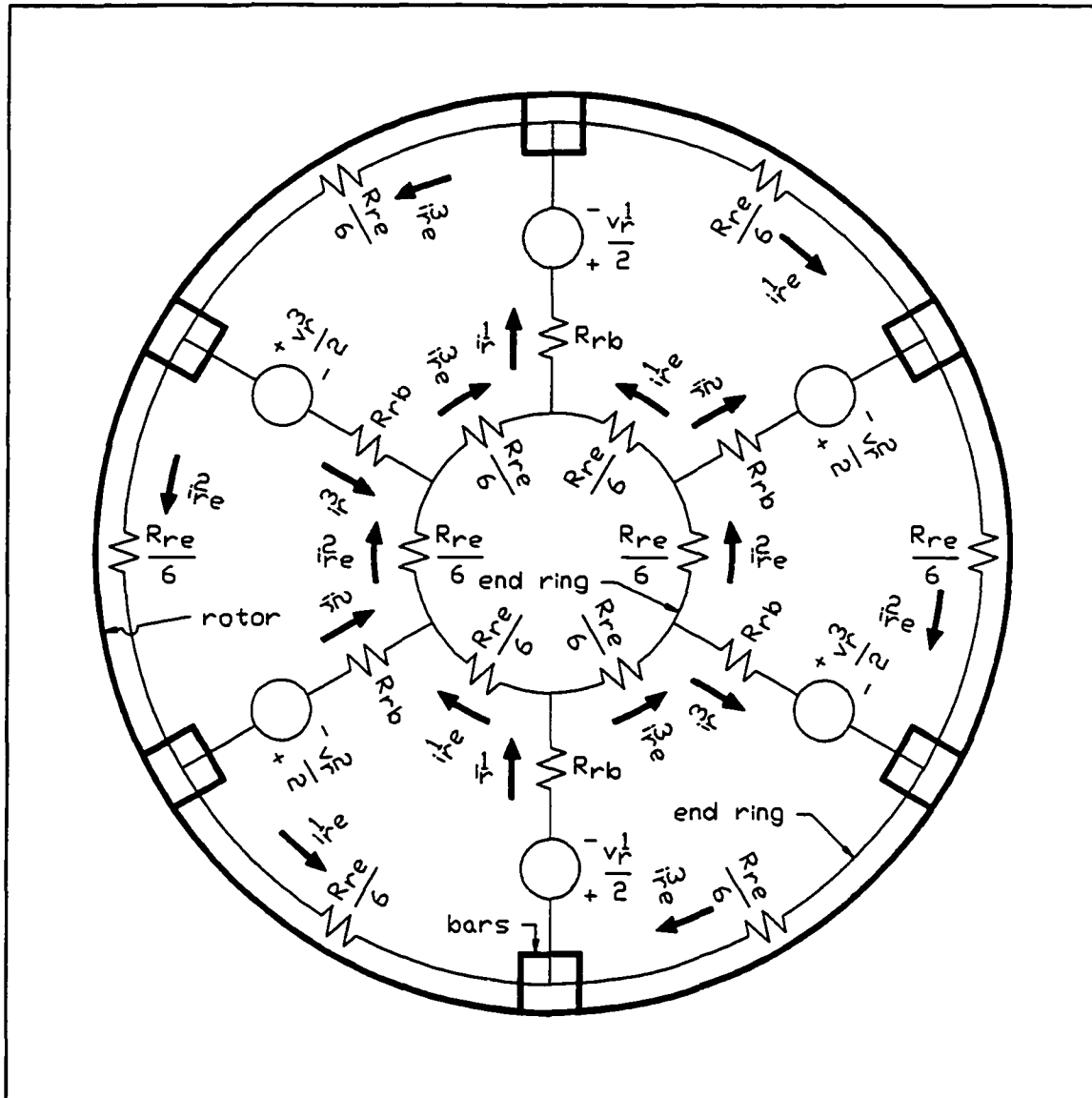
Figure 3.4 Planar squirrel cage resistance model for a six-bar rotor of a two-pole motor.

The model physically resembles the rotor when viewing from the axial direction. The end ring at the bottom is shown concentric to the one at the top, but with a smaller diameter. The heavy lines indicate

---

[25]Thomas A. Lipo, *Electromagnetic Design of AC Machines*, College of Engineering, Department of Electrical and Computer Engineering, University of Wisconsin-Madison, Madison, Wisconsin, Course Notes for ECE 713, 1990, Chapter 4, pp. 45-47.

the rotor outer diameter of the top end ring and the rotor bars connected to it. The rotor inner diameter for the motor shaft is not shown. According to the polarities that are defined in the EMF voltages, the current actually flows in the opposite direction as defined to be consistent with the rotor circuit of Figure 3.1. Resistances exist in the bars between the end rings. The end ring resistance is divided into segments between the bars. Temperature effects and skin effects on the resistances are not included for now, but will be incorporated after formulating the rotor resistance.

i_r^k and R_{rb} are associated with an entire bar not two half-bars. But, the current in Figure 2.6 follows two parallel paths through two half-bars. The current and resistance in the two paths can be combined into one path through the bar section of the path. In that one path, current through an entire bar is presented with resistance from that entire bar.

From Figure 3.1, the rotor current in each phase is induced by the sum of EMF voltages in that phase due to linkages with stator air gap flux, rotor air gap flux, and rotor leakage flux:

$$v_r^k = v_{rs}^k + v_{rg}^k + v_{rl}^k \qquad \text{III-2}$$

For each phase, v_r^k is in phase with the rotor current in the bar, i_r^k:

$$v_r^k = V_r \sin\left(\omega_s t - \alpha - \psi + \frac{n\pi k}{S_r}\right)$$

$$i_r^k = I_r \sin\left(\omega_s t - \alpha - \psi + \frac{n\pi k}{S_r}\right) \qquad \text{III-3}$$

where:

V_r	≡ amplitude of sum of EMF voltages in rotor phase
ω_s	≡ rotor bar slip frequency
t	≡ time
α	≡ phase angle lag from input stator winding voltage to stator winding current
ψ	≡ phase angle lag from stator winding current to rotor bar current
I_r	≡ rotor bar current amplitude

The two phase angles α and ψ serve to relate the phase angle of voltages and currents in the rotor to that in the stator after a common spatial reference is selected. The phase angles, which are derived later, do not serve any purpose here except to be consistent with later notations. When the flux density distribution across the air gap is assumed to be sinusoidal in space and time, v_r^k and i_r^k of every phase have identical

-59-

respective amplitudes but are phase shifted relative to other phases. The phase shifts stem from relative positions of the bars.

Currents in the end ring segments also have identical amplitude but are phase shifted relative to other segments due to relative positions of the segments:

$$i_{re}^{k} = I_{re} \sin\left(\omega t - \alpha - \psi - \gamma + \frac{n\pi k}{S_r}\right)$$

III-4

where:

I_{re} ≡ rotor end ring segment current amplitude
γ ≡ phase angle lag from rotor bar current to rotor end ring segment current

But, i_{re}^{k} is not in phase with i_{r}^{k} because the end ring segments are shared among all the latter currents. The amplitude of the rotor currents and EMF voltages is not required here in deriving the rotor resistance and so will be determined in a later section.

However, the current in the end ring segments as a function of the current in the bars is needed. Kirchhoff's current law is used to sum the currents in Figure 3.4 at a node:

$$i_{r}^{2} = i_{re}^{2} - i_{re}^{1}$$

III-5

After substitutions from Equation III-3 and Equation III-4, the relative amplitude and phase angle lag become:

$$I_{re} = \frac{I_r}{\sqrt{2\left[1 - \cos\left(\frac{n\pi}{S_r}\right)\right]}}$$

$$\gamma = \tan^{-1}\left[\frac{\sin\left(\frac{n\pi}{S_r}\right)}{1 - \cos\left(\frac{n\pi}{S_r}\right)}\right]$$

III-6

When many rotor phases exist, the end ring segments carry much more current than the bars. A large number of rotor phases is necessary to reduce harmonics in the rotor air gap flux density distribution.

Now that current in the end ring segments as a function of current in the bars is known, rotor

-60-

resistance is derived by formulating v_r^k as a function of i_r^k. Kirchhoff's voltage law is used to sum the voltages in Figure 3.4 around two adjacent bars and the end ring segments in between:

$$\frac{v_r^2}{n} - \frac{v_r^1}{n} = R_{rb}\left(i_r^1 - i_r^2\right) + \frac{2R_{re}}{S_r}i_{re}^1 \qquad \text{III-7}$$

This general equation holds for any pole count and bar count since the EMF is divided into the number of poles and the end ring resistance is divided into the number of rotor bars. To convert v_r^k to be on a per-bar basis, it is divided by the pole count. The difference of the EMF in two adjacent bars is a function of the current in the bars and in the end ring segments in between.

Since i_{re}^k relative to i_r^k is known, v_r^k in any phase can be written in terms of the current through that phase and the resistances associated with that phase. Through trigonometric identities and substitutions from Equation III-3, Equation III-4, and Equation III-6, v_r^k equals:

$$v_r^k = -n\left[R_{rb} + \frac{R_{re}}{2S_r \sin^2\left(\frac{n\pi}{2S_r}\right)}\right]i_r^k \qquad \text{III-8}$$

The negative sign associated with the rotor bar current arises because the actual direction of flow is opposite as defined in Figure 3.1 and Figure 3.4.

When temperature effects and skin effects are included, the rotor squirrel cage resistance per phase becomes:

$$R_r = \left[1 + K_{rT}\left(T_r - T_{rr}\right)\right]n\left[K_{rb}R_{rb} + \frac{K_{re}R_{re}}{2S_r \sin^2\left(\frac{n\pi}{2S_r}\right)}\right] \qquad \text{III-9}$$

where:

K_{rT}	= rotor squirrel cage mean temperature coefficient of resistivity
T_r	= rotor squirrel cage steady state temperature at operating speed
T_{rr}	= rotor squirrel cage reference temperature
K_{rb}	= rotor bar skin effects constant
K_{re}	= rotor end ring skin effects constant

Heating affects rotor resistance in the same manner as the stator resistance of Equation III-1. R_{rb} and R_{re} are calculated at their reference temperatures, then scaled to the temperature at the operating speed. The

-61-

temperature of the bars is usually very close to that of the end rings. If not, then the two resistances can be evaluated at different temperatures. The bars are usually constructed of the same material as the end rings. But, if different materials are used, another temperature coefficient can easily be applied. In motors with many rotor phases and a high end ring resistance, the end rings can be significant in the squirrel cage resistance.

In calculating R_{rb} and R_{re}, the current density distribution is assumed to be uniform. However, skin effects cause the distribution in bars and end rings to be nonuniform. Conceptually, if the rotor bar is sectioned into differential slices in the radial direction all connected in parallel, then slices at the radial top and bottom link different amounts of flux. This difference arises because leakage flux exists across the slot. Further description on this leakage flux is presented in section II.D.1. An induced voltage gradient occurs throughout the parallel slices of rotor bar causing the current distribution to be nonuniform. Circulating currents form pushing the through currents to the peripheral slices, thereby increasing the effective resistance of the bar. This phenomenon, called skin effects, occurs predominately in rotor bars and end rings.

The skin effects constants, which have been theoretically derived, simulate this phenomenon by increasing the effective bar and end ring resistances:[26]

---

[26]Thomas A. Lipo, *Electromagnetic Design of AC Machines*, College of Engineering, Department of Electrical and Computer Engineering, University of Wisconsin-Madison, Madison, Wisconsin, Course Notes for ECE 713, 1990, Chapter 5, pp. 2-8.

$$K_{rb} = \frac{l_{rz}}{d_r} \frac{\sinh\left(2\frac{l_{rz}}{d_r}\right) + \sin\left(2\frac{l_{rz}}{d_r}\right)}{\cosh\left(2\frac{l_{rz}}{d_r}\right) - \cos\left(2\frac{l_{rz}}{d_r}\right)}$$

$$K_{re} = \frac{D_{ro} - D_{ri}}{2d_r} \frac{\sinh\left(\frac{D_{ro} - D_{ri}}{d_r}\right) + \sin\left(\frac{D_{ro} - D_{ri}}{d_r}\right)}{\cosh\left(\frac{D_{ro} - D_{ri}}{d_r}\right) - \cos\left(\frac{D_{ro} - D_{ri}}{d_r}\right)} \qquad \text{III-10}$$

$$d_r = \sqrt{\frac{2[1 + K_{rt}(T_r - T_{rr})]\rho_r}{\mu_r \omega_s}}$$

where:

d_r = rotor squirrel cage skin effects depth
ρ_r = rotor squirrel cage resistivity at reference temperature
μ_r = rotor squirrel cage permeability

Permeability of the squirrel cage material is almost invariably equivalent to that of air for most practical rotors. Skin effects, which increase with slip frequency as well as radially deep bars and end rings, cause the rotor resistance to vary with rotor speed. An increase in skin effects boosts torque and heat generated at stall. Performance at high rotor speeds, however, remains almost undisturbed.

III.D. EMF Voltages

The lumped electrical model is used to determine induction motor performance. With stator and rotor resistances in the model already formulated, EMF voltages are derived in the following sections. From Faraday's law of induction, EMF voltages are induced in stator windings due to the linkage with stator air gap flux, stator leakage flux, and rotor air gap flux. EMF voltages are induced in rotor bars due to the linkage with rotor air gap flux, rotor leakage flux, and stator air gap flux.

The lumped magnetic model has derived the flux in a pole pair due to current of each stator and rotor phase. Superposition is applied to sum the linkage contribution from flux produced by current in each phase. Since flux in each pole pair behaves the same, identical EMF voltages are induced in each pole pair. The EMF voltages per pole pair summed over all pole pairs in series yield the EMF voltages per

-63-

phase.

Due to sinusoidal excitation that is balanced in time and space, the EMF per phase is independent of the spatial phase shift of flux linkages. Also, the EMF induced in each phase is in phase with the current in that phase. Therefore, the EMF can be modelled as a voltage drop across an inductance. The EMF is identical for all phases except for the phase shifts which account for the relative positions of the phases.

III.D.1. Time Derivative of Stator Air Gap Flux Linkage

Stator air gap flux links all stator windings as well as all rotor bars. The EMF voltages from the flux linkages are derived. A stator air gap inductance is defined and the EMF voltages are expressed as voltage drops across it.

When linking the stator, stator air gap flux produced by the current of each phase links the coils of each phase. The linkage must account for the spatial phase of the flux relative to the coils. Superposition is applied to sum the linkages in a pole pair. The linkage per pole pair is multiplied by the number of pole pairs to yield the linkage per phase.

The EMF in the kth stator phase from linkage with the stator air gap flux is:

$$v_{ag}^{k} = \frac{n}{2} \frac{d}{dt} \left[2K_d N_s \sum_{l=1}^{n} \phi_{ag}^{l} \frac{\displaystyle\int_{2\pi - \frac{2\pi}{n}(k-l)}^{\pi + 2\pi - \frac{2\pi}{n}(k-l)} \sin(\theta) \, d\theta}{\displaystyle\int_{2\pi}^{\pi + 2\pi} \sin(\theta) \, d\theta} \right] \qquad \text{III-11}$$

where:

θ = spatial phase angle

The concentric windings consist of a matching set of tiered wire bundles for each pole pair. Although the flux links both sets of the wire bundles, it does not completely link the coils of each tier due to the different tooth spans. K_d accounts for the different spans of the tiers in linking flux. The last term of the summation originates from self coupling while all other terms originate from mutual coupling.

Stator air gap flux has been derived in Equation II-4 by the lumped magnetic model:

-64-

$$v_{sg}^k = \frac{n}{2} \frac{d}{dt}\left\{ 2K_sN_s \sum_{l=1}^{m} \frac{4}{\pi} \frac{2}{\pi} \frac{K_dN_si_s^l}{K_cK_sK_w\Re_g} \cos\left[\frac{2\pi}{m}(k-l)\right]\right\} \qquad \text{III-12}$$

The stator currents, like rotor currents, have identical amplitude but are also phase shifted relative to other phases due to their relative positions:

$$i_s^k = I_s \sin\left(\omega_e t - \alpha + \frac{2\pi k}{m}\right) \qquad \text{III-13}$$

where:

I_s = stator winding current amplitude

As stated before, the phase angle α, which is derived later, does not serve any purpose now except to be consistent with later notations. It relates the phase angle of the stator currents to that of the input voltages.

After substituting for the stator currents in Equation III-12, the summation is simplified through the use of a trigonometric identity:

$$\begin{aligned}
v_{sg}^k &= K_{sv}\frac{n}{2} \frac{d}{dt}\left[2K_dN_s\frac{m}{2}\frac{4}{\pi}\frac{2}{\pi}\frac{K_dN_sI_s}{K_cK_sK_w\Re_g} \sin\left(\omega_e t - \alpha + \frac{2\pi k}{m}\right)\right] \\
&= K_{sv}\frac{4}{\pi^2}\frac{nmK_d^2N_s^2}{K_cK_sK_w\Re_g}\omega_e I_s \cos\left(\omega_e t - \alpha + \frac{2\pi k}{m}\right) \qquad \text{III-14}
\end{aligned}$$

$$K_{sv} = \begin{cases} 1, & m \geq 2 \\ 2, & m = 1 \end{cases}$$

where:

K_{sv} = stator EMF trigonometric identity constant

The constraint of the identity necessitates a scaling constant for the single-phase motor. For the two-phase motor, ninety degrees spatially separate the stator windings and temporally separate their currents. Otherwise, if 180 degrees separate the windings and currents according to Equation III-13, the motor would perform like the single-phase motor with pulsating, not rotating, air gap flux vectors.

The EMF from stator air gap flux linkage can be expressed in the frequency domain as the voltage drop across an inductance:

-65-

$$v_{sg}^k = j\omega_e L_{sg} i_s^k$$

$$L_{sg} = K_{sv}\frac{4}{\pi^2}\frac{nmK_d^2 N_s^2}{K_c K_s K_w \Re_g}$$

<div align="right">III-15</div>

where:

L_{sg} = stator air gap inductance per stator phase

The EMF in any stator phase is dependent on current in only that phase. Phase shifts in time and space all cancel.

Stator air gap flux also links rotor bars. The EMF in the kth rotor phase from linkage with the flux is:

$$v_{rs}^k = \frac{n}{2}\frac{d}{dt}\left[N_r \sum_{l=1}^{m} \phi_{sg}^l \frac{\displaystyle\int_{2\pi-\frac{n\pi k}{S_r}+\frac{2\pi l}{m}}^{\pi+2\pi-\frac{n\pi k}{S_r}+\frac{2\pi l}{m}} \sin(\theta)\, d\theta}{\displaystyle\int_{2\pi}^{\pi+2\pi} \sin(\theta)\, d\theta} \right]$$

$$= K_{sv}\frac{2}{\pi^2}\frac{nmK_d N_s N_r}{K_c K_s K_w \Re_g}\omega J_s \cos\left(\omega_s t - \alpha + \frac{n\pi k}{S_r}\right)$$

<div align="right">III-16</div>

The spatial phase of the flux relative to the bars is accounted for. The last stator phase is selected to be spatially aligned with the last rotor phase so that all stator and rotor phases relate to the same spatial reference. If the phases are not aligned or they do not exactly face each other across the air gap, then the phase angle of misalignment can be attached to the limits of the integrals. However, any misalignment is usually small because the squirrel cage is commonly designed with many bars to reduce harmonics in the rotor air gap flux density distribution. All terms of the summation originate from mutual coupling. The stator air gap flux oscillates at the slip frequency with respect to the rotor bars.

The EMF can be expressed in the frequency domain as a function of the stator air gap inductance:

$$v_{rs}^k = j\omega_s L_{sg}\frac{N_r}{2K_d N_s}i_s^k$$

<div align="right">III-17</div>

The stator current here oscillates at the slip frequency with a phase shift of the kth rotor phase. Although

<div align="center">-66-</div>

this stator current does not actually exist, the EMF is proportional to a stator current that is evaluated in the rotating reference frame relative to the rotor phase. When the rotor rotates at synchronous speed, no EMF is induced. At stall, the EMF is proportional to the excitation frequency. The EMF causes current that oscillates at the slip frequency to flow in the rotor bars, thereby producing rotor flux.

III.D.2. Time Derivative of Stator Leakage Flux Linkage

Stator leakage flux links only the stator windings and not the rotor bars. The EMF in the kth stator phase from linkage with the flux is:

$$v_{sl}^k = \frac{n}{2} \frac{d}{dt} \left[2K_d N_s \sum_{l=1}^{m} \phi_{sl}^l \frac{\displaystyle\int_{2\pi - \frac{2\pi}{m}(k-l)}^{\pi + 2\pi - \frac{2\pi}{m}(k-l)} \sin(\theta) \, d\theta}{\displaystyle\int_{2\pi}^{\pi+2\pi} \sin(\theta) \, d\theta} \right]$$

$$= K_{sv} \frac{2}{\pi} \frac{nmK_d^2 N_s^2}{\Re_{sl}} \omega_e I_s \cos\left(\omega_e t - \alpha + \frac{2\pi k}{m}\right)$$ III-18

The flux has been derived in Equation II-4 by the lumped magnetic model. The EMF can be expressed in the frequency domain as a function of the stator leakage inductance:

$$v_{sl}^k = j\omega_e L_{sl} i_s^k$$

$$L_{sl} = K_{sv} \frac{2}{\pi} \frac{nmK_d^2 N_s^2}{\Re_{sl}}$$ III-19

where:

L_{sl} = stator leakage inductance per stator phase

III.D.3. Time Derivative of Rotor Air Gap Flux Linkage

Like the stator air gap flux, rotor air gap flux links all rotor bars as well as all stator windings. The EMF in the kth rotor phase from linkage with the flux is:

-67-

$$v_{r\theta}^k = \frac{n}{2} \frac{d}{dt} \left[N_r \sum_{l=1}^{\frac{S_r}{n}} \phi_{r\theta}^l \frac{\displaystyle\int_{2\pi - \frac{n\pi}{S_r}(k-l)}^{\pi + 2\pi - \frac{n\pi}{S_r}(k-l)} \sin(\theta)\, d\theta}{\displaystyle\int_{2\pi}^{\pi+2\pi} \sin(\theta)\, d\theta} \right]$$

$$= K_{rv} \frac{S_r N_r^2}{\pi^2 K_c K_f K_w \Re_g} \omega_s J_r \cos\left(\omega_s t - \alpha - \psi + \frac{n\pi k}{S_r}\right) \qquad \text{III-20}$$

$$K_{rv} = \begin{cases} 1, & \dfrac{S_r}{n} > 1 \\[2mm] 2, & \dfrac{S_r}{n} = .5, 1 \end{cases}$$

where:

K_{rv} = rotor EMF trigonometric identity constant

The flux has been derived in Equation II-4 by the lumped magnetic model. After substituting for the rotor currents through Equation III-3, the summation is simplified through the use of another trigonometric identity. This identity for the rotor is similar to the one for the stator in Equation III-14 except the number of stator phases is replaced by twice the number of rotor bars per pole. The EMF can be expressed in the frequency domain as a function of the rotor air gap inductance:

$$v_{r\theta}^k = j\omega_s L_{r\theta} i_r^k$$

$$L_{r\theta} = K_{rv} \frac{S_r N_r^2}{\pi^2 K_c K_f K_w \Re_g} \qquad \text{III-21}$$

where:

$L_{r\theta}$ = rotor air gap inductance per rotor phase

Rotor air gap flux also links stator windings. The EMF in the kth stator phase from linkage with the flux is:

-68-

$$v_{sr}^k = \frac{n}{2}\frac{d}{dt}\left[2K_dN_s\sum_{l=1}^{\frac{S_r}{n}}\phi_{rg}^l\frac{\displaystyle\int_{2\pi-\frac{2\pi k}{m}+\frac{\pi\pi l}{S_r}}^{\pi+2\pi-\frac{2\pi k}{m}+\frac{\pi\pi l}{S_r}}\sin(\theta)\,d\theta}{\displaystyle\int_{2\pi}^{\pi+2\pi}\sin(\theta)\,d\theta}\right]$$

$$= K_{rv}\frac{2}{\pi^2}\frac{S_rK_dN_sN_r}{K_cK_sK_w\Re_g}\omega_eI_r\cos\left(\omega_et-\alpha-\psi+\frac{2\pi k}{m}\right)$$

III-22

The rotor air gap flux oscillates at the excitation frequency with respect to the stator windings. The EMF can be expressed in the frequency domain as a function of the rotor air gap inductance:

$$v_{sr}^k = j\omega_eL_{rg}\frac{2K_dN_s}{N_r}i_r^k$$

III-23

The rotor current here oscillates at the excitation frequency with a phase shift of the kth stator phase. Although this rotor current does not actually exist, the EMF is proportional to a rotor current that is evaluated in the stationary reference frame relative to the stator phase.

III.D.4. Time Derivative of Rotor Leakage Flux Linkage

Rotor leakage flux links only the rotor bars and not the stator windings. The EMF in the kth rotor phase from linkage with the flux is:

$$v_{rl}^k = \frac{n}{2}\frac{d}{dt}\left[N_r\sum_{l=1}^{\frac{S_r}{n}}\phi_{rl}^l\frac{\displaystyle\int_{2\pi-\frac{n\pi}{S_r}(k-l)}^{\pi+2\pi-\frac{n\pi}{S_r}(k-l)}\sin(\theta)\,d\theta}{\displaystyle\int_{2\pi}^{\pi+2\pi}\sin(\theta)\,d\theta}\right]$$

III-24

$$= K_{rv}\frac{S_rN_r^2}{2\pi\Re_{rl}}\omega_eI_r\cos\left(\omega_et-\alpha-\psi+\frac{n\pi k}{S_r}\right)$$

The flux has been derived in Equation II-4 by the lumped magnetic model. The EMF can be expressed in the frequency domain as a function of the rotor leakage inductance:

-69-

$$v_{rl}^k = j\omega_s L_{rl} i_r^k$$

$$L_{rl} = K_{rv} \frac{S_r N_r^2}{2\pi \mathfrak{R}_{rl}}$$

III-25

where:

L_{rl} $\equiv$ rotor leakage inductance per rotor phase

III.E. Stator and Rotor Currents from the Input Voltage

With the resistances and EMF voltages in the lumped electrical model derived, the currents are now solved. The defined inductances are used to replace the EMF voltages in Figure 3.1. Voltage equations are then written for the electrical circuits. By solving the simultaneous voltage equations, stator and rotor currents are formulated at any slip frequency from input voltages.

The lumped electrical model of Figure 3.5 consists of resistances and inductances, which have replaced the EMF voltages. Kirchhoff's voltage law is used to sum the voltages around the stator and rotor electrical circuits in the frequency domain:

$$v_{in}^k = R_s i_s^k + j\omega_s (L_{sl} + L_{sg}) i_s^k + v_{sr}^k$$

$$v_{rs}^l = - R_r i_r^l - j\omega_s (L_{rl} + L_{rg}) i_r^l$$

III-26

v_{sr}^k and v_{rs}^l are substituted from Equation III-23 and Equation III-17:

$$v_{in}^k = R_s i_s^k + j\omega_s (L_{sl} + L_{sg}) i_s^k + j\omega_s L_{rg} \frac{2K_d N_s}{N_r} i_r^k$$

III-27

$$j\omega_s L_{sg} \frac{N_r}{2K_d N_s} i_s^l = - R_r i_r^l - j\omega_s (L_{rl} + L_{rg}) i_r^l$$

By solving the simultaneous equations, stator and rotor currents in the kth phase are derived as functions of the input voltage in the kth phase:

-70-
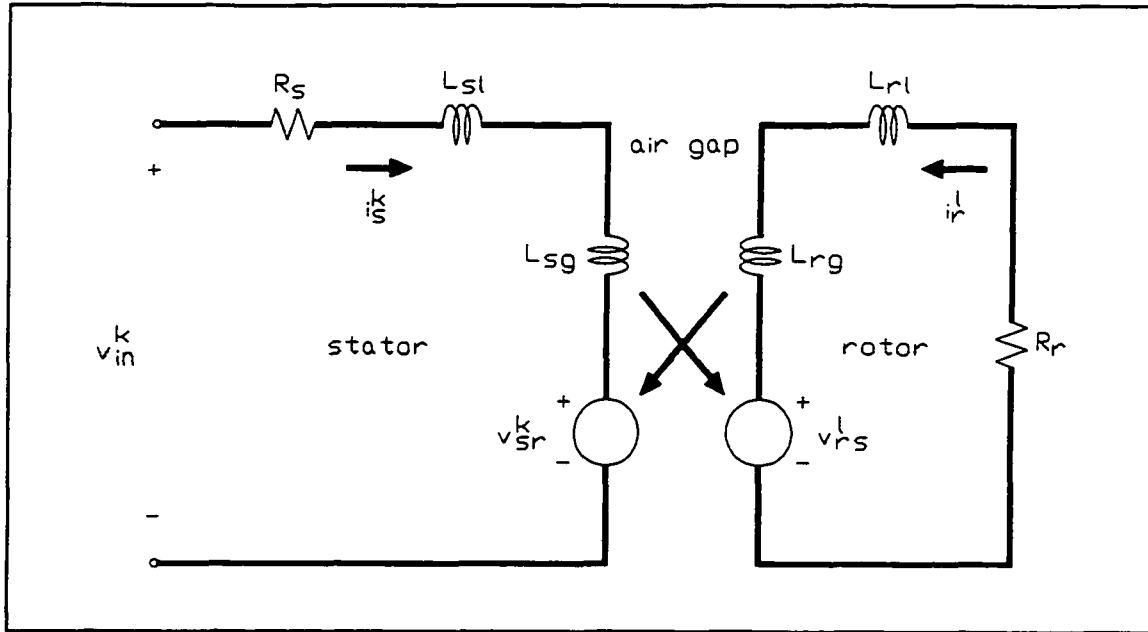
Figure 3.5 Lumped electrical circuit model per phase.

$$i_s^k = \cfrac{\dfrac{1}{R_s}\left[1 + j\dfrac{\omega_s}{R_r}(L_{rl}+L_{rg})\right]v_{in}^k}{1 - \dfrac{\omega_e\omega_s}{R_sR_r}\left[(L_{sl}+L_{sg})(L_{rl}+L_{rg}) - L_{sg}L_{rg}\right] + j\left[\dfrac{\omega_e}{R_s}(L_{sl}+L_{sg}) + \dfrac{\omega_s}{R_r}(L_{rl}+L_{rg})\right]}$$

III-28

$$i_r^k = -\cfrac{j\dfrac{\omega_s}{R_sR_r}L_{sg}\dfrac{N_r}{2K_dN_s}v_{in}^k}{1 - \dfrac{\omega_e\omega_s}{R_sR_r}\left[(L_{sl}+L_{sg})(L_{rl}+L_{rg}) - L_{sg}L_{rg}\right] + j\left[\dfrac{\omega_e}{R_s}(L_{sl}+L_{sg}) + \dfrac{\omega_s}{R_r}(L_{rl}+L_{rg})\right]}$$

A transformation from the excitation frequency to the slip frequency is necessary for the rotor current. Current in only the rotor bars spatially aligned with stator windings is represented. For current in the misaligned bars, the phase angle is shifted in time. The negative sign in the rotor current equation indicates the rotor current actually flows in the opposite direction as defined in Figure 3.1 and Figure 3.5.

To translate the currents to the time domain, the temporal reference for all voltages and currents is first chosen to be the phase angle of the input voltage in the last phase. The input stator voltage in the kth stator phase is:

$$v_{in}^k = V_{in}\sin\left(\omega_e t + \frac{2\pi k}{m}\right)$$

III-29

-71-

Stator and rotor currents are then expressed in the form of Equation III-13 and Equation III-3:

$$I_s = \frac{\frac{1}{R_s}\sqrt{1 + \left[\frac{\omega_s}{R_r}(L_{rl}+L_{rg})\right]^2}\, V_{in}}{\sqrt{\left\{1 - \frac{\omega_e \omega_s}{R_s R_r}\left[(L_{sl}+L_{sg})(L_{rl}+L_{rg}) - L_{sg}L_{rg}\right]\right\}^2 + \left[\frac{\omega_e}{R_s}(L_{sl}+L_{sg}) + \frac{\omega_s}{R_r}(L_{rl}+L_{rg})\right]^2}}$$

$$\alpha = -\tan^{-1}\left[\frac{\omega_s}{R_r}(L_{rl}+L_{rg})\right] + \tan^{-1}\left\{\frac{\frac{\omega_e}{R_s}(L_{sl}+L_{sg}) + \frac{\omega_s}{R_r}(L_{rl}+L_{rg})}{1 - \frac{\omega_e \omega_s}{R_s R_r}\left[(L_{sl}+L_{sg})(L_{rl}+L_{rg}) - L_{sg}L_{rg}\right]}\right\} \qquad \text{III-30}$$

$$I_r = \frac{\frac{\omega_s}{R_s R_r}L_{sg}\frac{N_r}{2K_d N_s}V_{in}}{\sqrt{\left\{1 - \frac{\omega_e \omega_s}{R_s R_r}\left[(L_{sl}+L_{sg})(L_{rl}+L_{rg}) - L_{sg}L_{rg}\right]\right\}^2 + \left[\frac{\omega_e}{R_s}(L_{sl}+L_{sg}) + \frac{\omega_s}{R_r}(L_{rl}+L_{rg})\right]^2}}$$

$$\psi = \frac{\pi}{2} + \tan^{-1}\left[\frac{\omega_s}{R_r}(L_{rl}+L_{rg})\right]$$

For the current driven motor, the rotor current amplitude can be defined in terms of the stator current amplitude:

$$I_r = \frac{\frac{\omega_s}{R_r}L_{sg}\frac{N_r}{2K_d N_s}I_s}{\sqrt{1 + \left[\frac{\omega_s}{R_r}(L_{rl}+L_{rg})\right]^2}} \qquad \text{III-31}$$

All other stator and rotor currents are extracted by phase shifting in time to account for the relative positions of the stator windings and rotor bars.

The trends in the stator and rotor currents are determined with eddy currents in the steel and skin effects neglected. Skin effects are usually small at low slip frequency where the induction motor typically operates. Stator current amplitude increases as rotor speed decreases except near synchronous speed. The phase angle of the stator current lags that of the input voltage from zero to ninety degrees over all slip frequencies. The phase lag increases as rotor speed decreases except near synchronous speed. Rotor current amplitude increases as rotor speed decreases in both current and voltage driven motors. When

-72-

operating near synchronous speed, induced rotor currents are small. Also, a phase lag of almost ninety degrees separates the rotor current from the stator current that is directly across the air gap. As slip frequency increases, the phase lag approaches 180 degrees where the rotor air gap flux completely cancels the stator air gap flux if rotor leakage flux is ignored.

III.F. Comparison with the General Equivalent "T" Circuit Model

The developed lumped electrical model of Figure 3.5 resembles the general equivalent "T" circuit model of Figure A.1, which has been the traditional approach to induction motor analysis. In fact, identical voltage equations describe both models. However, the developed electrical model allows for better physical representations through the physical separation of the stator and rotor as in the actual induction motor. The equivalent circuit model expresses all rotor parameters on a per-stator-phase, not per-rotor-phase, basis. Physical meaning is lost without using multipliers to convert the parameters back. The rotor parameters that are on a per-rotor-phase basis are not required in analyzing the induction motor, but are required in designing the motor.

Through transformations and substitutions, the equations describing the two models are identical. From the voltage equations of Equation III-27 describing the developed lumped model, the rotor air gap inductance is expressed in terms of the stator air gap inductance through Equation III-15 and Equation III-21:

$$v_{in}^k = R_s i_s^k + \hat{j}\omega_e L_s i_s^k + \hat{j}\omega_e L_{sg}\left(i_s^k + \frac{K_{rv}}{K_{sv}}\frac{S_r}{nm}\frac{N_r}{2K_d N_s}i_r^k\right)$$

$$0 = \frac{R_r}{s}\frac{2K_d N_s}{N_r}i_r^l + \hat{j}\omega_e L_{rl}\frac{2K_d N_s}{N_r}i_r^l + \hat{j}\omega_e L_{sg}\left(i_s^l + \frac{K_{rv}}{K_{sv}}\frac{S_r}{nm}\frac{N_r}{2K_d N_s}i_r^l\right)$$

III-32

The stator air gap inductance terms are grouped together. The rotor voltage equation is divided by slip and multiplied by twice the ratio of the number of stator to rotor turns. Slip defines the slip frequency as a percentage of the excitation frequency:

$$s = \frac{\omega_s}{\omega_e}$$

III-33

-73-

where:

s $\equiv$ slip

The rotor parameters are transformed from the rotating to the stationary reference frame. Therefore, the rotor currents oscillate at the excitation frequency. In addition, the rotor parameters are transformed to be on a per-stator-phase basis. The parameters are described, in effect, as referred to the stator.

After some substitutions are made, Equation III-32 is identical to Equation A-1 which describes the equivalent circuit model:

$$i_2^k = \frac{K_{rv}}{K_{sv}} \frac{S_r}{nm} \frac{N_r}{2K_dN_s} i_r^k$$

$$R_2 = \frac{K_{sv}}{K_{rv}} \frac{nm}{S_r} \frac{4K_d^2N_s^2}{N_r^2} R_r \qquad \text{III-34}$$

$$L_{2l} = \frac{K_{sv}}{K_{rv}} \frac{nm}{S_r} \frac{4K_d^2N_s^2}{N_r^2} L_{rl}$$

where:

i_2^k $\equiv$ referred rotor bar current in k^{th} rotor phase to k^{th} stator phase
R_2 $\equiv$ referred rotor squirrel cage resistance per rotor phase to per stator phase
L_{2l} $\equiv$ referred rotor leakage inductance per rotor phase to per stator phase

Only the current in rotor bars spatially aligned with stator windings is referred. The current in misaligned bars is referred with a phase shift in time. In the equivalent circuit model, the rotor circuit is connected to the stator circuit through the stator air gap inductance, which is contained in both circuits. In order to make the connection, all rotor variables are referred to the stator.

III.G. Output Performance Characteristics

With all the parameters in the lumped electrical model formulated, induction motor performance is derived. Input voltages, stator currents, rotor currents, resistances and inductances in the model are used to formulate steady state output performance expressions in closed form. Since the model parameters are derived from motor geometry and material properties, performance calculations can be related to them. Understanding these relationships is required for induction motor analysis and design. The performance characteristics comprise voltage and current driven torques, power factor, power losses, horsepower, and

-74-

efficiency.

The derivation of steady state torque begins with the conservation of instantaneous energy. By taking the time derivative of all the terms, the conservation of instantaneous power is derived. Steady state torque is then formulated.

The first law of thermodynamics is applied to electromechanical systems. The law states that the change in internal energy of a system equals the sum of heat absorbed by the system and work done by the system.[27] In the absence of friction, the energy input from the electrical source must equal the sum of the increase in energy stored in the magnetic field, the energy converted into heat, and the output mechanical energy. Friction can be incorporated by subtracting from the output torque.

Stored energy for motors with more than one stator phase and one rotor phase is constant when symmetry exists with no saturation. The symmetry is identical to the one that simplified the lumped magnetic and electrical models. Excitation is balanced in time and space, rotor bars are evenly spaced, and rotor bar count divides evenly into the pole count. The flux density distribution in the back iron has been assumed uniform between teeth but sinusoidal from tooth to tooth. Also, the flux density distribution in the teeth, like in the air gap, has been assumed sinusoidal.

By taking the time derivative of all terms in the conservation of instantaneous energy for an infinitesimal change, the conservation of instantaneous power is derived. Thus, input electrical power provides stored magnetic power, stator heat loss, rotor heat loss, hysteresis and eddy current losses in the steel, and output mechanical power:

$$\sum_{k=1}^{m} v_{bs}^{k} i_{s}^{k} = \sum_{k=1}^{m} R_{s}\left(i_{s}^{k}\right)^2 + \sum_{k=1}^{\frac{S_r}{n}} R_{r}\left(i_{r}^{k}\right)^2 + P_h + \dot{\theta}_r T \qquad \text{III-35}$$

where:

P_h = hysteresis and eddy current power losses in stator and rotor steel

Stored power designates the magnetic power reserved in the material for inducing currents. Stored power

---

[27]A. E. Fitzgerald, Charles Jr. Kingsley, and Stephen D. Umans, *Electric Machinery*, Fifth Edition, New York: McGraw-Hill, Inc., 1990, p. 101.

-75-

equals zero for motors with multiple stator and rotor phases since stored energy is constant. Though, local stored power in various steel regions may exist. Heat losses take the form of resistive power drops. Hysteresis and eddy current losses are formulated later from an empirical model. Output power arises from torque generated at a rotor speed.

Trigonometric manipulations are performed on the power balance after substituting for the voltages and currents from Equation III-29, Equation III-13, and Equation III-3:

$$\frac{m}{2}V_{in}I_s\cos(\alpha) = \frac{m}{2}R_sI_s^2 + \frac{S_r}{2n}R_rI_r^2 + P_h + \dot{\theta}_rT \qquad \text{III-36}$$

Input power is the product of half the number of stator phases, the input voltage amplitude, the stator current amplitude, and the power factor which is defined later. Stator heat loss is the product of the number of stator phases and the average power per phase dissipated across the stator winding resistance. Rotor heat loss is the product of the number of rotor phases and the average power per phase dissipated across the rotor squirrel cage resistance. Voltage and current harmonics, in reality, coexist with the fundamentals causing heating, vibration, and noise problems. However, many techniques are used to minimize these harmful harmonics.

To simplify the power balance even more, two identities are used. The first identity can be verified through Equation III-30:

$$\frac{m}{2}V_{in}I_s\cos(\alpha) - \frac{m}{2}R_sI_s^2 = \frac{\omega_e}{\omega_s}\frac{S_r}{2n}R_rI_r^2 \qquad \text{III-37}$$

The second identity relates the excitation frequency to the slip frequency and the rotor speed. Excitation frequency equals the sum of slip frequency and rotor electrical rotational frequency, which is the product of number of pole pairs and rotor mechanical rotational frequency:

$$\omega_e = \omega_s + \frac{n}{2}\dot{\theta}_r \qquad \text{III-38}$$

Torque is then numerically equivalent to the rotor heat loss scaled by the number of pole pairs divided by slip frequency when hysteresis and eddy current losses in the steel are ignored:

-76-

$$T = \frac{S_r}{4} \frac{R_r}{\omega_s} I_r^2 - \frac{P_h}{\dot{\theta}_r}$$

Although rotor heat loss produces no torque, the torque is related to the rotor heat loss. Hysteresis and eddy current losses are not included at synchronous speed because torque is zero and at stall because they can not divide by zero. The torque equation is consistent with the classical form derived from the general equivalent "T" circuit model of Figure A.1. With multiple stator and rotor phases, steady state torque at a rotor speed is independent of time. Torque produced by single-phase excitations, however, pulsates except at stall where no torque is produced.[28]

Since the rotor current amplitude and hysteresis and eddy current losses can be related to either input voltage amplitude or stator current amplitude, the torque can also be related to either amplitude. The torque expressed in terms of input voltage is used for the voltage driven motor. Motors driven by scalar control and vector control use the torque expressed in terms of stator current. The current driven torque is dependent on slip frequency and independent of excitation frequency when hysteresis and eddy current losses in the steel are ignored.

As slip frequency increases, voltage driven torque increases from zero at synchronous speed until a maximum, referred to as the breakdown torque. When a load on the induction motor operating in this stable region varies slightly, the rotor speed varies slightly inversely. In response, the output torque varies slightly in successfully countering the load change. The induction motor normally stalls if the load exceeds breakdown torque. Beyond breakdown torque, output torque decreases as slip frequency increases until stall. The motor normally stalls for an increase in load when operating in this unstable region. Therefore, the voltage driven motor is normally loaded slowly or loaded after the rotor attains synchronous speed to operate in the stable region. When the rotor rotates slower than at breakdown torque, it normally accelerates beyond the breakdown torque to operate in the stable region for a decrease in load.

Current driven torque follows the same trend, but maximum torque occurs much closer to synchronous speed. The torque decreases as slip frequency increases except near synchronous speed. With

---

[28]Cyril G. Veinott, *Theory and Design of Small Induction Motors*, New York: McGraw-Hill Book Company, Inc., 1959, pp. 191-195.

scalar control and vector control, the induction motor can be loaded from stall because the current delivered by the supply adjusts to accommodate the load and variations in the load.

Current driven torque can be represented in the frequency domain with hysteresis and eddy current losses neglected. The logarithm is taken after torque is scaled:

$$\log\left[\frac{4R_r}{S_r}\left(\frac{2K_dN_s}{L_{sg}N_rI_s}\right)^2 T\right] = \log(\omega_s) - \log\left\{1 + \left[\frac{\omega_s}{R_r}(L_{rl}+L_{rg})\right]^2\right\} \qquad \text{III-40}$$

Figure 3.6 displays the lumped model response with a solid line and the asymptotic response with a dashed line. The arrows denote that the lines continue endlessly. Rotor resistance is kept constant so that temperature effects and skin effects are constant. The asymptote rises with unity slope from synchronous speed and descends with negative unity slope toward stall. At low slip frequency, the middle logarithmic term dominates the response. The last term becomes significant near the maximum torque. At high slip frequency, the last term dominates the response and the middle term is insignificant.
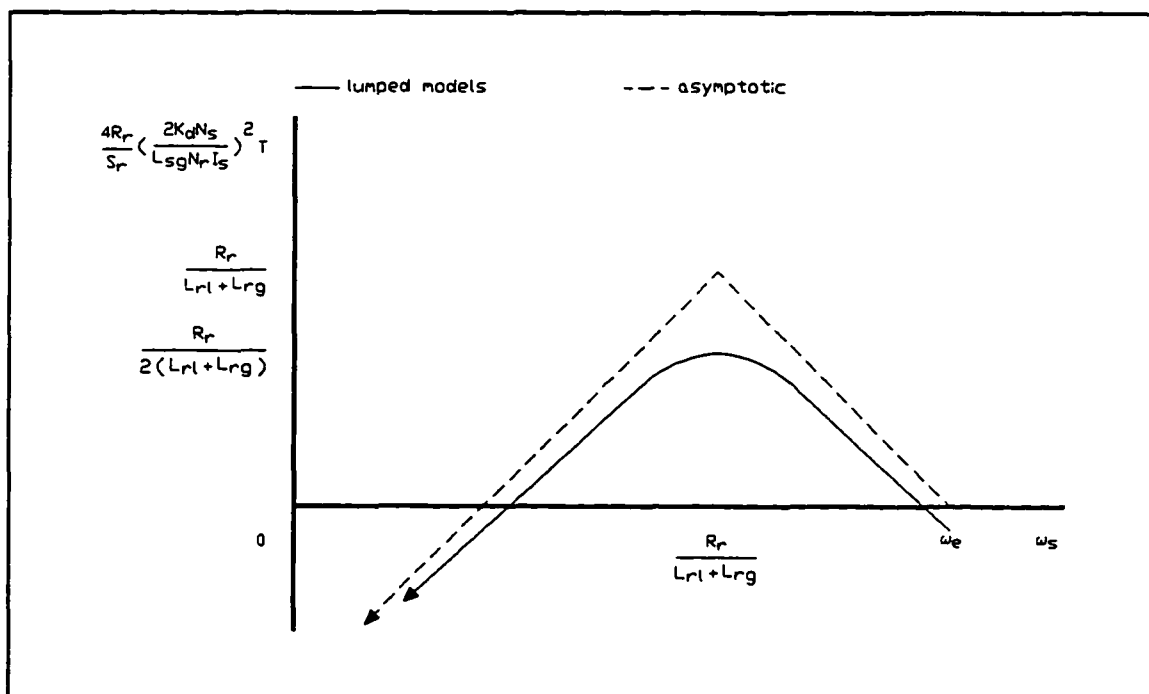
Figure 3.6 Frequency response of current driven torque on log-log plot.

All the other performance characteristics are also formulated from the input voltages, stator currents, rotor currents, resistances, and inductances. Power factor is expressed as cosine of the phase angle between the input voltage and the stator current of the same phase:

-78-

$$power\ factor\ =\ \cos(\alpha)$$

III-41

Power factor defines in the frequency domain the percentage portion of the stator current that is temporally in phase with the input voltage, or the percentage portion of the input impedance that is resistive. Power factor gives an indication of the economic efficiency of a motor. Power factor decreases as slip frequency increases except near synchronous speed.

Power losses comprise resistive losses as well as hysteresis and eddy current losses. Although hysteresis and eddy current losses have been ignored in the lumped electrical model, they are included in determining performance. Resistive power loss is formulated as the product of the resistance and the square of instantaneous current summed over all phases. The expression of stator and rotor resistive power losses is simplified for motors with multiple stator and rotor phases:

$$resistive\ power\ losses\ =\ \frac{m}{2}R_s I_s^2 + \frac{S_r}{2n}R_r I_r^2 \qquad \text{III-42}$$

The losses increase as slip frequency increases except near synchronous speed for the voltage driven motor.

For hysteresis and eddy current losses in the steel, an empirical model has been published:[29]

$$P_h\ =\ K_0 (B^{max})^{K_1} f^{K_2} \rho v \qquad \text{III-43}$$

where:

K_o	= lamination steel loss coefficient
K_1	= lamination steel loss flux density exponential coefficient
K_2	= lamination steel loss frequency exponential coefficient
B^{max}	= lamination steel maximum flux density
f	= lamination steel eddy current frequency
ρ	= lamination steel density
v	= lamination steel volume

The data range for flux density extends from a tenth to one tesla and for frequency extends from a hundred to ten thousand hertz. K_o, K_1, and K_2 are fixed for a lamination material and thickness. Since flux density and volume differ in the various regions, losses in the stator and rotor back irons and teeth are calculated separately, then summed. The maximum flux density at a rotor speed can be determined from Equation

---

[29]Steven R. Prina, "Considerations in the Design of Brushless DC Motors," *Proceedings From Twenty-First Annual Symposium of Incremental Motion Control Systems and Devices*, June, 1992, p. 8.

-79-

II-10 and Equation II-11 by using:

$$\phi^{max} = \left| \sum_{k=1}^{m} \phi_{sg}^{k} \cos\left(\frac{2\pi k}{m}\right) + \sum_{k=1}^{\frac{S_r}{n}} \phi_{rg}^{k} \cos\left(\frac{n\pi k}{S_r}\right) \right|$$

$$= \left| \sum_{k=1}^{m} \frac{4}{\pi} \frac{2}{\pi} \frac{K_s N_s j_s^{k}}{K_c K_s K_w \Re_g} \cos\left(\frac{2\pi k}{m}\right) + \sum_{k=1}^{\frac{S_r}{n}} \frac{4}{\pi} \frac{2}{\pi} \frac{N_r j_r^{k}}{2K_c K_s K_w \Re_g} \cos\left(\frac{n\pi k}{S_r}\right) \right|$$

III-44

Eddy currents in the stator oscillate at the excitation frequency, while eddy currents in the rotor oscillate at the slip frequency.

The last two performance characteristics are horsepower and efficiency. Steady state output horsepower is the product of rotor speed and steady state torque:

$$horsepower = \dot{\theta}_r T$$

III-45

Steady state efficiency is defined as output horsepower divided by input power. Since hysteresis and eddy current losses in the steel are neglected in the lumped electrical model, they are included in the denominator:

$$efficiency = \frac{\dot{\theta}_r T}{\frac{m}{2} V_{is} I_s \cos(\alpha) + P_h}$$

III-46

When P_h is neglected, efficiency decreases as slip frequency increases except near synchronous speed.

Induction motors normally operate near synchronous speed for high current driven torque, power factor, and efficiency. The rotor speeds at which maximum current driven torque, maximum power factor, and maximum efficiency occur bunch together near synchronous speed when excitation frequency is high and efficiency excludes hysteresis and eddy current losses. The difference among the three speeds is typically less than twenty percent of synchronous speed. The speed at maximum efficiency is the fastest, followed by the speed at maximum current driven torque, then the speed at maximum power factor. These speeds are independent of input voltage amplitude and stator current amplitude. Induction motors typically operate near synchronous speed for these characteristics as well as low resistive power losses. Rotor speed

-80-

at breakdown torque is even slower than that at maximum power factor. Voltage driven motors operate near synchronous speed to also avoid the risk of stalling when running close to breakdown torque.

III.H. Summary

In the analysis and design of induction motors, it is imperative to understand the direct relationships between physical parameters and motor performance. A lumped electrical model has been developed to determine the relationships in terms of motor geometry and material properties. The model uses flux information from the lumped magnetic model in the previous chapter and temperature information from the lumped thermal model in the next chapter. Performance calculations derived from the lumped models are compared to experimental results in Chapter VI. Errors are shown to be within fifteen percent over the practical region of the torque-speed curve. Equations describing the developed lumped electrical model have been shown to be identical to those describing the general equivalent circuit model.

The lumped electrical model formulates the relationship from input voltages to stator and rotor currents through resistances and EMF voltages. Deriving the stator resistance is relatively simple. The rotor resistance accounts for the bar resistance as well as the end ring resistance. The end ring resistance, though seemingly relatively small, significantly affects motor performance. Also, skin effects, which cause the rotor resistance to vary with rotor speed, are especially important in radially deep bars and end rings. Skin effects boost torque and heat generated at low rotor speeds, but performance at high rotor speeds remains almost undisturbed. The EMF voltages are induced by linkages with stator and rotor air gap and leakage fluxes. The voltages can be modelled as voltage drops across inductances. Stator and rotor currents are induced across the stator and rotor resistances from the input voltages and EMF voltages.

Output performance characteristics are expressed by input voltages along with stator and rotor currents, resistances, air gap inductances, and leakage inductances. The performance characteristics comprise voltage and current driven torques, power factor, power losses, horsepower, and efficiency. Induction motors are usually rated at low slips for high current driven torque, high power factor, low resistive heat losses, and high efficiency. Voltage driven motors operate at low slips to also avoid stalling. The effect of specific motor parameters on performance can be quantitatively determined. Induction motors of different geometric dimensions and material properties can be compared.

-81-

CHAPTER IV

LUMPED THERMAL MODEL

IV.A. Introduction

In the previous chapter, the lumped electrical model was developed to derive expressions of motor performance. The model used steady state temperature information from the thermal model that is formulated in this chapter. The thermal model uses heat transfer theory to describe the effect of heat generation on temperature in terms of motor geometry and material properties. Steady state and transient temperatures are derived.

The transient temperature information can be used to derive transient motor performance. Transient motor performance is especially important in analyzing short duration overloading capabilities and for motors driven by scalar control and vector control. In these motors, the current delivered by the supply adjusts to accommodate the load and variations in the load.

A simple four-lump thermal model is developed to obtain temperature information.[30] Heat sources, thermal capacitances, and thermal resistances in the model are formulated. The temperature in critical regions of the motor is then derived.

IV.B. Development of the Lumped Thermal Model

The thermal model consists of heat sources, thermal capacitances, and thermal resistances. Heat sources arise due to the power losses in the motor. Thermal capacitances and resistances are used to relate temperature to heat generation. Thermal capacitances arise as a result of materials storing thermal energy. Thermal resistances are a measure of materials' capability to transfer heat. From the thermal model, the temperature is solved in critical regions of the motor. The temperature in the stator windings and rotor bars is necessary to evaluate their resistance in the lumped electrical model of the previous chapter.

---

[30]C. K. Taft, R. G. Gauthier, T. J. Harned, S. R. Huard, and B. K. Fussell, *Brushless Motor System Design and Analysis*, Tenth Edition, College of Engineering & Physical Sciences, University of New Hampshire, Durham, New Hampshire, 1996, pp. 13-27 - 13-30.

Developing the thermal model is very complex. Heat flows in all directions through all bodies. Analytically determining the thermal resistances is difficult because properties of materials as well as their surroundings are needed. Commonly, empirical data are required.

Parameters of the lumped electrical and thermal models are interdependent. Heat generation is a function of resistance and current, both of which depend on temperature. But, the temperature is dependent on the heat generation. To determine the steady state quantities, an iterative process is used. The resistances and currents are determined from the lumped electrical model in the previous chapter. The steady state temperature is determined from the thermal model here.

Just as the lumped magnetic model only considered motor sections carrying significant levels of flux and the lumped electrical model only considered sections with significant current flow, the lumped thermal model, likewise, only considers sections with significant flow of heat. Most of the heat, which is generated by currents, flows to ambient through the housing, stator winding end turns, and rotor end rings. Heat is generated primarily from the stator and rotor currents. Heat from eddy currents in the steel is also considered although they tend to be relatively small because of the laminated stack construction.

Heat transfer exists through three processes known as conduction, convection, and radiation. Conduction occurs when a temperature gradient exists in a solid body. Convection occurs when a temperature difference in a liquid or gas exists. Radiation refers to the electromagnetic energy that is emitted by all objects. The amount of radiation is determined by the temperature difference.[31]

The rate of conduction heat transfer in a material is proportional to the temperature gradient in the material in the direction of heat flow. It is proportional through a thermal conductivity of the material.[32] Although this conductivity is dependent on temperature, it can be assumed constant if the temperature gradient is not too large. Otherwise, the material can be modelled as sections with smaller temperature gradients connected in series perpendicular to the direction of heat flow. Each section would contain its own constant thermal conductivity.

[31]David Halliday and Robert Resnick, *Fundamentals of Physics*, Second Edition, Extended Version, New York: John Wiley & Sons, Inc., 1970, pp. 360-361.

[32]J. P. Holman, *Heat Transfer*, Fifth Edition, New York: McGraw-Hill, Inc., 1981, p. 2.

-83-

The rate of convection heat transfer at the surface between a solid body and a liquid or gas is proportional to the temperature difference of the bodies. It is proportional through a convection heat transfer coefficient.[33] The coefficient can be analytically determined in some simple systems, but more complex ones require empirical models. Natural, or free, convection occurs when no external source of motion is used. Otherwise, forced convection utilizes external sources such as ventilating fans that protrude from the rotor end rings.

The rate of radiation heat transfer is proportional to the difference in temperature to the fourth power. It is proportional through the Stefan-Boltzmann proportionality constant.[34] Since the constant applies only to blackbodies, correction for any other material surface is made through its emissivity.

Thermal behavior, like magnetic behavior, is directly analogous to electrical behavior. Thus, well-known electrical circuit theory is used to develop the lumped thermal circuit model. A voltage across an electrically conductive material produces a current flowing through the material electrical resistance. Similarly, a temperature difference within a material causes thermal heat flow through the material. The voltage is analogous to the temperature, the current is analogous to the heat flow, and the material electrical resistance is analogous to material thermal resistance. The thermal resistance resists heat flow just as the electrical resistance resists current flow. Heat flow through a material is derived from the temperature difference across the material divided by the thermal resistance.

Figure 4.1 shows the lumped thermal model for the entire motor where:

T_h	= motor housing steady state temperature at operating speed
C_h	= motor housing thermal capacitance
R_h^{cnv}	= housing to ambient convection thermal resistance
R_h^{rad}	= housing to ambient radiation thermal resistance
R_{sh}^{cnd}	= stator stack to housing conduction thermal resistance
T_{ss}	= stator stack steady state temperature at operating speed
q_{sh}	= stator hysteresis and eddy current heat source
C_{ss}	= stator stack thermal capacitance
R_{ss}^{cnd}	= stator windings to stator stack conduction thermal resistance
q_s	= stator winding heat source
C_s	= stator winding thermal capacitance
R_{seh}^{cnd}	= stator end turns to housing conduction thermal resistance
R_s^{cnd}	= air gap conduction thermal resistance

---

[33]J. P. Holman, *Heat Transfer*, Fifth Edition, New York: McGraw-Hill, Inc., 1981, p. 12.

[34]J. P. Holman, *Heat Transfer*, Fifth Edition, New York: McGraw-Hill, Inc., 1981, p. 14.

-84-

q_{rh}	≡ rotor hysteresis and eddy current heat source
q_r	≡ rotor squirrel cage heat source
C_{rs}	≡ rotor stack thermal capacitance
C_r	≡ rotor squirrel cage thermal capacitance
R_{reh}^{cnd}	≡ rotor end rings to housing conduction thermal resistance
T_∞	≡ ambient temperature
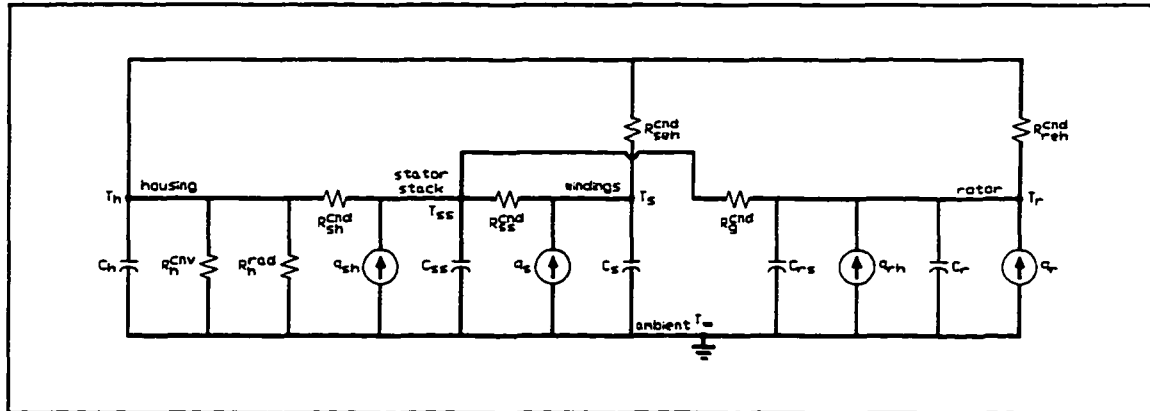
Figure 4.1 Lumped thermal circuit model for the entire motor.

Although other thermal paths may exist, these are usually sufficient for good temperature estimations. The housing and stator stack are at different temperatures because they do not have perfect contact. Usually they are either welded together or pressed together with adhesive so that heat does not easily flow between them. Stator windings are insulated from the stator stack so that the two bodies are also at different temperatures. Slot liners pad the stator slots to protect the windings and the winding wires are coated with insulation. Rotor bars, on the other hand, are assumed to have perfect contact with the rotor stack so that the two bodies are at the same temperature.

The temperature in the characteristically small air gap of the induction motor is not at ambient because heat trapped in there can not easily dissipate out to ambient. As a result, heat in the air gap is assumed to flow only between the stator and rotor. The ambient temperature is the temperature of the surrounding environment.

When the resistance of a material body to conduction heat transfer is much smaller than the resistance to convection heat transfer at the surface, it can be neglected. The body is then considered a perfect heat conductor and a uniform temperature distribution in the body results.[35] Because of this, the

---

[35] J. P. Holman, *Heat Transfer*, Fifth Edition, New York: McGraw-Hill, Inc., 1981, pp. 109-114.

-85-

conduction thermal resistance is neglected in the stator windings and rotor bars as well as the stator and rotor steel stacks. Consequently, temperatures are assumed uniform in these regions.

The lumped thermal model shows many thermal paths. Heat flows from housing to ambient through convection and radiation. Radiation heat transfer is usually small for small temperature differences and smooth metals. It is therefore omitted in the lumped thermal model except from housing to ambient. For the large temperature difference from housing to ambient, the radiation heat transfer can even be larger than the convection heat transfer.

A conduction thermal resistance is used to model heat transfer from the stator windings to stator stack. This thermal path is complicated by the presence of slot liners, wire insulation, and trapped air in the wire bundles. Simply using the thermal conductivity of the slot liners or the windings alone would cause large errors. Instead, empirical data has been used to determine an effective thermal conductivity of the inhomogeneous mixture.

Conduction thermal resistances are also used to model heat transfer through the other thermal paths. The housing and stator stack do not have perfect contact and the thermal path through the stagnant air trapped in between is short, so a conduction thermal resistance is used. The convection thermal resistance is neglected here. Due to the characteristically small air gap in the induction motor, conduction is also used from the air gap to the stator and rotor stacks. This thermal resistance is small so that not much error is introduced even when the rotor rotates. Air enclosed by the end caps in the stator end turns and rotor end rings is also somewhat trapped despite fans protruding from the end rings causing some air flow when the rotor rotates. Therefore, conduction is also used in these two places.

From the lumped thermal model, heat transfer equations are written:

$$0 = C_h \frac{dT_h}{dt} + \frac{T_h - T_\infty}{R_h^{conv}} + \frac{T_h^4 - T_\infty^4}{R_h^{rad}} + \frac{T_h - T_{ss}}{R_{sh}^{cnd}} + \frac{T_h - T_s}{R_{ssh}^{cnd}} + \frac{T_h - T_r}{R_{rsh}^{cnd}}$$

$$q_{sh} = C_{ss} \frac{dT_{ss}}{dt} + \frac{T_{ss} - T_h}{R_{sh}^{cnd}} + \frac{T_{ss} - T_s}{R_{ss}^{cnd}} + \frac{T_{ss} - T_r}{R_g^{cnd}}$$

$$q_s = C_s \frac{dT_s}{dt} + \frac{T_s - T_h}{R_{ssh}^{cnd}} + \frac{T_s - T_{ss}}{R_{ss}^{cnd}}$$

$$q_{rh} + q_r = C_{rs} \frac{dT_r}{dt} + C_r \frac{dT_r}{dt} + \frac{T_r - T_h}{R_{rsh}^{cnd}} + \frac{T_r - T_{ss}}{R_g^{cnd}}$$

IV-1

Numerical integration is then applied to solve for the temperatures at each time step from the previous step. Heat in the stator windings flows to ambient through end turns and to the stator stack. Heat in the stator stack flows to ambient through the housing and to the rotor across the air gap. Because of end turns, heat can not easily flow from the stator stack to ambient through the axial ends. Heat in the rotor flows to ambient through end rings and to the stator across the air gap.

Heat sources in the lumped thermal model arise from heat generated by the power losses formulated in the previous chapter. The losses comprise stator and rotor resistive losses in Equation III-42 as well as hysteresis and eddy current losses in Equation III-43:

$$q_{sh} = P_{hs}$$

$$q_s = \frac{m}{2} R_s I_s^2$$

$$q_{rh} = P_{hr}$$

$$q_r = \frac{S_r}{2n} R_r I_r^2$$

IV-2

where:

P_{hs} = hysteresis and eddy current power losses in stator steel
P_{hr} = hysteresis and eddy current power losses in rotor steel

P_h is the sum of the losses in the stator and rotor.

Thermal capacitances are used to model materials storing thermal energy:

-87-

$$C_h = c_{ph}\rho_{hd}\nu_h$$

$$C_{ss} = c_{pss}\rho_{ssd}\nu_{ss}$$

$$C_s = c_{ps}\rho_{sd}\nu_s \qquad\qquad \text{IV-3}$$

$$C_{rs} = c_{prs}\rho_{rsd}\nu_{rs}$$

$$C_r = c_{pr}\rho_{rd}\nu_r$$

where:

c_{ph}	= motor housing specific heat
ρ_{hd}	= motor housing density
v_h	= motor housing volume
c_{ps}	= stator winding specific heat
ρ_{sd}	= stator winding density
v_s	= stator winding volume
c_{pss}	= stator lamination steel specific heat
ρ_{ssd}	= stator lamination steel density
v_{ss}	= stator stack volume
c_{pr}	= rotor squirrel cage specific heat
ρ_{rd}	= rotor squirrel cage density
v_r	= rotor squirrel cage volume
c_{prs}	= rotor lamination steel specific heat
ρ_{rsd}	= rotor lamination steel density
v_{rs}	= rotor stack volume

The motor housing thermal capacitance, C_h, can be composed of two parts, housing body and end caps, if they are constructed of different materials. Although the stacks consist of laminations coated with insulation, they can be assumed to be solid steel because the coating is thin. In addition, heat transfer through the stack is mostly in the radial not axial direction so that the insulation does not cause much error. C_h, C_{ss}, C_s, C_{rs}, and C_r can all be set to zero to determine the steady state temperatures T_h, T_{ss}, T_s, and T_r. However, the capacitances are included to solve for the transient temperatures.

Material volume is needed in calculating the thermal capacitances. For simplicity, the stator and rotor stacks in C_{ss} and C_{rs} are calculated without including steel ears. Rotor ears are added to the squirrel cage instead. Not much error is introduced from this. Volume in the stator windings includes end turns. Wire insulation is also included despite having different material properties than the wire. Volume in the rotor squirrel cage includes end rings.

Thermal resistances are used to model heat flow:

-88-

$$R_h^{cnv} = \frac{1}{h_h A_h}$$

$$R_h^{rad} = \frac{1}{e\sigma A_h}$$

$$R_{sh}^{cnd} = \frac{t_h}{k_h \pi D_{so} z}$$

$$R_{ss}^{cnd} = \frac{t_{sl}}{k_{sl} 2[S_s l_{ss} + \pi(D_{sl} + l_{ss}) - S_s w_{ss}] z}$$
IV-4

$$R_{seh}^{cnd} = \frac{z_{seh}}{k_{air} \dfrac{\pi}{2}(D_{so}^2 - D_{sl}^2)}$$

$$R_g^{cnd} = \frac{l_g}{k_{air} \pi \dfrac{D_{sl} + D_{ro}}{2} z}$$

$$R_{reh}^{cnd} = \frac{z_{reh}}{k_{air} \dfrac{\pi}{2} D_{ro}^2}$$

where:

h_h	= housing to ambient convection heat transfer coefficient
A_h	= motor housing surface area
ϵ	= emissivity of nonblackbody material surface
σ	= Stefan-Boltzmann radiation heat transfer proportionality constant
t_h	= motor housing radial thickness
k_h	= effective thermal conductivity of housing body
t_{sl}	= slot liner thickness
k_{ss}	= effective thermal conductivity of slot liner
z_{seh}	= end turns to end cap axial height
k_{air}	= thermal conductivity of air
z_{reh}	= end ring to end cap axial height

For the convection heat transfer coefficient h_h from housing to ambient, an empirical model for free convection is used based on the Grashof, Nusselt, and Prandtl numbers.[36] Properties of air for the coefficient are evaluated at the approximate average temperature of the housing. The thermal conductivity of the housing body k_h is also evaluated at this temperature. For the radiation thermal resistance R_h^{rad}, heat transfer from housing to ambient is assumed to be in a large room. The thermal resistance can be composed of two parts, housing body and end caps, if they are constructed of different materials because

---

[36]J. P. Holman, *Heat Transfer*, Fifth Edition, New York: McGraw-Hill, Inc., 1981, pp. 270-275.

-89-

the emissivity for them is different.

In calculating R_{sr}^{cnd}, k_w is determined from empirical data. Although only the thermal path through the slot liners is used in calculating the thermal resistance, the paths through the windings, wire insulation, and trapped air in the wire bundles are all incorporated in the empirical data. Stator windings are assumed to fill the entire slot so that contact is made with all four sides.

Heat from stator end turns and rotor end rings flows to end caps at both axial ends so that R_{sch}^{cnd} and R_{rch}^{cnd} are half the thermal resistance per end. The thermal conductivity of air, k_{air}, in these thermal resistances is evaluated at the approximate average temperature of the stator windings and rotor squirrel cage. R_{rch}^{cnd} also includes the cross-sectional area of the shaft, but does not include the surface area from the protrusion of the shaft from the rotor back iron. Heat transfer from the protrusion by itself is usually small relative to the housing. However, the shaft is connected when the motor is applied to an application, thereby creating a significant thermal path. In this case, heat dissipated out from the rotor through the shaft may be significant.

IV.C. Summary

A lumped thermal model has been developed to describe the effect of heat generation on temperature in terms of motor geometry and material properties. Steady state and transient temperatures are derived. The steady state temperature information is used by the lumped electrical model in the previous chapter to evaluate resistances. Since the temperatures vary with rotor speed, the resistances are evaluated at every operating speed.

The transient temperature information can be used to derive transient motor performance. Transient motor performance is especially important in analyzing short duration overloading capabilities and for motors driven by scalar control and vector control. Calculated transient temperatures at stall are compared to experimental results in Chapter VI. Errors in estimating the steady state temperatures used to evaluate the resistances are shown to be within ten percent.

The lumped thermal model consists of heat sources, thermal capacitances, and thermal resistances. Heat sources arise from heat generated by power losses in the motor. Thermal capacitances are used to model materials storing thermal energy. Thermal resistances are a measure of materials' capability to

-90-

transfer heat through conduction, convection, and radiation.

The developed lumped thermal model is a basis upon which other application dependent models can be developed. For motors with an external source of cooling, forced instead of free convection heat transfer can be utilized.

CHAPTER V

METHODS USING TWO-DIMENSIONAL MAGNETIC FEA

V.A. Introduction

Magnetic finite element analysis, FEA, is another important tool beside the lumped models for analyzing and designing electric motors. While the lumped magnetic, electrical, and thermal models incorporate only bodies carrying significant levels of flux, current, and heat, the FEA considers magnetic behavior of the entire motor. Through a numerical process, FEA can model complicated motors with more detail. Understandably, much longer computing time is required, but more precise results are attained.

A two-dimensional static FEA field solver is commonly sufficient to accurately model permanent magnet motors. The magnetic field is assumed to be temporally static. Also, induced currents are ignored. The instantaneous field is determined given the excitation.

Using two-dimensional FEA to accurately model the induction motor is more difficult due to induced rotor currents and three-dimensional effects. Induced currents require either a steady state harmonic field solver or a transient field solver. A steady state solver yields magnetic field solutions that vary sinusoidally with time so that nonlinear magnetic effects from saturation are ignored. A transient field solver, on the other hand, can include nonlinear magnetic effects as well as temporal harmonics in the field. However, solution time is much longer than that of the steady state solver.

In modelling the induction motor through the two-dimensional FEA, three-dimensional effects that are commonly ignored in permanent magnet motors must be included. These effects arise due to rotor end rings and three-dimensional leakage flux. End rings, which are nonexistent in permanent magnet motors, must be included in modelling the induction motor because they significantly affect motor performance. When modelling permanent magnet motors using a two-dimensional solver, three-dimensional leakage flux is often neglected since it produces no torque. The leakage flux is usually very small relative to the air gap flux. In the voltage driven induction motor, three-dimensional leakage flux must be incorporated because it also significantly influences performance.

-92-

The traditional strategy of modelling the induction motor through the FEA is briefly described in Appendix A. The equivalent "T" circuit model parameters are first extracted from the field solutions. Then, performance is evaluated from the equivalent circuit model. The model loses some physical interpretation because rotor parameters are referred to the stator.

Three methods have been developed in this chapter to evaluate performance in current and voltage driven induction motors directly from the FEA field solutions. The equivalent circuit model is not needed. Three-dimensional effects are externally incorporated in all three methods. The first FEA method uses a steady state solver followed by a static solver in calculating torque from the method of virtual work. The second FEA method, which requires much less computing time, uses only a steady state solver to calculate torque from the conservation of instantaneous energy. The third FEA method uses a transient solver.

V.B. Inclusion of Three-Dimensional Effects

Three-dimensional FEA packages that are commercially available are capable of accurately modelling the induction motor. Flux flowing in all directions is considered. Unfortunately, these FEA packages are still not very practical because they are expensive, mesh development is tedious, and solution time is long.

Two-dimensional FEA packages, in contrast, cost much less and require dramatically reduced mesh development time and solution time. But, currents are confined to travel only in the axial direction producing flux flowing only in the radial and tangential directions. In reality, flux also flows in the axial direction because of rotor skewing as well as currents in the stator end turns and rotor end rings. These three-dimensional effects significantly affect motor performance and must be considered.

A two-dimensional steady state field solver is used in the first two FEA methods and a two-dimensional transient field solver is used in the third method. To include three-dimensional effects, the rotor resistance is increased in all three methods to account for skewing and end rings. In the first two methods, the input impedance is also increased to account for linkages with three-dimensional leakage flux. In the third method, linkages with three-dimensional leakage flux are used to calculate stator currents from the input voltages.

-93-

V.B.1. Rotor End Ring Resistance

The two-dimensional steady state solver accounts for rotor resistance from only bars that run axially. Rotor end rings are not included. However, the end ring resistance can be significant relative to the bar resistance as shown in Equation III-9. Also, skewing slightly increases the resistance even more.

To account for these effects, the rotor bar resistivity is adjusted in the FEA so that its effective rotor resistance per phase equals the resistance in Equation III-9 of the lumped electrical model:

$$\rho_{r2D} = \frac{a_{rb}}{K_{rb} n z} R_r \qquad \qquad \text{V-1}$$

where:

ρ_{r2D} ≡ rotor bar resistivity in the two-dimensional FEA
a_{rb} ≡ rotor bar cross-sectional area

The resistivity is adjusted at each rotor speed because the skin effects constants in R_r vary with slip frequency. Skin effects in the rotor bars are inherently incorporated in the FEA when meshes are drawn with enough resolution. Therefore, the rotor bar skin effects constant, K_{rb}, appears in the above equation. Skin effects in the end rings, on the other hand, are not inherently incorporated in the FEA, but are accounted for through the resistivity adjustment.

V.B.2. End and Skew Leakage Fluxes

In the voltage driven induction motor, three-dimensional leakage flux not only reduces stator currents that induce rotor currents, but also directly reduces the rotor currents. The leakage flux influences torque through both stator flux produced by stator currents and rotor flux produced by rotor currents. Thus, torque estimation errors from exclusion of the leakage flux are compounded.

Performance in the current driven motor, however, is not significantly affected by three-dimensional leakage flux. Therefore, the leakage flux is neglected there when determining performance. As a result, FEA calculations are slightly overestimated.

Performance in the voltage driven motor, on the other hand, is dependent on three-dimensional leakage flux. In the first two FEA methods, the leakage flux is considered when calculating input impedance from the two-dimensional FEA. The impedance is used to determine stator currents from the

-94-

input voltages. Despite three-dimensional leakage flux incorporated in the stator currents, some performance calculations in the voltage driven motor are still slightly overestimated. This is because those calculations are scaled from the slightly overestimated current driven performance calculations. In the third FEA method, the inductance from linkages with three-dimensional leakage flux is used to directly determine instantaneous stator and rotor currents. Explanation on this is presented in section V.E.

To include stator three-dimensional leakage flux in the first two FEA methods, the portion of the input impedance attributed to linkages with the flux is simply added to the two-dimensional input impedance calculated by the FEA. The flux linkages are estimated from the lumped models. When excitation is balanced in time and space, rotor bars are evenly spaced, and an integral number of rotor phases exists, the input impedance of each stator phase is identical.

Including rotor three-dimensional leakage flux is not as easy. The portion of the input impedance attributed to linkages with this flux is dependent on rotor currents which are affected by the flux. To incorporate the three-dimensional leakage flux in the rotor currents, rotor leakage flux can be increased in the FEA. But, it is difficult to increase the rotor leakage flux by an appropriate amount. When a simplifying assumption is made, however, three-dimensional leakage flux in the rotor can be included in a simple manner similar to that in the stator.

In the assumption, the EMF from linkages with the rotor leakage flux and the voltage drop across the rotor resistance are neglected because their sum is much smaller than the EMF in each rotor phase from linkages with the rotor air gap flux. The assumption is reasonable because to attain high torque and efficiency levels, the air gap flux is normally much larger than the leakage flux. The assumption fails only near synchronous speed where the EMF voltages are small relative to the voltage drop across the resistance due to the low slip frequency. In that narrow speed region, the input impedance is slightly overestimated, which may cause performance in the voltage driven motor to be slightly underestimated.

With the assumption, the impedance of each stator phase attributed to linkages with three-dimensional leakage flux in the stator and rotor can be included together:

$$Z_{3D} = j\omega_e L_{3D}$$

$$L_{3D} = K_{rv}\frac{4}{\pi^2}nmK_d^2 N_s^2\left(\frac{1}{\mathfrak{R}_{sle}}+\frac{1}{\mathfrak{R}_{slw}}+\frac{1}{\mathfrak{R}_{rle}}+\frac{1}{\mathfrak{R}_{rlw}}\right)$$

V-2

where:

Z_{3D} = stator and rotor three-dimensional end and skew leakage impedance per stator phase

L_{3D} = stator and rotor three-dimensional end and skew leakage inductance per stator phase

The three-dimensional leakage flux comprises stator and rotor end and skew leakage fluxes. The stator and rotor end and skew leakage inductances have been estimated by Equation III-19 and Equation III-25 of the lumped electrical model. The reluctances are formulated by Equation II-16 and Equation II-18 of the lumped magnetic model. The rotor leakage inductances are transformed from the rotating to the stationary reference frame then referred to the stator before being included in L_{3D}. These inductances are referred to the stator through Equation III-34. Z_{3D} is simply added to the two-dimensional input impedance calculated by the FEA to include three-dimensional leakage flux.

V.C. Method of Virtual Work

In the first FEA method, torque is determined from the method of virtual work[37]. The equivalent "T" circuit model is not needed because torque[38] and all other performance characteristics are directly evaluated from the FEA field solution. The lumped magnetic and electrical models are used only to incorporate stator resistance and three-dimensional effects.

Instantaneous torque can be approximated through the method of virtual work:

$$T = \frac{\partial W_c}{\partial \theta_r} \approx \frac{\Delta W_c}{\Delta \theta_r}$$

V-3

where:

θ_r = rotor squirrel cage spatial phase angle

[37]A. E. Fitzgerald, Charles Jr. Kingsley, and Stephen D. Umans, *Electric Machinery*, Fifth Edition, New York: McGraw-Hill, Inc., 1990, pp. 114-117.

[38]J. L. Coulomb and G. Meunier, "Finite Element Implementation of Virtual Work Principle for Magnetic or Electric Force and Torque Computation," *IEEE Transactions on Magnetics*, Vol. MAG-20, No. 5, September, 1984, pp. 1894-1896.

-96-

W_c ≡ coenergy

The approximation of torque is valid for coenergy[39] evaluated at two slightly different rotor positions. All currents must be held constant over the two positions. Friction can be incorporated by subtracting from the calculated output torque. The following two sections describe the implementation of the method of virtual work in calculating performance in current and voltage driven motors.

V.C.1. Calculating Performance in the Current Driven Induction Motor

Torque in the current driven motor is directly determined from the FEA field solution through the method of virtual work. A steady state solver is first used to calculate induced rotor currents from specified input stator currents. Then, the rotor currents are used as additional inputs to two static field meshes along with the original stator currents. A static solver is used to determine torque from the meshes by the method of virtual work. Expressions for horsepower and power losses are also derived. Horsepower is determined from the torque. Power losses are calculated directly from the steady state field solution after the rotor currents are determined.

To calculate performance, rotor currents are first determined by a steady state solver. The solver yields complex solutions in one step for each rotor speed. By evaluating the solution at various phase angles, field quantities are determined at any instant in time. However, symmetry must exist, nonlinear effects are ignored, and the rotor is always considered stalled.

The symmetry is required in order for the field quantities to vary sinusoidally with time as assumed by the steady state solver. The symmetry exists from excitation that is balanced in time and space, evenly spaced rotor bars, and an integral number of rotor phases. Even when the number of rotor phases is not an integer, the number of rotor bars is usually large enough so that it does not introduce much error. Any nonsymmetry causes errors in estimating performance.

The steady state solver ignores nonlinear magnetic effects, including hysteresis, because its solutions are based on field quantities that vary sinusoidally with time. In magnetically linear materials, the permeability is constant so flux density is proportional to field intensity. But, the magnetization curve

---

[39]A. E. Fitzgerald, Charles Jr. Kingsley, and Stephen D. Umans, *Electric Machinery*, Fifth Edition, New York: McGraw-Hill, Inc., 1990, pp. 107-109.

-97-

for steel in Figure 2.8 is nonlinear. To compensate for that, new materials can be defined where their permeabilities would be assigned using averages estimated over a temporal cycle. When operating at low flux density levels in the steel where the magnetization curve can be assumed linear, only one material is needed. At high flux density levels, saturation can be artificially included by defining new regions with materials of different permeabilities. However, temporal harmonics generated by effects of saturation are lost.

The steady state solver also can not account for rotor rotation. The rotor is always considered stalled. Fortunately, rotor currents are induced at the slip frequency instead of the excitation frequency. Therefore, the magnetic field can be modelled as varying at the slip frequency with the rotor stalled. Effectively, the rotating reference frame of the rotor is selected. Voltages and currents induced in the stator at the excitation frequency are instead modelled as being induced at the slip frequency. However, given the assumption of linear materials, those voltages and currents can be transformed to the stationary reference frame of the stator through scaling. The scaling constant of the ratio of excitation frequency to slip frequency arises due to Faraday's law of induction.

To determine induced rotor currents by the steady state solver, the known stator current amplitude and phase angles are specified as inputs into a mesh. Currents rather than voltages are inputs because performance in the current driven motor is a function of the stator currents. If necessary, EMF voltages can always be extracted from the solution by the time derivative of flux linkages. The phase angle of the currents is chosen as the temporal reference in the steady state field solution. This differs from the lumped electrical model where the phase angle of the input voltages was chosen as the reference.

Since performance in the current driven motor is a function of the stator currents, it is desirable to keep them constant with respect to rotor speed. Unfortunately, EMF voltages induced in the stator windings change the currents at every speed. However, by assigning infinite resistivity to the stator windings, the currents are kept directly regulated. The windings experience no additional currents beside the input stator currents despite the existence of EMF voltages. Current driven torque is not affected by stator resistance anyway. In calculating power losses, however, the stator resistance is externally included.

With stator currents as inputs and stator windings assigned infinite resistivity, induced rotor

-98-

currents are determined. After the rotor bar resistivity is adjusted in the FEA for skewing and end ring resistance, the steady state solver reveals the magnetic field. The field varies at the slip frequency since the stator currents are energized at that frequency. From the field solution, rotor currents are computed using the time derivative of flux linkages. A transformation to the stationary reference frame is unnecessary because rotor currents are indeed induced at the slip frequency.

With the rotor currents known, motor performance is then determined. Performance calculations are repeated for every desired rotor speed. Because three-dimensional leakage flux does not significantly affect performance in the current driven motor, it is not included here.

Torque is derived from the method of virtual work using the static solver. Two new meshes are created with the same motor geometry but with instantaneous stator and rotor currents evaluated at a desired instant in time specified as inputs. The phase angle of the currents then becomes meaningless. The two meshes have only one difference, a small change in rotor position. All currents, including eddy currents in the steel, must be identical.

When eddy currents are small, the simplest way to ensure they are identical in the two static field meshes is to set them to zero. Because of the laminated stack construction, eddy currents tend to be small relative to the currents in much more conductive materials of the stator windings and rotor bars. However, the eddy currents can be relatively significant in the stator for high excitation frequency when operating near synchronous speed. Therefore, hysteresis and eddy current losses in the steel are externally included in calculating performance. Although eddy current losses in the steel can be inherently incorporated in the steady state solver, it is not done here.

For the eddy currents to be nonexistent in the two static field meshes, steel in the stator and rotor of the steady state field mesh is assigned infinite resistivity. Induced currents are then confined to only the rotor bars because stator windings have also been assigned infinite resistivity. With no eddy currents induced in the steel, they do not need to be considered in the two static field meshes. Otherwise, instantaneous eddy currents evaluated at the desired instant in time would need to be specified as additional inputs.

Torque is evaluated from the two meshes with their instantaneous currents by using a

-99-

two-dimensional static solver. Even though this solver can incorporate nonlinear magnetic effects, the steady state solver can not. Thus, the two static field meshes also contain only linear materials to be consistent with the steady state field mesh. From the static field solution of the two meshes, coenergy is calculated. Current driven torque is approximated in Equation V-3 as the coenergy difference divided by the rotor spatial phase angle difference between the two meshes. The torque multiplied by rotor speed yields the horsepower in the current driven motor.

Hysteresis and eddy current losses are included by dividing the losses by rotor speed and subtracting from the output torque. As in the lumped electrical model, the losses are not included at synchronous speed because torque is zero and at stall because they can not divide by zero. Hysteresis and eddy current losses, which are empirically derived in Equation III-43, are extracted directly from the steady state field solution. The losses are summed over all steel elements in the stator and rotor.

Power losses in the current driven motor have contributions from both the stator and rotor as well as the hysteresis and eddy current losses:

$$power\ losses = \sum_{k=1}^{m} R_s \left(i_s^k \right)^2 + \sum_{k}^{rotor\ bars} \frac{a^k z}{\rho_{r2D}} \left[Re \left(-\frac{\partial}{\partial t} \left\{ A^k \left[\cos(\omega_s t) + \hat{j} \sin(\omega_s t) \right] \right\} \right) \right]^2 + P_h \qquad \text{V-4}$$

where:

a^k ≡ cross-sectional area in k^{th} element
A^k ≡ magnetic vector potential in k^{th} element

Since stator windings have been assigned infinite resistivity, the stator resistive power loss must be externally added. The stator resistance is used from Equation III-1 of the lumped electrical model. Because steel in the stator and rotor has also been assigned infinite resistivity and the steady state solver ignores nonlinear effects, hysteresis and eddy current losses must be externally added. All three power loss terms remain constant over time at any given rotor speed because excitation is balanced in time and space, rotor bars are evenly spaced, and an integral number of rotor phases exists.

The rotor resistive power loss is the sum over all rotor bar elements of the resistance multiplied by the square of the real component of induced current. The resistance equals axial height multiplied by resistivity and divided by cross-sectional area. All mesh elements are constrained to the same axial height.

-100-

The induced rotor current in the rotor resistive power loss equals the cross-sectional area divided by resistivity and multiplied by the negative partial derivative with respect to time of vector potential.[40] Since vector potentials from the steady state solution are complex variables, they can be represented by phasors. The vector potentials can then be evaluated at any desired phase angle because the solution is based on field quantities that vary sinusoidally with time.

In determining power losses, the vector potential in an element is needed to compute the induced rotor currents. But, the chosen two-dimensional steady state solver determines the vector potential at a node. Since the solver uses first-order triangular elements, the vector potential along any elemental side between two nodes is the linear interpolation of the two nodal vector potentials.[41] As a result, the vector potential in an element is approximated by averaging its surrounding nodal vector potentials.

A steady state field mesh is drawn for the simple two-pole polyphase motor of Figure 2.2 and Figure 2.4. Figure 5.1 shows the outline of the complete motor cross section, while Figure 5.2 shows the mesh for a quarter of the motor cross section. Within each element of the mesh is defined a material with an associated resistivity and constant permeability. After input currents are specified in the stator winding elements, the steady state solver determines the vector potential at each node of the mesh. The magnetic field is plotted in Figure 5.3. The highest flux density levels, occurring at the highest concentration of flux lines, are in the stator tooth ears around the stator slots at the top and bottom of the figure.

V.C.2. Calculating Performance in the Voltage Driven Induction Motor

Calculating performance in the voltage driven motor is more difficult than in the current driven motor. Stator currents that are needed as mesh inputs are unknown. The currents are calculated from the input voltages only after the input impedance is determined from the field solution. The impedance is determined at every desired rotor speed since it varies with the speed. In addition, it is also necessary to consider three-dimensional leakage flux.

---

[40]P. P. Silvester and R. L. Ferrari, *Finite Elements for Electrical Engineers*, Second Edition, Cambridge: Cambridge University Press, 1990, pp. 195-197.

[41]P. P. Silvester and R. L. Ferrari, *Finite Elements for Electrical Engineers*, Second Edition, Cambridge: Cambridge University Press, 1990, p. 29.
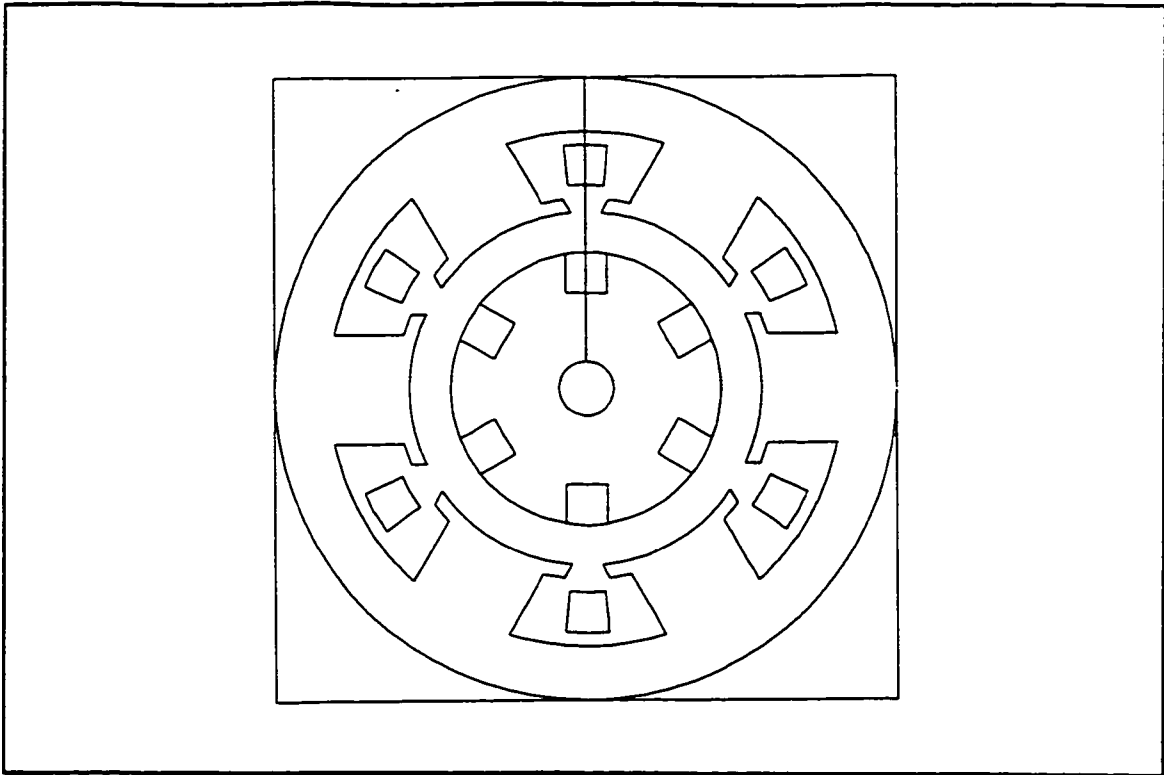
-101-

Figure 5.1 FEA mesh outline of cross section for a simple two-pole polyphase motor.
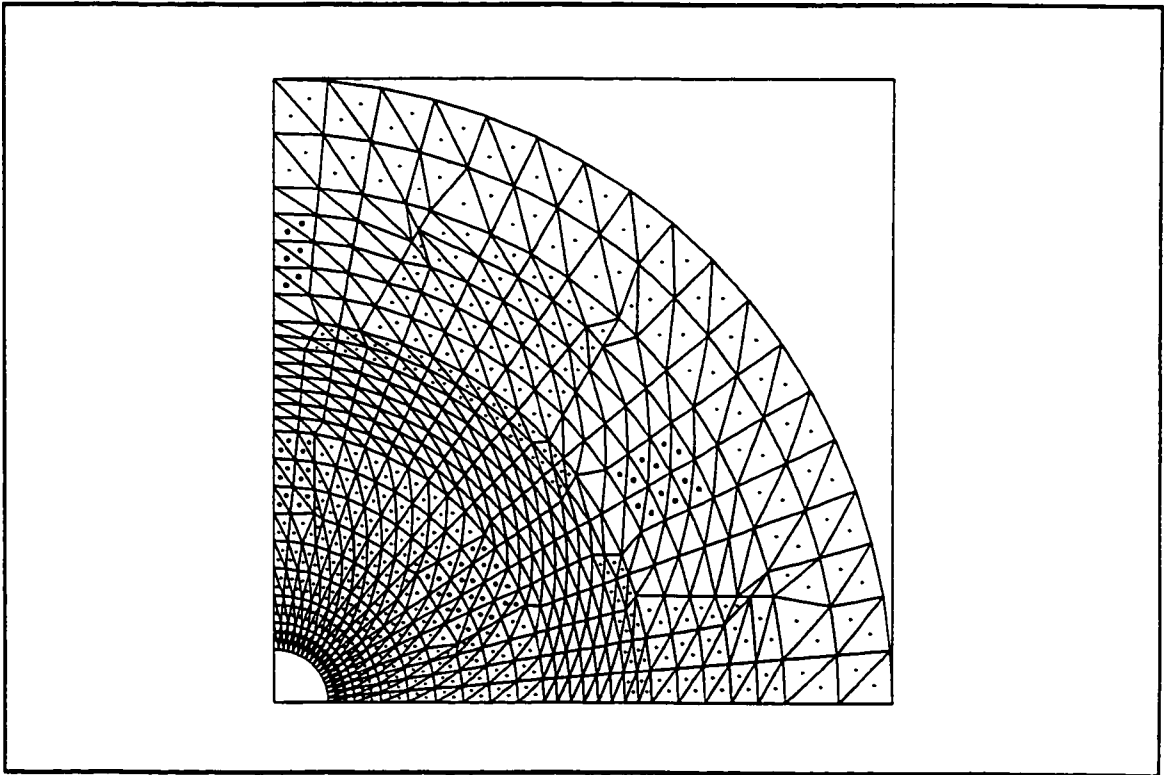

Figure 5.2 FEA mesh of quarter cross section for a simple two-pole polyphase motor.
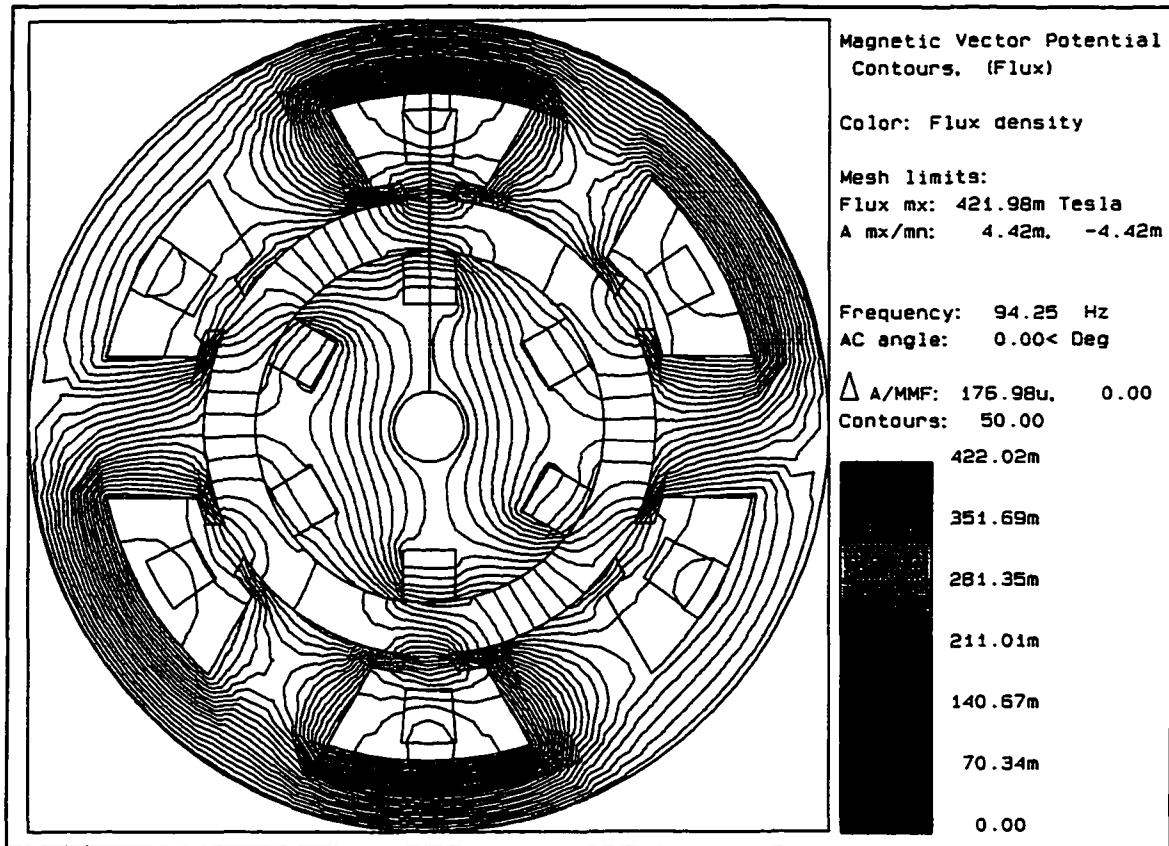
Figure 5.3 FEA magnetic field of cross section for a simple two-pole polyphase motor.

Torque in the voltage driven motor, as in the current driven motor, is directly determined from the FEA field solution through the method of virtual work. Arbitrarily small stator currents are first specified as inputs and a steady state solver is used to determine the induced rotor currents and input impedance. Then, the rotor currents are used as additional inputs along with the original arbitrary stator currents to two static field meshes. From these meshes, a static solver is used to determine torque at the arbitrary stator currents by the method of virtual work. The actual stator currents at the input voltages are solved from the input impedance extracted from the steady state solution. Once these stator currents are known, performance at these currents is evaluated by scaling. Expressions for horsepower, power losses, power factor, and efficiency are also derived, like torque, directly from the FEA field solution.

As in determining performance in the current driven motor, eddy currents in the steel are neglected by assigning infinite resistivity to steel in the stator and rotor of the steady state mesh. Furthermore, stator windings are also assigned infinite resistivity. Thus, the stator resistance must be externally included similar to the previous section in calculating input impedance, power losses, and

-103-

efficiency. The resistance affects voltage driven torque only indirectly through the input impedance. Also, hysteresis and eddy current losses must be externally included in calculating torque, horsepower, power losses, and efficiency.

After assigning infinite resistivity to the stator windings and steel in the stator and rotor, the steady state solver calculates the field solution. From the solution, rotor currents, hysteresis and eddy current losses, and input impedance are computed at the same time. The first two are used to determine current driven torque from the method of virtual work just like in the previous section. The input impedance is used to determine the stator currents at the input voltages. Voltage driven torque is simply the current driven torque scaled for the stator currents. From Equation III-31 and Equation III-39 of the lumped electrical model, current driven torque is proportional to the square of stator current amplitude since P_h is also proportional to the square of the current amplitude.

It is unnecessary to generate new field solutions for the stator currents at the input voltages. Since the steady state solver assumes linear materials, torque, horsepower, and power losses can be scaled for any stator current amplitude. Also, input impedance remains constant regardless of the stator current amplitude. Therefore, performance is calculated initially at the arbitrary input stator current amplitude, then scaled once the stator currents are determined from the input impedance. Unfortunately, if saturation occurs, scaling performance would suffer in accuracy without defining new materials in the saturated regions.

The input impedance used to determine the stator currents comprises the stator resistance of Equation III-1, the two-dimensional input impedance from the field solution, and the three-dimensional leakage impedance of Equation V-2:

$$Z_{in} = R_s + Z_{2D} + Z_{3D} \qquad \text{V-5}$$

where:

Z_{in} = input impedance per stator phase
Z_{2D} = input impedance per stator phase in the two-dimensional FEA

Since the input voltages and corresponding stator currents are not temporally aligned, the input impedance is a complex variable with an imaginary component called the reactance. Input voltages divided by the

-104-

input impedance yield the stator currents.

The two-dimensional input impedance equals the EMF in the stator windings of one phase divided by the input stator current of that phase:

$$Z_{2D} = \frac{\displaystyle\sum_{l}^{\text{stator windings of } k^{th} \text{ stator phase}} \frac{a^l z J_s^l}{I_s} \frac{\partial}{\partial t}\{A\{\cos(\omega_e t) + j\sin(\omega_e t)\}\}}{I_s\left[\cos\left(\omega_e t + \frac{2\pi k}{m} - \frac{\pi}{2}\right) + j\sin\left(\omega_e t + \frac{2\pi k}{m} - \frac{\pi}{2}\right)\right]} \qquad \text{V-6}$$

where:

J_s^l $=$ input stator current density amplitude in l^{th} element

The impedance is identical for every phase because excitation is balanced in time and space, rotor bars are evenly spaced, and an integral number of rotor phases exists.

The EMF in the numerator is derived from Faraday's law of induction in terms of vector potential[42]. Vector potentials in the field solution are with respect to the rotating reference frame, while EMF voltages in stator windings are with respect to the stationary reference frame. Therefore, a transformation to the excitation frequency is necessary. In calculating flux linkages for the EMF, the number of winding turns is used. This number equals the cross-sectional area multiplied by the input stator current density amplitude and divided by the input stator current amplitude.

The stator currents in the denominator, like the vector potentials, are also complex variables in the field solution represented by phasors. Thus, the currents can likewise be evaluated at any phase angle. The currents are consistent with the form taken in Equation III-13 when expressed in the complex plane. The temporal phase lag angle α is omitted here because it is already incorporated in the vector potentials. Since the input stator currents have been chosen as the temporal reference in the steady state field solution, the vector potentials are solved relative to them. Also, a temporal phase lag of ninety degrees is added here to be consistent with the convention taken by the FEA solver.

From the input impedance, the stator currents are solved at the input voltages. Motor performance is then calculated. Voltage driven torque is simply the current driven torque scaled for the currents by the

---

[42]P. P. Silvester and R. L. Ferrari, *Finite Elements for Electrical Engineers*, Second Edition, Cambridge: Cambridge University Press, 1990, p. 188.

-105-

square of their amplitude. Horsepower in the voltage driven motor is the product of rotor speed and the voltage driven torque. Similar to the torque, power losses can also be scaled for the stator currents. From Equation III-31 and Equation III-42 of the lumped electrical model, the losses are also proportional to the square of stator current amplitude. Power factor equals the real component divided by the magnitude of the input impedance.

Efficiency equals output horsepower divided by input power:

$$
\text{efficiency} =
$$

$$
\frac{\dot{\theta}_r T}{\sum_{k=1}^{m} R_s \left(i_s^k\right)^2 + \sum_{l}^{\text{stator windings}} a^l z J_s^l \cos\left(\omega_e t + \frac{2\pi k^l}{m} - \frac{\pi}{2}\right) Re\left(\frac{\partial}{\partial t}\left\{A\left[\cos(\omega_e t) + j\sin(\omega_e t)\right]\right\}\right) + P_h} \qquad \text{V-7}
$$

where:

k^l = k^{th} stator phase in l^{th} element

Input power comprises stator resistive power loss, input power from flux linkages, and hysteresis and eddy current losses. Input power from flux linkages is extracted from the field solution as the sum over all stator winding elements of the real component of input stator current multiplied by the real component of EMF. Vector potentials are transformed to the excitation frequency because EMF voltages in stator windings are with respect to the stationary reference frame.

The input power from flux linkages in the denominator can also be formulated using Equation V-6 as the product of the input stator current in the denominator and the EMF in the numerator. Only the real components of the two are multiplied here. The product is summed over stator winding elements of all phases instead of just over one phase. In addition, an appropriate phase shift is made for the stator current in the kth phase.

V.D. Power Difference Method

Another method has been developed to calculate induction motor torque through the FEA. In this second FEA method, the power difference method, the static solver and the two static field meshes become unnecessary. Merely one mesh and the steady state solver are required for all rotor speeds. Torque and all other performance characteristics at each speed are directly evaluated in one step from the steady state

-106-

field solution. As a result, computing time is dramatically reduced. Torque calculations are also more accurate relative to the first FEA method because finite approximations of the partial derivative of coenergy with respect to rotor position are not made.

Torque is derived from the conservation of instantaneous energy. The equivalent "T" circuit model is not needed. The lumped magnetic and electrical models are used only to incorporate stator resistance and three-dimensional effects. In deriving torque, terms in the conservation of instantaneous energy are first formulated in terms of field quantities in the steady state solution. Then, torque is solved.

The derivation of torque in this FEA method, as in the lumped electrical model, begins with the conservation of instantaneous energy. The time derivative of all terms in the conservation of instantaneous energy is taken for an infinitesimal change to yield the conservation of instantaneous power. Thus, input electrical power provides stored magnetic power, stator heat loss, rotor heat loss, hysteresis and eddy current losses in the steel, and output mechanical power:

$$\sum_{k=1}^{n} v_{in}^{k} i_{s}^{k} = \frac{dW_{s}}{dt} + \sum_{k=1}^{n} R_{s}\left(i_{s}^{k}\right)^{2} + \sum_{k=1}^{\frac{S_r}{n}} R_{r}\left(i_{r}^{k}\right)^{2} + P_{h} + \dot{\theta}_{r} T \qquad \text{V-8}$$

where:

W_{s} = magnetic stored energy

Although friction is neglected, it can be incorporated by subtracting from the calculated output torque. Hysteresis and eddy current losses are also included by subtracting from the torque. The losses are empirically derived in Equation III-43.

Except for the addition of the stored power term, the above equation is identical to the conservation of instantaneous power in Equation III-35 of the lumped electrical model. In that model, when no saturation exists stored power was zero for motors with more than one stator phase and one rotor phase. Since the number of phases is not restricted here, stored power is included.

Torque is solved after relating all other terms in Equation V-8 to field quantities extracted from the solution. The first term was already formulated in the denominator of Equation V-7:

-107-

$$\sum_{k=1}^{m} v_{in}^{k} i_{s}^{k} =$$

V-9

$$\sum_{k=1}^{m} R_{s}(i_{s}^{k})^{2} + \overset{\text{stator windings}}{\sum_{l}} a^{l}z J_{s}^{l} \cos\left(\omega_{e}t + \frac{2\pi k^{l}}{m} - \frac{\pi}{2}\right) Re\left(\frac{\partial}{\partial t}\left(A\left\{\cos(\omega_{e}t) + \hat{j}\sin(\omega_{e}t)\right\}\right)\right)$$

The input power comprises stator resistive power loss and input power from flux linkages. Hysteresis and eddy current losses are not included here because they are subtracted from the torque.

The second term in Equation V-8 is stored power, which arises due to the increase in energy stored in the magnetic field. For linear materials used exclusively by the steady state solver, stored energy can be formulated in terms of a volume integral of flux density and material permeability.[43] The flux density is constant throughout the volume of each of the first-order triangular elements used by the two-dimensional steady state solver. As a result, stored energy becomes the volume multiplied by half of the square of flux density and divided by the material permeability. The sum over all mesh elements of the time derivative of stored energy yields stored power:

$$\frac{dW_{s}}{dt} = \frac{d}{dt}\left[\overset{\text{nonrotor}}{\sum_{k=1}} a^{k}z \frac{\left(\nabla \times Re\{A^{k}[\cos(\omega_{e}t) + \hat{j}\sin(\omega_{e}t)]\}\right)^{2}}{2\mu^{k}}\right] +$$

$$\frac{d}{dt}\left[\overset{\text{rotor}}{\sum_{k=1}} a^{k}z \frac{\left(\nabla \times Re\{A^{k}[\cos(\omega_{s}t) + \hat{j}\sin(\omega_{s}t)]\}\right)^{2}}{2\mu^{k}}\right]$$

V-10

where:

μ^{k} = material permeability in k^{th} element

In deriving the stored power, the relationship of flux density with vector potential must first be known. Through Maxwell's fourth equation, the curl of vector potential defines flux density.[44] Since the field solution contains only nodal vector potentials, the flux density is approximated through them and the nodal positions by using linear interpolation for the first-order triangular elements. Due to the nature

---

[43]A. E. Fitzgerald, Charles Jr. Kingsley, and Stephen D. Umans, *Electric Machinery*, Fifth Edition, New York: McGraw-Hill, Inc., 1990, p. 105.

[44]P. P. Silvester and R. L. Ferrari, *Finite Elements for Electrical Engineers*, Second Edition, Cambridge: Cambridge University Press, 1990, p. 61.

-108-

of the two-dimensional steady state solver, the vector potential only has a component in the axial direction causing the flux density to only have components in the radial and tangential directions.

Stored power is now derived in terms of the real component of vector potential extracted from the field solution. The vector potentials can be evaluated at any desired phase angle because the steady state solution is based on field quantities that vary sinusoidally with time. Since stored power extracted from the field solution is always in the rotating reference frame, a transformation to the stationary reference frame is necessary for all but the rotor elements.

The last term in Equation V-8 that needs to be solved before torque can be formulated is the rotor resistive power loss. This loss is derived by applying the conservation of instantaneous power to the FEA system. No output mechanical power exists in this system since the steady state solver can not account for rotor rotation. Therefore, input power from flux linkages provides only stored magnetic power and rotor heat loss:

$$\sum_{i}^{stator\ windings} a^i z J_s^i \cos\left(\omega_s t + \frac{2\pi k^i}{m} - \frac{\pi}{2}\right) Re\left(\frac{\partial}{\partial t}\{A^i\{\cos(\omega_s t) + \hat{j}\sin(\omega_s t)\}\}\right) =$$

$$\frac{d}{dt}\left[\sum_{k=1}^{all\ elements} a^k z \frac{\left(\nabla \times Re\{A^k\{\cos(\omega_s t) + \hat{j}\sin(\omega_s t)\}\}\right)^2}{2\mu^k}\right] + \sum_{k=1}^{\frac{s_r}{n}} R_r\left(i_r^k\right)^2 \qquad \text{V-11}$$

All terms here are in the rotating reference frame because the steady state solver models the magnetic field in that reference frame.

Except for the stator resistive power loss, the hysteresis and eddy current losses, and the reference frame, this equation is identical to Equation V-8 without output power after substitutions from Equation V-9 and Equation V-10. Without a transformation to the stationary reference frame, the input power and stored power in the FEA system can not estimate the actual power in the induction motor. Regardless, the two terms in the rotating reference frame serve solely in formulating the rotor resistive power loss.

Stator resistive power loss is omitted from the FEA system because stator windings are assigned infinite resistivity in the mesh like in the first FEA method. This keeps stator currents directly regulated. Consequently, stator resistance is externally included in power losses, input impedance, and efficiency. Hysteresis and eddy current losses are also omitted from the FEA system because steel in the stator and

-109-

rotor is assigned infinite resistivity like in the first FEA method. Consequently, these losses are externally included in torque, horsepower, power losses, and efficiency.

In the FEA system of Equation V-11, heat loss comprises only the rotor resistive power loss since stator resistive heat loss and eddy current losses in the steel are zero. Induced currents are confined to only rotor bars because steel in the stator and rotor is assigned infinite resistivity like the stator windings. However, the eddy currents can be easily included if necessary. An appropriate resistivity would be assigned to the steel in the stator and rotor. Also, an extra term for the eddy current losses would be added to the conservation of instantaneous power of Equation V-11.

Torque can now be solved since all other terms in Equation V-8 have been related to field quantities in the steady state solution:

$$
\begin{aligned}
T = &\sum_{l}^{\text{stator windings}} \frac{a^l z J_s^l}{\dot{\theta}_r} \cos\left(\omega_e t + \frac{2\pi k^l}{m} - \frac{\pi}{2}\right) Re\left(\frac{\partial}{\partial t}\{A[\cos(\omega_e t) + \hat{j}\sin(\omega_e t)]\}\right) - \\
&\frac{d}{dt}\left[\sum_{k=1}^{\text{nonrotor}} \frac{a^k z}{\dot{\theta}_r} \frac{(\nabla \times Re\{A^k[\cos(\omega_e t) + \hat{j}\sin(\omega_e t)]\})^2}{2\mu^k}\right] - \\
&\sum_{l}^{\text{stator windings}} \frac{a^l z J_s^l}{\dot{\theta}_r} \cos\left(\omega_s t + \frac{2\pi k^l}{m} - \frac{\pi}{2}\right) Re\left(\frac{\partial}{\partial t}\{A[\cos(\omega_s t) + \hat{j}\sin(\omega_s t)]\}\right) + \\
&\frac{d}{dt}\left[\sum_{k=1}^{\text{nonrotor}} \frac{a^k z}{\dot{\theta}_r} \frac{(\nabla \times Re\{A^k[\cos(\omega_s t) + \hat{j}\sin(\omega_s t)]\})^2}{2\mu^k}\right] - \frac{P_h}{\dot{\theta}_r}
\end{aligned}
\qquad \text{V-12}
$$

Substitutions are made for the input power from Equation V-9, the stored power from Equation V-10, and the rotor power loss from Equation V-11. Like in the previous section, P_h is not included at synchronous speed because torque is zero and at stall because it can not divide by zero. When hysteresis and eddy current losses are neglected, torque is the difference of the input power in the two reference frames subtracted by the difference of the stored power in the same two reference frames.

The torque expression can be simplified for motors with multiple stator and rotor phases. The input power from flux linkages becomes constant over time at a given rotor speed. As a result, the input power in the stationary and rotating reference frames is related:

-110-

$$\sum_{l}^{\text{stator windings}} a^l z J_s^l \cos\!\left(\omega_e t + \frac{2\pi k^l}{m} - \frac{\pi}{2}\right) Re\!\left(\frac{\partial}{\partial t}\{A\{\cos(\omega_e t) + \hat{j}\sin(\omega_e t)\}\}\right) =$$

$$\frac{\omega_e}{\omega_s} \sum_{l}^{\text{stator windings}} a^l z J_s^l \cos\!\left(\omega_s t + \frac{2\pi k^l}{m} - \frac{\pi}{2}\right) Re\!\left(\frac{\partial}{\partial t}\{A\{\cos(\omega_s t) + \hat{j}\sin(\omega_s t)\}\}\right) \qquad \text{V-13}$$

Also, the stored power becomes zero in both reference frames.

Torque is then simplified after substitutions from the above equation and Equation III-38, which relates rotor speed to the excitation and slip frequencies. Torque becomes the input power from flux linkages in the rotating reference frame scaled by the number of pole pairs divided by slip frequency when hysteresis and eddy current losses are neglected:

$$T = \sum_{l}^{\text{stator windings}} \frac{n}{2\omega_s} a^l z J_s^l \cos\!\left(\omega_s t + \frac{2\pi k^l}{m} - \frac{\pi}{2}\right) Re\!\left(\frac{\partial}{\partial t}\{A\{\cos(\omega_s t) + \hat{j}\sin(\omega_s t)\}\}\right) - \frac{P_h}{\dot{\theta}_r} \qquad \text{V-14}$$

Field quantities in the input power term are summed only over the stator winding elements, which dramatically reduces computing time relative to the first FEA method. At the same time, estimation accuracy is not sacrificed. The following two sections describe the implementation of the power difference method in calculating performance.

Except for torque, calculating performance in current and voltage driven motors through this second FEA method is the same as through the first FEA method. Expressions for horsepower, power losses, power factor, and efficiency are identical in the two methods. Performance calculations are repeated for every desired rotor speed. Torque, on the other hand, is determined instead by the power difference method directly from the steady state field solution through the conservation of instantaneous energy.

The traditional method of determining torque in the induction motor by FEA is through the equivalent "T" circuit model. Torque is formulated like in Equation III-39 of the lumped electrical model. Without hysteresis and eddy current losses, torque equals the rotor resistive power loss derived in the

middle term of Equation V-4 scaled by the number of pole pairs and divided by slip frequency.[45] The steady state torque is based on symmetry from excitation that is balanced in time and space, evenly spaced rotor bars, and an integral number of rotor phases. Also, motors are assumed to have multiple stator and rotor phases.

The implementation of the traditional method for calculating torque differs from that of the power difference method. Without hysteresis and eddy current losses, the former sums resistive power loss over all rotor bar elements. For motors with multiple stator and rotor phases, the latter sums input power from flux linkages over all stator winding elements when hysteresis and eddy current losses are neglected. Though, Equation V-11 establishes that the rotor resistive power loss equals the input power in the rotating reference frame when stator power loss, eddy current losses, and stored power are neglected. Stator power loss and eddy current losses are zero due to the assignment of infinite resistivity to the applicable materials. Stored power is zero due to the symmetry. Consequently, the two methods yield the same result despite different implementations. However, the traditional method requires motors to have multiple stator and rotor phases. The power difference method, on the other hand, does not require this.

V.D.1. Calculating Performance in the Current Driven Induction Motor

In calculating performance in the current driven motor, the known stator currents energized at the slip frequency are specified as inputs into the mesh. After the rotor bar resistivity is adjusted in the FEA for skewing and end ring resistance, the solver reveals the magnetic field. Current driven torque is then determined from Equation V-12 or Equation V-14 depending on whether the motor has multiple stator and rotor phases. Horsepower in the current driven motor is the product of rotor speed and current driven torque. Power losses in the current driven motor is calculated from Equation V-4.

V.D.2. Calculating Performance in the Voltage Driven Induction Motor

In calculating performance in the voltage driven motor, an arbitrary input stator current amplitude is initially assumed in the mesh. After the rotor bar resistivity is adjusted in the FEA for skewing and end

---

[45]R. Belmans, D. Verdyck, T. B. Johansson, W. Geysen, and R. D. Findlay, "Calculation of the No-Load and Torque Speed Characteristic of Induction Motors Using Finite Elements," *International Conference on Electrical Machines*, August 13-15, 1990, pp. 724-729.

-112-

ring resistance, the solver reveals the magnetic field. Input impedance is then determined from Equation V-5 with stator resistance and three-dimensional leakage flux externally included.

From the input impedance, the stator currents are solved at the input voltages. Performance is then evaluated. Voltage driven torque is the current driven torque scaled for the stator currents by the square of their amplitude. Input impedance and current driven torque are calculated at the same time so that voltage driven torque is computed quickly. Horsepower in the voltage driven motor is the product of rotor speed and the voltage driven torque. Power losses, similar to the torque, are also scaled for the stator currents by the square of their amplitude. Power factor equals the real component divided by the magnitude of the input impedance. Efficiency from Equation V-7 is the output horsepower divided by input power.

V.E. Transient FEA Method

The third method to calculate induction motor performance through the FEA uses a transient solver. This solver determines the instantaneous magnetic field like the static solver, but also determines the induced currents. Therefore, eddy current losses in the steel can be inherently incorporated. But, in order to obtain steady state response at a rotor speed, enough solutions must be determined to time step beyond the transient response. Computing time becomes extremely long. However, with rapid development of faster microprocessors, transient FEA is becoming more feasible.

To determine performance from the two-dimensional transient solver, three-dimensional effects are incorporated. Rotor bar resistivity is adjusted for skewing and end ring resistance just like in the first two FEA methods. Also, stator and rotor currents are adjusted at each time step for three-dimensional leakage flux. Torque can then be solved directly from the field solution by either using a static solver like in the first FEA method or through the conservation of instantaneous power applied to transient FEA.

Using the steady state solver is a relatively simple approach to modelling electric motors. Field solutions vary sinusoidally with time and materials are magnetically linear. Saturation is typically avoided in the induction motor because it causes unfavorable harmonics. Also, in order for the field quantities to vary sinusoidally with time, symmetry is required. The symmetry exists from excitation that is balanced in time and space, evenly spaced rotor bars, and an integral number of rotor phases. Since the induction

-113-

motor is typically designed with this symmetry, performance estimations are then accurate. But, nonsymmetry and saturation cause errors in the estimations.

In this case, a transient solver can be utilized. Much longer solution time is required to reveal the magnetic field at every instant in time. But, instantaneous performance can be evaluated without assuming symmetry and linear materials. However, similar to the steady state solver, hysteresis is ignored and rotor rotation is not account for. Therefore, the rotating reference frame of the rotor is selected.

When modelling with the transient solver, performance can no longer be scaled for the stator currents like in the first two FEA methods because materials are not assumed to be linear. Instantaneous stator currents are first specified as inputs into the mesh. For the current driven motor, the stator currents are known. But, for the voltage driven motor, the stator currents are determined by incorporating three-dimensional leakage flux in the two-dimensional transient solver. Torque can then be solved directly from the field solution by either a static solver or through the conservation of instantaneous power applied to the transient solution. Using the static solver is laborious because it is necessary to specify rotor currents as inputs to two additional meshes. In contrast, torque through the conservation of instantaneous power is determined directly from the transient solution.

Many similarities exist between determining performance through the transient solver in this third FEA method and through the steady state solver in the first two methods. Currents rather than voltages are specified as inputs into the mesh. Also, infinite resistivity is assigned to the stator windings to keep the input stator currents directly regulated. Thus, stator resistance must be externally included in calculating stator currents, power losses, and efficiency. The stator resistance does not affect current driven torque and affects voltage driven torque only indirectly through the stator currents. In addition, three-dimensional effects are incorporated in all three methods.

To include three-dimensional effects, the rotor bar resistivity is adjusted at each rotor speed for skewing and end ring resistance just like in the first two FEA methods. Also, three-dimensional leakage flux is accounted for. Instantaneous stator currents at the input voltages are adjusted for linkages with stator three-dimensional leakage flux. Instantaneous rotor currents are adjusted for linkages with rotor three-dimensional leakage flux. The assumption made in the first two FEA methods to include this flux

-114-

in the rotor is not needed here because the flux is included in the rotor currents not stator currents.

Linkages with three-dimensional leakage flux in the stator and rotor are included through inductances similar to L_{3D} in the first two FEA methods:

$$L_{s3D} = K_{sv}\frac{4}{\pi^2}nmK_d^2N_s^2\left(\frac{1}{\mathfrak{R}_{sle}} + \frac{1}{\mathfrak{R}_{slw}}\right)$$

$$L_{r3D} = K_{rv}\frac{S_rN_r^2}{\pi^2}\left(\frac{1}{\mathfrak{R}_{rle}} + \frac{1}{\mathfrak{R}_{rlw}}\right)$$

V-15

where:

L_{s3D} $\equiv$ stator three-dimensional end and skew leakage inductance per stator phase
L_{r3D} $\equiv$ rotor three-dimensional end and skew leakage inductance per rotor phase

When materials are linear and symmetry exists, these inductances are constant. However, even if the inductances are not, they can be assumed constant. This is because the three-dimensional leakage flux is normally much smaller than the air gap flux to attain high torque and efficiency levels.

Stator three-dimensional leakage flux does not affect performance in the current driven motor because stator currents are known. In the voltage driven motor, however, the flux is used to determine the stator currents from the input voltages. The input voltage per phase equals the sum of stator resistive voltage drop, stator EMF from the two-dimensional transient solver, and voltage drop across the stator three-dimensional inductance:

$$v_{in}^k = R_s i_s^k + \frac{d\lambda_{s2D}^k}{dt} + L_{s3D}\frac{di_s^k}{dt}$$

V-16

where:

λ_{s2D}^k $\equiv$ stator winding flux linkage in k^{th} stator phase in the two-dimensional FEA

Numerical integration is applied to adjust the currents at each time step, $n+1$, from the previous steps, n and n-1:

-115-

$$i_s^k\Big|_{n+1} = \left[1 - \frac{R_s}{L_{s3D}\left(\dfrac{1}{t\big|_{n+1} - t\big|_n} + \dfrac{n}{2}\dot\theta_r\right)}\right]i_s^k\Big|_n + \frac{v_{ts}^k\Big|_n - \left(\lambda_{s2D}^k\Big|_n - \lambda_{s2D}^k\Big|_{n-1}\right)\left(\dfrac{1}{t\big|_n - t\big|_{n-1}} + \dfrac{n}{2}\dot\theta_r\right)}{L_{s3D}\left(\dfrac{1}{t\big|_{n+1} - t\big|_n} + \dfrac{n}{2}\dot\theta_r\right)} \qquad \text{V-17}$$

Since the rotating reference frame is selected in the FEA, the time derivatives are transformed to the stationary reference frame by considering rotor speed. The time increment must be chosen small enough so that the change in currents does not go unstable. Also, L_{s3D} can not be zero.

From the stator currents, induced rotor currents are calculated. Rotor currents are corrected for rotor three-dimensional leakage flux by specifying additional current as input in the bars:

$$i_r^l = i_{r3D}^l + i_{r2D}^l$$

$$R_r i_{r3D}^l = -L_{r3D}\frac{di_r^l}{dt} \qquad \text{V-18}$$

where:

i_{r3D}^l = rotor bar current in l^{th} rotor phase from rotor three-dimensional leakage flux linkage
i_{r2D}^l = rotor bar current in l^{th} rotor phase in the two-dimensional FEA

i_{r3D}^l is defined in the same direction as i_{r2D}^l. The resistive voltage drop due to this additional current accounts for the voltage drop from linkages with the rotor three-dimensional leakage flux. Numerical integration is then applied to adjust the currents at each time step, $n+1$, from the previous steps, n and n-1:

$$i_{r3D}^l\Big|_{n+1} = \left(1 - R_r\frac{t\big|_{n+1} - t\big|_n}{L_{r3D}}\right)i_{r3D}^l\Big|_n - \left(\frac{i_{r2D}^l\Big|_n - i_{r2D}^l\Big|_{n-1}}{t\big|_n - t\big|_{n-1}}\right)\left(t\big|_{n+1} - t\big|_n\right) \qquad \text{V-19}$$

The time increment must again be chosen small enough so that the change in currents do not go unstable. Also, L_{r3D} can not be zero.

When the stator and rotor current corrections were implemented, solution convergence problems were encountered. More research is necessary to solve these problems before performance can be calculated by this method.

V.F. Summary

-116-

Magnetic FEA is a powerful tool for analyzing and designing electric motors. A two-dimensional static solver is commonly sufficient to accurately model permanent magnet motors. Modelling the induction motor purely from two-dimensional FEA yields poor results until three-dimensional effects estimated by the lumped models are included. Any errors in deriving these effects from the lumped models cause errors in estimating performance from the FEA.

Three FEA methods have been developed to determine performance in current and voltage driven induction motors directly from the two-dimensional field solutions. The equivalent "T" circuit model is not needed. The first method uses a steady state harmonic field solver followed by a static field solver in calculating torque from the method of virtual work. The second method, which requires much less computing time, uses only a steady state solver to calculate torque from the conservation of instantaneous energy. The third method uses a transient field solver.

To include three-dimensional effects, the rotor bar resistivity is adjusted to account for skewing and end rings. In the first two FEA methods, the input impedance is also increased to account for linkages with three-dimensional leakage flux. The impedance is used to determine stator currents from the input voltages in calculating performance in the voltage driven motor. Three-dimensional leakage flux does not significantly affect performance in the current driven motor. Three-dimensional effects are included through the same process in the first two methods. In the third FEA method, linkages with three-dimensional leakage flux are used to directly determine instantaneous stator and rotor currents.

After including three-dimensional effects in the first two FEA methods, expressions for torque, horsepower, and power losses are derived for the current driven motor. For magnetically linear materials, these performance characteristics can be scaled for any stator currents by the square of their amplitude. Accurate performance estimations in current driven induction motors, such as in motors driven by scalar control and vector control, are possible when saturation levels are low. For the voltage driven motor, expressions for power factor and efficiency are also derived.

Performance calculations from the two FEA methods for both current and voltage driven induction motors are compared to experimental results in the next chapter. Calculations are almost identical for the two methods. Errors are shown to be within fifteen percent over the practical region of the torque-speed

-117-

curve. Performance calculations from the third FEA method are not compared because solution convergence problems were encountered.

The traditional method of modelling the induction motor using the FEA is through the equivalent "T" circuit model. The model loses some physical interpretation because rotor parameters are referred to the stator. Torque in this method is derived based on symmetry. Torque from this traditional method is equivalent to torque from the second FEA method when based on the same symmetry. However, the implementation of the two differs. Also, the power difference method does not require motors to have multiple stator and rotor phases.

CHAPTER VI

EXPERIMENTAL VERIFICATIONS

VI.A. Introduction

The lumped magnetic, electrical, and thermal models have been developed to determine the relationships of motor geometry and material properties to motor performance. In addition, three FEA methods have been developed to evaluate performance in current and voltage driven induction motors directly from the field solutions. The third FEA method is not used here because of solution convergence problems. The lumped models and the first two FEA methods are now applied to two commercial induction motors. Current and voltage driven torques are calculated at numerous rotor speeds and compared with experimental results. Also, transient temperature is determined at stall for one of the motors from the lumped thermal model and compared to experimental results.

VI.B. Description of the Experimental Configuration

Calculations of torque and temperature from the lumped models are individually compared to experimental results to independently verify the accuracy of the models. Sources of error are then isolated. The lumped magnetic and electrical models are used to determine torque at a known temperature instead of using the steady state temperature estimated from the lumped thermal model. Near stall, the stator windings may not be able to withstand operating at the steady state temperature anyway. The torque is then compared to experimental results. In addition, the lumped thermal model is used to determine the temperature at stall with known heat sources. The temperature is also compared to experimental results.

Experimentally measuring torque in permanent magnet motors is relatively simple. Hysteresis brakes can be used since there are no unstable regions in the torque-speed curve. For the voltage driven induction motor, the brake can only be used in the stable region of the torque-speed curve where the rotor speed is faster than at breakdown torque. For any other speed, the brake would normally cause the motor to stall. Therefore, another process is used where a more powerful second motor, a permanent magnet

-119-

motor, controls the speed of the induction motor. Torque can now be measured at any rotor speed.

To experimentally measure torque, the shaft of the induction motor is solidly coupled to that of a brushless permanent magnet DC motor with a torquemeter in between as shown in Figure 6.1. The permanent magnet motor must generate more torque at every rotor speed. The speed of the system is thereby controlled. The induction motor no longer stalls unintentionally even when operating in the unstable region. Torque produced by the induction motor acts as a load on the permanent magnet motor.
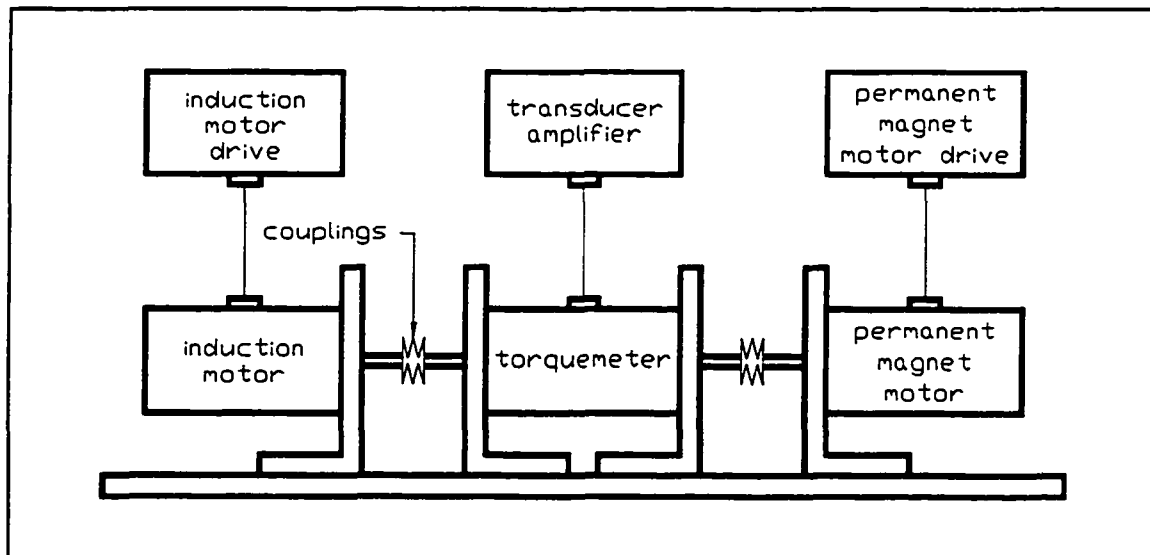

Figure 6.1 Experimental configuration for measuring torque and rotor speed.

Input voltage, excitation frequency, stator current, and torque are measured at each desired rotor speed. The first two are measured with an oscilloscope and a current probe manufactured by TEKTRONIX. Instantaneous torque and rotor speed are measured with a non-contact strain gage torquemeter manufactured by S. Himmelstein and Company. The torquemeter has a torque range of 160 ounce-inches and a maximum speed of fifty thousand revolutions per minute. Measurements have a nonlinearity tolerance of one tenth of a percent of full scale and a nonrepeatability tolerance of five hundredth of a percent of full scale.

Experimental results were collected for two commercial polyphase induction motors. Both voltage driven motors were purchased from Eastern Air Devices, Incorporated (EAD). One motor is wound for two poles and has twenty-four stator slots and seventeen skewed aluminum rotor bars. It produces approximately a fifteenth horsepower when supplied with 120 volts per phase at sixty hertz. The other

-120-

motor is wound for eight poles and has twenty-four stator slots and nineteen skewed brass rotor bars. It produces approximately a twentieth horsepower when supplied with 120 volts per phase at four hundred hertz. However, the power supply of this motor actually produces 122 volts per phase at 420 hertz.

VI.C. Comparison of Voltage Driven Torque

After experimental results are collected for the two motors, they are compared with calculations from the lumped models and FEA methods. Also, stator resistance which affects voltage driven torque is determined from the lumped electrical model and compared with measurements. Sources of error are explained.

In comparing calculated torque from the lumped models and FEA methods with experimental results, known stator and rotor temperatures are used. Experimental measurements were taken at these temperatures instead of at steady state temperatures to isolate sources of error. For simplicity, the known temperatures were kept constant over the entire torque-speed curve.

The temperature of the stator is monitored easily by placing a thermocouple wire of type J manufactured by Omega in the stator slot against the windings. The wire has a temperature range of zero to 750 degrees Celsius and a limit of error at 1.1 degrees Celsius for temperatures up to 275 degrees Celsius. However, the temperature of the rotor can not be monitored without an expensive wireless temperature sensing instrument except at stall. As an approximation, the temperature of the rotor is assumed to be equal to that of the stator. At rated speed near synchronous speed where heat losses are low, not much error is introduced. But, near stall where heat losses are usually the highest, slightly more error may result.

Voltage driven torque is affected by stator resistance which can be experimentally measured. From the lumped models, the resistance is calculated using Equation III-1 and the torque is calculated using Equation III-39. This resistance is also used in the FEA methods. The calculated resistance is compared with measured resistance.

Stator resistance for all three phases was measured with a four-wire digital multimeter manufactured by Fluke and the average is used. Accuracy is within four thousandths for the range of two hundred ohms. Measurements were taken at room temperature and scaled to the known experimental

-121-

temperature. The calculations are low by ten percent for the sixty-hertz motor and a quarter percent for the four-hundred-hertz motor. The error is due to the approximated length of wire in the end turns. Although current driven torque is unaffected, the error causes voltage driven torque to be slightly high.

Torque is also affected by rotor resistance. Unfortunately, this resistance can not be measured over a phase because of end rings. Therefore, R_r in the lumped electrical model that is also used in the FEA methods is not verified.

Voltage driven torque versus rotor speed for the two EAD motors is plotted in Figure 6.2 and Figure 6.3. The measured torque remained constant over time at any rotor speed even though symmetry from an integral number of rotor phases does not exist. Because enough rotor bars exist in both motors, any torque ripple from the nonsymmetry is small. A jump occurs in the measured torque at stall in Figure 6.2 because of the high heat losses.
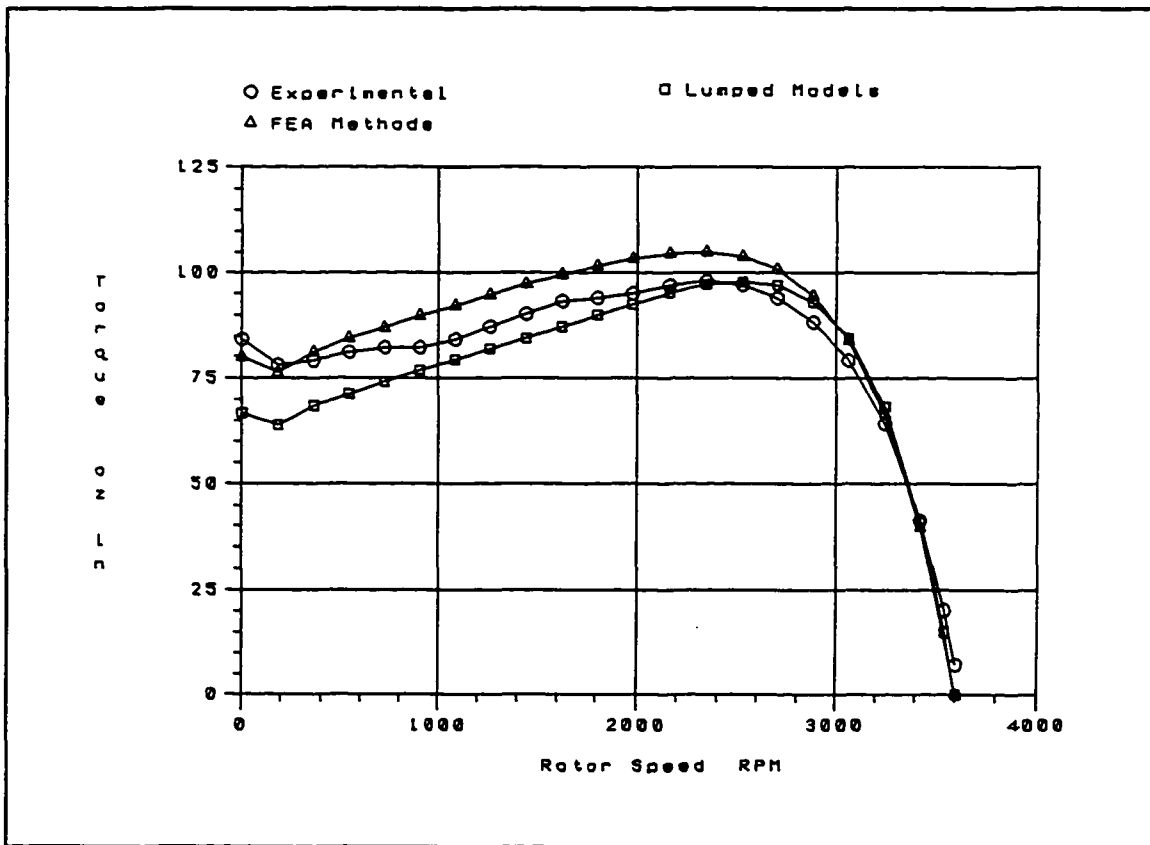

Figure 6.2 Comparison of voltage driven torque versus rotor speed for the sixty-hertz motor.

Figure 6.4 through Figure 6.7 show the outline and mesh of the two motors used in the FEA methods. Elements in the mesh are small enough so that flux density can be assumed constant throughout
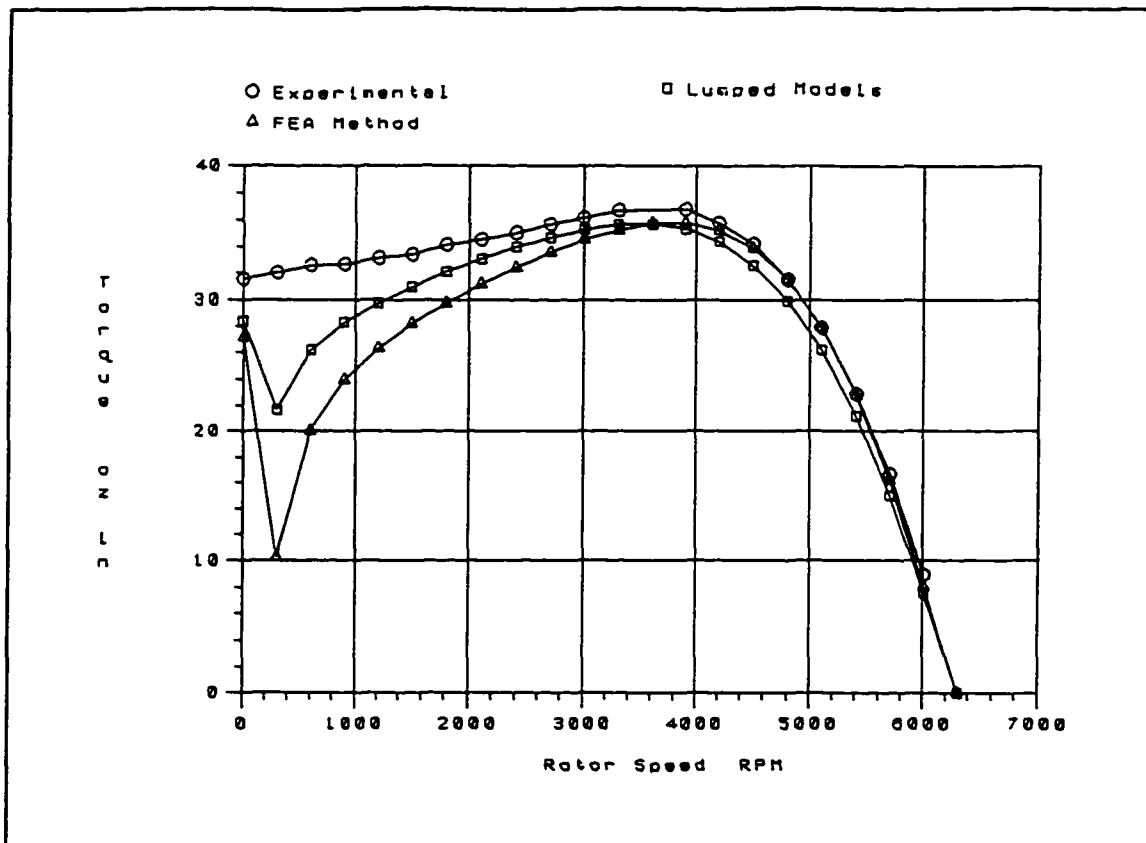
-122-

Figure 6.3 Comparison of voltage driven torque versus rotor speed for the four-hundred-hertz motor.

their volume. Torque from the two FEA methods described in sections V.C and V.D differs by less than two percent at every rotor speed. The difference arises from the finite approximations made in the first FEA method of the partial derivative of coenergy with respect to rotor position. Due to the small error, results from only the second method, the power difference method, is plotted for the sixty-hertz motor. Also, only the faster second FEA method is used for the four-hundred-hertz motor. Torque from that method is calculated from Equation V-14 for the two motors with multiple stator and rotor phases.

Errors in the lumped models are within fifteen percent for both motors except near synchronous speed, less than five percent slip, and near stall, more than ninety percent slip. Errors in the FEA methods for the sixty-hertz motor are within ten percent except at synchronous speed. For the four-hundred-hertz motor, errors in the FEA method are within fifteen percent except near stall, more than seventy-six percent slip.

When operating near synchronous speed, output torque is extremely sensitive to excitation frequency. In this region, torque varies dramatically with rotor speed. Therefore, any slight error in
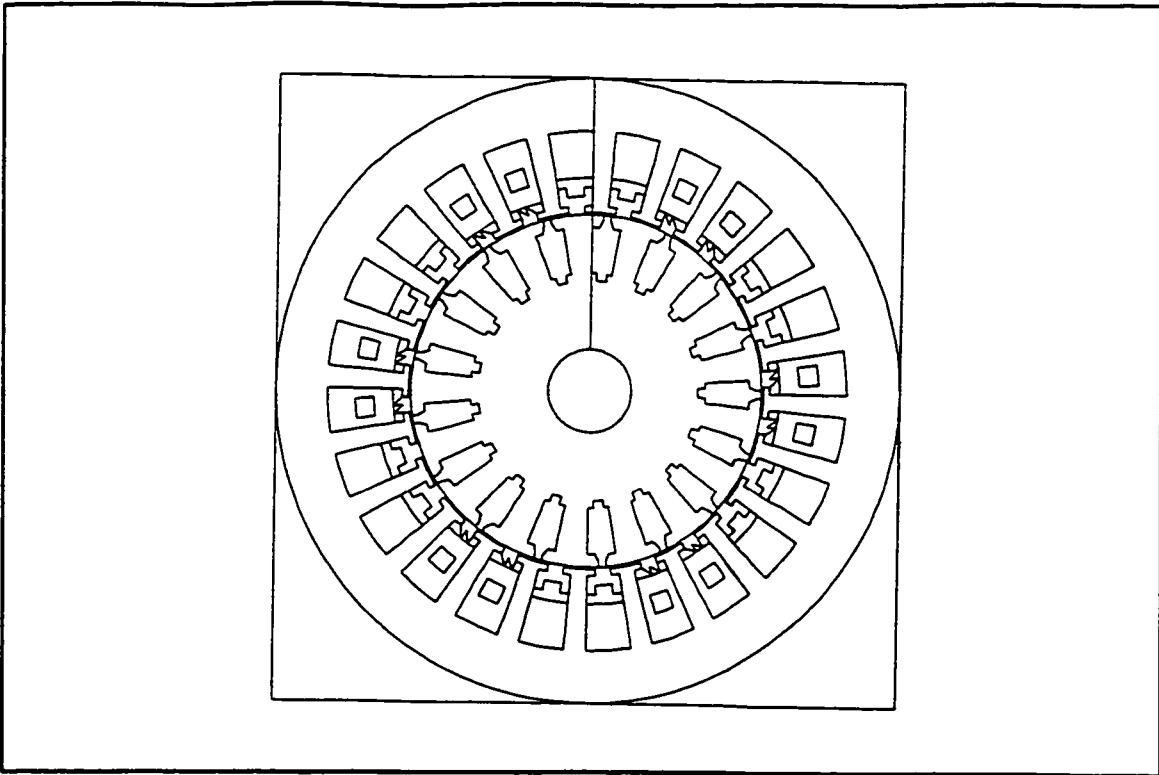
-123-

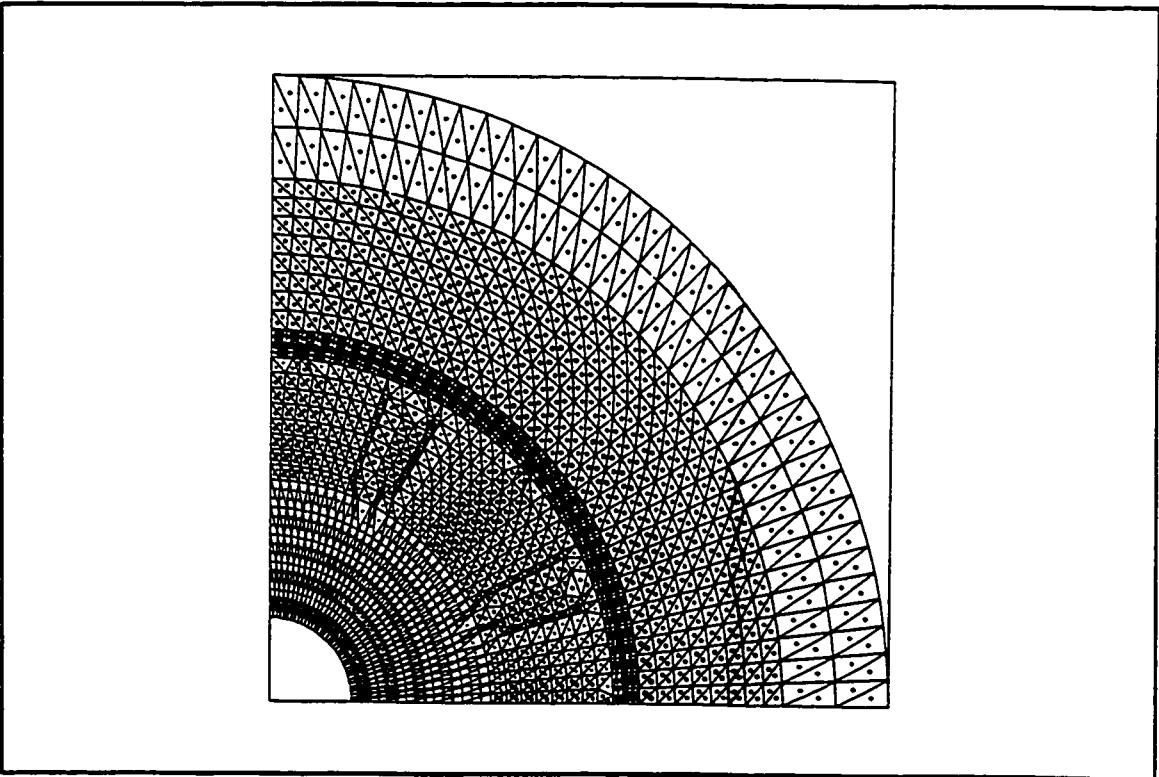**Figure 6.4** FEA mesh outline of cross section for the sixty-hertz motor.

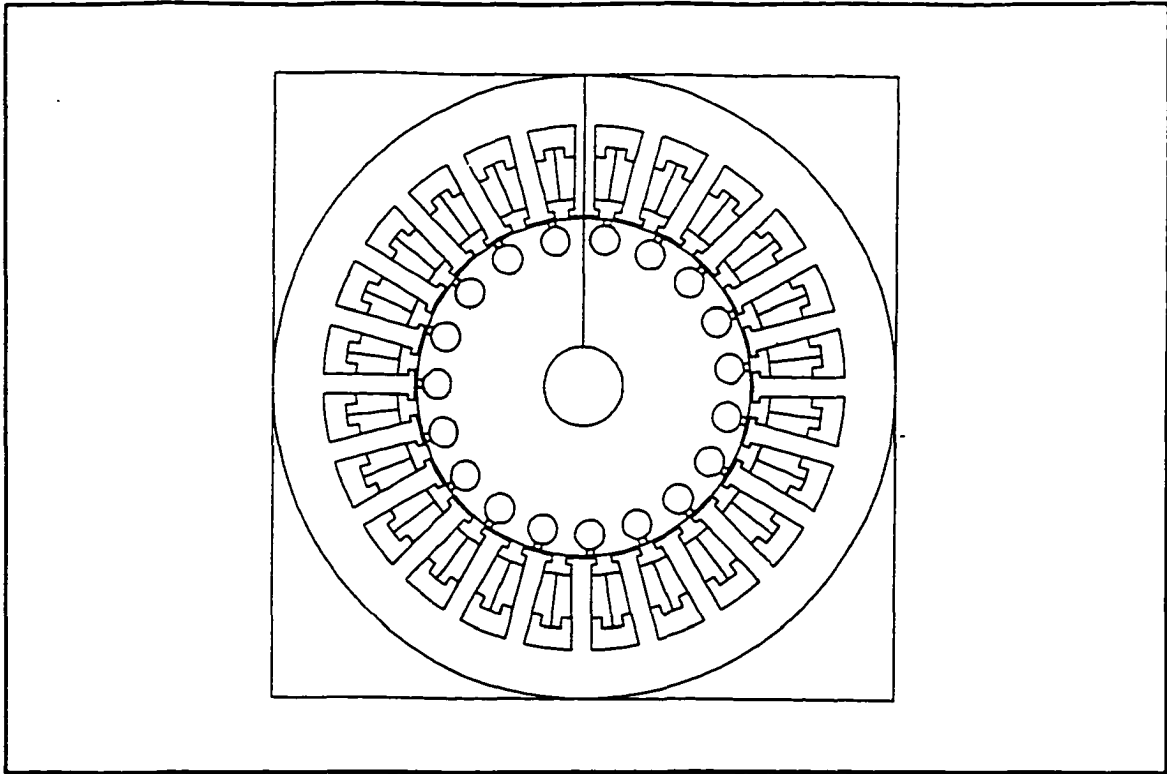**Figure 6.5** FEA mesh of quarter cross section for the sixty-hertz motor.

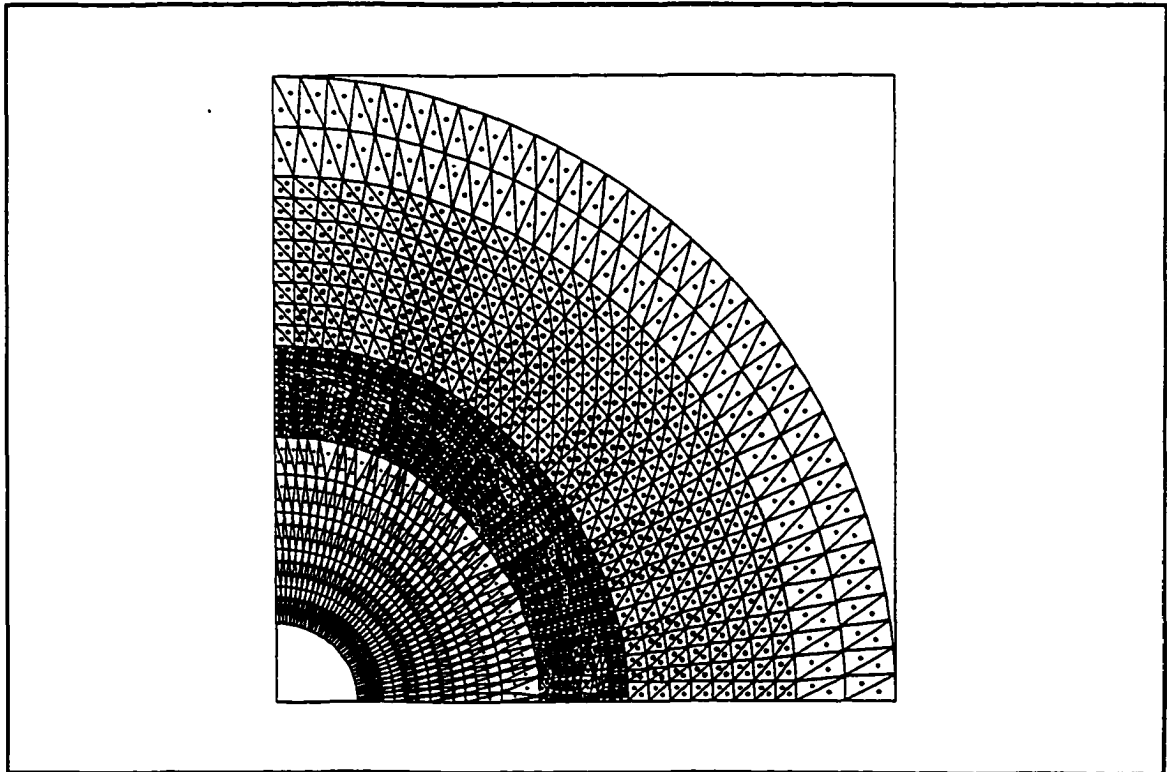**Figure 6.6** FEA mesh outline of cross section for the four-hundred-hertz motor.

Figure 6.7 FEA mesh of quarter cross section for the four-hundred-hertz motor.

-125-

determining the excitation frequency causes magnified errors in estimating torque.

Near stall, hysteresis and eddy current losses in the steel for the lumped models and FEA methods seem to be overestimated by the empirical model of Equation III-43. The losses are not included at stall and synchronous speed causing the calculated torque-speed curves to be discontinuous there. The overestimation of the losses may be due to extrapolation from operating outside the range of the empirical data. The error is more dramatic in the four-hundred-hertz motor. When this motor operates at three hundred revolutions per minute, torque estimation is reduced by twenty-six percent when the calculated hysteresis and eddy current losses are included. Torque estimation error at this speed increases from nine to thirty-two percent.

Torque estimation error is also introduced because harmonics are neglected. Since the temperatures are not at steady state, some slight error results from harmonics that arise in the stator and rotor currents. Any error in the stator currents causes error in the voltage driven torque that is squared. This is because voltage driven torque is calculated from current driven torque scaled for the square of stator currents. The concentric windings of the four-hundred-hertz motor contain just one tier causing harmonics in the flux density distribution. Enough rotor bars exist in both motors so that only some slight error results from harmonics due to the nonintegral rotor phases. Any saturation also causes harmonics. However, the error from this is small because flux density levels are low.

Additional error in the FEA methods is due to three-dimensional effects. Any error in deriving these effects from the lumped models causes error in not only the lumped models but the FEA methods as well. Also, the assumption made to include rotor three-dimensional leakage flux in only the stator currents and not the rotor currents results in some error.

Error results also from equipment sensitivity and friction. Experimental error due to measurement tolerances is small. Friction is negligible at around a quarter ounce-inch. The measurement was taken with a torque watch gauge manufactured by Waters that has a range from one to twenty ounce-inches and an accuracy of two percent of full scale.

VI.D. Comparison of Current Driven Torque

Current driven torque determined from the lumped models and FEA methods is also compared

with experimental results. The torque versus rotor speed is plotted in Figure 6.8 and Figure 6.9 for the two EAD motors. At each rotor speed, the experimental current driven torque is the measured voltage driven torque scaled for stator currents of one rms ampere by dividing by half the square of the measured current amplitude. Because of the scaling, any saturation still results in error.
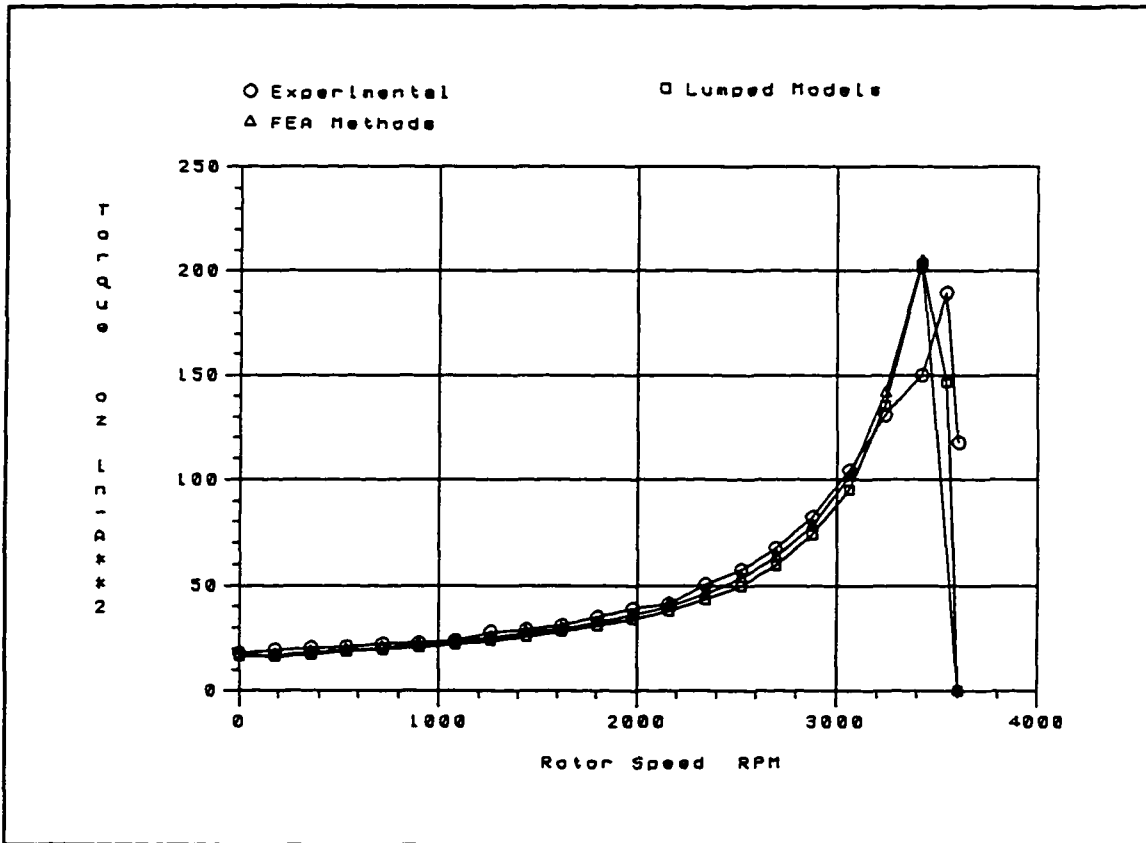
Figure 6.8 Comparison of current driven torque versus rotor speed for the sixty-hertz motor.

Errors in the lumped models and FEA methods are within fifteen percent for the sixty-hertz motor except near synchronous speed, five percent slip or less, where excitation frequency is critical and near stall, ninety-five percent slip or more, due to extrapolation. For the four-hundred-hertz motor, the errors in the lumped models are within fifteen percent except near synchronous speed, less than five percent slip, and near stall, more than fifty-seven percent slip. Errors in the FEA method for this motor are extremely large because of the difficulty in modelling three-dimensional leakage flux. Also, the windings in the mesh may need to be better distributed in the slots. In addition, elements in the mesh may not be small enough so that flux density can not be assumed constant throughout their volume.

-127-
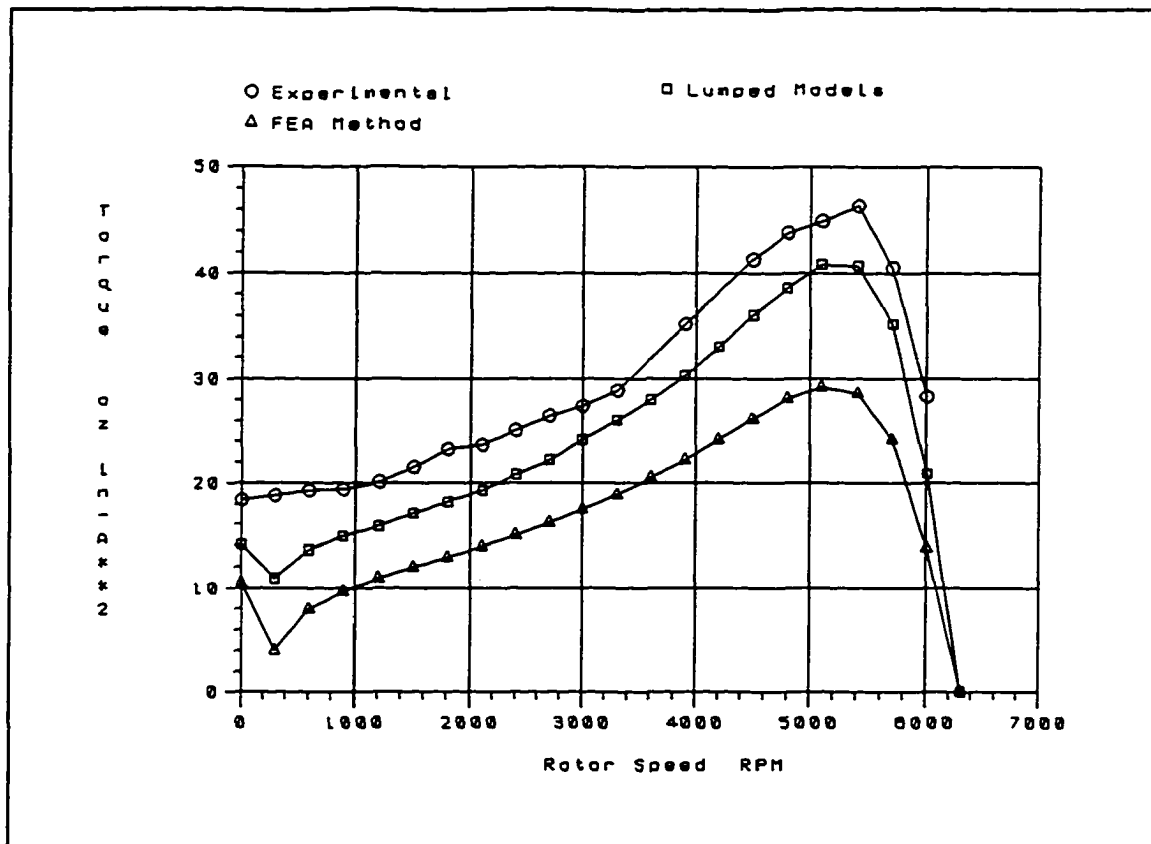
Figure 6.9 Comparison of current driven torque versus rotor speed for the four-hundred-hertz motor.

VI.E. Comparison of Temperatures

The lumped thermal model is applied to the sixty-hertz motor. Transient temperature in the housing, stator stack, stator windings, and rotor bars are calculated at stall and compared to experimental results. Sources of error are explained.

To experimentally measure transient temperature at stall, the induction motor was energized with the shaft clamped still. Thermocouple wires were placed in the housing body, in the stator stack, in a stator slot against the windings, and in the rotor end ring. With the motor initially at room temperature, measurements were taken for two hours until steady state temperatures were attained. The ambient temperature was also recorded.

In calculating temperatures from the lumped thermal model of Figure 4.1, the heat sources, thermal capacitances, and thermal resistances were first determined. Then, numerical integration was applied to solve for the transient temperatures. The heat sources were kept constant at their steady state values despite currents and resistances, which determine heat generation, varying with temperature. For

-128-

the conduction thermal resistance R_{th}^{cnd} in Equation IV-4, the housing and stator stack were assumed to have perfect contact so that k_h is the actual thermal conductivity of the housing body.

Transient temperature at stall versus time for the sixty-hertz motor is plotted in Figure 6.10 with the comparison of only the stator winding and rotor temperatures in Figure 6.11. In order to attain steady state results at this speed without exceeding the maximum temperature that the stator windings can withstand, the input voltages were reduced by about sixty-five percent. The temperature in the stator windings and rotor differs only slightly. The approximation of equal stator and rotor temperatures made in the voltage and current driven torque calculations using the lumped models and FEA methods is thereby validated.

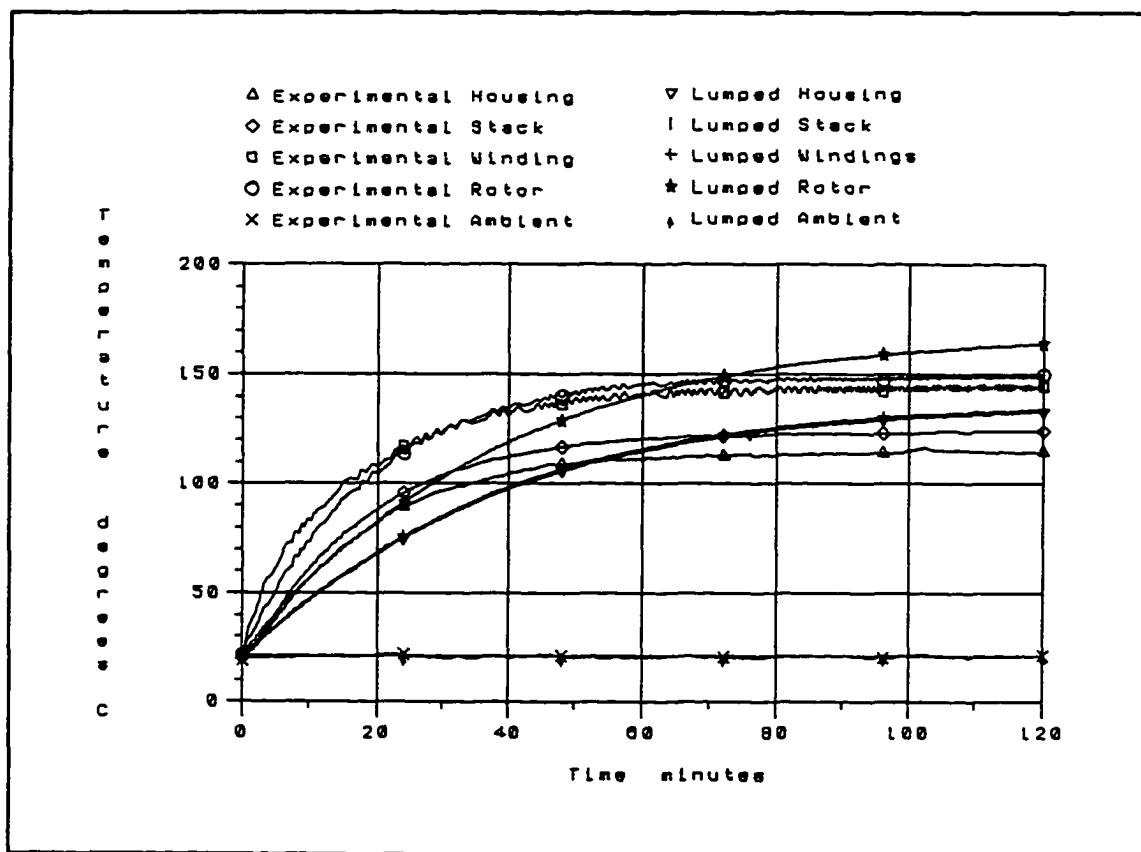**Figure 6.10** Comparison of transient temperature at stall versus time for the sixty-hertz motor.

The calculated temperatures are compared with experimental results. Errors at steady state are within ten percent for the stator winding, stator stack, and rotor temperatures. For the housing temperature, error at steady state is about fifteen percent. Estimation errors of transient temperatures are larger.

-129-

Figure 6.11 Comparison of transient temperature at stall versus time for the sixty-hertz motor.

Temperature estimation error is primarily due to the convection heat transfer coefficient and the shaft protrusion. Determining the convection heat transfer coefficient is difficult because it requires an empirical model. The shaft protruding from the rotor back iron and fans protruding from rotor end rings allow for more heat flow. Additional error is introduced from heat sources in the lumped thermal model that are kept constant at their steady state values. Also, the lumped thermal model may not be complete in analyzing all the significant processes of heat transfer in all the critical regions of the motor.

Heat transfer from the shaft protrusion by itself is usually small relative to the housing. However, in the experimental configuration of Figure 6.1, the induction motor shaft is coupled to the torquemeter, thereby creating a significant thermal path. In this case, heat dissipated out from the rotor through the shaft may be significant, resulting in dramatically reduced rotor temperature and smaller errors.

VI.F. Summary

Despite the complex models required to attain acceptable errors, induction motor torque and

-130-

temperature have been estimated with reasonable accuracy from the lumped models and FEA methods. Torque is calculated and compared with experimental results for two commercial polyphase induction motors. Temperature is calculated at stall for one of the motors and compared to experimental results.

Over the practical region of the torque-speed curve, errors in voltage and current driven torques from the lumped models and FEA methods are within fifteen percent for both motors. For the four-hundred-hertz motor, current driven torque errors in the FEA method are much larger than fifteen percent because of the difficulty in modelling three-dimensional leakage flux. Also, the windings in the mesh may need to be better distributed in the slots. Since voltage driven torque has been calculated from the FEA method to within fifteen percent for this motor, the calculated input impedance must be low resulting in large stator currents.

Torque estimation error is primarily due to harmonics in the flux density distribution. The concentric windings of the four-hundred-hertz motor contain just one tier causing harmonics. Additional error in the FEA methods is due to three-dimensional effects. Any error in deriving these effects from the lumped models causes error in not only the lumped models but the FEA methods as well. Also, the assumption made to include rotor three-dimensional leakage flux in only the stator currents and not the rotor currents results in some error.

Stator resistance, which affects only the voltage driven torque, is calculated from the lumped electrical model and compared with measurements. Any error in estimating stator currents, which are affected by the resistance, causes error in the voltage driven torque that is squared. The resistance is low by ten percent for the sixty-hertz motor and a quarter percent for the four-hundred-hertz motor. The error is due to the approximated length of wire in the end turns. This error causes the torque from the lumped models and FEA methods to be slightly high.

The transient temperature is determined at stall for one of the motors from the lumped thermal model and compared to experimental results. Errors at steady state are within ten percent for the stator winding, stator stack, and rotor temperatures. For the housing temperature, error at steady state is about fifteen percent. Estimation errors of tra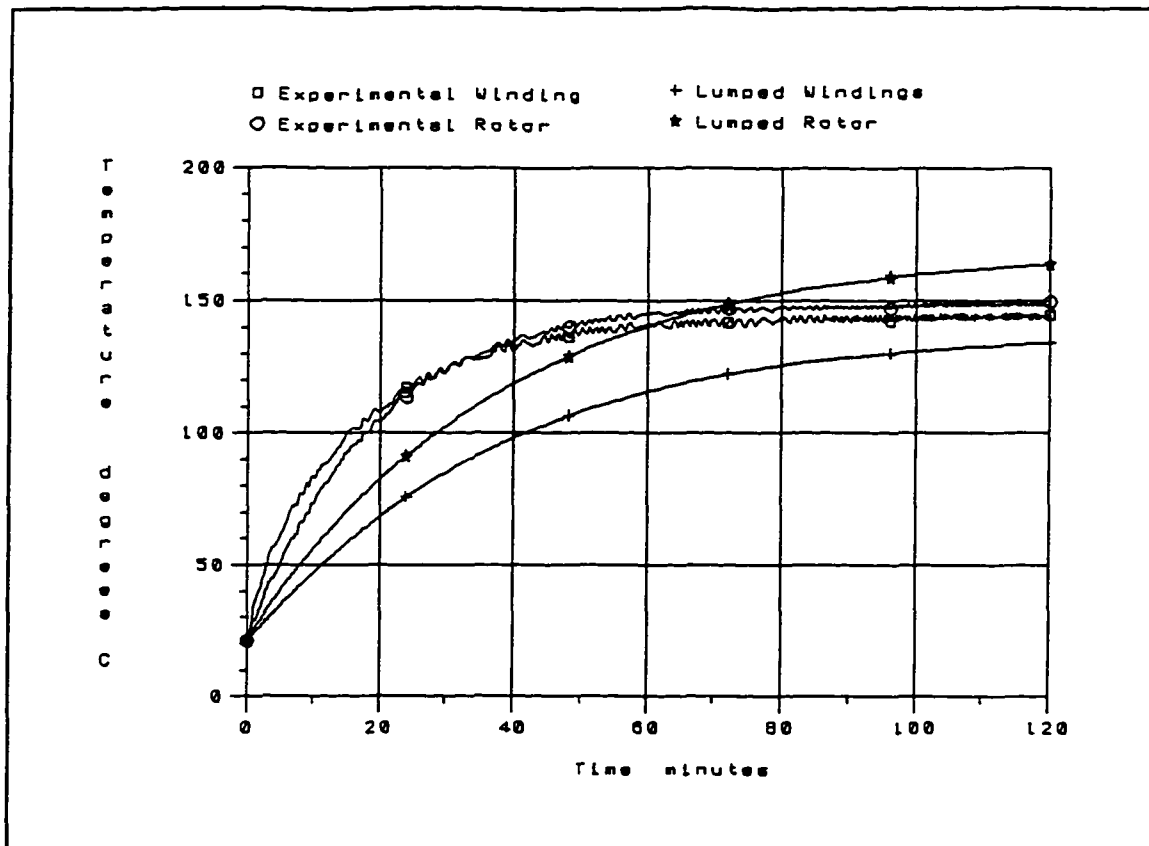nsient temperatures are larger. Error is primarily due to the difficulty in determining the convection heat transfer coefficient, and not considering heat dissipated out

-131-

from the rotor through the shaft. The shaft is coupled to the torquemeter, thereby creating a significant thermal path.

-132-

CHAPTER VII

DESIGN MODEL

VII.A. Introduction

In the analysis of the induction motor, the relationships from basic motor variables to motor performance are derived from the lumped magnetic, electrical, and thermal models. In the design of the induction motor, the motor geometry and winding scheme that result in the required performance are determined. The design model incorporates the lumped magnetic and electrical models.

To design the voltage driven induction motor, an iterative model is developed. After necessary inputs are provided, the design model iterates around specified ranges of main motor dimensions. In each permutation, slot dimensions are designed. For feasible designs, performance is determined and compared with desired requirements.

To verify the design model, two motors with known performance are used. Calculated performance is compared with experimental results. The model is then utilized to design an induction motor for desired requirements. The motor is fabricated and calculated performance is again compared with experimental results.

VII.B. Development of the Design Model

Designing the induction motor is an underconstrained process. Dependent variables such as motor geometry and material properties severely outnumber the independent variables such as performance requirements. Therefore, an iterative design model is developed for the voltage driven induction motor with a squirrel cage rotor. The model for the current driven motor is just a simplified version of this model. The model includes magnetic, electrical, thermal, and mechanical considerations.

The traditional design approach, briefly described in Appendix A, relies on empirical data from existing motors and the equivalent circuit model. However, designing motors outside the range of empirical data through extrapolation may cause large errors. The iterative design model is based on the

-133-

analytically derived lumped models which are reliable over a wide range of parameters.

Figure 7.1 presents the flow diagram of the iterative design model. Computer software was written to automate this process. Necessary inputs such as power supply specifications, design requirements, iteration variables, and performance requirements are first provided. The model iterates around specified ranges of the iteration variables. In each permutation, motor dimensions are designed to attain desired flux density levels in critical regions of the motor. For magnetically feasible designs, performance is determined from the lumped magnetic and electrical models. Designs that meet desired mechanical and physical limitations as well as satisfy performance requirements are compared for the optimal solution of a given application.

VII.C. Design Model Inputs

In the design model, inputs which remain constant throughout the iterations are first provided. The design inputs are arranged into seven categories labelled power supply specifications, excitation scheme, rotor configuration, design requirements, iteration variables, flux density levels, and performance requirements. The individual categories are explained in the following sections. The described effects of the inputs on performance are approximated using the lumped models and neglecting magnetic saturation as well as hysteresis and eddy current losses. From these design inputs, motor dimensions are designed and motor performance is evaluated.

VII.C.1. Power Supply Specifications

Power supply specifications describe the available voltage supply used to energize the designed motor. They comprise input voltage amplitude, excitation frequency, and number of stator phases. To reduce harmful harmonics in the air gap flux density distributions, the sinusoidal excitation is balanced in time and space.

Input voltage dramatically affects performance. Torque, resistive power losses, and horsepower are proportional to the square of the input voltage amplitude. But, power factor and efficiency are independent of the amplitude. Also, increasing the number of stator phases increases both torque and efficiency.
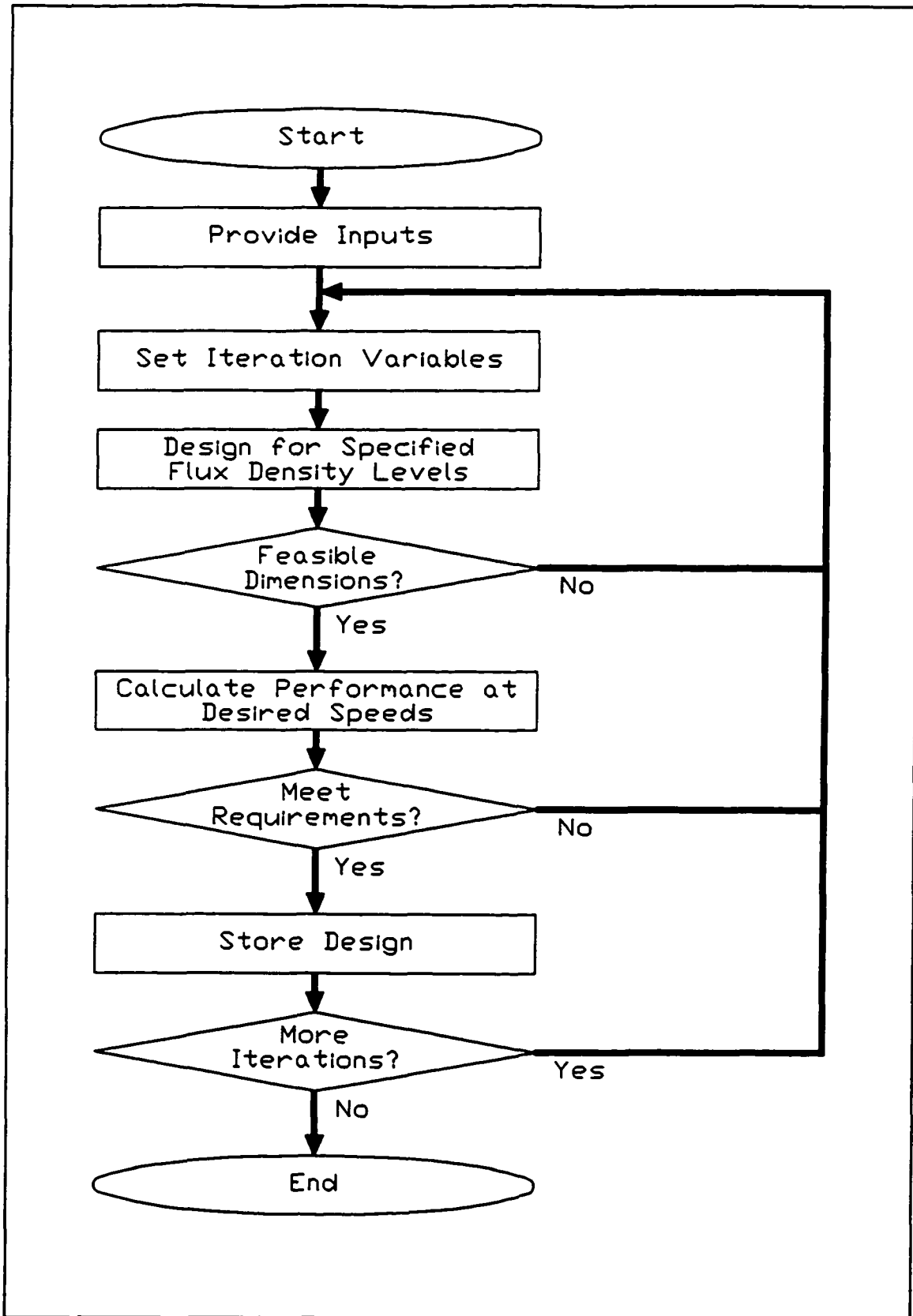
-134-

Figure 7.1 Flow diagram of iterative design model.

-135-

Induction motors typically operate from either single-phase excitation or polyphase excitation. The former is common for most fractional horsepower applications, while the latter is common for most integral horsepower applications. With single-phase excitation, additional starting mechanisms are required because no inherent starting torque is produced. With polyphase excitation, no starting mechanisms are necessary and operation is more efficient, but cost is generally higher. Also, polyphase excitation, whose windings demand more patience to insert, requires more slots for windings or larger slot fill percentage.

VII.C.2. Excitation Scheme

Excitation scheme describes the strategy by which the input voltage is applied to energize the designed motor. These inputs comprise number of poles, maximum fill factor, number of stator slots, and winding configuration. The pole count is usually selected to yield the slowest synchronous speed that still exceeds the desired operating speed. Synchronous speed equals excitation frequency divided by the number of pole pairs. It is generally desired for the induction motor to operate near synchronous speed because heat generation typically increases as slip frequency increases. Most voltage driven motors operate near synchronous speed also for high power factor and efficiency as well as to avoid stalling.

In the voltage driven motor, winding the stator with small wire sizes, or large diameter wires, for a fixed number of winding turns, boosts torque and efficiency even more while usually generating even less heat. But, fill factor increases. Fill factor designates the fill percentage of wire in the slot that carries the most number of wires. It equals the ratio of total wire cross-sectional area including insulation to slot cross-sectional area excluding slot liners. Slot liners usually of standard thicknesses pad the stator slots to protect the windings. Winding difficulties may accompany fill factors greater than fifty percent. Therefore, designs are wound with the thickest possible wire determined from the number of winding turns, maximum fill factor, and slot geometry.

With fill factor specified, specifying wire size becomes unnecessary. Otherwise, another iteration variable can be created for the wire size. Motors wound with various wire sizes would be designed, but at the expense of dramatically increased computing time. The additional iterations are not needed because fill is always set at the largest practical value for the most efficient use of stator slots.

The highest wire count per slot that is used to determine fill depends on the winding configuration.

-136-

Concentric windings are commonly used to decrease harmonics in the air gap flux density distributions. Only the fundamental produces useful torque, while harmonics cause vibration, noise, and heat. Long tooth ears, corresponding to narrow slot mouths, also improve the flux density distributions, but mouth openings must be adequate for winding insertion. Steel ears that tangentially protrude at the tooth tips dampen slotting effects by redistributing flux more evenly across the air gap.

To support a sufficient number of concentric winding tiers, enough stator slots must exist. Utilizing many tiers leads to flux density distributions that are more sinusoidal, but also requires many slots. The ideal percentage allocation of winding turns in each tier has been theorized to minimize harmonics in the air gap flux density distributions.[46] Coils of each tier are inserted into two slots per pole. Having many slots causes high slot leakage flux and low torque at rated speed. It is also more burdensome to wind many tiers. To reduce the slot count, slots can be shared between outer tiers of adjacent poles or among tiers of different phases. However, this multi-layer technique sacrifices wire thickness since fill factor is kept constant.

Using many wide slots to support thick wires causes narrow teeth and saturation in the teeth from high flux density levels. To avoid this while keeping fill factor constant, thinner wires can be used in smaller slots. But, torque and efficiency decrease and heat generation usually increases.

VII.C.3. Rotor Configuration

The induction motor rotor is either wound with copper wires like the stator or has a squirrel cage construction. Wound rotors are normally for large horsepower applications because of the wire cost advantage. Small motors utilize the squirrel cage rotors. The squirrel cage contains bars and end rings that are customarily composed of the same material.

The design model considers only the squirrel cage rotor, although designing the wound rotor is similar. Rotor configuration inputs comprise rotor squirrel cage material, number of rotor slots, and rotor skew. Selecting rotor slot count presents the same dilemma as selecting the stator slot count. A high slot count allows for air gap flux density distributions that are more sinusoidal, but decreases torque at rated

---

[46]W. R. Appleman, "The Cause and Elimination of Noise in Small Motors," *Electrical Engineering*, November, 1937, pp. 1359-1367.

speed from higher slot leakage flux and more skin effects. In addition, some combinations of stator and rotor slot counts produce exceptionally large harmonics. General rules of thumb for favorable slot count combinations are published.[47]

The rotor is ordinarily skewed to further reduce harmonics in the rotor air gap flux density distribution despite causing some slight torque disturbance and increase in leakage flux. Skewing is performed before rotor bars are inserted or cast in a mold. An ideal skew is formulated that theoretically diminishes the third harmonic which is usually the worst offender.[48]

VII.C.4. Design Requirements

Design requirements dictate conditions under which, and parameters within which, motors are designed. The requirements comprise temperature at desired rotor speeds and stall in addition to dimension ratio limits. The temperature in the stator windings and rotor bars is used to evaluate resistances. The temperatures are specified instead of calculated from the lumped thermal model because they are commonly known. The stator temperature can be specified as the maximum temperature that the stator windings can withstand. The rotor temperature at stall is necessary to design for end ring thickness. If desired, the lumped thermal model can be included to determine the steady state temperatures in calculating performance.

Two different dimension ratio limits help to ensure robustness of the motor designs for practical considerations. One ratio pertains to the motor overall dimensions and the other pertains to the stator tooth dimensions. The ratio of stack height to stator outer diameter must fall within a specified range to reject motors that are abnormally fat and short or thin and long. In the latter, balance complications and vibration problems may arise.

For the other dimension limit, the length to width ratio of stator teeth must not exceed a specified maximum to reduce structural weaknesses and manufacturing hardships. Winding around teeth that are

---

[47]Cyril G. Veinott, *Theory and Design of Small Induction Motors*, New York: McGraw-Hill Book Company, Inc., 1959, p. 391.

[48]"The Effect of Harmonics on Induction Motor Performance," Eastern Air Devices, Incorporated, Dover, New Hampshire, Internal Report.

-138-

long and narrow is difficult because they may bend. A maximum dimension ratio for rotor teeth is unnecessary due to the squirrel cage construction. The teeth are supported on both sides by bars and are sandwiched at the axial ends by end rings.

VII.C.5. Iteration Variables

The design model ranges through four iteration variables in search of valid designs. The variables consist of stack height, stator outer diameter, stator inner diameter, and air gap length. Their maximum and minimum values along with their step increments are specified. These inputs represent the main motor geometry from which slot dimensions are designed.

Due to the iterative nature of the design model, significant computing time may be required. The total number of permutations taken is equal to the product of the four step increment counts. In order to gain just ten times the resolution, the permutation count increases ten thousand times. To conserve time, large iteration increments can initially be taken followed by smaller ones around the better designs. This can be repeated until iteration increments are satisfactorily small.

It is unnecessary to iterate around the rotor inner diameter. Since a small diameter leads to lower rotor back iron flux density and lower heat generation, it is set to the motor shaft diameter. The shaft must exceed a minimum diameter to withstand the mechanical sheering force at breakdown torque.

Stator and rotor stack heights are usually almost identical for low end leakage flux and high air gap flux. Air gap flux produces useful torque from tangential force, while end leakage flux produces a harmful radial force. Unequal stack heights provide no advantage anyway.

The iteration variables do affect performance. Motors with a large stator outer diameter dissipate more heat because of the large outer surface area, but also weigh more and take up more volume. A small stator inner diameter supports more copper in the slots by allowing for larger diameter wires or more winding turns at a constant fill factor. However, stator tooth length is extended causing increased structural stress.

A large air gap reduces flux across it resulting in reduced current driven torque. But for the voltage driven motor, stator currents increase resulting in increased torque. However, efficiency decreases due to high heat generation. A small air gap, on the other hand, leads to reduced heat generation, but

-139-

demands tighter manufacturing tolerances.

VII.C.6. Flux Density Levels

The iteration variables are used to design for specified maximum flux density levels in the stator and rotor back irons and teeth. Designs with low flux density, due to low flux, produce low torques, while designs with low flux density due to large cross-sectional area in the steel are oversized. High flux density, on the other hand, results in high torque per motor volume, but also high eddy current losses in the steel. However, saturation must be avoided because it causes harmonics in the air gap flux density distributions. For large torque from a small motor volume without significant harmonics, flux density levels in the steel are generally designed just shy of saturation.

To design for flux density levels in the steel, the number of stator winding turns is needed. The number of turns is determined by specifying the maximum air gap flux density. For low horsepower applications, this flux density can be set between a quarter and one tesla. Increasing winding turns of a fixed wire size leads to higher input impedance and lower stator currents. Torque decreases as well as heat generation, but efficiency increases. Efficiency increases even when stator slot copper cross-sectional area is kept constant by increasing the number of turns with a decrease in the cross-sectional area per wire. The percentage decline in input power surpasses the percentage decline in torque.

VII.C.7. Performance Requirements

Designs of all the permutations that meet performance requirements are saved. The requirements can be specified as minimum horsepower or torque, maximum allowed heat generation, minimum efficiency, and minimum power factor at the operating speed. In addition, minimum stall torque is specified. A large stall torque for starting a loaded motor results in higher heat generation. The maximum allowable heat generation is related to the ability of a motor to dissipate heat. Motors with a high minimum efficiency and power factor operate more economically. When the minimum power factor is unattainable, however, external capacitors can be used for power factor correction. But, the capacitors may physically be quite large in order to withstand the input power.

VII.D. Design of the Induction Motor

-140-

With all the design inputs specified, the design software searches through all permutations. For each permutation, the number of stator winding turns along with stator and rotor slot dimensions are designed to meet specified flux density levels. Also, the stator winding wire thickness is designed for the specified fill factor and the end ring thickness is designed from the specified minimum stall torque. Designs that are magnetically feasible as well as meet design dimension ratio limits and satisfy performance requirements are stored.

To design for flux density levels at the operating speed, flux from the stator and rotor currents must first be known. The rotor currents result purely from induction and are a function of the stator currents as well as geometric dimensions, material properties, and slip frequency. Material properties and desired rotor speed are usually known. But, without geometric dimensions which are designed from the flux density, rotor currents are unknown.

An iterative process can be used where the rotor currents at the operating speed are first determined from initial geometric dimensions. Then, the dimensions are adjusted using the flux density calculated from the rotor currents. The iterative process continues until the change in the dimensions is within an acceptable margin. Computing time is extremely long.

With a conservative approximation, the iterative process becomes unnecessary and computing time is reduced. The geometric dimensions are instead designed at the maximum flux density levels determined from the maximum air gap flux. For most practical current and voltage driven motors, this maximum flux occurs at synchronous speed where no rotor currents are induced. Since the operating speed is typically near synchronous speed, this approximation does not introduce much error.

Before the maximum air gap flux can be calculated, the number of stator winding turns must first be solved. The number of turns is designed from the specified maximum flux density in the air gap. The maximum flux is then used to design stator and rotor tooth dimensions for specified maximum flux density in the steel regions.

The number of stator winding turns is designed by formulating the maximum air gap flux density from the maximum flux:

-141-

$$B_g^{max} = \frac{\pi}{2} \frac{n\phi^{max}}{\pi(D_{si}-l_g)z}$$

VII-1

where:

B_g^{max} = maximum air gap flux density per pole

Since the flux density distribution has been assumed sinusoidal, the constant $\pi/2$ is utilized. It was used to scale the air gap reluctance in Figure 2.5 in order to take the lumped magnetic model approach for a sinusoidal flux density distribution instead of a uniform distribution. Maximum air gap flux density is formulated by first dividing ϕ^{max} by the air gap cross-sectional area over a pole to arrive at the amplitude of the uniform distribution. Then, that amplitude is scaled by $\pi/2$ to arrive at the amplitude of the sinusoidal distribution.

With the cross-sectional area in the air gap known, the number of winding turns is designed to yield the flux that results in the specified air gap flux density. The necessary number of turns for the current driven motor is solved after substituting for ϕ^{max} from Equation II-8:

$$N_s = \frac{\frac{\pi}{4}\frac{l_g}{\mu_0}B_g^{max}}{\left| \sum_{k=1}^{n} i_s^k \cos\left(\frac{2\pi k}{m}\right) \right|}$$

VII-2

Since the winding distribution constant, K_d, and Carter's coefficient, K_c, are unknown for now, they are set to one. The necessary number of turns for the voltage driven motor is solved after substituting for ϕ^{max} from Equation II-9:

$$N_s = \frac{V_{in}}{2(D_{si}-l_g)z\omega_e B_g^{max}}$$

VII-3

Because the number of winding turns is an integer, N_s is rounded to the nearest integer. With the approximation from rounding, the actual air gap flux density may differ slightly from the specified value.

For simplicity, N_s remains constant throughout the permutations. Therefore, it is calculated from the average stack height, stator inner diameter, and air gap length over of all permutations. Since these quantities vary from one permutation to the next, the actual air gap flux density fluctuates around the

-142-

specified value. However, as the iteration ranges become smaller around the better designs, the fluctuation becomes smaller.

With the number of stator winding turns solved, the winding distribution constant is calculated. The maximum air gap flux per pole is then determined for the current driven motor from Equation II-8 and for the voltage driven motor from Equation II-9. Since the Carter's coefficient is still unknown at the moment, it is still set to one. This maximum flux is used only in designing for geometric dimensions and not used to directly calculate motor performance. In reality, the air gap flux at the operating speed is slightly less than this maximum flux because of rotor flux from induced rotor currents, leakage flux, K_d, and K_c. Also, stator resistive voltage drops along with hysteresis and eddy current losses in the steel absorb a fraction of the input voltages.

With the maximum air gap flux determined, stator and rotor back iron and tooth widths are designed for specified maximum flux density levels in the steel regions. The necessary stator and rotor back iron widths are determined by solving Equation II-10:

$$w_{sib} = \frac{\phi^{max}}{2 z B_{sib}^{max}}$$

$$w_{rib} = \frac{\phi^{max}}{2 z B_{rib}^{max}}$$

VII-4

The necessary stator and rotor steel tooth average widths are determined by solving Equation II-11:

$$w_{sit} = \frac{\pi}{2} \frac{n\phi^{max}}{S_r z B_{sit}^{max}}$$

$$w_{rit} = \frac{\pi}{2} \frac{n\phi^{max}}{S_r z B_{rit}^{max}}$$

VII-5

The teeth are designed for parallel sides to avoid localized saturation within the teeth.

The effects of some design inputs on performance at the operating speed near synchronous speed are shown in Table 7.1 where:

X   ≡ independent relationship
↑   ≡ increasing relationship
↓   ≡ decreasing relationship
?   ≡ relationship is highly sensitive to rated speed

-143-

Table 7.1 Effects of Increasing Some Design Inputs on Performance Near Synchronous Speed

	I_a	T	power factor	resistive power losses	P_h	horsepower	efficiency
V_{in}	↓	X	X	X	X	X	X
l_g	↑	↑	?	↑	↓	↑	↓
B_g^{max}	↑	↑	↑	↑	↑	↑	↓
B_{sb}^{max}	↑	↑	↓	?	↑	↑	↑
B_{st}^{max}	↑	↑	?	?	↑	↑	↑
B_{rb}^{max}	↓	↓	↓	↓	↑	↓	?
B_{rt}^{max}	↑	↑	↑	↑	?	↑	?

These are general trends for feasible designs as one input increases while holding all others constant. For example, as air gap length varies, the number of winding turns and slot dimensions also vary while input voltages, flux density levels, and main motor dimensions remain constant.

The trends help in specifying the design inputs. It may seem contrary that the input voltage amplitude does not affect performance except for the stator current amplitude. But, the number of winding turns varies with the input voltage causing stator resistance and flux linkages to also vary. Increasing air gap flux density increases currents, torque, and resistive heat losses, but decreases efficiency. Overall, it is beneficial to increase flux density in the stator back iron and tooth to support bigger slots and thicker wires if the increased eddy current losses in the steel are acceptable. Though, operating in saturation should be avoided. Overall, it is also beneficial to decrease flux density in the rotor back iron and increase it in the rotor tooth if the increased resistive heat losses are acceptable.

Before calculating performance, stator and rotor resistances are determined. The stator resistance is dependent on winding wire thickness. With the highest wire count per slot, slot dimensions, and standard slot liner thickness known, the wire thickness is designed for the specified fill factor and wire insulation thickness. The highest wire count is determined from the allocation of winding turns in each tier of the concentric windings.

-144-

The rotor resistance is dependent on end ring thickness. The end rings are designed from the specified minimum stall torque. A range of rotor resistances can be derived to obtain the specified stall torque. However, since Figure 3.3 shows that increasing rotor resistance reduces torque at the operating speed near synchronous speed, the smallest resistance is used to design for the end rings. As a result, the thickest end ring that meets the minimum stall torque is selected. The outer diameter of the end ring is commonly designed just slightly smaller than that of the rotor. The inner diameter can be designed just slightly larger than the shaft diameter.

Determining end ring thickness from the rotor resistance is complicated due to skin effects. The resistance is a function of these effects, and is not a simple function of the end ring thickness. An iterative process can be used. But, because skin effects are small unless excitation frequency is abnormally high and rotor bars and end rings are abnormally radially deep, they are neglected without much error in designing end ring thickness. These effects are included, however, in performance calculations. Consequently, the calculated stall torque may be slightly larger than the specified minimum stall torque because skin effects increase the rotor resistance.

VII.E. Analysis of the Induction Motor

With the excitation scheme, motor geometry, and material properties known for each permutation, performance for various magnetically feasible designs is calculated from the lumped magnetic and electrical models formulated in Chapter III. Designs that meet dimension ratio limits and satisfy performance requirements are saved for finer iteration increments. Performance characteristics such as torque, power factor, power losses, horsepower, and efficiency are calculated at many rotor speeds.

Some meaningful rotor speeds at which performance is determined include speeds at maximum current driven torque, breakdown torque, maximum power factor, and maximum efficiency. These speeds are found by setting the derivative of Equation III-39, Equation III-41, and Equation III-46 with respect to slip frequency equal to zero and solving. For maximum current driven torque, the stator current of Equation III-31 is substituted before taking the derivative. For breakdown torque, the input voltage of Equation III-30 is substituted before taking the derivative.

Performance is also calculated at stall and synchronous speed as well as speeds at specified

-145-

continuous and maximum torque or horsepower. Designs whose maximum torque or horsepower do not exceed the specified amount are discarded. Designs that generate more heat at the operating speed of continuous torque or horsepower than the specified maximum are also discarded.

Solving for the rotor speed at the specified torque or horsepower is complicated because of skin effects as well as hysteresis and eddy current losses in the steel. However, an iterative process is unnecessary because these effects and losses can be neglected in determining the speed. The skin effects are small unless slip frequency is abnormally high and rotor bars and end rings are abnormally radially deep. Hysteresis and eddy current losses tend to be small unless excitation frequency is high and operation is near synchronous speed. Laminations are coated with insulation anyway to decrease the eddy currents in the steel. Therefore, the speed at the specified torque or horsepower may be slightly in error, but performance calculations there incorporate skin effects as well as hysteresis and eddy current losses.

Performance is determined from the lumped magnetic and electrical models using Equation III-39 and Equation III-41 through Equation III-46. The stator and rotor resistances are evaluated at the specified temperatures. Also, friction is ignored because it is usually small.

VII.F. Design Model Verification

To verify performance calculations in the design model, the two EAD motors whose experimental results are shown in the previous chapter are used. Design inputs that result in the actual excitation scheme and motor dimensions are provided. Torque is determined and compared with experimental results.

Most of the design inputs are directly retrieved from the existing motors. Others require some calculations. Air gap flux density is specified by using Equation VII-3 for the voltage driven motors with known N_s. The maximum flux density levels in the steel regions are specified by using Equation VII-4 and Equation VII-5 with known lamination dimensions and stack height. Fill factor is specified with known slot dimensions, wire thickness, wire insulation, and the highest wire count per slot. Stall torque is specified to result in the actual end ring thickness.

After all the design inputs are provided, performance is determined. One iteration is made for each motor around the actual axial height, stator outer diameter, stator inner diameter, and air gap length. The temperature in the stator windings and rotor bars are specified by the temperature at which the

-146-

experimental results were collected. Torque calculated by the design model is identical to that by the lumped models in Figure 6.2 and Figure 6.3.

VII.G. The Prototype Design

With the performance calculations verified, the model is applied to design an induction motor, given the necessary requirements. The motor is designed to have performance characteristics for vector control. The motor was fabricated and experimental results were collected with a current supply. The results are compared with the calculated performance from the design model and FEA method.

Motors driven by vector control, briefly described in Appendix B, have a high maximum torque and low stall torque. The latter is achieved by a low rotor resistance which results in a high torque at the operating speed near synchronous speed. These motors are designed to always operate at the maximum torque. It is unnecessary to avoid the unstable region of the torque-speed curve because vector control ensures optimal output even under changing load conditions. Overloading occurs only when the maximum supply current is exceeded.

Although the motor is designed for vector control, the input voltage is limited. Enough voltage must be available to provide the necessary stator currents especially near synchronous speed where input impedance is usually the highest. Therefore, the design model that is developed for the voltage driven motor can be used here to design for performance at the operating speed near synchronous speed with the maximum input voltage.

After all the design inputs are specified, the iterative design software searches through all permutations of the stack height, stator outer diameter, stator inner diameter, and air gap length. For each permutation, the number of stator winding turns, slot dimensions, stator winding wire thickness, and the end ring thickness is designed. From all the feasible designs that satisfy the performance requirements, the one with the smallest volume that can still withstand the heat it generates is selected. Figure 7.2 shows the design inputs for the selected prototype motor. Figure 7.3 shows the motor dimensions of the design and performance estimations. After the motor was fabricated, experimental results were collected.

The experimental configuration for measuring torque and rotor speed is identical to the one used for the two EAD motors in Figure 6.1. However, the motor is driven from a current supply rather than

-147-

```
$ RUN DESIGN

(L)umped model, (A)nalysis, or (D)esign of induction motors = D
Unit of measure in English or Metric System using (F)oot, (I)nch, (M)eter, or (C)entimeter = I
Minimum stall torque (oz-in) = 250
Continuous and peak output (T)orque (oz-in) or (H)orsepower (hp) = 400 450 T
Maximum amount of heat dissipation (W) = 250

At stall the motor is assumed to be at half the hot temperature rise.
Ambient and maximum rated temperatures (degrees Celsius) = 120 120
Input voltage (V rms), frequency (Hz), and number of phases = 108. 71.5 3
Number of magnetic poles = 2
Stack length minimum, maximum, and increment (in) = 4.2 4.2 .001
Stator OD minimum, maximum, and increment (in) = 5. 5. .001
Stator ID minimum, maximum, and increment (in) = 2.5 2.5 .001
Air gap length minimum, maximum, and increment (in) = .035 .035 .0005
Rotor magnetic ID (in) = .625
Rotor end-ring ID or shaft OD (in) = .67
Number of stator and rotor slots = 18 23
Input total stator winding turns per phase per pole (T) or magnetic flux density in air gap (B) = B

Magnetic flux density in air gap, calculated from average stack length, stator ID, and air gap length,
    is approximated due to discretization in number of stator winding turns.
Peak magnetic flux density level (kilolines/in**2) in stator core, stator tooth,
    rotor core, rotor tooth, and air gap =
109.8141956 109.6484517 116.9449875 116.7692648 46.91250127
Number of stator concentric winding tiers = 3
Use standard ideal winding distributions (Y/N) = N

Total stator winding turns per phase per pole is 35
Number of stator winding turns per phase of tier 1 = 14
Number of stator winding turns per phase of tier 2 = 12
(S)ingle or (H)eavy stator winding wire insulation build = H

Fill factor is the cross-sectional ratio of copper area including insulation to slot area less slot liner.
Stator slot fill factor = .516702451
Maximum stator tooth length to width ratio = 8
(A)luminum, (B)rass, or (C)opper rotor squirrel-cage = C
Use standard ideal amount of circumferential rotor skew (Y/N) = N
Amount of circumferential rotor skew (in) = .4018
Also print designs with lower stator core density (Y/N) = Y
Print impractical design error messages (Y/N) = Y
Print impractical performance error messages (Y/N) = Y
Print (H)ighlight or (G)raph data = H
```

Figure 7.2 Inputs of iterative design software for the prototype motor.

a voltage supply. Also, since the torque produced here is much higher, a torquemeter that has a range of 1600 ounce-inches and a maximum speed of fifteen thousand revolutions per minute is used instead. This torquemeter, however, has the same nonlinearity and nonrepeatability percentage tolerances as the 160 ounce-inches torquemeter.

The current supply for the induction motor was set at 9.12 rms amperes. Unfortunately, measurements in the current amplitude of the three phases differed by ten percent from the average of the phases. This imbalanced excitation causes unfavorable harmonics. To compensate for this, three torques

-148-

		speed (rpm)	h.p.	torque (oz-in)	eff.	p.f.	loss (W)	Ri**2 (W)	i_in (A rms)
Rated_c	=	4241.93	1.568	372.75	0.9004	0.4744	109.86	092.15	9.12
Rated_m	=	4217.84	1.871	447.28	0.9126	0.6240	116.76	102.35	9.12
Synch	=	4290.00	0.000	000.00	0.0000	0.0267	100.80	079.28	9.12
Eff_max	=	4228.41	1.734	413.42	0.9082	0.5587	113.03	097.51	9.12
T_I_max	=	4210.29	1.890	452.63	0.9130	0.6573	118.35	105.05	9.12
PF_max	=	4016.92	0.980	246.05	0.8439	0.8484	129.59	126.99	9.12
T_V_max	=	3514.14	0.325	093.23	0.6434	0.7299	131.10	130.57	9.12
Stall	=	0000.00	0.000	019.67	0.0000	0.4034	139.18	138.99	9.12

Volume, Z, D_so, D_si, gap = 82.466807 4.200000 5.000000 2.500000 0.035000
d_ss, w_st, d_rs, w_rt = 0.635000 0.215000 0.325000 0.158000
D_w, th_end_ring, R_s, R_r (dc) = 0.067900 0.800000 0.317715 2.541E-04
L_s, L_sg, L_r, L_rg = 2.844E-02 4.510E-04 3.045E-05 1.729E-03
d/w_s,d/w_r,gap_leakage = 2.953488 2.056962 1.052366 1.055486
Peak magnetic flux density level (kilolines/in**2) in stator core, stator tooth,
    rotor core, rotor tooth, and air gap = 96.404879 96.259374 99.866282 99.716222 46.815723

Figure 7.3 Outputs of iterative design software for the prototype motor.

are measured by individually setting the stator current in each phase to 9.12 rms amperes and the average is used to approximate the torque produced from balanced excitation.

Current driven torque versus rotor speed for the motor is plotted in Figure 7.4 with an exploded view near synchronous speed in Figure 7.5. Torque measured experimentally is depicted by the line with circles, torque from the design model is depicted by the line with squares, and torque from the FEA is depicted by the line with triangles. The measured torque remained constant over time at any rotor speed even though symmetry from an integral number of rotor phases does not exist. Because enough rotor bars exist, any torque ripple from the nonsymmetry is small. Friction is negligible at one ounce-inch.

Only the faster second FEA method, the power difference method, is used for the prototype motor because the two FEA methods described in sections V.C and V.D yield almost identical results. Figure 7.6 and Figure 7.7 show the outline and mesh used in the FEA method. The magnetic field at the maximum torque is plotted in Figure 7.8. At this high operating speed of less than two percent slip, the highest flux density levels occur in the ears of the stator and rotor teeth where flux flowing in opposite directions merge and emerge. Flux density levels in critical regions of the motor are expectedly slightly less than the specified maximum levels for the design. This is because rotor flux, leakage flux, stator resistive voltage drops, and hysteresis and eddy current losses in the steel were neglected in designing for the flux density levels.
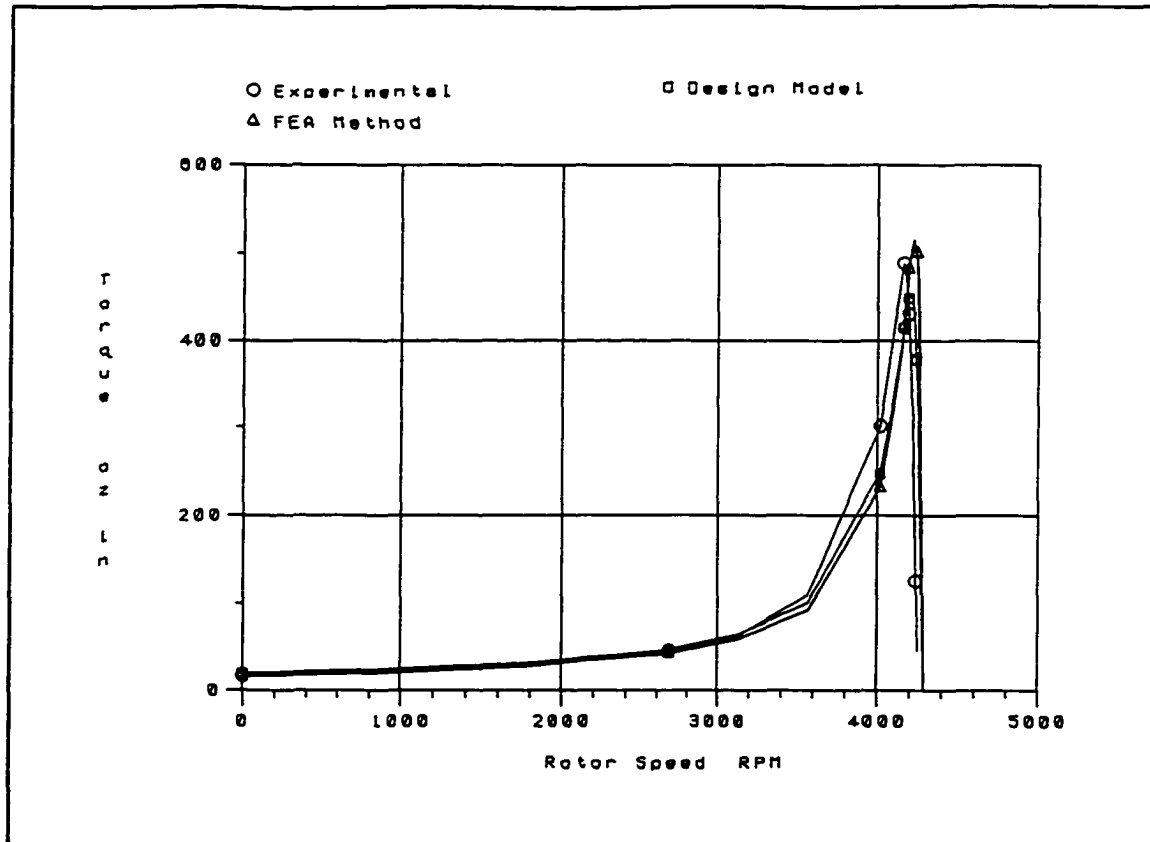
-149-

Figure 7.4 Comparison of current driven torque versus rotor speed for the prototype motor.

Errors in the design model are within fifteen percent except near synchronous speed, less than seven percent slip, where excitation frequency is critical and near stall, more than seventy-seven percent slip, due to extrapolation of hysteresis and eddy current losses by the empirical model. Errors in the FEA method are within fifteen percent except near synchronous speed, less than seven percent slip. However, the error in the maximum torque from the design model and FEA method is only around seven percent. Therefore, if the excitation frequency from the current supply can be measured more accurately, the torque errors may be even smaller over the entire torque-speed curve.

VII.H. Summary

In the design of the induction motor, the motor geometry and winding scheme that result in the required motor performance are determined. An iterative design model is developed for the voltage driven induction motor with a squirrel cage rotor. Magnetic, electrical, thermal, and mechanical considerations are all included. The traditional design approach relies on empirical data from existing motors and the
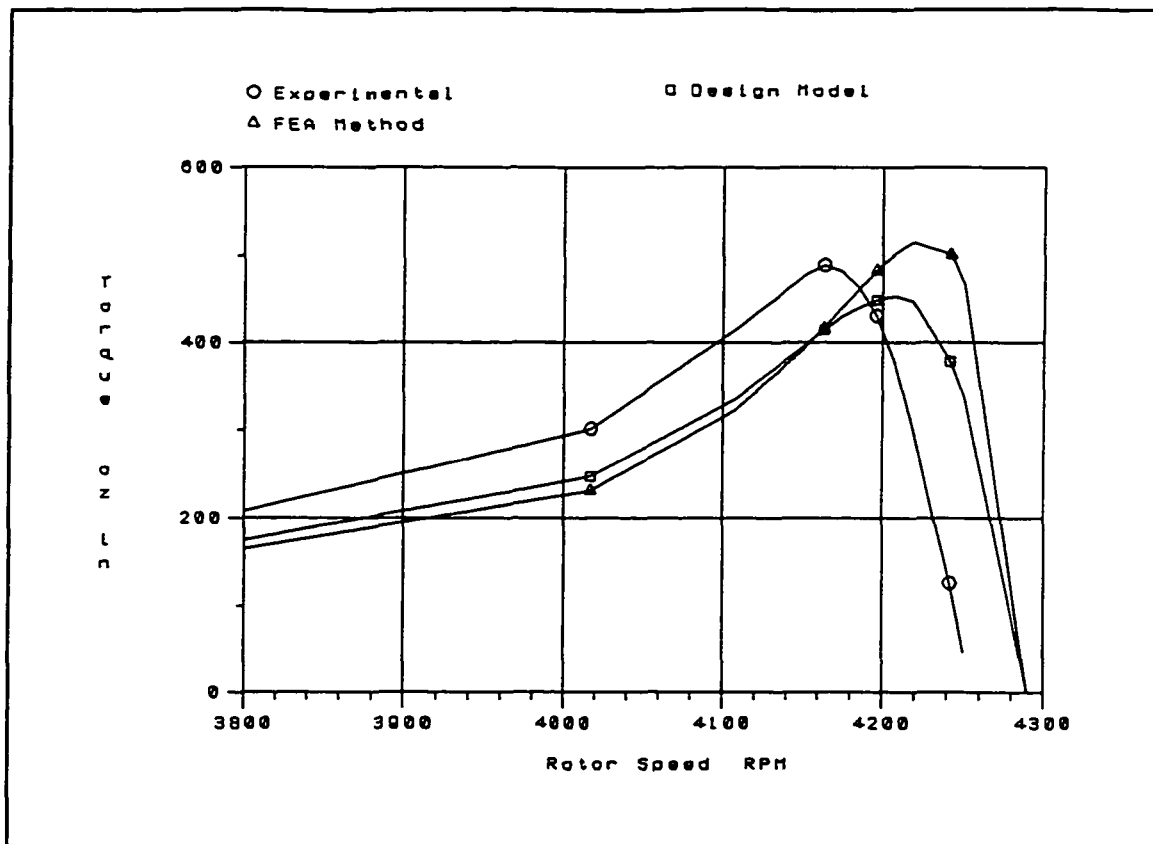
-150-

Figure 7.5 Comparison of current driven torque versus rotor speed for the prototype motor.

equivalent circuit model. However, designing motors outside the range of empirical data through extrapolation may cause large errors. The iterative design model is based on the analytically derived lumped models that are reliable over a wide range of parameters.

In the design model, necessary inputs are first provided. The model iterates around specified ranges of main motor dimensions. In each permutation, slot dimensions are designed to attain desired flux density levels. For magnetically feasible designs, performance is determined. Designs that satisfy desired requirements are compared for the optimal solution of a given application. To conserve computing time, large iteration increments can initially be taken followed by smaller ones around the better designs. Computer software that automates the design process was written to quickly obtain feasible designs. The FEA methods can then be used to gain more accuracy in performance estimations and to refine designs.

Design inputs are arranged into the following seven categories. Power supply specifications describe the available voltage supply. The excitation scheme describes the strategy by which input voltage is applied. Rotor configuration characterizes the squirrel cage. Design requirements comprise temperature
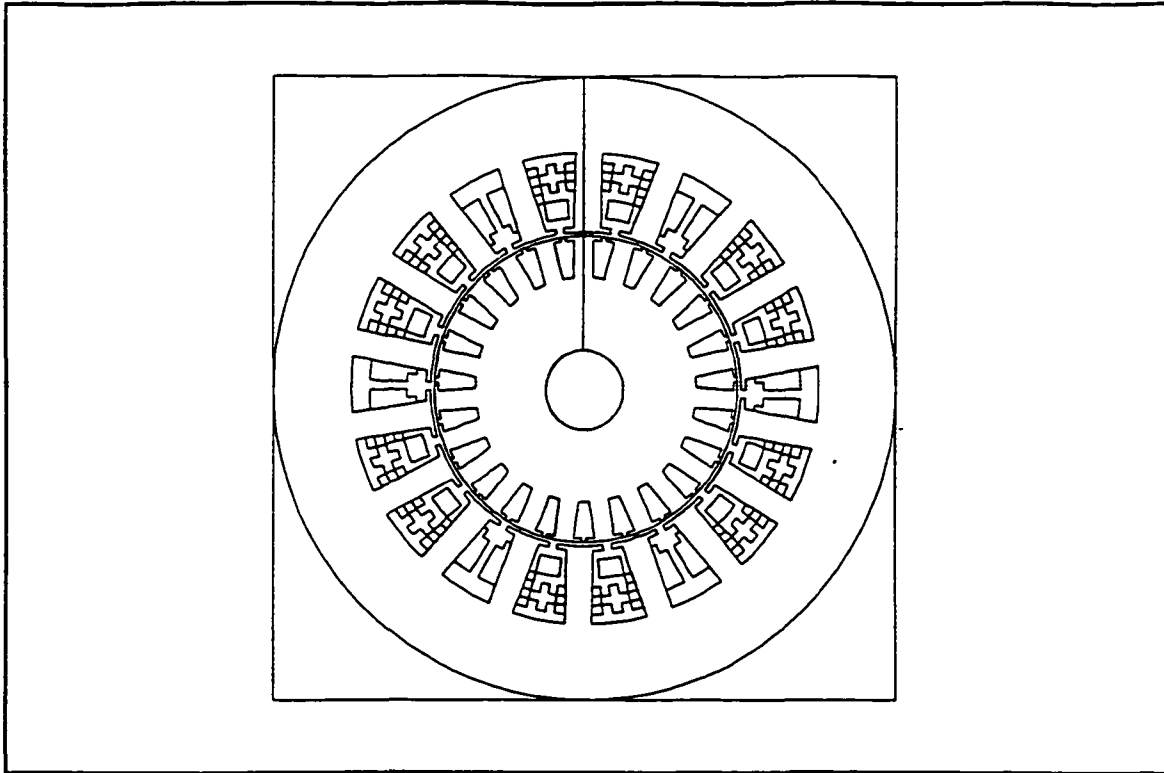
-151-

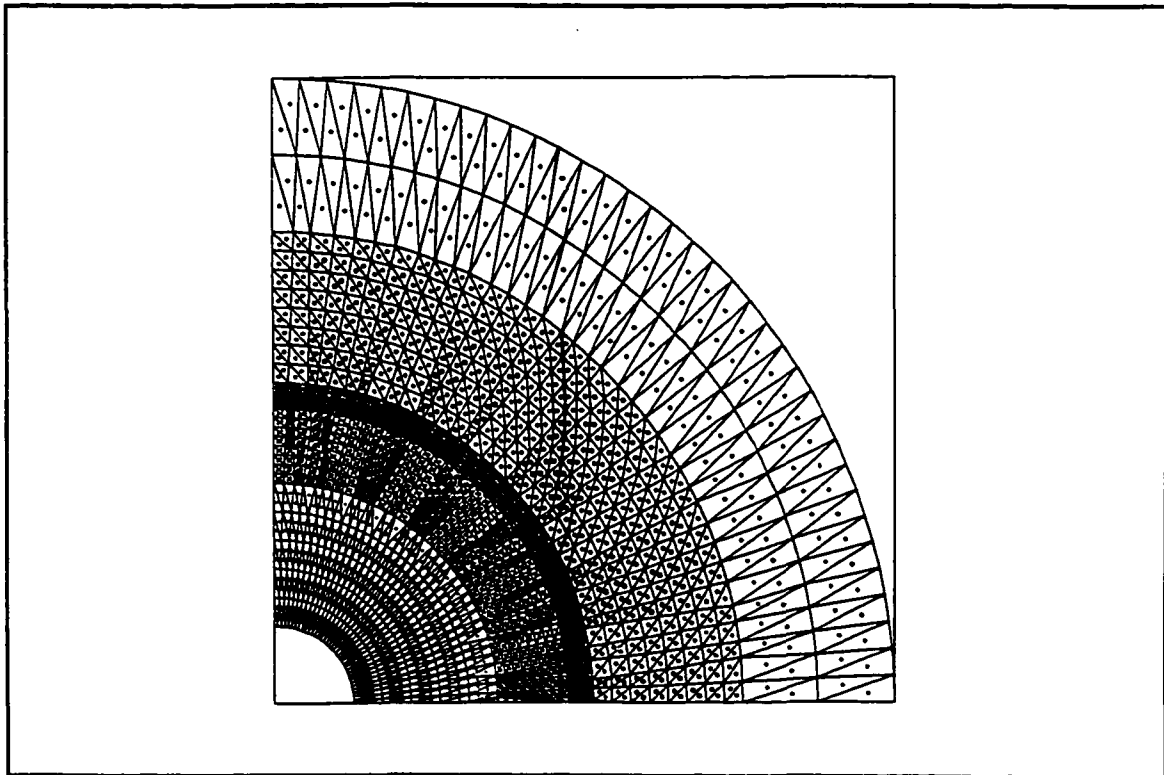**Figure 7.6** FEA mesh outline of cross section for the prototype motor.

Figure 7.7 FEA mesh of quarter cross section for the prototype motor.

Magnetic Vector Potential
Contours. (Flux)

Color: Flux density

Mesh limits:
Flux mx: 4.94 Tesla
A mx/mn: 20.83m. -20.87m

Frequency: 7.54   Hz
AC angle: 0.00< Deg

Δ A/MMF: 834.15u.   0.00
Contours: 50.00

2.00
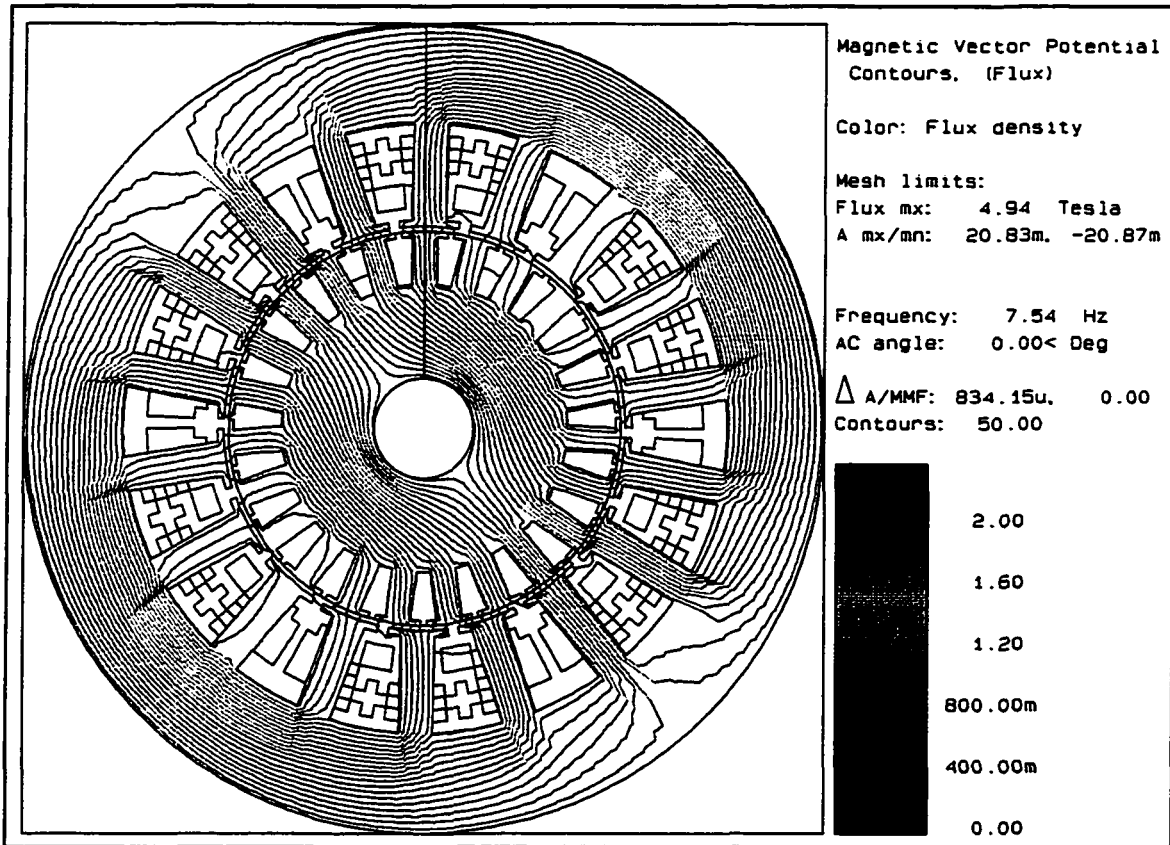
1.60

1.20

800.00m

400.00m

0.00

Figure 7.8 FEA magnetic field of cross section for the prototype motor.

at desired rotor speeds and stall in addition to dimension ratio limits. Four iteration variables consisting of main motor dimensions are ranged through. Specified flux density levels in critical regions are designed for. Performance requirements can be specified as minimum and maximum performance characteristics at the operating speed as well as minimum stall torque.

Performance characteristics comprising torque, power factor, power losses, horsepower, and efficiency are determined from the lumped magnetic and electrical models at many rotor speeds. Some meaningful speeds include those at some of the maximum performance characteristics, at stall, and at synchronous speed. Also, the speed at specified continuous and maximum torque or horsepower is included.

To verify the performance calculations in the design model, two motors with known performance are used. Torque calculated by the design model is identical to that by the lumped models. The model is then applied to design an induction motor for vector control, given the necessary requirements. The motor is fabricated and experimental results are collected with a current supply. The experimental results

are compared with performance estimations from the design model and FEA method. Torque estimation errors are within fifteen percent.

The iterative design model for the voltage driven motor is a basis upon which other application dependent models can be developed. Three major types of the induction motor are voltage driven, variable frequency motors, and current driven. For variable speed motors driven from the constant voltage and variable frequency supply, another iteration can be added around the excitation frequency. For motors driven by vector control, slight modifications are possible to design slot dimensions from stator currents instead of input voltages.

-154-

CHAPTER VIII

CONCLUSIONS AND SUGGESTIONS FOR FUTURE WORK

VIII.A. Conclusions

In order to analyze and design AC induction motors, the relationships of basic motor variables to motor performance must be known. In the traditional approach, a set of mathematical equations derived from the well-known equivalent "T" circuit model is developed to determine the relationships. The traditional design approach relies on empirical data and the equivalent circuit model. The traditional approach of modelling the induction motor using the FEA is through the equivalent circuit model. In these traditional approaches, however, the direct connection from geometry to performance is suppressed.

For better understanding of magnetic, electrical, and thermal behaviors, three new models based on actual motor geometry were developed that is similar to the equivalent circuit model. The lumped magnetic model describes flux behavior. The lumped electrical model is used to derive simple closed-form expressions of performance. The lumped thermal model describes the effect of heat generation on temperature in critical regions of the motor. Based on these lumped models, an iterative design model was developed to design motor geometry and winding scheme to meet given required performance. In addition, three new FEA methods were developed to calculate motor performance directly from the finite element field solution instead of through the equivalent circuit model.

The developed lumped models and FEA methods were applied to two commercial induction motors. Calculated performance was shown to closely match experimental results. The developed iterative design model was then utilized to design an induction motor for desired requirements. The motor was fabricated and calculated performance was also shown to closely match the experimental results.

The lumped magnetic model describes flux behavior in critical regions of the motor. Accurate magnetic modelling of the induction motor is more difficult than the permanent magnet motors. The latter is often represented by very simple magnetic models that contain only air gap flux. Leakage flux is neglected because it is relatively small. In the induction motor, the characteristically small air gap causes

-155-

MMF drops in the steel to be significant. Leakage flux is also significant in determining motor performance. Due to the difficulties of analytically modelling leakage flux, commonly applied approximate or empirical techniques were used.

The lumped electrical model is used to formulate performance characteristics from resistances and EMF voltages. The resistances are evaluated using the temperature information from the lumped thermal model. The rotor resistance must account for end ring resistance, which though seemingly relatively small, significantly affects motor performance. The EMF voltages in the lumped electrical model are induced by linkages with flux derived from the lumped magnetic model. Equations describing the developed lumped electrical model were shown to be identical to those describing the general equivalent circuit model.

Output performance characteristics derived from the lumped electrical model comprise voltage and current driven torques, power factor, power losses, horsepower, and efficiency. Induction motors are usually rated at low slips for high current driven torque, high power factor, low resistive heat losses, and high efficiency. Voltage driven motors operate at low slips to also avoid stalling.

Magnetic FEA is another important tool beside the lumped models for analyzing and designing electric motors. A two-dimensional static FEA solver is commonly sufficient to accurately model permanent magnet motors. For the induction motor, three-dimensional effects must be included. Three FEA methods were developed to calculate performance in the induction motor directly from the field solutions. These methods differ from the traditional approach of using a combination of the FEA and the equivalent circuit model.

The three developed FEA methods use two-dimensional FEA to calculate performance after incorporating three-dimensional effects. The first method uses a steady state harmonic solver followed by a static solver in calculating torque from the method of virtual work. The second method uses only a steady state solver to calculate torque from the conservation of instantaneous energy. The third method uses a transient solver. Performance calculations from the first two methods are almost identical. In the third method, solution convergence problems were encountered.

Voltage and current driven torques calculated from the lumped models and FEA methods were compared with experimental results for two commercial polyphase induction motors. Over the practical

-156-

region of the torque-speed curve, errors were within fifteen percent. For the four-hundred-hertz motor, current driven torque errors in the FEA method are much larger than fifteen percent. Torque estimation error is primarily due to harmonics in the flux density distribution. Additional error is due to the difficulty in modelling three-dimensional leakage flux. Also, the lumped magnetic and electrical models only consider motor sections carrying significant levels of flux and with significant current flow. It may be necessary to include additional flux paths and sources of current.

Transient temperature was also determined at stall for one of the motors from the lumped thermal model and compared to experimental results. Estimation errors at steady state were fifteen percent or less. The error is primarily due to the difficulty in determining the convection heat transfer coefficient, and not considering heat dissipated out from the rotor through the shaft. The shaft was coupled to the torquemeter, thereby creating a significant thermal path.

Despite the complex models required to attain acceptable errors, induction motor performance has been estimated with reasonable accuracy from the lumped models and FEA methods. The effect of specific motor parameters on performance can be quantitatively determined from the lumped models. Induction motors of different geometric dimensions and material properties can be compared.

An iterative design model was developed for the voltage driven induction motor. Magnetic, electrical, thermal, and mechanical considerations are all included. The traditional design approach relies on empirical data from existing motors and the equivalent circuit model. However, designing motors outside the range of empirical data through extrapolation may cause large errors. The iterative design model is based on the analytically derived lumped models that are reliable over a wide range of parameters.

The developed design model iterates around specified ranges of main motor dimensions to design slot dimensions for desired flux density levels. Designs that satisfy the given requirements are compared for the optimal solution of a given application. Computer software was written to automate the design process. The FEA methods can then be used to gain more accuracy in performance estimations and to refine designs.

To verify the performance calculations in the design model, two commercial motors with known performance were used. Torque calculated by the design model was identical to that by the lumped

-157-

models. The design model was then applied to design an induction motor for vector control, given the necessary requirements. The motor was fabricated and experimental results were collected with a current supply. The experimental results were compared with performance estimations from the design model and FEA method. Torque estimation errors were within fifteen percent.

VIII.B. Suggestions for Future Work

Improvements and additions can still be made in the developed lumped models, design model, and FEA methods. These modifications are left for future work. The foundation has been built.

The simplistic lumped models establish a framework around which more complex models may be developed. To model transient motor performance, rotor speed can be allowed to vary in the lumped models by incorporating mechanical considerations such as moment of inertia and damping. The transient performance is especially important in analyzing short duration overloading capabilities and for motors driven by scalar control and vector control. Also, a better method needs to be developed near stall to include hysteresis and eddy current losses in calculating torque. Furthermore, three-dimensional leakage flux in the four-hundred-hertz motor needs to be modelled better in order to reduce the extremely large current driven torque estimation errors in the FEA method.

Transient performance can be estimated from the lumped models by including temporal and spatial harmonics. Imbalanced excitation, which causes temporal harmonics, can be incorporated by adding harmonics in the voltages and currents. Imbalanced windings and slotting effects, which cause spatial harmonics, can be incorporated by adding harmonics in the air gap flux density distributions. Temporal harmonics in input voltages cause temporal harmonics in the stator currents, which produce temporal harmonics in the stator flux. Temporal harmonics in the stator flux in conjunction with spatial harmonics in the air gap produce harmonics in the stator air gap flux density distribution. As a result, temporal harmonics in the rotor currents are induced, producing temporal harmonics in the rotor flux.

The interaction from only the fundamentals of stator and rotor air gap fluxes produces useful torque. The interaction from harmonics is undesirable because it causes heating, vibration and noise problems. For transient performance, the lumped magnetic and electrical models can be used to analyze the interaction of these harmonics. In deriving the transient performance, transient temperatures obtained

-158-

from the lumped thermal model can also be used.

Although closed-form expressions of transient performance characteristics may not be possible, more general applications and more accurate solutions may be attained. If a numerical solution process is used, however, the additional harmonics can be easily included. But, the direct relationships of geometry to performance from the approximate closed-form expressions are usually more practical to designers than more precise numerical solutions.

The iterative design model developed for the voltage driven induction motor is a basis upon which other application dependent models can be developed. For variable speed motors, another iteration can be added around the excitation frequency. For motors driven by vector control, slight modifications are possible to design from stator currents instead of input voltages.

Improvements can be also made in the FEA methods which use two-dimensional field solvers. Three-dimensional FEA can be used so that approximations of three-dimensional effects are not needed. Unfortunately, these FEA packages are still not very practical because they are expensive, mesh development is tedious, and solution time is long. Also, the solution convergence problems in the transient FEA method need to be solved to calculate transient performance.

APPENDIX A

EQUIVALENT "T" CIRCUIT MODEL

A.1. Introduction

The traditional approach to modelling the induction motor revolves around the well-known equivalent "T" circuit model. The model is presently the most common method of induction motor analysis and design. To model the induction motor, the general equivalent circuit model is presented. Output performance expressions derived from the model are discussed. The traditional strategy of modelling the induction motor by FEA through the equivalent circuit model is briefly described. The traditional design approach which uses the equivalent circuit model is introduced.

A.2. Description of the Equivalent "T" Circuit Model

The equivalent circuit model is derived from the transformer model. The induction motor is often modelled through the analysis of the transformer. Rotor bar currents are induced in the induction motor as currents in the secondary coils are induced in the transformer. In the former, however, leakage flux is much more significant and the rotor rotates.

Figure A.1 shows the general equivalent "T" circuit model[49] for one stator phase. Hysteresis and eddy current losses in the steel are commonly neglected from the model because they tend to be small. Kirchhoff's voltage law is used to write voltage equations describing the model:

$$v_{in}^k = R_1 i_s^k + j\omega_e L_s i_s^k + j\omega_e L_m\left(i_s^k + i_2^k\right)$$

$$0 = \frac{R_2}{s} i_2^k + j\omega_e L_2 i_2^k + j\omega_e L_m\left(i_s^k + i_2^k\right)$$

A-1

All actual rotor parameters are hidden because they are referred to the stator. Some physical interpretation is lost in the process. The rotor parameters are expressed on a per-stator-phase, not per-rotor-phase, basis

---

[49]A. E. Fitzgerald, Charles Jr. Kingsley, and Stephen D. Umans, *Electric Machinery*, Fifth Edition, New York: McGraw-Hill, Inc., 1990, pp. 328-334.

-160-

and transformed from the rotating to the stationary reference frame. Therefore, referred rotor currents oscillate at the excitation frequency.
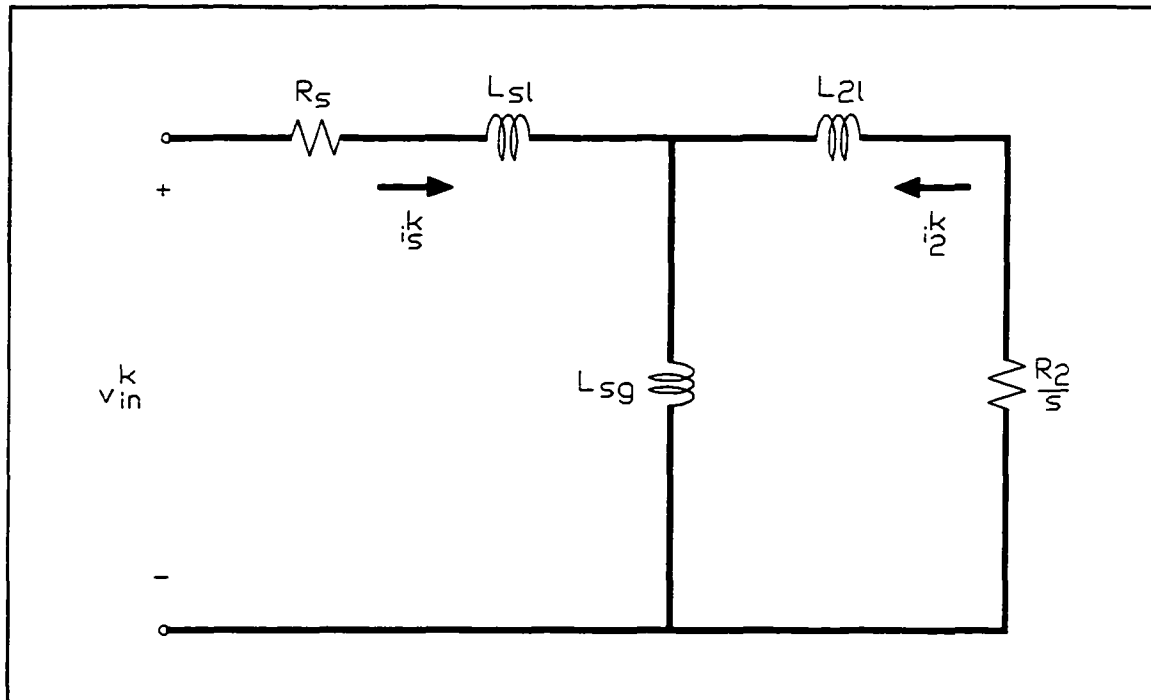

Figure A.1 General equivalent "T" circuit model per stator phase.

A.3. Output Performance Characteristics

To calculate induction motor performance, P. H. Trickey implemented the equivalent circuit model in a Fortran computer program. Hysteresis and eddy current losses, which have been ignored in the equivalent circuit model, are included in determining performance as in the developed lumped electrical model of Chapter III. From a known set of motor geometry and material properties, output performance characteristics[50] are calculated. Performance equations are consistent with those from the developed lumped electrical model, although the implementation of the two approaches differs.

A.4. Extracting Parameters from Magnetic FEA

The equivalent circuit model is also used in the traditional strategy of modelling the induction motor by FEA. The model parameters are first extracted from the field solutions. Then, performance is

---

[50]A. E. Fitzgerald, Charles Jr. Kingsley, and Stephen D. Umans, *Electric Machinery*, Fifth Edition, New York: McGraw-Hill, Inc., 1990, pp. 332-336.

-161-

evaluated from the equivalent circuit model.

Torque equals the rotor resistive power loss scaled by the number of pole pairs and divided by slip frequency when hysteresis and eddy current losses are neglected.[51] The steady state torque is based on symmetry from excitation that is balanced in time and space, evenly spaced rotor bars, and an integral number of rotor phases. Also, motors are assumed to have multiple stator and rotor phases.

A.5. Design Model

The traditional design approach relies on empirical data from existing motors and the equivalent circuit model.[52] However, designing motors outside the range of empirical data through extrapolation may cause large errors.

The design strategy begins with desired output power and number of poles. From this, a minimum motor volume is determined using empirical data of existing motors. A good combination of stator outer diameter and stack height is chosen to avoid lopsided proportions causing twisting and vibration problems. The stator inner diameter, air gap length, and stator and rotor slot dimensions are designed from empirical data of existing motors. General rules of thumb for favorable combinations of stator and rotor slot counts are published that produce small harmonics. Number of stator winding turns is selected from a desired maximum stator tooth flux density level through maximum air gap flux. The thickest stator winding wire is used for the highest practical fill factor. Rotor end ring thickness is designed from the minimum stall torque requirement.

A.6. Summary

The traditional approach to modelling the induction motor revolves around the well-known equivalent "T" circuit model. The model is presently the most common method of induction motor analysis and design. But, all actual rotor parameters in the model are hidden because they are referred to the stator.

---

[51]R. Belmans, D. Verdyck, T. B. Johansson, W. Geysen, and R. D. Findlay, "Calculation of the No-Load and Torque Speed Characteristic of Induction Motors Using Finite Elements," *International Conference on Electrical Machines*, August 13-15, 1990, pp. 724-729.

[52]Cyril G. Veinott, *Theory and Design of Small Induction Motors*, New York: McGraw-Hill Book Company, Inc., 1959, pp. 371-467.

-162-

Some physical interpretation is lost in the process.

To calculate induction motor performance, P. H. Trickey implemented the equivalent circuit model in a Fortran computer program. Performance equations are consistent with those from the developed lumped electrical model, although the implementation of the two approaches differs.

The equivalent circuit model is also used in the traditional strategy of modelling the induction motor by FEA. Torque equals the rotor resistive power loss scaled by the number of pole pairs and divided by slip frequency when hysteresis and eddy current losses are neglected. The steady state torque is based on symmetry and motors are assumed to have multiple stator and rotor phases.

The traditional design approach relies on empirical data from existing motors and the equivalent circuit model. However, designing motors outside the range of empirical data through extrapolation may cause large errors. The design strategy begins with desired output power and number of poles. Then, stator outer and inner diameters, stack height, air gap length, stator and rotor slot dimensions, stator and rotor slot counts, number of stator winding turns, stator winding wire size, and rotor end ring thickness are all designed.

-163-

APPENDIX B

VECTOR CONTROL

B.1. Introduction

In today's competitive motion control market more demanding specifications require better designs. In response, vector control has been recently developed to provide the induction motor with the ability to produce higher torque at variable speeds and to attain higher running efficiency. Motors are designed to always operate at optimal torque production by monitoring steady state as well as transient performance characteristics. With vector control, the induction motor can provide accurate position control. Vector control ensures optimal output even under changing load conditions. Overloading occurs only when the maximum supply current is exceeded. Vector control can even provide better dynamic performance than DC drives due to faster allowable speeds and shorter motor time constants.[53]

B.2. Description of Vector Control

The classical approach to vector control of the induction motor is through the rotor flux vector. With rotor speed and output torque monitored, vector control adjusts both the amplitude and phase angle of the currents from the current supply to achieve desired performance. The adjustments are based on the rotor flux vector.

A significant amount of research led by Thomas A. Lipo and Donald W. Novotny has been done in the Department of Engineering Professional Development at the University of Wisconsin-Madison. A thorough discussion of vector control and its application is in the footnoted reference.[54]

Ideally, optimal torque is produced when stator and rotor flux vectors are orthogonal. Although

---

[53] Andrzej M. Trzynadlowski, *The Field Orientation Principle in Control of Induction Motors*, Boston: Kluwer Academic Publishers, 1994, p. xvi.

[54] Deepakraj M. Divan, Thomas A. Lipo, Robert D. Lorenz, Donald W. Novotny, Allan B. Plunkett, and Joseph T. Warnemuende, "Dynamics and Control of AC Drives," Department of Engineering Professional Development, College of Engineering, University of Wisconsin-Madison, Madison, Wisconsin, Short Course Notes, August 12-15, 1991.

-164-

the stator flux vector is easily controlled, independent control of the rotor flux vector is not simple. This is because the rotor flux vector in the induction motor is purely the result of the induction process and depends on the stator currents and rotor speed.

However, optimal torque production can be achieved through decoupling of the stator currents into two components, flux producing and torque producing. In the decoupling, motor parameters are transformed to any one of several reference frames. In the stationary reference frame, which is fixed on the stator, all rotor parameters are referred to the stator. The excitation reference frame rotates at the excitation frequency. In the rotating reference frame, which is fixed on the rotor, Park's transformation is used to refer all stator parameters to the rotor.

Many methods of implementation exist for vector control. Two classical approaches are commonly used to detect the rotor flux vector which varies with rotor speed. Direct rotor flux oriented scheme uses flux feedback control from direct measurements through flux observers such as Hall-effect sensors. Indirect rotor flux oriented scheme uses flux feedforward control from the monitored stator currents and rotor speed.[55]

---

[55]Peter Vas, *Vector Control of AC Machines*, Oxford: Oxford University Press, 1990, pp. 124-125.

REFERENCES

[1] Akiyama, Yuji and Takaku, Kaneo, "A Study of the Most Suitable Design of Inverter-Driven Induction Motors," *Powerconversion Intelligent Motion*, June, 1994, pp. 38-44.

[2] Alger, Philip L., *The Nature of Polyphase Induction Machines*. New York: John Wiley & Sons, Inc., 1951.

[3] Appleman, W. R., "The Cause and Elimination of Noise in Small Motors," *Electrical Engineering*, November, 1937, pp. 1359-1367.

[4] Belmans, R., Verdyck, D., Johansson, T. B., Geysen, W., and Findlay, R. D., "Calculation of the No-Load and Torque Speed Characteristic of Induction Motors Using Finite Elements," *International Conference on Electrical Machines*, August 13-15, 1990, pp. 724-729.

[5] Blaschke, F., "The Principle of Field-Orientation as Applied to the New 'Transvektor' Closed-Loop Control System for Rotating-Field Machines," *Siemens Review*, Vol. 34, No. 5, 1972, pp. 217-220.

[6] Chan, C. C., Yan, Lietong, Chen, Pizhang, Wang, Zezhong, and Chau, K. T., "Analysis of Electromagnetic and Thermal Fields For Induction Motors During Starting," *IEEE Transactions on Energy Conversion*, Vol. 9, No. 1, March, 1994, pp. 53-60.

[7] Coulomb, J. L. and Meunier, G., "Finite Element Implementation of Virtual Work Principle for Magnetic or Electric Force and Torque Computation," *IEEE Transactions on Magnetics*, Vol. MAG-20, No. 5, September, 1984, pp. 1894-1896.

[8] Divan, Deepakraj M., Lipo, Thomas A., Lorenz, Robert D., Novotny, Donald W., Plunkett, Allan B., and Warnemuende, Joseph T., "Dynamics and Control of AC Drives," Department of Engineering Professional Development, College of Engineering, University of Wisconsin-Madison, Madison, Wisconsin, Short Course Notes, August 12-15, 1991.

[9] "Electric Machines: Analysis and Design Innovation, Summary of Publications 1981-1991/Parts 1 and 2," Wisconsin Electric Machines and Power Electronics Consortium, College of Engineering, Department of Electrical and Computer Engineering, University of Wisconsin-Madison, Madison, Wisconsin.

[10] "Field Orientation and High Performance Motion Control, Summary of Publications 1981-1988," Wisconsin Electric Machines and Power Electronics Consortium, College of Engineering, Department of Electrical and Computer Engineering, University of Wisconsin-Madison, Madison, Wisconsin, March, 1989.

[11] Fitzgerald, A. E., Kingsley, Charles Jr., and Umans, Stephen D., *Electric Machinery*, Fifth Edition. New York: McGraw-Hill, Inc., 1990.

[12] Halliday, David and Resnick, Robert, *Fundamentals of Physics*, Second Edition, Extended Version. New York: John Wiley & Sons, Inc., 1970.

[13] Harned, Timothy J. and Prina, Steven R., "Finite Element Analysis of Electro-Mechanical Devices," *Proceedings From Sixteenth Annual Symposium of Incremental Motion Control Systems and Devices*, June, 1987, pp. 275-296.

[14] Harned, Timothy J., "Transient Finite Element Analysis of Permanent Magnet Magnetization," *Proceedings From Nineteenth Annual Symposium of Incremental Motion Control Systems and Devices*, June, 1990, pp. 52-61.

[15] Hasse, K., "About the Dynamics of Adjustable-Speed Drives with Converter-Fed Squirrel-Cage Induction Motors" (in German), Dissertation, *Darmstadt Technische Hochschule*, 1969.

[16] Holman, J. P., *Heat Transfer*, Fifth Edition. New York: McGraw-Hill, Inc., 1981.

[17] Hoole, S. Ratnajeevan H., *Computer-Aided Analysis and Design of Electromagnetic Devices*. New York, New York: Elsevier Science Publishing Co., Inc., 1989.

[18] Ho, Shine, Prina, Steven R., and Fussell, Barry K., "Lumped Model Torque Prediction For AC Induction Motors," *Proceedings From Twenty-Second Annual Symposium of Incremental Motion Control Systems and Devices*, June, 1993, pp. 386-400.

[19] Ho, Shine, Prina, Steven R., Fussell, Barry K., and Huard, Steven R., "An Iterative Design Process for Voltage-Driven AC Induction Motors with Squirrel-Cage Rotors," *Proceedings From Twenty-Third Annual Symposium of Incremental Motion Control Systems and Devices*, June, 1994, pp. 115-128.

[20] Ho, Shine, Prina, Steven R., Fussell, Barry K., and Taft, Charles K., "A Magnetic Model For Polyphase Induction Motor Torque Prediction," *Proceedings From Twenty-First Annual Symposium of Incremental Motion Control Systems and Devices*, June, 1992, pp. 324-333.

[21] Lipo, Thomas A., *Electromagnetic Design of AC Machines*. College of Engineering, Department of Electrical and Computer Engineering, University of Wisconsin-Madison, Madison, Wisconsin, Course Notes for ECE 713, 1990.

[22] Liwschitz-Garik, Michael and Whipple, Clyde, *Electric Machinery*, Volumes I and II. New York: D. Van Nostrand Company, Inc., 1946.

[23] Lloyd, Tom C., *Electric Motors and Their Applications*. New York: John Wiley & Sons, Inc., 1969.

[24] Lorrain, Paul and Corson, Dale R., *Electromagnetism, Principles and Applications*. San Francisco, California: W. H. Freeman and Company, 1978.

[25] Novotny, Donald W. and Lorenz, Robert D., "Introduction to Field Orientation and High Performance AC Drives, Second Edition", presented at IEEE Industry Applications Society Annual Meeting, Denver, CO, September 28-29, 1986.

[26] Prina, Steven R., "Considerations in the Design of Brushless DC Motors," *Proceedings From Twenty-First Annual Symposium of Incremental Motion Control Systems and Devices*, June, 1992, pp. 1-16.

[27] Richardson, Donald V., *Rotating Electric Machinery and Transformer Technology*, Second Edition. Reston, Virginia: Reston Publishing Company, Inc., 1982.

[28] Silvester, P. P. and Ferrari, R. L., *Finite Elements for Electrical Engineers*, Second Edition. Cambridge: Cambridge University Press, 1990.

[29] Stoll, Richard L., *The Analysis of Eddy Currents*. Oxford: Oxford University Press, 1974.

[30] Taft, C. K., Gauthier, R. G., Harned, T. J., Huard, S. R., and Fussell, B. K., *Brushless Motor System Design and Analysis*, Tenth Edition. College of Engineering & Physical Sciences, University

-167-

of New Hampshire, Durham, New Hampshire, 1996.

[31] "The Effect of Harmonics on Induction Motor Performance," Eastern Air Devices, Incorporated, Dover, New Hampshire, Internal Report.

[32] Trzynadlowski, Andrzej M., *The Field Orientation Principle in Control of Induction Motors*. Boston: Kluwer Academic Publishers, 1994.

[33] Vas, Peter, *Vector Control of AC Machines*. Oxford: Oxford University Press, 1990.

[34] Veinott, Cyril G. and Martin, Joseph E., *Fractional and Subfractional Horsepower Electric Motors*, Fourth Edition. New York: McGraw-Hill Book Company, Inc., 1986.

[35] Veinott, Cyril G., *Theory and Design of Small Induction Motors*. New York: McGraw-Hill Book Company, Inc., 1959.